



**This electronic thesis or dissertation has been
downloaded from Explore Bristol Research,
<http://research-information.bristol.ac.uk>**

Author:

Krajangsawasdi, Knight

Title:

**Highly aligned discontinuous fibre thermoplastic filaments as feedstock for fused
deposition modelling**

production, printing and performance

General rights

Access to the thesis is subject to the Creative Commons Attribution - NonCommercial-No Derivatives 4.0 International Public License. A copy of this may be found at <https://creativecommons.org/licenses/by-nc-nd/4.0/legalcode>. This license sets out your rights and the restrictions that apply to your access to the thesis so it is important you read this before proceeding.

Take down policy

Some pages of this thesis may have been removed for copyright restrictions prior to having it been deposited in Explore Bristol Research. However, if you have discovered material within the thesis that you consider to be unlawful e.g. breaches of copyright (either yours or that of a third party) or any other law, including but not limited to those relating to patent, trademark, confidentiality, data protection, obscenity, defamation, libel, then please contact collections-metadata@bristol.ac.uk and include the following information in your message:

- Your contact details
- Bibliographic details for the item, including a URL
- An outline nature of the complaint

Your claim will be investigated and, where appropriate, the item in question will be removed from public view as soon as possible.

Highly Aligned Discontinuous Fibre Thermoplastic Filaments as Feedstock for Fused Deposition Modelling: Production, Printing and Performance

By
Narongkorn Krajangsawasdi



Department of Aerospace Engineering
UNIVERSITY OF BRISTOL

A dissertation submitted to the University of Bristol in accordance with the requirements for award of the degree of DOCTOR OF PHILOSOPHY in the Faculty of Engineering.
April 2023

Word count: ~66,200 words

Abstract

Fused deposition modelling (FDM), a thermoplastic layer-by-layer additive manufacturing technique also known as 3D printing, can quickly build complex geometries, reducing design limitations and production costs of conventional manufacturing methods. Using a fibrous reinforcement strengthens the thermoplastic matrix, allowing FDM to be used in more structural complex-shape small-size applications. Aligned discontinuous fibre composites (ADFRC) incorporate a high-performance reinforcement architecture that, owing to a sufficient fibre length and high alignment, results in mechanical performance comparable to those of continuous fibre composites as well as higher formability and fewer manufacturing defects.

DcAFF (Discontinuous Aligned Fibre Filament) is a novel ADFRC filament developed for 3D printing aiming to achieve both high mechanical performance and formability. The ADFRC used in this thesis is produced with the High Performance Discontinuous Fibre (HiPerDiF) technology. The DcAFF filament was studied in three main areas: production, printing, and performance. A high production rate filament-forming machine was designed to compress the high aspect ratio cross-section of the tape outputted by the HiPerDiF into a square cross-section filament before its pultrusion to obtain a circular cross-section filament. The designed filament-forming process ensures that a large fraction of the fibres in the final product is well aligned with the longitudinal axis of the filament and the void content is minimised. The printability of the DcAFF filament is relatively good in straight rasters, but there are some discrepancies between the desired and deposited raster at sharp deposition turnings. This discrepancy was minimized with a first-order lag relationship and PI controller that offered an additional path to compensate for the turning corner. The DcAFF material was evaluated with different testing approaches: tensile, open-hole and short beam shear. Overall,

considering the information available in the literature for 3D printed composites using the same matrix, *i.e.* PLA, DcAFF shows mechanical performances superior to those reinforced with short fibres and comparable to those employing continuous ones. It is concluded that the use of ADFRC in DcAFF filament is sufficient to provide performance comparable to continuous fibre composites and relatively better formability compared to the 3D printing of continuous fibre. This paves the way for this material as a candidate for high-performance 3D printing.

Dedication and Acknowledgements

I would like to thank Dr. Dmitry Ivanov, my primary supervisor, for his supervision and for always stepping in to take this primary supervisor role in my PhD.

I also would like to thank Dr. Marco Longana, who used to be my primary supervisor during the most important time in my PhD, for his continual support not only from the academic point of view but also from mental health and everyday problems, anytime I wanted.

I thank Prof. Ian Hamerton for his supervisory role, guidance, and special advice on chemistry plus well English writing support.

I thank Dr. Benjamin Woods, king of creativity, for his innovative idea for building the DcAFF machine and upgrading my project.

I thank you Prof. Paul Weaver for choosing me to join this wonderful ACCIS CDT programme which offered me opportunities to work with wonderful colleagues. Moreover, I would like to acknowledge the Engineering and Physical Sciences Research Council (EPSRC) for funding the Centre for Doctoral Training in Advanced Composites for Innovation and Science (EP/L016028/1) for this opportunity to explore new manufacturing methods for composite materials.

Most importantly, I want to thank and acknowledge the Office of the Civil Service Commission (OCSC) and Faculty of Engineering, Kasetsart University, Thailand for financial support and the Office of Educational Affairs (OEA), Royal Thai Embassy, London for helpful guidance and support during the difficult times.

My gratitude extends to the BCI lab staff for their unwavering commitment to arranging the lab during the pandemic and providing assistance at every stage of my experiment. Without you guys, none of the BCI students would graduate.

For CDT-18 cohort and HiPerDiF crew, you are so inspired, without you my PhD journey would be boring and may take longer than this to finish. Thank you.

And lastly, I would like to thank my family, my partner and everyone who passed in my life since the first day of my PhD for their mental support and for making my life in the UK enjoyable enough for me to finish this horrid Ph.D.

Author's Declaration

I declare that the work in this dissertation was carried out in accordance with the requirements of the University's Regulations and Code of Practice for Research Degree Programmes and that it has not been submitted for any other academic award. Except where indicated by specific references in the text, the work is the candidate's own work. Work done in collaboration with, or with the assistance of, others, is indicated as such. Any views expressed in the dissertation are those of the author.

SIGNED: DATE:

Narongkorn Krajangsawasdi

List of Publications

The works presented in this thesis have been published in some peer-reviewed journals.

Published articles

- I. [1] **N. Krajangsawasdi**, L. G. Blok, I. Hamerton, M. L. Longana, B. K. S. Woods, and D. S. Ivanov, "Fused Deposition Modelling of Fibre Reinforced Polymer Composites: A Parametric Review," *Journal of Composites Science*, vol. 5, no. 1, p. 29, 2021. DOI: 10.3390/jcs5010029.
- II. [2] **N. Krajangsawasdi**, M. L. Longana, I. Hamerton, B. K. Woods, and D. S. Ivanov, "Batch production and fused filament fabrication of highly aligned discontinuous fibre thermoplastic filaments," *Additive Manufacturing*, vol. 48, p. 102359, 2021. DOI: 10.1016/j.addma.2021.102359.
- III. [3] **N. Krajangsawasdi**, I. Hamerton, B. K. S. Woods, D. S. Ivanov, and M. L. Longana, "Open Hole Tension of 3D Printed Aligned Discontinuous Composites," *Materials*, vol. 15, no. 23, p. 8698, 2022. DOI: 10.3390/ma15238698.
- IV. [4] **N. Krajangsawasdi et al.**, "DcAFF (Discontinuous Aligned Fibre Filament)– Investigation of mechanical properties of multilayer composites from 3D printing," *Composites Part B: Engineering*, vol. 264, p. 110903, 2023. DOI: 10.1016/j.compositesb.2023.110903.
- V. [5] **N. Krajangsawasdi**, D. H. Nguyen, I. Hamerton, B. K. Woods, D. S. Ivanov, and M. L. Longana, "Steering Potential for Printing Highly Aligned Discontinuous Fibre Composite Filament," *Materials*, vol. 16, no. 8, p. 3279, 2023. DOI: 10.3390/ma16083279.

Use of published work in this thesis

This thesis is prepared by following the guidance on the integration of publications as chapters within the dissertation. Chapters 2, 3, 5 and 6 are adapted from articles *I*, *II*, *IV* and *V*, respectively. Chapter 4 uses the main content in article *III* plus some content in article *IV*.

Table of Contents

Abstract	i
Dedication and Acknowledgements	iii
Author's Declaration.....	iv
List of Publications	v
Table of Contents.....	vi
List of Figures	xii
List of Table	xxvi
Abbreviations.....	xxviii
Symbols.....	xxx
Chapter 1 Introduction	1
1.1. Background.....	1
1.1.1. Previous research on printing of ADFRC	6
1.2. Aim and objectives	8
1.3. Novelty statement.....	9
1.4. Dissertation outline	9
Chapter 2 Literature Review.....	13
2.1. Chapter introduction.....	14
2.2. Printing parameters.....	15
2.2.1. Printing speed	16
2.2.2. Material feed rate or extrusion rate.....	18
2.2.3. Nozzle temperature.....	19

2.2.4. Bed temperature and environmental control	22
2.2.5. Building orientation	23
2.2.6. Raster angle	27
2.2.7. Raster distance (raster width and air gap)	32
2.2.8. Raster/layer thickness	33
2.2.9. Contour numbers.....	34
2.2.10. Infill volume (% infill)	35
2.2.11. Nozzle geometry.....	36
2.3. Material parameters	38
2.3.1. Matrix	38
2.3.2. Reinforcement	41
2.3.3. Additional materials.....	59
2.4. Chapter discussion	60
2.5. Chapter conclusion.....	61
2.6. List of the available literature on FDM.....	63
Chapter 3 Manual Moulding Filament.....	72
3.1. Chapter introduction.....	73
3.2. Materials properties.....	74
3.3. Manual filament forming manufacturing	74
3.3.1. Stage (A): preparation of fibre and matrix	74
3.3.2. Stage (B): consolidation.....	75
3.3.3. Stage (C): manual moulding	76

3.3.4. Stage (D): pultrusion	78
3.4. Filament characterisation.....	80
3.4.1. Thermogravimetric analysis of the HiPerDiF-PLA tape.....	80
3.4.2. Fibre alignment calculation with microscopic image method	80
3.4.3. Fibre content investigation in filament.....	81
3.4.4. Filament mechanical performance	85
3.5. Printing parameter study	87
3.5.1. Parametric selection	87
3.5.2. Set-up printing trial with 4-piece moulded 1.2-mm circular filament.....	88
3.5.3. Refined printing trial with 2-piece moulded 1.1-mm circular filament ..	90
3.5.4. Single-layer printing trial	91
3.6. Mechanical performance investigation	92
3.6.1. Comparison of the different stages of filament manufacturing	92
3.6.2. Failure mechanism during tensile testing.....	96
3.6.3. Properties comparison to other 3D printing composites	98
3.7. Chapter conclusion.....	99
Chapter 4 Automated Filament Forming Machine	101
4.1. Chapter introduction.....	102
4.2. Materials and filament forming method	103
4.2.1. Roller compaction machine.....	104
4.2.2. Movable nozzle pultrusion	106
4.3. Filament characterisation.....	107

4.3.1. Fibre content investigation in filament.....	107
4.3.2. DcAFF filament fibre alignment angle measurement	108
4.4. Tensile properties characterisation	114
4.4.1. Single-layer tensile specimen preparation.....	114
4.4.2. Tensile testing and result.....	117
4.4.3. Comparison of the DcAFF to literature (considering fibre content)	118
4.5. Open-hole testing.....	119
4.5.1. Open-hole specimen fabrication.....	120
4.5.2. Open-hole testing method.....	124
4.5.3. Open-hole testing result	124
4.6. Chapter conclusion.....	129
Chapter 5 Multilayer Printing	132
5.1. Chapter introduction.....	133
5.2. DcAFF filament quality.....	134
5.2.1. DcAFF filament production	134
5.2.2. Fibre content investigation.....	135
5.3. Multilayer Tensile testing.....	136
5.3.1. Tensile specimen preparation and testing procedure	136
5.3.2. Tensile testing result.....	139
5.4. Short beam shear testing (SBS)	143
5.4.1. SBS specimen preparation and testing procedure	144
5.4.2. SBS testing result.....	146

5.5. Multilayer open-hole tensile testing	149
5.5.1. Open-hole tensile specimen preparation and testing.....	149
5.5.2. Open-hole tensile testing procedure	152
5.5.3. Open-hole tensile test result.....	153
5.6. Chapter conclusion.....	158
Chapter 6 Printing Accuracy Improvement	160
6.1. Chapter introduction.....	161
6.2. Material and printing methodology	163
6.3. Dimension accuracy study	164
6.4. Printing modification by tuning printing parameters.....	165
6.5. Printing modification by adding compensation coordinates.....	168
6.5.1. Algorithm development	168
6.5.2. Tuning the compensation algorithm	171
6.5.3. Path compensation of curvilinear printing.....	175
6.6. Chapter conclusion.....	179
Chapter 7 Overall Discussion	181
7.1. Production of DcAFF filament.....	181
7.2. Printing.....	185
7.2.1. Printing parameter trial	186
7.2.2. In-plane printing defect and mitigation	187
7.2.3. Inter-raster defects, in-plane and through-thickness, and mitigation ...	194
7.3. Performance.....	196

7.3.1. Fibre alignment	196
7.3.2. Fibre volume fraction.....	198
7.3.3. Mechanical performance	198
Chapter 8 Thesis conclusion	203
8.1. Conclusions.....	203
8.2. Suggestions for future work.....	205
Appendix A: Microscopic method.....	208
References.....	209

List of Figures

Figure 1.1 Effect of fibre architectures on mechanical performance and processability/formability [46].....	4
Figure 1.2. Schematic describing the HiPerDiF process starting from spraying fibre onto a plate to create an aligned fibre preform about 5 mm in width and ending with impregnated preform tape [47].	5
Figure 1.3 Potential continuous tape transformation machine by feeding the tape to a convergence channel under heat using a stepper motor proposed by Blok [50].	7
Figure 1.4 Problems of the tape feeding to the convergence channel: (a) micro-buckling effect under compressive force caused by pressure-drop (Δp) between inlet and outlet; (b) folding upon entry [50].	7
Figure 1.5 3D printing of spiralling square printing path using 1.3-mm diameter HiPerDiF-PLA filament with different printing speeds at 270 °C, 0.5 mm nozzle height, with different speeds: (a) 10 mm/s; (b) 15 mm/s [50].	7
Figure 2.1 Investigated parameters and properties of the FDM process.	15
Figure 2.2 Tensile strength at different speeds of different materials: T for layer thickness, S.CF for short carbon fibre, C.CF for continuous carbon fibre, and BF for basalt fibre (the information is shown in Tables 2.2-2.4 along with all printing parameters used in the study).	17
Figure 2.3 (a) Temperature distribution of the printed rasters from the highest temperature (red) of the current printing to cold raster (blue) away from the nozzle; raster fusion formation after deposition from (b) initial surface contacting of rasters; (c) heat dissipation from the current deposition and neck growth; (d) molecular chain diffusion between rasters; (e) chain randomization and cold rasters.	20
Figure 2.4 Printing temperature ranges used for selected polymers and composite materials (the information is shown in Tables 2.2-2.4 along with all printing parameters used in the study).	21
Figure 2.5 Bed temperature ranges used for selected polymers and composite materials (the information is shown in Tables 2.2-2.4 along with all printing parameters used in the study).	23

Figure 2.6 Building orientation definition (a) “flat”(F); (b) “on-edge”(E); (c) “upright”(Z) [67].	23
Figure 2.7 Different printing orientations: (a) “flat”; (b) “on-edge”, printing with $[0^\circ/90^\circ]$ raster angle under bending load [71].	25
Figure 2.8 Tensile strengths of different building orientations (the information is shown in Tables 2.2-2.4 along with all printing parameters used in the study). The $[\pm 45^\circ]$ and $[0^\circ/90^\circ]$ are the printing raster pattern described in the raster angle section (Section 2.2.6), (the short fibre samples (ABS/S.CF) are printed and tested mainly in the longitudinal direction).	26
Figure 2.9 Description of printing parameters from the top view including air gaps, raster width, number of contours, and raster width [39].	27
Figure 2.10 Tensile strength of a single raster angle, normally the strength decreases as an increase in the raster angle from 0° to 90° , but there are some fluctuations shown as a dashed line that strength increases when the raster angle increases (the information is shown in Tables 2.2-2.4 along with all printing parameters used in the study).	29
Figure 2.11 Tensile strength of crisscrossing raster angle of neat thermoplastic printing and composite printing (the information is shown in Tables 2.2-2.4 along with all printing parameters used in the study).	30
Figure 2.12 (a) Smooth radius printing path; (b) stop-and-turn trajectory path simulated by Comminal <i>et al.</i> [77]; (c) printing of continuous fibre with the spiral printing path obtained by Blok <i>et al.</i> [43].	31
Figure 2.13 Tensile strength at the various raster/layer thickness of neat thermoplastics and short fibre reinforced thermoplastics, most of the findings show a modest reduction in strength when the thickness increases (the information is shown in Tables 2.2-2.4 along with all printing parameters used in the study).	34
Figure 2.14 Nozzles for Markforged dual-nozzle 3D printer: (a) neat thermoplastic 0.4 mm diameter nozzle; (b) nylon continuous fibre 0.9 mm diameter nozzle [88].	36
Figure 2.15. (a) Conical shape 3D printing nozzle dimension and area of pressure-drop from zone A (large inlet area), B (convergence area), and C (small outlet area); (b) parameters for error calculation of circular nozzle, in Equation (2.5), where R is the radius of the extrusion orifice and β is the angle of the modelled conical nozzle geometry using in the simulation [89].	38

Figure 2.16. Investigation of the different nozzle outlet geometry: circular; square; and star on the deposition geometry at the outlet using ANSYS fluent computational fluid dynamic modelling studied by Papon <i>et al.</i> [76].....	38
Figure 2.17 (a) Six polymers for 3D printer benchmarks according to a study from 3D Matter [92]; (b) sensitivity study of different thermoplastics for producing highly aligned discontinuous fibre thermoplastic 3D printing filament suggested by Blok <i>et al.</i> [47].	39
Figure 2.18 Range (minimum to maximum) of (a) tensile strength; (b) tensile stiffness of neat thermoplastics as a filament (bulk) according to the information and their reference in Table 2.1 and as-printed (chequered pattern) from Table 2.2.	41
Figure 2.19 Short fibre FDM filament processing by mixing and extrusion used by Ning <i>et al.</i> [54].	43
Figure 2.20 Schematic of (a) Markforged dual-nozzle printer for feeding separate impregnated fibre and thermoplastic matrix, modified from Pertuz-Comas <i>et al.</i> [123]; (b) customized co-extrusion continuous FDM process feeding fibre to the melted matrix in the melted pool [51].	45
Figure 2.21. SEM images of the 3D printing filament with the different materials: (a) neat ABS; (b) ABS/CNT; (c) ABS/S.CF; (d) and (e) enlarging of the last two filaments from Zhang <i>et al.</i> [12]; (f) Markforged continuous fibre cross-section showing the large matrix-rich area in the middle of the cross-section from Blok <i>et al.</i> [43].	46
Figure 2.22. Micrograph cross-section of FDM printed part using (a) neat ABS; ABS/S.CF with (a) 10 wt%; (b) 20 wt%; (c) 30 wt%, manufactured by Tekinalp <i>et al.</i> [45].	47
Figure 2.23. Cross-section of printed parts from (a) ABS; (b) ABS/CNT; (c) ABS/S.CF with 0° raster angle and the difference in the inter-raster void formation which shows larger voids in the fibre-reinforced specimen than the neat ABS and nanofibre samples observed by Zhang <i>et al.</i> [12].	48
Figure 2.24. (a) Fibreless area inspected in continuous fibre printed parts; (b) small space between raster of short fibre printed part studied by Blok <i>et al.</i> [43].	52
Figure 2.25. Tensile strength of several reinforcement types: CF, GF, and KF, and architectures: nano-, short, and continuous, with ABS, PLA, and nylon (the information is shown in Tables 2.2-2.4 along with all printing parameters used in the study).	52

Figure 2.26. SEM images showing details of fibre breakage on the rupture surface of the tensile samples with different fibres: (a) C.CF; (b) C.KF; (c) C.GF at 140x magnification, as observed by Chacón <i>et. al</i> [11].	55
Figure 2.27. Fibre breakage at the high amount of randomly aligned fibre in the matrix resulted in minor strength improvement showing the optimized fibre volume fraction in ABS/S.CF filament, observed by Tekinalp <i>et al.</i> [45].	56
Figure 2.28. Tensile strength of composite FDM parts with different percentages of short fibre reinforcements in (a) ABS; (b) PLA with the average neat thermoplastics (as printed) strength shown in the red line (the information was gathered from several studies from Table 2.2-2.4).	57
Figure 2.29 Surface modification of continuous carbon fibre and PLA, proposed by Li <i>et al.</i> [126].	60
Figure 2.30 Printing and material parameters, that can be assigned to the FDM process to high tensile strength and the outgrowths from the setting such as crystalline structure, low porosity, and surface finishing.	60
Figure 3.1 Summarized manual moulding method to produce a circular-shaped DcAFF filament from stages (A) preparation of discontinuous fibre (HiPerDiF) and PLA matrix; (B) consolidation of HiPerDiF-PLA; (C) manual moulding; (D) pultrusion.	75
Figure 3.2. Cross-section of 5 mm wide HiPerDiF-PLA tape.	76
Figure 3.3. (a) Schematic of the 4-piece mould including three aluminium blocks and a press plate with a preform tape inside; (b) cross-section of the moulded filament after moulding with the 4-piece mould; (c) schematic of the 2-piece mould designed with a perfect sharp machined corner shape of the female and male mould; (d) cross-section of the moulded filament with the 2-piece mould under 150°C and 2 MPa condition showing folding tape without thermoplastic fusion; (e) and (f) cross-section of the moulded filament with the 2-piece mould under 200°C and 1 MPa condition at different positions: 120 mm and 240 mm.	76
Figure 3.4. (a)-(c) cross-section microscopy of a 1.2 mm filament produced from the 4-piece mould filament at the different positions along the length; (d)-(e) cross-section microscopy of a 1.1 mm filament produced from 2-piece mould filament at the different positions along the length.	79

Figure 3.5. TGA result of a HiPerDiF-PLA composite material showing no degradation of a sample before 250°C as the mass loss around 0.5%, which is less than the 5% mass loss criterion, at 250°C.	80
Figure 3.6. (a) Concept of fibre alignment calculation using trigonometry concept in the elliptical cut cross-section; (b) histogram of alignment angle in the cross-section of a filament; (c) the analysed filament.....	81
Figure 3.7. Special TGA programme, using Netzsch STA 449 F1 Jupiter, to investigate fibre weight fraction by considering residual fibre content after matrix burn-off including fibre, PLA and DcAFF filament with the temperature profile (red). The FT indicates the filament produced from the 4-piece moulding method and the numbers is the different filaments in the tensile testing below.	83
Figure 3.8. Threshold adjustment to identify fibre in the cross-section of filament in Figure 3.4(b) showing the fibre, red highlighted colour, is 8.1% of the total area in the yellow circle.	83
Figure 3.9. Schematic of circular filament specimen produced from moulded filament with 4-piece and 2-piece mould and the end-tab position in top and side view.....	85
Figure 3.10. Comparison of (a) stiffness and (b) strength of circular filament produced from moulded filament with the 4-piece and 2-piece mould.	87
Figure 3.11. (a) Drawing of the designed nozzle with a 1.4 mm diameter and 1.25 mm fillet radius; (b) brass nozzle used in the printing process.....	88
Figure 3.12. Set-up printing trial with single raster at different conditions for comparison: (a) high deposition speed; (b) low deposition speed; (c) low process temperature; (d1) high process temperature with the fuzzy fibre surface; (d2) high magnification of the fuzzy fibre surface when printing at high process temperature; (e1) low layer thickness with the matrix-rich area; (e2) high magnification at the matrix rich area when printing at low layer thickness.....	89
Figure 3.13. Examples of the printing trial at different conditions from the top view printing with conditions: (a1) Raster-1; (b1) Raster-2; (c1) Raster-3, and cross-section of the printing in conditions: (a2) Raster-1; (b2) Raster-2; (c2) Raster-3.	91
Figure 3.14. (a) Printing path of a rectangular shape with one layer; the rectangle printed part on (b) top surface; (c) side attached to the printing bed surface.	92

Figure 3.15. Schematic of tensile specimens with the end-tab position in top and side view: (a) moulded; (b) filament; (c) printed single raster; (d) printed single layer.	93
Figure 3.16. Stress-strain data clouds of the tested samples presented as the range of the curve for moulded, filament, printing single layer with Raster-1, Raster-2 (M.1-Raster), Raster-3 condition, and single layer printing.	95
Figure 3.17. Comparison of tensile (a) stiffness and (b) strength between DcAFF material at different manufacturing stages from original HiPerDiF-PLA tape [47], moulded, circular filament, single raster printed with Raster-1, Raster-2 (M.1-Raster), Raster-3 condition, and single layer printed with Raster-2 condition (M. 1-Layer).	96
Figure 3.18 Failed samples for each stage of filament development: (a) moulded; (b) filament; (c) Raster-1; (d) Raster-2; (e) Raster-3; and (f) full layer printing (M. 1-Layer).	96
Figure 3.19. SEM images of fibre pull-out failure with fibre-sized holes on the breakage surface investigated in a circular filament after tensile breakage and their high magnification to indicate the pull-out holes.	97
Figure 3.20. SEM images of (a) a moulded filament with a bundle of fibre in the middle that was pulled out under tensile load; (b) a circular filament with a large hole in the middle that leads to failure; (c) a printing part with Raster-3 condition fails at the filament bonding position leaving with clean failure surface without fibre pull-out holes or fibre failure on the surface.	98
Figure 3.21. Comparison of (a) tensile stiffness; (b) tensile strength between the DcAFF printed as single-layer rectangular part and other composite 3D printing from publications: PLA [10, 20, 29, 31, 55, 56, 134, 137, 139-145], PLA-short carbon fibre (PLA/S.CF) [20, 27, 29, 70, 90, 132-137, 159], PLA-continuous carbon fibre (PLA/C.CF) [60, 61, 126, 148-150].	99
Figure 4.1 (a) Concept of male and female roller compaction module with motor driving and cartridge heater temperature control that can produce a square-like cross section filament; (b) 3D sketch of the rollers.	104
Figure 4.2. Square filament after passing through the rollers: (a) folding of tape with poor bonding; (b) microvoids in the filament ; (c) - (d) material overflow at the corners.	105

Figure 4.3. (a) - (b) A schematic of a two-side assembly convergent nozzle before and after assembly; (c) - (d) circular filament after passing through the two-side convergent nozzle.	106
Figure 4.4 (a) The cross section of final pultrusion nozzle; (b) the final perfect circular cross section filament.	107
Figure 4.5 Special TGA programme, using TGA Q500 V20, to investigate fibre weight fraction by considering residual fibre content after matrix burn-off showing the fibre, DcAFF (HiPerDiF-PLA) composite, and PLA with the temperature profile (red line).	108
Figure 4.6 (a) Reference axis to calculate the fibre orientation; (b) FASEP fibre length measurement distribution of fibres processed from the HiPerDiF 3G machine.	111
Figure 4.7 (a) 3D modelling of the μ CT scanned image for cropped tape (2.4 mm wide); (b) fibre orientation angle distribution deviation from the longitudinal axis of the tape.	113
Figure 4.8 (a) 3D modelling of the μ CT scanned image for square-like filament; (b) fibre orientation angle distribution deviation from the longitudinal axis of the square-like filament.	113
Figure 4.9 (a) 3D modelling of the μ CT scanned image for final pultruded circular filament; (b) fibre orientation angle distribution deviation from the longitudinal axis of the circular filament.	114
Figure 4.10 (a) Printing path of large square shape with 90° sharp turning corners to produce four tensile samples starting from inside; (b) top surface of the sharp corner printed part with a zoom-in of a corner [163]; (c) high magnification of the large square as printed; (d) high magnification of the same large square printed after post-printing consolidation.	116
Figure 4.11. Breakage sample of tensile sample: (a) inter-raster failure parallel to the load direction; (b) favourable failure perpendicular to the load direction showing the load transfer to the fibre direction; (c) breakage of the post-printing consolidated sample showing the breakage, parallel to the raster direction.	118

Figure 4.12. Comparison of (a) tensile stiffness; (b) tensile strength between the DcAFF printed as single layer 3D printed part, “DcAFF A. 1-Layer”, (20 tested specimens), the DcAFF printed with manually moulding filament from Chapter 3, “DcAFF M.1-Layer”, (5 specimens) and other composite 3D printing from publications: PLA [10, 20, 29, 31, 55, 56, 134, 137, 139-145] (Table 2.2), PLA-short carbon fibre (PLA/S.CF) [20, 27, 29, 70, 90, 132-137, 159] (Table 2.3), PLA-continuous carbon fibre (PLA/C.CF) [60, 61, 126, 148-150] (Table 2.4), plotting against their fibre weight content. 119

Figure 4.13. (a1) and (b1) Designed curvilinear 3D printing path for 10- and 4-curvature samples; (a2) and (b2) high magnification at the curvature hole of 10- and 4-curvature samples on the bottom side (attached to the printing bed) [163]. 121

Figure 4.14. (a) 4-curvature printed part before post-printing consolidation; (b) the sample after the consolidation under heat and pressure (4C-Oven) showing a smoother surface and better raster fusion. 122

Figure 4.15. (a) Stacking sequence of the layup sample showing four layers with trimming lines to make a 25 mm wide sample; an example of a layup part with a cutting hole using a hollow punching tool: (b) top surface and (c) lower surface (surface attached to the metallic mould) [163]. 123

Figure 4.16. (a) Open-hole strength of different sample types; (b) open-hole stress *versus* average longitudinal strain curves of each sample type showing different failure behaviours. 125

Figure 4.17. Breakage of the open-hole samples: (a) 10C showing hole closing by the inter-raster separation following raster breakage [163]; (b) 4C showing the raster separations with defect at the linear line that occurs before the breakage of the raster at the curvature area; (c) 4C-Oven showing the catastrophic failure in the rasters perpendicular to the load direction; (d) tape lay-up showing breakage perpendicular to the fibre/load direction at the middle of the hole [163]. 126

Figure 4.18. DIC analysis of longitudinal strain (ϵ_x) at the maximum load of each sample in different types: (a) printed 10C; (b) 4C; (c) 4C-Oven (post-printing consolidated part); (d) tape (lay-up part with a punched hole). 126

Figure 4.19. DIC analysis of transverse strain (ϵ_y) at the maximum load of each sample in different types: (a) printed 10C; (b) 4C; (c) 4C-Oven (post-printing consolidated part); (d) tape (lay-up part with a punched hole). 127

Figure 4.20. DIC analysis of in-plane shear strain (ϵ_{xy}) at the maximum load of each sample in different types: (a) printed 10C; (b) 4C; (c) 4C-Oven (post-printing consolidated part); (d) tape (lay-up part with a punched hole).	127
Figure 5.1 Schematic of the HiPerDiF-3G, larger-lab-scale, machine located at the National Composites Centre, UK (developed within EP/P027393/1, High Performance Discontinuous Fibre Composites - a sustainable route to the next generation of composites).....	133
Figure 5.2 Cross-section microscopy of (a) square-like filament after the compression process in the DcAFF machine; (b) final circular filament ready to use in a 3D printer.	135
Figure 5.3 Special TGA programme, using TGA Q500 V20, to investigate fibre weight fraction by considering residual fibre content after matrix burn-off showing the fibre, four DcAFF composite specimens produced from the HiPerDiF-3G machine, and the current used PLA film with the temperature profile (red line).....	136
Figure 5.4 (a) Printing path for 4-layer stacking tensile specimen; (b) top and bottom surface of an as-printed 100-mm-long tensile specimen; (c) cross-section of the printed part showing four layers with four adjacent rasters on each layer.....	137
Figure 5.5 (a) Comparison of the tensile specimen before and after post-printing consolidation; (b) cross-section of the tensile specimen after post-printing consolidation (the cross-section microscopic image was taken after the tensile testing).	138
Figure 5.6 Tensile stress-strain curve of the as-printed and consolidated specimens.	139
Figure 5.7 Comparison of as-printed and consolidated (under heat and pressure) tensile testing mechanical properties: (a) tensile stiffness; (b) tensile strength.	140
Figure 5.8 SEM image of tensile fracture surface: (a) as-printed; (b) post-printing consolidation.	140

Figure 5.9 Comparison of tensile properties: (a) stiffness; (b) strength, between neat PLA [10, 15, 20, 29, 31, 55, 56, 134, 139, 143], short carbon fibre-PLA (PLA-S.CF) [20, 27, 29, 70, 132-134, 136, 137, 159], DcAFF as-printed single layer achieved from Chapter 4 (DcAFF A. 1-Layer), the current test DcAFF multiple layers as-printed indicated by a star “★” (DcAFF M. Multi. L), continuous carbon fibre-PLA (PLA-C.CF) [60, 61, 126, 149, 150] and continuous carbon fibre nylon (Nylon-C.CF) [11, 41, 122, 132, 146, 172-175], the whole composite sample was normalized with fibre weight content to 25 wt% as the average fibre content of the current DcAFF in the checked pattern bar according to the literature data in Table 2.2-2.4. 141

Figure 5.10 (a1)-(b1) Top view of SBS specimen: as-printed and post-printing consolidation; (a2)-(b2) cross-section of 8-layer printed specimen: as-printed and consolidated. 145

Figure 5.11 SBS test setup on the testing machine following the ASTM D2344. 146

Figure 5.12 SBS stress *versus* displacement of the SBS testing: (a) as-printed; (b) post-printed consolidated sample. 147

Figure 5.13 As-printed SBS failure sample: (a) tensile fracture on bottom side; (b) inelastic deformation with side layer separation. 147

Figure 5.14 Post-printed consolidated SBS failure sample: (a) compressive failure on the top surface; (b) mid-layer separation with the kink on the top surface. 148

Figure 5.15 Comparison of the DcAFF SBS strength to other SBS testing in the literature of nylon-continuous carbon fibre reinforcement [9, 58, 125, 177] and PLA-short carbon fibre reinforcement [10, 90, 178]. 148

Figure 5.16 Normal curvilinear open-hole printing (OPH-N): (a) continuous printing path; (b) and (c) example of the printed sample on top and bottom (attached to bed) surface, respectively. 150

Figure 5.17 Modified curvilinear open-hole printing: (a) modified printing path with the overshooting inward through the centre of the hole; (b) and (c) example of the printed sample on top and bottom (attached to bed) surface. 151

Figure 5.18 Drilled sample on three layers 3D printed part: (a) top side; (b) bottom (bed) side. 152

Figure 5.19 Open-hole tensile stress-strain curve of: (a) OPH-N; (b) OPH-M; (c) OPH-D; (d) open-hole strength comparison between three groups of the sample. 154

Figure 5.20 DIC strain map in longitudinal (ϵ_x) at the maximum load of each sample: (a) OPH-N; (b) OPH-M; (c) OPH-D.....	155
Figure 5.21 DIC strain map in transverse (ϵ_y) at the maximum load of each sample: (a) OPH-N; (b) OPH-M; (c) OPH-D.....	155
Figure 5.22 DIC shear (ϵ_{xy}) strain map at the maximum load of each sample: (a) OPH-N; (b) OPH-M; (c) OPH-D.....	156
Figure 5.23 Open-hole tensile testing breakage sample: (a) OPH-N; (b) OPH-M; (c) OPH-D.....	158
Figure 6.1 (a) Open hole printed part with normal curvilinear printing path; (b) open hole printed part with an empirical printing path modification (Chapter 5) by moving the nozzle further inwards.....	162
Figure 6.2 Depsotied rasters at different radii from 5 - 20 mm presenting with the desired path (red line), same as the nozzle path, to show the dimension accuracy....	165
Figure 6.3 Gap between the filament and the bed because of the nozzle fillet end creating an offset of full contact position and the deviation of filament to the vertical middle line of the nozzle due to the smaller filament diameter than the nozzle diameter.....	165
Figure 6.4 Additional machine actions to increase the printing accuracy following the P1 to P5 described above.....	167
Figure 6.5 Schematic of the raster dynamics simulation (a) without; (b) with proportional and integral (PI) compensation.....	169
Figure 6.6 Preliminary shape study (before compensation): (a) 90° square; (b) parallelogram 135° - 45°.	170
Figure 6.7 Simulated nozzle path (a) without; (b) with compensation showing with predicted raster path (the proportional and integral gains used by the PI controllers in (b) are $K_P = 1.5$ and $K_I = 2.5$).	170
Figure 6.8 Triangle deposited rasters: (a) without compensation; (b)-(e) after path compensation with different levels of K_I from 1.5 to 3; (f) with varied K_I ($K_I = 1.5$ at 90°, 2.5 at 120°, 3 at 150° turning angle).....	174
Figure 6.9 Parallelogram deposited rasters: (a) without compensation; (b)-(e) after path compensation with different levels of K_I from 1.5 to 3; (f) with varied K_I ($K_I = 1.5$ at 45°, 2.75 at 135° turning angle).....	175

Figure 6.10 Controller gains, K_P and K_I , that are suitable for specific turning angles according to the experimental result	175
Figure 6.11 10-mm diameter curvilinear open hole part (D10): (a) coordinates of desired raster (red), compensated nozzle path (yellow dotted) and predicted raster (green); (b) deposited raster.	176
Figure 6.12 Curvilinear printed parts of (a) 20 mm; (b) 30 mm diameter without path compensation.	177
Figure 6.13 (a1) and (b1) Compensated path of 20 and 30 mm diameter circle calculated with the PI controller (yellow dotted) showing with the predicted printed path (green) and the desired raster (red); (a2) and (b2) curvilinear printed part of 20 mm and 30 mm diameter with the compensation.	178
Figure 6.14 Example of the vertical deviation calculation of 10-mm compensated curvilinear part showing the assessment points (yellow point), at the middle of the intersection line between the divided line and the deposited raster, and the measured vertical deviation.	179
Figure 7.1 Development of DcAFF 3D printing material from the manual moulding with (a1) the first 4-piece mould to (b1) a single-slot simpler 2-piece mould and (c1) the semi-automated filament forming machine showing the compacted tape (square filament) (a2, b2, c2 according to the developed stages) and the final circular filament after the pultrusion of the compacted filament (a3, b3, c3 according to the developed stages).	181
Figure 7.2 Available short fibre composite filament: (a) SEM image of ABS/S.CF 15 wt% achieved from [12] (Recalled from Figure 2.21(c)); (b) μ CT scanned image of commercial nylon/S.CF from Markforged achieved from [192]; (c) and (d) cross-section microscopy of Markforged nylon/C.CF achieved from [43] and [127], respectively.	183
Figure 7.3 Aerofoil printing presenting different direction changes along the printing path and showing the deposition discrepancy, especially at the leading edge.	187
Figure 7.4 Corners of rectangular full layer printing expected to be used as a tensile specimen: (a) printing at high fibre content (28-32 wt%); (b) printing at lower fibre content (18-25 wt%).....	188
Figure 7.5 High magnification at a corner of a large square printing part: (a) with a sharp 90° corner; (b) a replacement of the sharp turning corner with a 3-mm radius fillet corner.	189

Figure 7.6 Action during printing 90° turning angle with filleted nozzle from (a) side view of the filament feeding to nozzle before deposition on the bed and top view of the deposition when reaching the 90° turning corner showing the misaligned of the filament centre and the nozzle centre (nozzle path); (b) top view of the deposition at the moment just after passing the 90° corner, the filament slightly recover back to the nozzle movement direction; (c) top view of the deposition when the filament fully reaching the nozzle movement and attached to the lower side nozzle wall while the nozzle moving up presenting a blunt corner deposition..... 190

Figure 7.7 Manually adding an overshooting feature at the turning corner to provide a full contact: (a) initial study in a square case; (b) single raster half-circle curvilinear open hole tensile test sample; (c) full-circle curvilinear open hole tensile test sample showing an asymmetric hole shape..... 191

Figure 7.8 Curvilinear open hole printing with the developed algorithm: (a) large hole size 30-mm showing promising deposited hole size and decent deposited raster (recalled from Figure 6.13)); (b) small hole size 10-mm showing large discrepancy.. 193

Figure 7.9 Schematic of void formations found on the cross-section of a multilayer DcAFF 3D printing: (i) inter-raster microvoids, (ii) inter-layer microvoids, (iii) large cavity inter-raster diamond-shaped voids. 194

Figure 7.10 Schematic of open moulding for post-printing consolidation of the 3D printed part used in this thesis..... 196

Figure 7.11 Fibre alignment distribution of HiPerDiF-PLA tape (brown), DcAFF square filament (light yellow dash) and DcAFF circular filament (yellow)..... 197

Figure 7.12 Comparison between the different manufacturing techniques and format of DcAFF: manual moulding as the filament (M. Filament), single raster deposition (M. 1-Raster) and single layer printed part (M. 1-Layer) to the semi-automated filament forming process as a filament (A. Filament), single layer printed part (A. 1-Layer) and finally the multilayer printing (A. Multi-L) showing with the properties obtained from the post-printing consolidation technique of the layer printed part (highlighted in red) comparing with the HiPerDiF/PLA tape achieved from the previous study and normalised all the as-printed part result to the fibre content 25 wt%. 200

Figure 7.13 Tensile stiffness-strength plot of the available composite 3D printed part from literature: PLA [10, 20, 29, 31, 55, 56, 134, 137, 139-145], PLA-short carbon fibre (PLA-S.CF) [20, 27, 29, 70, 90, 132-137, 159], PLA-continuous carbon fibre (PLA-C.CF) [60, 61, 126, 148-150] and continuous carbon fibre nylon (Nylon-C.CF) [11, 41, 42, 122, 132, 146, 172-174], compared with our DcAFF tensile properties studied in this thesis from the thin tape, single filament forming with the manual and semi-automated technique, DcAFF printed as single-layer and the multilayer printing.201

Figure 8.1 Possible application of the high-performance DcAFF filament in the future, *e.g.* automotive replacement parts [195], formula one frame [196], high-strength tooling [197], prosthesis leg [198], UVA parts [199], new design wind turbine [200].205

List of Table

Table 1.1 Work step through the development of the DcAFF material.	11
Table 2.1 Tensile strength and stiffness of neat thermoplastic as a 3D printing filament gathered from various sources.	41
Table 2.2 Summary of parametric study in neat thermoplastic of the FDM process. ...	63
Table 2.3 Summary of parametric study in nano/short fibre thermoplastic FDM process.	66
Table 2.4 Summary of parametric study in continuous fibre thermoplastic FDM process.	69
Table 3.1 Physical and mechanical properties of PLA filament and carbon fibre.	74
Table 3.2 Comparison of fibre content by volume of the same filament batch at the different positions along the length calculated with microscopic image over the polished cross section area and TGA burn-off methods over a certain length (~10-30 mg).....	84
Table 3.3 Properties comparison of circular cross-section filament produced from moulded filament with the 4-piece and 2-piece mould.....	86
Table 3.4 Testing parameters and their levels in the printing trial.	88
Table 3.5 Printing trail with refined conditions.	90
Table 3.6 Tensile properties result from DcAFF at different stages with the HiPerDiF-PLA tape.	94
Table 4.1 Fibre alignment comparison over the development of DcAFF from tape to square-like and finally circular cross-section filament.	112
Table 4.2 Tensile properties comparison of the current DcAFF samples to the previous studies.	118
Table 4.3 DIC technique parameters.....	124
Table 5.1 Collection of 3D printed short beam shear (SBS) strength from literature. .	143

Table 5.2 SBS strength between as-printed and post-printing consolidated specimens.	147
Table 5.3 DIC technique parameters.....	153
Table 6.1 Printing parameter adjustment to tackle the 90° turning corner.....	166
Table 6.2 RMS of vertical deviation measuring from the desired and the centre of the deposited raster.	179
Table A1 Polishing step for microscopy.....	208

Abbreviations

10C	10-curvilinear path
3D	Three dimension
4C	4-curvilinear path
A.	Automated filament forming machine
ABS	Poly(acrylonitrile-butadiene-styrene)
ADFRFC	Aligned discontinuous fibre composite
ALM	Additive layer manufacturing
ATL	Automated tape layup
BF	Basalt fibre
C.CF	Continuous carbon fibre
C.GF	Continuous glass fibre
C.KF	Continuous Kevlar fibre
CAD	Computer-aided design
CF	Carbon fibre
CNC	Computer numerical control
CNT	Carbon nanotube
CTE	Coefficient of thermal expansion
CVS	Curvilinear variable stiffness
DcAFF	Discontinuous aligned fibre filament
DMTA	Dynamic mechanical thermal analysis
DIC	Digital image correlation
EVA	Ethylene-vinyl acetate
FDM	Fused deposition modelling
GF	Glass fibre
HiPerDiF	High performance discontinuous fibre
KF	Kevlar fibre, aramid fibre
LLDPE	Linear low-density polyethylene
M.	Manual filament forming
MWCNT	Multi-walled carbon nanotubes
OPH	Open-hole tensile testing
PA	Polyamide, nylon
PC	Polycarbonate
PEEK	Poly(ether ether ketone)
PEI	Polyetherimide, ULTEM1000
PET	Poly(ethylene terephthalate)
PETG	Poly(ethylene terephthalate glycol)
PI	Proportional–integral controller

PID	Proportional–integral–derivative controller
PLA	Poly(L-lactic acid)
PP	Polypropylene
PPS	Poly(phenylene sulphide)
PTFE	Polytetrafluoroethylene, Teflon
S.CF	Short carbon fibre
S.GF	Short glass fibre
S.KF	Short Kevlar fibre
SBS	Short beam shear
SEM	Scanning electron microscope
STL	Standard triangle language, Stereolithography
TGA	Thermogravimetric analysis
TPU	Thermoplastic polyurethane
VGCFs	Vapour-grown carbon fibres
μCT	Micro-computed tomography

Symbols

1-Layer	Single layer 3D printed part
% infill	Infill volume
D	Filament diameter
d	Nozzle diameter
d_f	Fibre diameter
E	On-edge building orientation
F	Flat building orientation
FR	Feed rate of filament
l_c	Critical fibre length
Multi-L	Multilayer 3D printing part
NC	Number of contours
PS	Printing speed
T	Layer thickness, nozzle height
$T_{5\%}$	Degradation temperature, 5% mass loss
T_D	Calculated composite density
T_g	Glass transition temperature
T_m	Melting temperature
V_f	Fibre volume fraction
vol%	Percentage by volume
wt%	Percentage by weight
X_c	Percentage of crystallinity
Z	Upright building orientation
Δp	Pressure drop
ϵ_x	Longitudinal strain
ϵ_y	Transverse strain
ϵ_{xy}	Shear strain
θ	Fibre orientation angle

Chapter 1 Introduction

1.1. Background

Additive layer manufacturing (ALM) fabricates objects from a three-dimensional (3D), computer-aided design (CAD) model by stacking material in a layer-by-layer arrangement [6]. ALM, also known as rapid prototyping [7, 8], as a layer-based manufacturing method, allows for the fabrication of complex geometries within a short time compared to conventional subtractive manufacturing methods and automates currently labour-intensive operations, *i.e.* composite layup [9-11]. The reduction in design limitations shortens the design and manufacturing cycle whilst speeding up the development process leading to high-efficiency products, especially for mass-customized items [12, 13]. ALM is also cost-effective since it minimises additional expenses, associated with tooling or moulds. The higher degree of automation of ALM can reduce human error and increase product accuracy. After the invention of the first ALM methods, laser-based and photochemical stereolithography (SLA) [7], various other approaches based on layer manufacturing were developed, *e.g.*, selective laser sintering (SLS), powder bed and inkjet head 3D printing (3DP), *etc.* [14, 15].

Among the several ALM methods, one of the most widely used [16, 17] is a polymer fused deposition technique known variously as Fused Deposition Modelling (FDM) [15], Fused Filament Fabrication (FFF) [18], Solid Filament Freeform (SFF) [14, 19], or Material Extrusion Additive Manufacturing (MEAM) [20]. In this thesis, it will be referred to as FDM or 3D printing. The reasons for its popularity compared to other ALM methods are immediately clear: ease of use [21] and no extra equipment required (*e.g.* mould, oven, or tools) [7, 22, 23], leading to lower costs of machines and processes. Typically, raw materials for FDM are thermoplastics in the form of solid feedstock, which are of low toxicity and are easy and safe to handle during processing [24, 25]. Besides, the nature of thermoplastics, which can be heated and reshaped, allows the

products to be recycled [26, 27]. FDM was first developed by S. Scott Crump, co-founder of Stratasys, in 1988 [28-31] and generally, the process starts with generating a 3D CAD model and transforming it into a generic geometry file (typically an .STL file). This geometry file is then “sliced” using one of the many open-source or proprietary slicing software, which cuts the geometry into a series of layers and encodes the machine commands (position, temperature, *etc.*) into a G-code file readable by the FDM machine [28, 29, 32].

During the 3D printing operation, a thermoplastic feedstock is fed into a melt pool where it is heated above its extrusion temperature (T_e) which is dictated by the melting (T_m) and glass transition temperatures (T_g) of the material and the machine’s feeding system configuration [33]. Then, it is finally extruded through a finely-tipped nozzle [20, 24, 33]. The deposited filaments, called rasters (or sometimes road lines or beads), are placed side by side in the horizontal (XY) plane to build a layer. When the first layer is built on the printing bed, the material is deposited on top of the previous raster in the through-thickness direction. The relative movement of the extrusion head and printing bed is defined by computer numerical control (CNC) [7, 32]. The adjacent and overlaid deposited rasters fuse and become a solid part after cooling below the T_g [34]. Sometimes, overhung sections of the geometry need support structures, which are usually made from removable materials (*via* a second nozzle) or perforated junctions [35]. The nature of layer-by-layer deposition and plastic fusion makes the part highly anisotropic [34-36]. Hence, the strength depends mainly on the process parameters to achieve good raster fusion and the mechanical performance of the material itself. The process is restricted to those thermoplastics, of which the most common are listed below, that can be processed at easily achievable temperatures, *i.e.* below 300°C. Most of the commonly used thermoplastics in FDM are commodity thermoplastics, such as polypropylene (PP), poly(acrylonitrile-butadiene-styrene) (ABS), poly(lactic acid) (PLA), polycarbonate (PC), polyamide (PA, nylon) which have low to intermediate

thermal and mechanical properties for general applications [15,28,32,33]. However, these polymers typically have low thermal properties, *i.e.* low T_g , melting temperature (T_m), high tendency to shrink during solidification, *etc.*, and low mechanical performance compared to thermosetting polymers or metals. This usually limits the use of the product to prototypes [20, 33, 37, 38]. To increase the mechanical performance for manufacturing of functional products, high-end thermoplastics such as poly(ether ether ketone) (PEEK) or polyetherimide (PEI, ULTEM1000) can be selected but they require higher processing temperatures, *i.e.* from 350°C, achievable only with special high-temperature machines, high-performance heaters, and heat protection [24, 25, 39]. Another method to improve the low material properties of the common thermoplastics is the composite concept, *i.e.* the reinforcement of the polymeric feedstock with a second phase in the form of fillers or fibres.

Several fibre architectures are available to reinforce the polymer in order to expand the FDM to facilitate more structural applications. The highest strength improvement is achieved when using continuous fibre [40]. Several studies on continuous fibre composite 3D printing by Markforged show an increase in longitudinal tensile strength of the printed part from approximately 30 MPa, for neat nylon, to 400-500 MPa, for pre-impregnated nylon carbon fibre [11, 41, 42]. Although the presence of the continuous fibre strengthens the structure, the low flexibility of the continuous fibre reduces the capability for steering around sharp radii causing defects, *i.e.* matrix-rich pockets and unreinforced areas, and causes weak spots in the part. In contrast, thermoplastics reinforced with either short or chopped fibres, *i.e.* with fibre lengths less than 1 mm, show higher flexibility and formability [43]. Even though short fibre composites are better suited for complex geometries, the overall mechanical performance of the short fibre composite is always lower than one reinforced with continuous fibres. Therefore, only relatively limited improvements over neat thermoplastics can be achieved. This is because the fibre length in the short fibre filaments for FDM, typically below 1 mm, is

usually below the fibre critical length, *i.e.* the length that allows full load transfer from matrix to fibre [44]. The fibre length cannot be controlled due to the nature of the filament manufacturing process, fibre-matrix mixing and extrusion, which are aggressive thermomechanical processes that lead to high levels of fibre breakage. According to short fibre mixing and extrusion studies, the filament production process reduces the fibre length from the initial 1-3 mm to less than 0.3 mm in the filament [27, 44, 45]. At high fibre contents, there is an increase in the fibre interaction that creates more fibre breakage than the lower fibre content [45], so the fibre content of short fibre composite filaments gathered from literature is normally no more than 25% by volume [1]. Moreover, the commercial short fibre filaments present a random fibre distribution without alignment. These two phenomena lower the mechanical performance of the short fibre filaments still further.

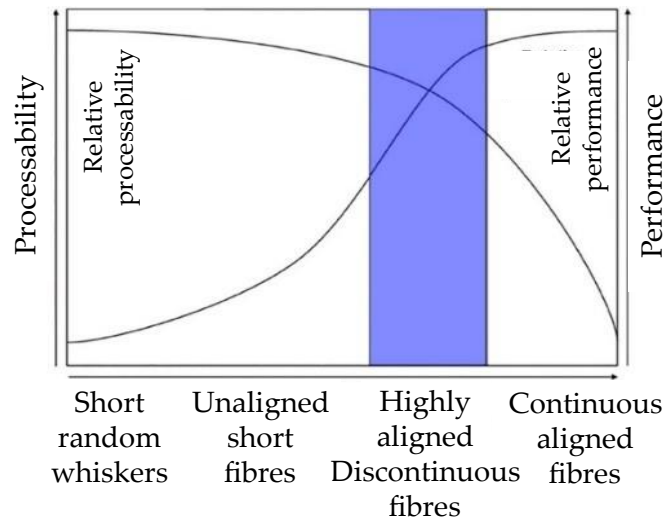


Figure 1.1 Effect of fibre architectures on mechanical performance and processability/formability [46].

Among the fibre architectures presented in Figure 1.1, the aligned discontinuous fibre composite (ADFRC) is a good candidate for the 3D printing filament reinforcement as it offers mechanical performance comparable to that of continuous fibres, as the fibre alignment and fibre longer than the fibre critical length, while retaining the formability of short fibres due to the discontinuous fibre.

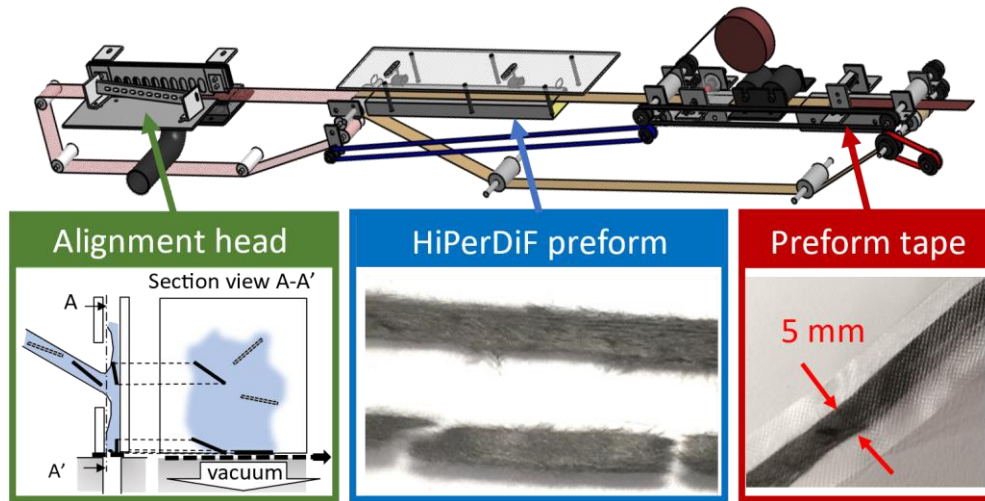


Figure 1.2. Schematic describing the HiPerDiF process starting from spraying fibre onto a plate to create an aligned fibre preform about 5 mm in width and ending with impregnated preform tape [47].

One such novel fibre alignment method, called High Performance Discontinuous Fibre (HiPerDiF) technology, was invented at the University of Bristol [48]. The sudden change in momentum of a fibre-water suspension when impacted against parallel plates is exploited to align the fibre along the gap direction; the suspension is then deposited on a conveyor mesh belt where the water is extracted by suction to obtain a dry fibre preform [48]. The dry preform can be easily disintegrated by pulling, so it is finally impregnated with a matrix, either thermosetting, thermoplastic, or vitrimeric in nature, to obtain a thin prepreg tape [47]. The overall conceptual processes are illustrated in Figure 1.2 the second-generation, laboratory-scale machine. With this process, it was determined that 67% of the fibres were aligned in the main tape direction within a range of $\pm 10^\circ$ [49]. When a HiPerDiF preform was impregnated with PLA to produce a composite tape (5 mm x 0.2 mm in cross-section with approximately 12.5 % fibre fraction by volume, V_f), it showed a substantial improvement over the unreinforced plastic matrix, *i.e.* 300 MPa in strength and 20 GPa in stiffness [47] compared with 30-60 MPa in strength and 2-3 GPa in stiffness of the unreinforced polymers. This high mechanical performance of the HiPerDiF reinforcement leads to the initial idea of using it as a

reinforcement for 3D printing material. The 3D printing process is expected to exploit the high formability of the HiPerDiF material when formed into a fine-diameter filament allowing the production of complex geometries instead of using it as a thin tape for automated tape layup (ATL) which would only allow large curvature steering.

1.1.1. Previous research on printing of ADFRC

A first attempt to produce a 3D printing filament from the HiPerDiF pre-impregnated thermoplastic tape was conducted by Blok [50]. The extrusion concept illustrated in Figure 1.3 was used to reduce the aspect ratio of the flat tape aiming to finally turn it into a circular one by extrusion. The first method, based on the concept of continuous tape feeding to a converging channel with a stepper motor, did not work as a continuous process because the tape, subjected to a “pushing” compressive force, buckled in the nozzle and folded at the entry, as seen in Figure 1.4 (a) and (b), respectively. Owing to these problems, many extrusion stages were required where the nozzle diameter was sequentially reduced. An alternative concept, tested in that study, was a two-step method: a manual moulding technique which compressed the thin tape in a heated aluminium mould to form a rectangular cross-section followed by a pultrusion stage to achieve a circular cross-section. After the pultrusion, the filament contained a large void inside which affected the deposition quality of the raster, as can be seen in Figure 1.5. This 1.3-mm-diameter produced filament could be printed at a very low printing speed showing a poor surface finishing and could not be printed at higher speeds.

This study highlighted the importance of controlling the quality of the produced filament and the challenges associated with creating material forms appropriate for printing. In particular, it can be concluded that minimisation of the void content is an essential challenge to tackle. It also demonstrated the importance of a continuous process that would improve the consistency of the filament quality.

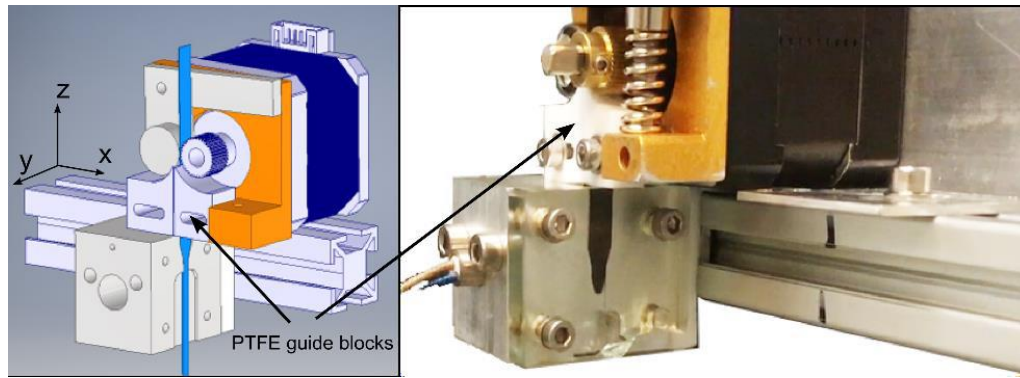


Figure 1.3 Potential continuous tape transformation machine by feeding the tape to a convergence channel under heat using a stepper motor proposed by Blok [50].

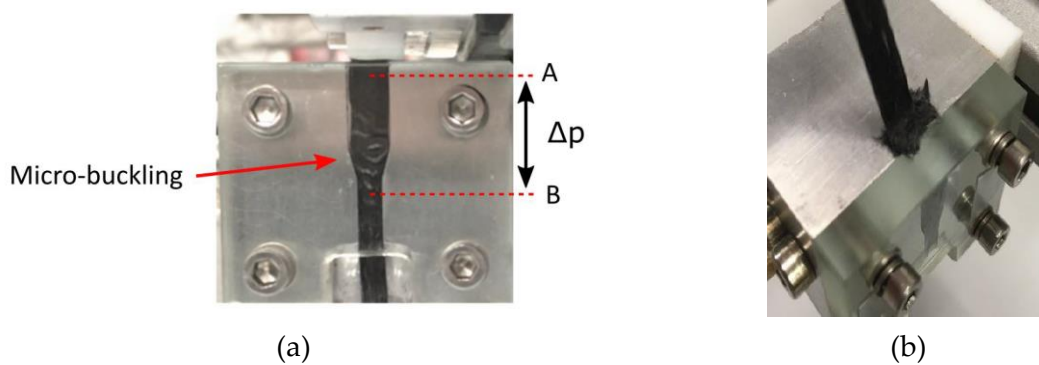


Figure 1.4 Problems of the tape feeding to the convergence channel: (a) micro-buckling effect under compressive force caused by pressure-drop (Δp) between inlet and outlet; (b) folding upon entry [50].

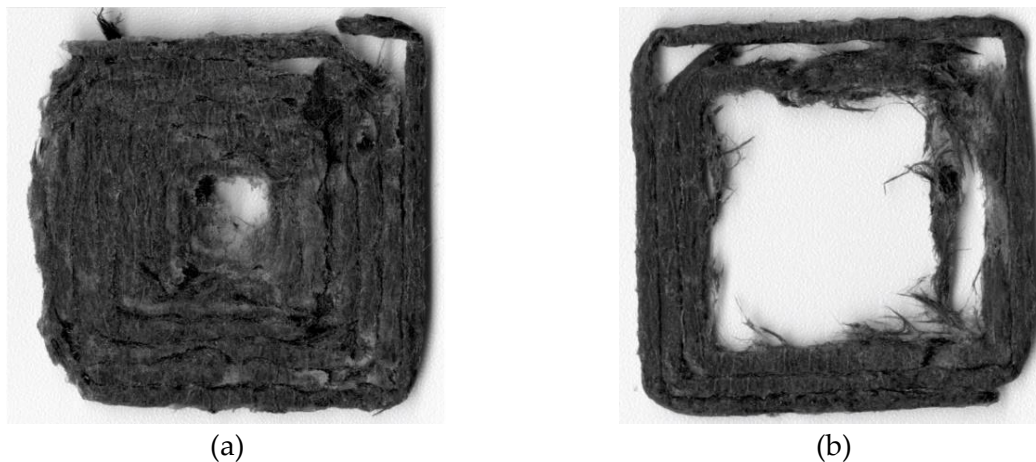


Figure 1.5 3D printing of spiralling square printing path using 1.3-mm diameter HiPerDiF-PLA filament with different printing speeds at 270 °C, 0.5 mm nozzle height, with different speeds: (a) 10 mm/s; (b) 15 mm/s [50].

1.2. Aim and objectives

This thesis aims to produce a novel FDM 3D printing filament reinforced by ADRFC produced with the HiPerDiF technology, known herein as DcAFF¹ (Discontinuous Aligned Fibre Filament), with a method that can be scaled up to an industrial or commercial level. These filaments should be readily adapted for commercially available printers without the need for modification of machinery and processing/printing strategies which can lead to producing a high performance/quality product in a shorter time. This more available stronger product and faster production will progress the world of design and manufacturing to another level. To complete the DcAFF 3D printing material development, the following objectives need to be achieved:

- Assess the state-of-the-art of fibre-reinforced FDM 3D printing and the effect of process parameters on the physical and mechanical properties of the obtained products.
- Develop a filament-forming method, with a continuous and automated process, for HiPerDiF reinforced thermoplastic to produce a composite 3D printing feedstock material with low porosity, fibre breakage and fibre misalignment.
- Create filaments that can be used in conventional commercially available 3D printers and require minor modifications of the machines.
- Develop practical 3D printing techniques for the produced DcAFF filament to fabricate complex geometry parts with minimised defects.
- Characterise the mechanical and physical properties of DcAFF 3D printed parts and benchmark them against the available FDM 3D printing composite materials reported in the literature.

¹ For 3D printing without the headaches.

1.3. Novelty statement

Among the FDM 3D printing composite materials available in the literature and market, short/micro or continuous fibre-reinforced thermoplastic materials for 3D printing are widely present, but there is no evidence of using aligned discontinuous fibre reinforcement in this technology. In this work, for the first time, aligned discontinuous fibre composite 3D printing filament has been mass-produced with a bespoke continuous, semi-automated machine. The novel ability to create long lengths of filament allows for investigations into the 3D printing of complex geometries with discontinuous fibre filament, which has never been done before. In addition to the overarching novelty of this work, there are also a series of more specific novel developments and achievements:

- The feasibility of novel methods for continuously creating good-quality ADFRC filaments is explored. Their potential for mass production is examined.
- The moulding technique for transforming the ADFRC pre-impregnated tape into a filament was designed with the aim of preserving fibre alignment, avoiding tearing the material apart, and minimising internal defects.
- The creation of an industrially scalable filament-forming machine (the DcAFF machine) is attempted with the perspective of a high filament manufacturing rate and low filament defect.
- Multilayer structural parts are constructed using the new materials forms and their morphology and properties are investigated.
- A novel method to improve printing accuracy when steering the filament along complex shapes was devised.

1.4. Dissertation outline

This dissertation was constructed by integrating the first-authored publications of the author as chapters, according to the University of Bristol's guidance, to offer a narrative

of the DcAFF material development from the study of the available material, *i.e.* the HiPerDiF initial format, passing through the different filament-forming methods, from manual moulding to a semi-automated machine, and ending with the final filament performance investigation and its printing technique development. These project stages are presented in sequence in the forthcoming chapters, organised as follows.

Chapter 2 is a literature review aimed at identifying the processing parameters of FDM 3D printing that affect the part quality, and the effects of the fibre reinforcement in the 3D printing material. This will identify the research gap, give an idea to develop or produce a new composite 3D printing filament and summarise the good practices for composite 3D printing. The content of Chapter 2 was published in *Journal of Composites Science* [1].

The first step of DcAFF development, the filament-forming method, was a manual moulding technique, inspired by Blok's work [50]. This chapter shows the new mould design, which was developed from Blok's mould, to achieve a promising compacted filament geometry and compares the physical and mechanical properties to the performance achieved from the previously moulded filament. Then, the first printing trial of the new filament was conducted to investigate the different printing parameters. This manual moulding result will be presented in Chapter 3, the content of this chapter was published in *Additive Manufacturing* [2].

After the success of the manual filament-forming, Chapter 4 will present the further development of the filament-forming technique to an industrial scalable semi-automated machine that reduces energy consumption, labour and production time. The whole new process will be detailed in the first part of the chapter. Then, the filament properties will be characterised, *e.g.* fibre content and fibre alignment, to show the evolution of the fibre and its alignment through the filament-forming machine. The larger amount of filament produced, thanks to the newly designed machine, leads to

the printing of more structural parts used for the mechanical testing described in this chapter, *i.e.* single layer tensile specimens, and curvilinear open-hole tensile specimens, that can show more aspects of the material performance. Most of the content in Chapter 4 was published in *Materials* [3] and the filament characteristic section is part of an article published in *Composite part B: Engineering* [4].

The upscaling of the HiPerDiF machine production capabilities and the development of the DcAFF machine facilitated the production of enough material to investigate the properties of multilayer 3D printing, which is closer to realistic applications. In Chapter 5, multilayer tensile, short-beam-shear, and open-hole samples were fabricated and tested to compare the properties to the single-layer DcAFF printed part and the available materials in the literature. The content in this chapter was published in *Composite part B: Engineering* [4].

The 3-year work of my PhD study to complete the thesis aim, developing a filament-forming method for composite HiPerDiF reinforcement, and how it has been organised in the chapters of this thesis are summarised in Table 1.1.

Table 1.1 Work step through the development of the DcAFF material.

Chapter	Production		Printing (layer)		Performance		
	Manual	Semi-auto	1-layer	Multi	Tensile	OPH	SBS
3							
4							
5							

Owing to the steering challenges associated with this new material form, an approach to improve the printing accuracy of DcAFF is proposed in Chapter 6. This content was published in *Materials* [5].

Finally, the overall thesis discussion which critically appraises the outputs of the experimental chapters, in terms of DcAFF filament production, printing, and

performance, is summarised in Chapter 7, before proposing the final thesis conclusions and possible future works in Chapter 8.

Chapter 2 Literature Review

This chapter reviews the available literature on fibre-reinforced FDM materials to investigate how the mechanical, physical, and thermal properties of 3D-printed fibre-reinforced thermoplastic composite materials are affected by printing parameters (*e.g.* printing speed, temperature, building principle, *etc.*) and constitutive materials properties, *i.e.* polymeric matrices, reinforcements, and additional materials. In particular, the reinforcement fibres are categorized in this review considering the different available types (*e.g.* carbon, glass, aramid, and natural), and resultant architectures are classified according to the fibre length (nano, short, discontinuous, and continuous). This review attempts to distil the optimum processing parameters that could be deduced from different studies and present the relationship between process parameters and properties graphically. A review of the literature is used to identify a good material/process combination to produce composite FDM filaments and to create a benchmark for the experimental work undertaken herein.

This literature review chapter was constructed based on the work published in *Journal of Composite Science* in 2021 under the title of “Fused Deposition Modelling of Fibre Reinforced Polymer Composites: A Parametric Review” [1]. The whole review was prepared by N.K. and amended by all the authors.

N. Krajangsawadi, L. G. Blok, I. Hamerton, M. L. Longana, B. K. S. Woods, and D. S. Ivanov, "Fused Deposition Modelling of Fibre Reinforced Polymer Composites: A Parametric Review," *Journal of Composites Science*, vol. 5, no. 1, p. 29, 2021. DOI:10.3390/jcs5010029.

2.1. Chapter introduction

The conventional FDM process suggests feeding a solid thermoplastic filament through a heated nozzle – Figure 2.1. The fed thermoplastic filament is melted in the convergent zone of the heated nozzle called the “melt pool”. The pressure difference between the inlet (larger section) and the outlet (smaller section) due to the convergence of the nozzle plus the difference between the pressure in the nozzle and pressure outside is called here a “pressure-drop”. The higher pressure in the nozzle will push the molten thermoplastic through the nozzle outlet to deposit the material. The deposited material in the horizontal (XY) plane following the movement of the nozzle is called a “raster”. The rasters are deposited side-by-side to make a “layer”, and then the building of several layers on top of the previous layer will make a part. According to the layer-by-layer building concept of the 3D printing process, the 3D printed part quality will depend not only on the raw material but also on the fusion between the rasters, which can be controlled by printing/machine parameters. There are several studies to link the quality of the part manufactured by FDM to the machine parameters and the constituent material properties. This chapter gathers the articles relating to the FDM process, mainly experimental-based studies, and then describes the effect of printing parameters and material properties on the mechanical, physical, and thermal properties of FDM manufactured parts. Section 2.2 describes the FDM process parameters that relate the setup values of G-code to the process parameters and the mechanical performance. This relationship is shown graphically and can be used to reduce the trial-and-error process for the material developer, which means faster R&D and less material wastage. Section 2.3 describes the material parameters including three constituents: (i) thermoplastics, (ii) reinforcements, and (iii) additional materials. In this thesis, the focus is placed on several reinforcement fibres, *e.g.* carbon fibre (CF), glass fibre (GF), and *para*-aramid fibre (Kevlar fibre, KF), and architectures classified according to the fibre length, *e.g.* nano, short, and continuous. The performance of FDM composites will be analysed at

different structural scales from microstructure (*i.e.* fibre, matrix, and their interactions) to mesostructures (*i.e.* the sintering between the printed rasters, inter-raster bonding) and then the part-scale structure (*i.e.* the finished part). The summary of studied parameters (printing and material) and achieved properties, considered in this review, is illustrated in Figure 2.1.

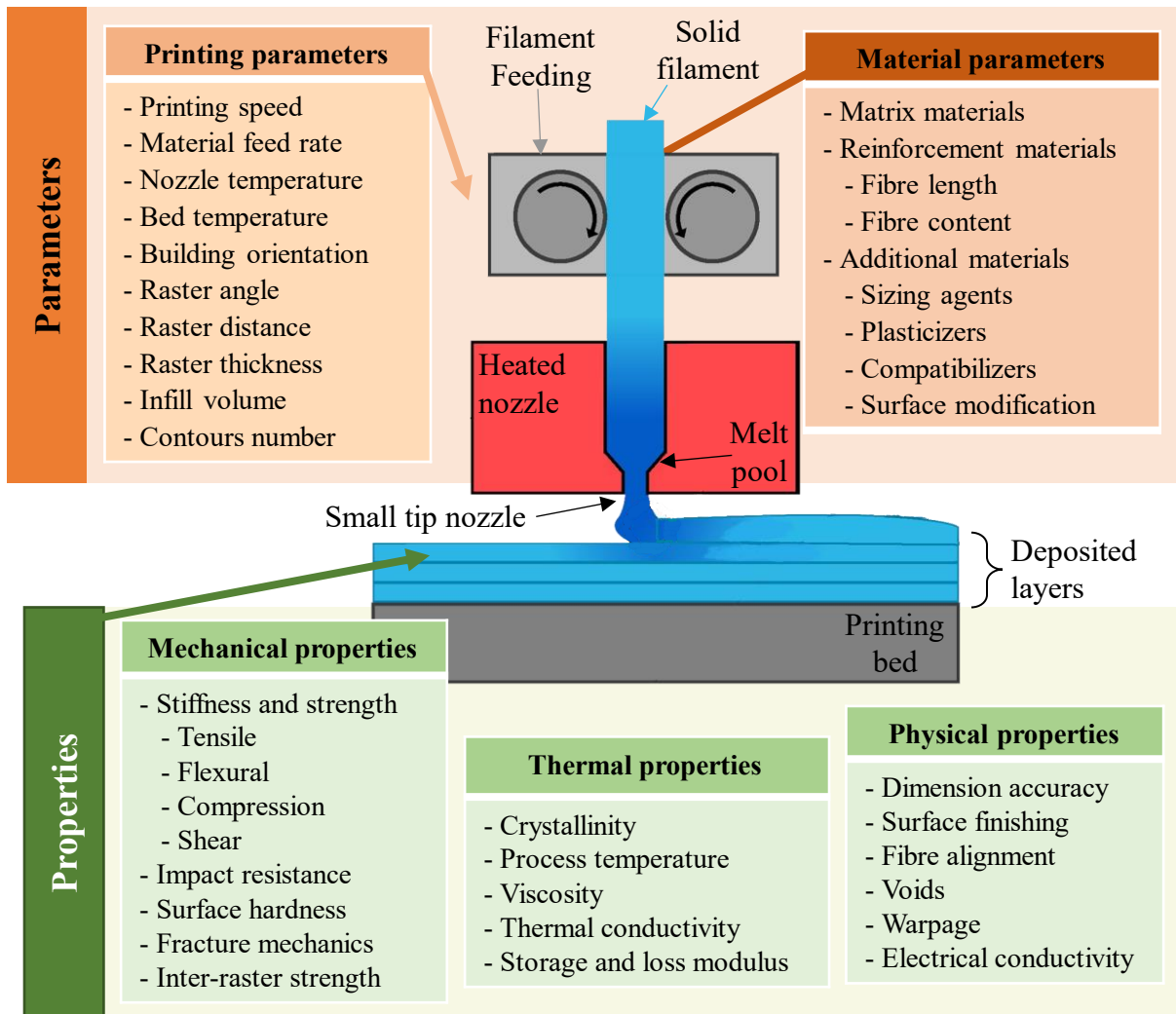


Figure 2.1 Investigated parameters and properties of the FDM process.

2.2. Printing parameters

This section describes the adjustable parameters in the FDM process and their influence on mechanical, thermal, and physical properties, as detailed in Figure 2.1. The tensile strength is the main focus of this study and will be shown graphically as a function of

several independent printing parameters. Furthermore, other variables characterising material state, *e.g.* viscosity and crystallinity, are described to explain possible mechanisms for flow or deformation in fibre-reinforced thermoplastic FDM products. For some printing parameters, there are only a few studies on fibre-reinforced thermoplastics. Thus, neat polymer studies are also mentioned to give a context to the FDM process and product behaviour that can be applied to develop FDM with fibre-reinforced plastics.

2.2.1. Printing speed

Printing speed is the velocity of the nozzle in the XY plane to fill a layer and in the vertical (Z) direction when finishing a layer. In most of the commercially available devices, it is controlled by a series of stepper motors connected to screws or drive belts. The speed (usually designated in mm/min) can be assigned in the G-code and affects the part strength, manufacturing time, and part appearance [31]. It influences the neat polymer printed part internal structure *i.e.* internal porosity and interlayer bonding.

At high printing speeds, the inter-raster bonding period is limited, resulting in weak interlayer bonding and porosity. Moreover, for fibre-reinforced thermoplastic materials, high printing speed shortens the fibre-matrix impregnation time resulting in poor fibre-matrix interaction [45]. Consequently, printing at higher speeds causes lower tensile, flexural and shear properties than printing at lower speeds [12, 35, 51, 52]. Moreover, the high speed shortens the cooling time before the deposition of the next layer and leaves a high amount of material at a high temperature. Exposing the material to high temperatures may help the raster fusion but leaving the thermoplastic at such temperatures for a long period can cause sagging due to gravity. The sagging changes the dimensions of the printed part and can hinder the continuous printing process, as detailed by Brenken *et al.* [53]. The printing speed also affects dimensional accuracy. A low printing speed moves the nozzle slowly, so the deposited rasters are steadily placed

on top of the previous layer, allowing for more ordered rasters and higher accuracy [31]. The pressure-drop that controls the melt flow is affected by the speed as described in the study by Geng *et al.* [24] on PEEK 3D printing. The speed (<65 mm/min) was so low as to cause an insufficient pressure-drop to spread the melt flow material; the highest printing speed (>400 mm/min) resulted in material slippage. Both cases reduced the raster width.

In some G-code generators, the printing speed of the first layer, *i.e.* the one in contact with the printing bed, can be assigned differently from other layers and the first layer speed is normally set to be lower than the rest. This can be justified by the fact that a lower printing speed for the first layer may improve the adhesion of the material to the bed, due to the higher time for compaction, *i.e.* the pressure applied by the nozzle to the material. To reduce the printing time, the printing speed can be increased when printing the plastic on plastic, in the following layers, which can more easily fuse together than the fusion of plastic with the bed [20, 27, 54].

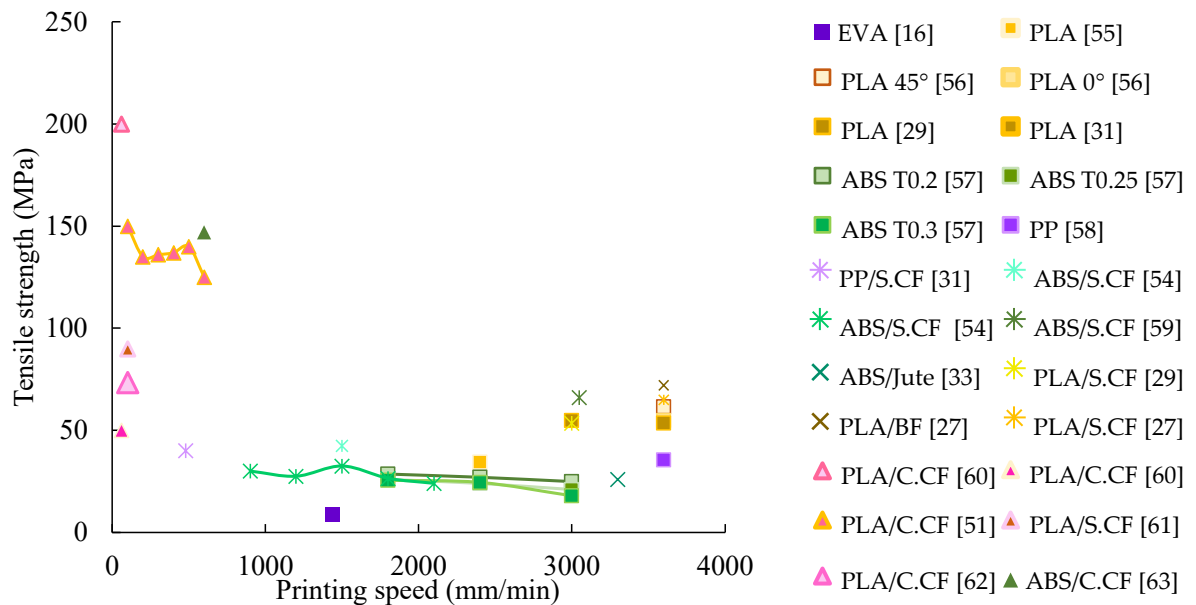


Figure 2.2 Tensile strength at different speeds of different materials: T for layer thickness, S.CF for short carbon fibre, C.CF for continuous carbon fibre, and BF for basalt fibre (the information is shown in Tables 2.2-2.4 along with all printing parameters used in the study).

Figure 2.2 shows the influence of speed used in various publications with a wide array of materials on the tensile strength (■, *, and ▲ refer to neat thermoplastic, short and continuous fibre-reinforced plastic, respectively). It is obvious that the continuous fibre reinforcement materials used lower speeds (<600 mm/min) while the short fibre reinforcement and neat thermoplastic materials were deposited at higher speeds (up to 3600 mm/min). Comparing the speed in the same studies, shown as data points linked by a continuous line in Figure 2.2, the higher printing speed slightly reduces the tensile strength, but the printing speed has a limited effect compared to the tensile strength of different materials used.

2.2.2. Material feed rate or extrusion rate

The feed rate or extrusion rate is the velocity at which the solid filament is fed to the heated nozzle; it is controlled by a stepper motor connected to a roller with a grooved, toothed, or gear-like surface that grips the filament by friction and pushes it to the hot-end. This velocity controls the amount of material in the heated nozzle that controls the pressure-drop, the reduction of pressure along with the convergence printing nozzle following Bernoulli's principle, extruding the molten material from the nozzle. The feed rate needs to match with the T_g and T_m to achieve proper melting and extrusion. The feed rate (FR) can be calculated from the material flow rate (Q) and the expected dimension of the printed raster (width (W) and layer thickness (T)) or the angular velocity of the feeder motor (ω) and the feeder roller radius (R_f) using Equation (2.1)

$$FR = \frac{Q}{W \times T} = \omega R_f \quad (2.1)$$

The maximum force (F_{max}) to drive the filament to the nozzle is limited by buckling of the filament according to critical force (P_{cr}) in Euler's bucking equation (Equation (2.2))

$$F_{max} = P_{cr} = \frac{\pi^2 E D^2}{16 L_f^2} \quad (2.2)$$

where E is the elastic modulus of the filament, D is the solid filament diameter, and L_f

is the filament length from the rollers to the entrance of the melt pool. At a high feed rate, the high amount of material fed to the liquefier leads to high melted pressure and high pressure-drop [64]. This reduces expansion and bubble generation in the material, so the surface defects are minimized [24, 64]. However, a feed rate that is too high, *e.g.* over 80 mm/min observed by Geng *et al.* [24], may cause an excessive melting pressure resulting in insufficient power and the molten polymer flows upward along the gap between the nozzle wall and the convergence zone in the nozzle, blocking the nozzle. The print speed and feed rate need to be synchronized to avoid inconsistent dimensions of the printed part. The printing speed (PS) and feed rate have a relationship following Equation (2.3):

$$\frac{PS}{FR} = \left(\frac{D}{d}\right)^2 \quad (2.3)$$

where d is the diameter of the nozzle [24]. For continuous fibre-reinforced plastic with the co-extrusion method, the synchronisation between the feed rate and deposition speed is the key control of the fibre content, especially in the separate fibre and matrix printing systems (described below in Section 2.3.2.1).

For pre-impregnated continuous fibre-reinforced thermoplastics, the feed rate of fibre and deposition speed of the printed composite should be set at the same value. If the printing speed is higher than the feed rate, the fibre will be pulled causing residual tensile stress in the fibre that may cause them to be torn apart or broken. By contrast, a printing speed lower than the feed rate is expected to result in fibre wrinkling or nozzle clogging by excessive material.

2.2.3. Nozzle temperature

This is the material extrusion temperature driven by an active response heater commanded by the printer controller. The temperature relates to the T_g and T_m of the printing materials. It is usually set above the T_g to allow the material to soften and fuse to the previously deposited rasters, but below the degradation temperature ($T_{5\%}$) to

avoid property changes. The nozzle temperature affects the chemical structure of polymers. A high nozzle temperature increases the crystallinity of the printed rasters, this can increase the tensile strength [16, 56]. A series of research publications [52, 53, 56], suggested that the high temperature also heated the previously deposited material, this, in combination with the residual heat of the currently deposited raster enhanced the raster fusion, as seen in the raster temperature distribution in Figure 2.3(a). A better fusion and low viscosity at high temperatures allow the adjacent deposited rasters to sinter with each other. When the rasters are completely welded, the polymer chains can be intermingled to form a randomized chain in the fusion structure (the process is shown in Figure 2.3(b)-(e)) reflecting the development of good inter-raster bonding strength of the part [65].

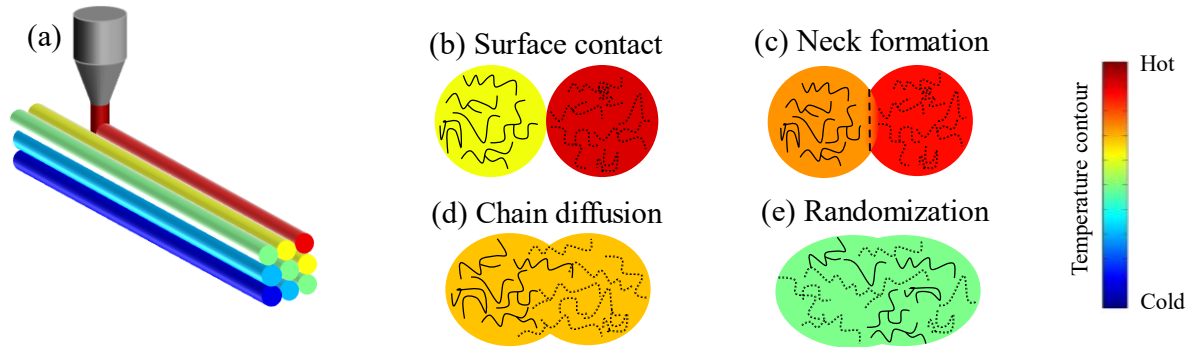


Figure 2.3 (a) Temperature distribution of the printed rasters from the highest temperature (red) of the current printing to cold raster (blue) away from the nozzle; raster fusion formation after deposition from (b) initial surface contacting of rasters; (c) heat dissipation from the current deposition and neck growth; (d) molecular chain diffusion between rasters; (e) chain randomization and cold rasters.

By contrast, the low printing temperature cannot sufficiently reduce the viscosity of the polymer, so the polymer chains have low mobility, causing poor inter-raster bonding [53]. However, the highest temperature achievable without causing degradation is not always the best printing temperature. Tian *et al.* [51] found that excessive temperature decreased surface accuracy when testing with continuous carbon fibre-reinforced PLA

(PLA/C.CF). Moreover, heating the material to a completely molten state while printing could induce pores in the inner structure of the printed part, which reduces the strength [52]. From a manufacturing perspective, a high nozzle temperature causes edge warping of the part, as seen in the study reported by Nazan *et al.* [66]. According to their findings, the optimum temperature should be high enough to allow the molten material to flow and fuse, but not too high to completely melt the polymer.

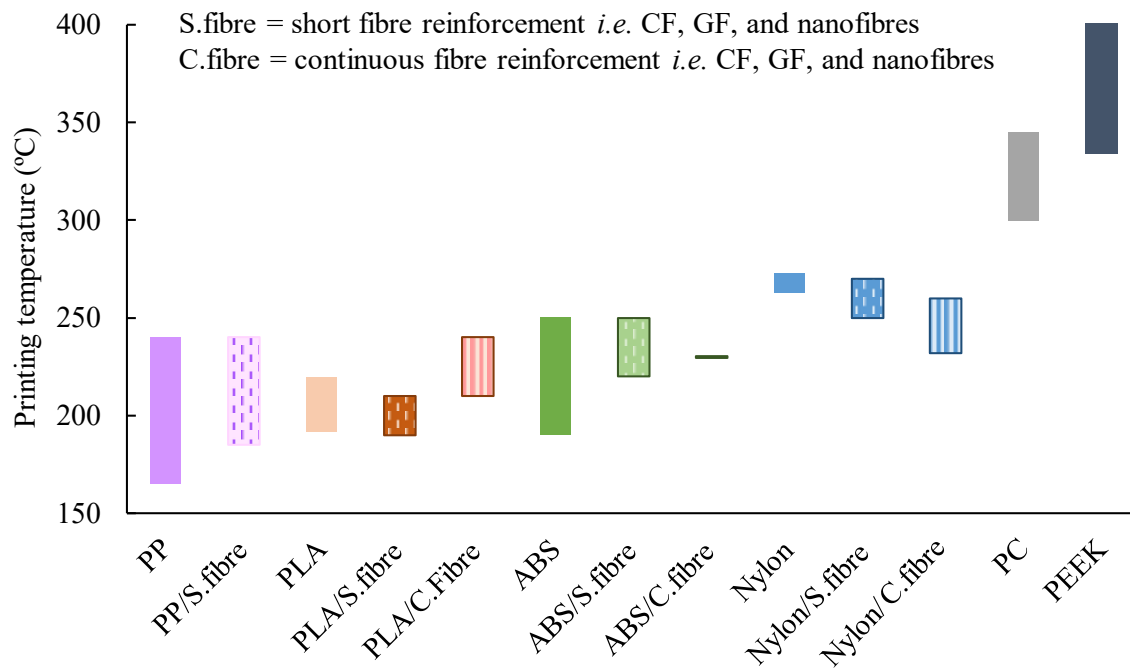


Figure 2.4 Printing temperature ranges used for selected polymers and composite materials (the information is shown in Tables 2.2-2.4 along with all printing parameters used in the study).

The bar chart in Figure 2.4 shows the range of the temperature used by several papers to achieve a proper printed part with different types of polymers, from which it can be seen that the low-end polymers (low mechanical performance thermoplastic *e.g.* ABS, PLA, *etc.*) can be fabricated at lower processing temperatures than the high-end polymers (PEI, PEEK). Amorphous thermoplastics, such as ABS or PC, have a wide processing temperature range because of the higher flexibility in molecular structure. Comparing the neat polymers to fibre-reinforced samples, the short-fibre

thermoplastics and the neat polymers can be printed using similar nozzle temperatures. Yet, according to gathered data, for continuous-fibre thermoplastics, different level of temperature is used, *e.g.* PLA/C.CF is printed at a higher temperature than neat PLA, while commercial nylon/C.CF produced by the commercial company, Markforged, is printed at a lower nozzle temperature than neat nylon. This difference may be because of the difference in the printing procedure between the co-extrusion of PLA continuous fibre and the printing of pre-impregnated continuous carbon fibre with nylon. The co-extrusion requires a higher temperature to completely melt the thermoplastic and allow for the impregnation of the dry fibre fed to the nozzle head before the deposition. While the pre-impregnated carbon-nylon from Markforged needs only heat to soften the impregnated nylon to be able to bond to the previous deposited.

2.2.4. Bed temperature and environmental control

FDM can operate at room temperature and “standard” environmental conditions but environmental control can improve the performance of the printed part. The heated bed is one of the main environmental control methods. The temperature of the heating plate attached to the printing bed is usually set below the glass transition temperature of the printed filament. This heat prevents rapid cooling of the thermoplastic and improves inter-raster bonding [13]. Improper temperature control and rapid cooling can reduce the crystallinity of printed thermoplastic and induce defects in the printed part. General thermoplastics have low rates of nucleation and crystallisation, so they cannot form a crystalline structure in a short time, this can reduce the part strength when printing without the heated bed [20, 56]. The heated bed could reduce the voids between rasters by improving raster fusion [26]. It has been observed that the raster fusion at the bottom layers is better than the higher layers because of the short distance from the heated bed [12]. The correct bed temperature also enhances the adhesion on the platform and eliminates the edge warpage. Environmental control can also be achieved by encasing the printer in a closed envelope that stabilizes the overall temperature and minimizes

any disturbance. The trend of the selected bed temperature for neat thermoplastic filament (in Figure 2.5) is similar to the nozzle temperature as low-performance polymers need low bed temperature. There is no specific study for the heated bed temperature in the composite 3D printing. However, the bed temperature used for composite 3D printing can be adopted from the neat polymer bed temperature with some increment, as can be seen in the pre-defined bed temperature of PLA/S.CF and ABS/S.CF in Figure 2.5.

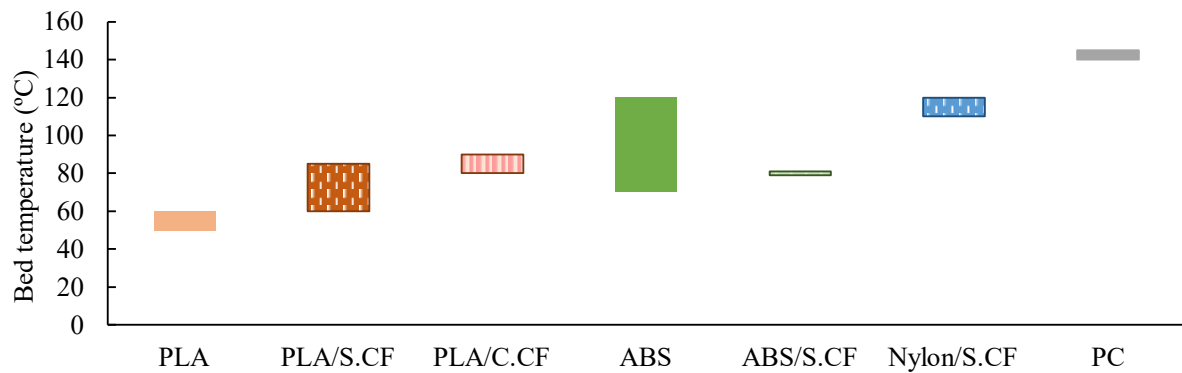


Figure 2.5 Bed temperature ranges used for selected polymers and composite materials (the information is shown in Tables 2.2-2.4 along with all printing parameters used in the study).

2.2.5. Building orientation

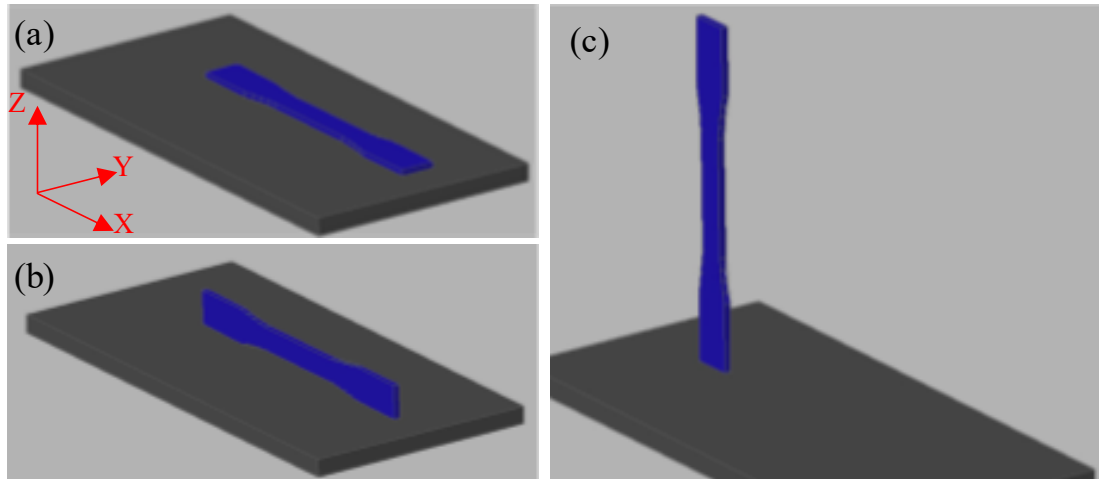


Figure 2.6 Building orientation definition (a) “flat”(F); (b) “on-edge”(E); (c) “upright”(Z) [67].

In this thesis, building orientation is categorized into three types: (a) “flat”, (b) “on-

edge", and (c) "upright". Figure 2.6 shows the different building orientations [67]. Considering dumbbell-shape 3D printed tensile testing specimen geometry, the "flat" and "on-edge" orientation deposit rasters mainly in tensile load direction (X); the "flat" (Figure 2.6(a)) builds a larger surface on the XY plane while the "on-edge" (Figure 2.6(b)) builds a smaller edge on the XY plane. By contrast, the "upright" orientation stacks layers in the Z direction (Figure 2.6(c)), so the tensile load might be applied to the Z direction accordingly to the figure axes. It can be implied that the longitudinal tensile strength of the "flat" and "on-edge" samples depends mainly on the strength of the material, but the "upright" depends on the inter-raster bonding strength which is controlled by fusion between the adjacent rasters [53]. Thus, the "upright" building parts are always weaker than the others [32, 36, 56, 67, 68] because the inter-raster bonding strength is always lower than the material strength.

Comparing "flat" and "on-edge" samples of neat polymer printing, both have similar strength as a result of the same number of longitudinal rasters [68]. The differences in the strengths of "on-edge" and "flat" samples have been investigated in a number of research studies. Durgan and Ertan [68] found that the "on-edge" ABS samples showed higher strength than the "flat" samples. This may be because the number of outer rasters (contour), which needs to print to be an outer shell of the 3D printed part, of "on-edge" is greater than the "flat". Another reason is that "on-edge" prints display more contours in the Z direction, which offers better compaction by pressure for nozzle and weight of the deposition in Z direction compared to a few layers built in the Z direction of the "flat" printing. For the shear sample ($\pm 45^\circ$ raster angle) of neat ABS and PC, in the internal structure of the "on-edge" there is a smaller contact area between crisscrossing rasters, than in the "flat", leading to a weaker through-thickness bonding of layers [32].

Considering short fibre reinforcement, the fibre reduces the flexibility of the matrix, so the softened/melted material has a high surface tension that holds the melted rasters in

a circular shape. This reduces the contact area between rasters, creates inter-raster voids, and decreases interlayer strength leading to lower tensile strength in the “upright” direction of the short fibre reinforced sample compared to the “upright” orientation of neat polymers [44, 59, 69]. The weakness of the “upright” orientation of PLA/S.CF was compared to the “flat” by Ding *et al.* [70]. The tensile strength of the “flat” and “upright” orientations in the article are approximately 52 MPa and 35 MPa, respectively. Wang *et al.* [71] compared flexural properties of the “flat” and “on-edge” printing with ABS reinforced with different short fibre types; CF, GF, and KF, at the same fibre content from the mix-extrusion filament forming mentioned by the manufacturer. The author claimed that the “on-edge” shows higher energy absorption than the “flat” referring to higher flexural strength and stiffness than the “flat” specimen by 19% and 24%, respectively [71]. According to the printing of $[0^\circ/90^\circ]$ raster angle with “flat” and “on-edge” in Figure 2.7(a) and (b), the rasters in “on-edge” printing act as short columns resisting the bending load rather than the long beam raster in the “flat”. This may be implied by the higher bending load-bearing capabilities.

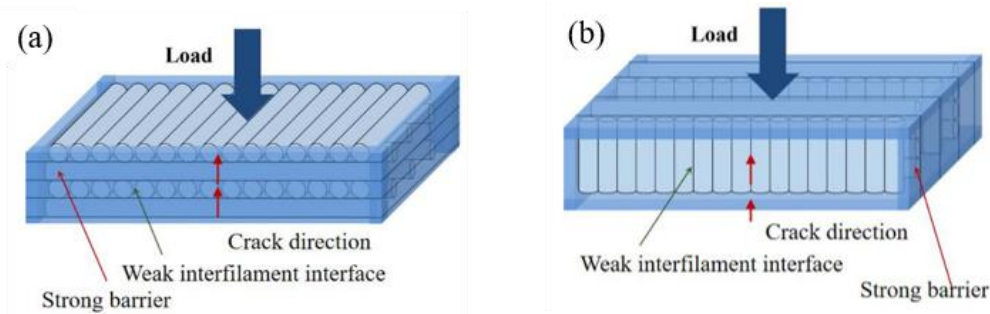


Figure 2.7 Different printing orientations: (a) “flat”; (b) “on-edge”, printing with $[0^\circ/90^\circ]$ raster angle under bending load [71].

For Markforged nylon reinforced with continuous fibre, Chacón *et al.* [11] claimed that the “flat” building orientation shows a higher fibre volume fraction than the “on-edge” by the printing principle designed by Markforged, so the “flat” has higher strength than the “on-edge”. There is a comparison of impact resistance between the “flat” and “on-

edge” orientation of Markforged continuous fibres using Charpy impact tests. The notch was manufactured by the print path of Markforged printer. The “on-edge” shows higher impact strength than the “flat” in any type of fibre: CF, GF, or KF. This relates to a difference in fibre volume content when printing with “flat” and “on-edge” orientations using Markforged printing scheme that requires neat polymer in the first and last layer. Hence, the “on-edge” orientation builds more fibre layers, in the Z direction, compared to the “flat” that deposits fibre in the XY plane [58]. Figure 2.8 shows the tensile strength of different building orientations, raster angle, and material of each orientation are divided by filling pattern and colour (grey for PC, green for ABS). Overall, the strengths of “flat” and “on-edge” are the same and they are higher than the “upright”.

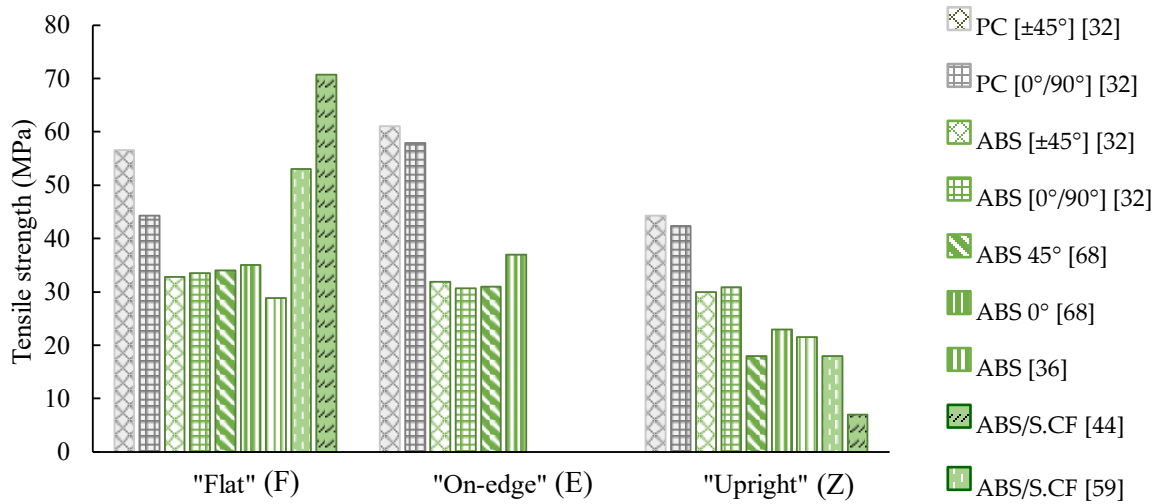


Figure 2.8 Tensile strengths of different building orientations (the information is shown in Tables 2.2-2.4 along with all printing parameters used in the study). The [±45°] and [0°/90°] are the printing raster pattern described in the raster angle section (Section 2.2.6), (the short fibre samples (ABS/S.CF) are printed and tested mainly in the longitudinal direction).

The difference in building orientation also affects fracture mechanics under tensile load. In neat polymer samples, the “flat” and “on-edge” have ductile behaviour (plastic-dominated failure) [32]. The crack runs transversely to the rasters and fails

perpendicular to the load direction after yielding [67, 68]. By contrast, the “upright” has brittle behaviour (inter-raster bonding dominant). Various studies have reported that the crack between deposition lines or interfacial crack could leave a smooth failure surface [36, 67, 68]. For short jute reinforced thermoplastic printing in the “upright” direction, the failure is the trans-filament fracture, due to the presence of voids [33].

The surface roughness of the different building orientations was studied in [68], printing with neat PC polymer. The “on-edge” and “upright” samples showed high surface roughness in the layer stacking direction (Z-direction) while the “flat” sample had similar surface roughness in Z and Y directions when the main printing direction along the X-axis according to Figure 2.6(a) [68].

In the manufacturing process, “upright” and “on-edge” samples are more difficult to build compared to “flat” because of the low attachment area to the printing bed and high stacking layers away from the heated bed that has a low temperature to fuse the raster after printing [67].

2.2.6. Raster angle

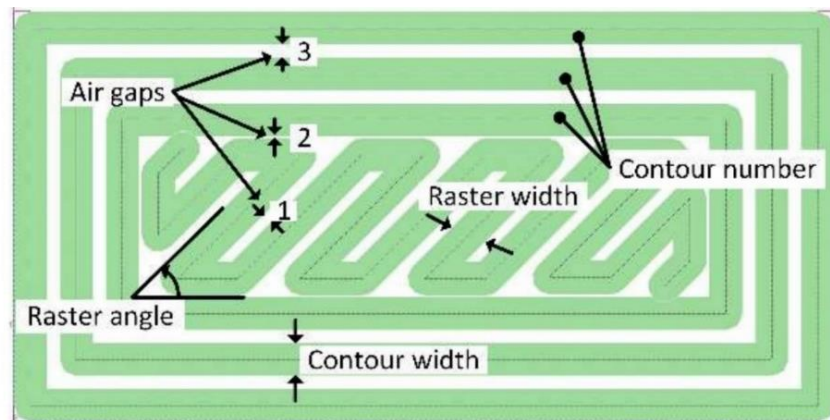


Figure 2.9 Description of printing parameters from the top view including air gaps, raster width, number of contours, and raster width [39].

In this thesis, the raster angle is the deposition direction on an XY plane (Figure 2.9). The X-axis is parallel to the tensile load direction, referred to as low raster angle (0°),

and the Y-axis is perpendicular to the load direction, referred to as high raster angle (90°). The raster angle is a significant factor in defining the strength of the printed part [12]. The building of a component usually follows two principles: a single raster angle for all layers or layer-by-layer crisscrossing raster angles.

For a single raster angle in neat thermoplastic, the ideal angle for the tensile strength is 0° , *i.e.* aligned to the longitudinal load direction. The mechanical performance decreases when there is an increase in the raster angle as the load-bearing capabilities of the printed structure decrease [22, 25, 31, 39, 72]. For angles higher than 45° , the tensile modulus stays constant when the raster angle increases [72]. This may be caused by the fact that the component stiffness is dictated by the stiffness of the inter-raster welding, rather than the material stiffness. However, some researchers reported contradictory findings. Song *et al.* [56] minimized the contour effect of PLA by cutting only the inner structure of the printed part before the tensile testing. They found that the 0° samples had a stress drop after yielding while the 45° had no stress drop before breakage. Onwubolu and Rayegani [34] found that the high porosity in 0° samples decreased the tensile strength, which was lower than that of 45° . Carneiro *et al.* [73] used a new printing procedure by printing only inner filling (infill structure described in Section 2.2.10) to various angles without contour, the tensile test of the new printing path shows that the 90° sample has higher mechanical performance than 45° because of the poor fusion at the extremity of the 45° part, which has no closing contour. Under tensile load, Hill and Haghi [72] found that the raster angle between 45° to 60° failed by shear of the inter-raster bonding, but the small raster angle (15° to 30°) had unpredictable failures as 15° failed at bonding following perpendicular to load failure and 30° showed interfacial failure without material failure. Figure 2.10 shows a generalised decrease in the tensile strength when the raster angle increases in specimens printed with a single angle. There are some cases, shown with dashed lines, which have a fluctuation in their trend.

In the flexural test, parts printed with a raster angle of 0° have higher bending strength and stiffness than those printed with 45° or 90° , as found in the study by Durgun and Ertan [68], so the low printing angle increases the flexural strength of the part. Under bending load, the 0° fails by material failure and the crack grows transverse to load direction while the 90° also fails mainly by delamination or interfacial failure according to the low bonding strength [12, 72].

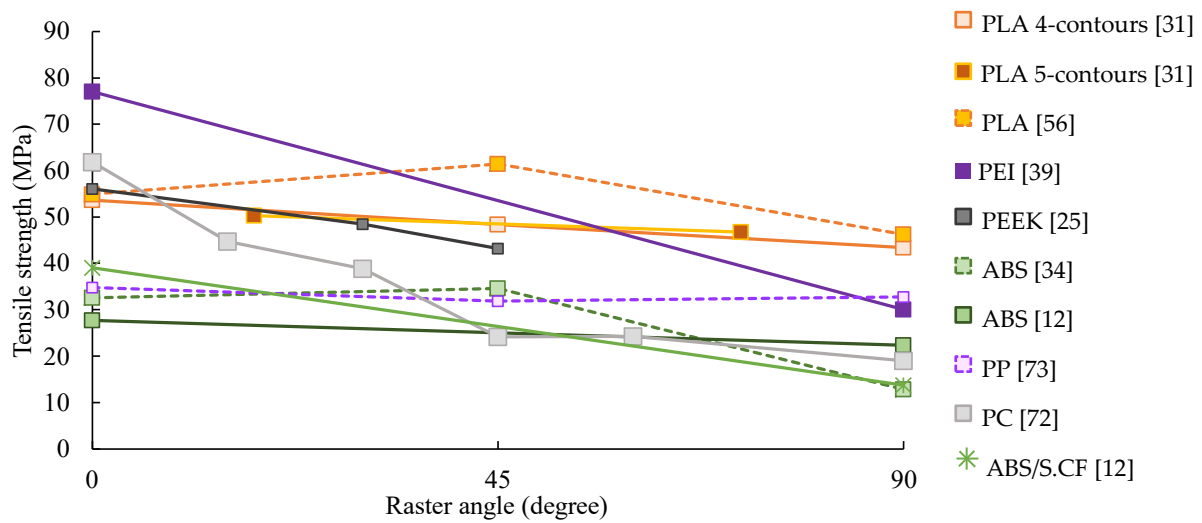


Figure 2.10 Tensile strength of a single raster angle, normally the strength decreases as an increase in the raster angle from 0° to 90° , but there are some fluctuations shown as a dashed line that strength increases when the raster angle increases (the information is shown in Tables 2.2-2.4 along with all printing parameters used in the study).

Considering crisscrossing raster in neat polymers, crisscrossing is commonly used in commercial G-code generators because of their ability to distribute stress. The balanced $[\pm 45^\circ]$ is expected to be the strongest angle because of an even load distribution and the $[0^\circ/90^\circ]$ crisscrossing is expected to be the weakest angle because of the loss of all material strength along the 90° angle which inter-raster-bonding dominates the tensile strength [74]. The $[\pm 45^\circ]$ angle shows more uniform strain thanks to the balance in load distribution, but the $[0^\circ/90^\circ]$ angle shows a bi-modal strain pattern alternating between the different orientation layers, and consequently, a high-stress gradient, which

indicates a high strain in the individual 90° raster layers as mentioned by Cantrell *et al.* [32], this causes the $[0^\circ/90^\circ]$ to fail sooner than $[\pm 45^\circ]$. Nevertheless, there are some deviation trends found by Carneiro *et al.* [73] and Cantrell *et al.* [32], the less effective raster angle was the $[\pm 45^\circ]$ that showed lower performance than the $[0^\circ/90^\circ]$. In the PC sample, Hossian *et al.* [75] found a slight difference in strength between different raster angles, the highest ultimate strength was recorded in the $[30^\circ/60^\circ]$ sample. By investigating inter-raster void, the $[\pm 45^\circ]$ samples have diamond-shaped voids but the $[0^\circ/90^\circ]$ have triangular voids. The triangular void has more contact area ($\sim 75\%$) than diamond-shaped voids which generates a lower void content and a better interfacial strength [59, 76]. Figure 2.11 shows the tensile strength when printing with different crisscrossing angles. Overall, a fluctuating trend can be observed, as mentioned above.

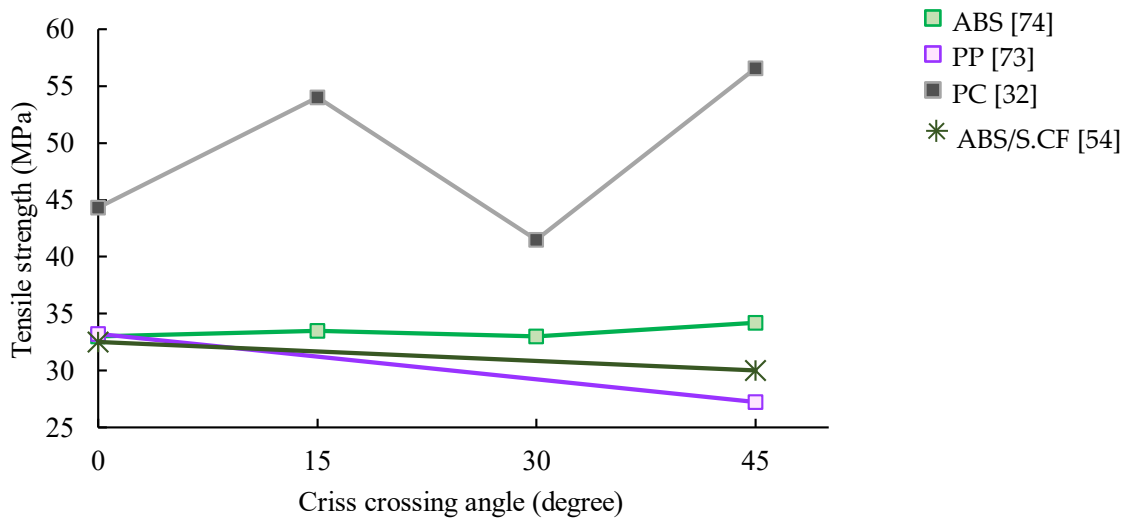


Figure 2.11 Tensile strength of crisscrossing raster angle of neat thermoplastic printing and composite printing (the information is shown in Tables 2.2-2.4 along with all printing parameters used in the study).

For fibre-reinforced samples, the fibre is supposed to be the main load-bearing component, so the alignment of the fibres in the load direction is the most efficient way to strengthen the part. Angle printing may reduce the performance of the fibre reinforcement, as seen in the research conducted by Ning *et al.* [52] with short,

approximately 0.15 mm, carbon fibre reinforcement. They found that the raster angle of $[0^\circ/90^\circ]$ had better mechanical performance, *i.e.* higher tensile strength and stiffness, than $[\pm 45^\circ]$. Load transferring in the fibre until fibre rupture was observed in $[0^\circ/90^\circ]$ samples, but fibre pull-out failure was observed in $[\pm 45^\circ]$ samples.

Zhang *et al.* [12] compared the difference between $[\pm 45^\circ]$ crisscrossing and purely 0° or 90° printing. For neat polymer fabrication, the $[\pm 45^\circ]$ raster angle has lower porosity and achieves a better interface than only one angle. By contrast, in the case of fibre filler, the one angle printed (0° or 90°) has lower voids and shows better mechanical properties than the crisscrossing.

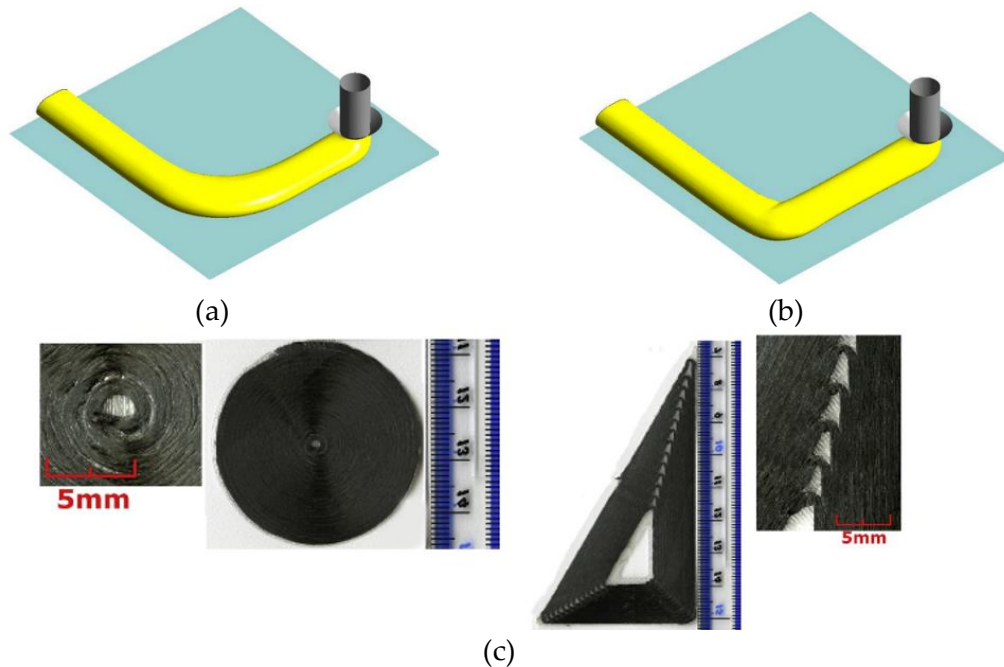


Figure 2.12 (a) Smooth radius printing path; (b) stop-and-turn trajectory path simulated by Comminal *et al.* [77]; (c) printing of continuous fibre with the spiral printing path obtained by Blok *et al.* [43].

Some studies show the relationship between the raster angle appearance and printing speed and extrusion rate using flow simulation [77, 78]. The synchronized printing speed, federate and smooth tool path (Figure 2.12(a)) can present a smoother turning radius compared to a stop-and-turn trajectory used in the conventional path (Figure

2.12(b)). This printing principle can be applied to smaller-angle printing to achieve smoother turning. In continuous fibre printing, the Markforged continuous fibre is printed with a different aspect from conventional printing. It places the fibre filament in each layer as a continuous spiral without stopping from the outer edge to avoid cutting the continuous fibre. It can be seen in Figure 2.12(c) that it is difficult to fill the smaller turning radius at the inner raster with the stiff fibre; resulting in an unfinished part and a fibreless area.

2.2.7. Raster distance (raster width and air gap)

Raster distance is the in-plane length between the two adjacent printing paths that can control the raster width and air gap. Both parameters can be adjusted by the same action related to the nozzle movement on the XY plane. The amount of material fed to the nozzle and the defined raster thickness limits the raster width while the spacing between the in-plane adjacent rasters is called an air gap or raster gap. The air gap influences part density. For “negative” air gaps, an overlap of rasters can compact them together and allow them to achieve a good interface, high part density and good flexural strength. A small gap size increases raster fusion that achieves proper polymer chain diffusion creating a good bonding interface [74, 75, 79-81]. By contrast, for the “positive” gap there is no touching between adjacent rasters being a predefined space expected for perfect raster fusion. However, improper raster spacing leads to an imperfect bonding that causes inter-raster voids and reduces the density of the part. This results in a reduction in tensile and flexural properties. From a manufacturing perspective, the small gap consumes more material and increases the time required to finish a part compared to the larger gap, however, it offers higher printing resolution. A large gap, which leaves voids, decreases part resolution and accuracy [61, 72, 74].

The effect of the assigned raster width on the strength was investigated by several researchers. Tian *et al.* [51] found that the high width created an overlap region that

disrupted the printing process. Hill and Haghi [72] suggested that high width slowed down the movement of the printing head leading to longer manufacturing time and requiring more materials to build the part. Moreover, it also showed a poor surface finish. The high number of inter-raster bonding reduces the overall part strength because of the lower strength compared to the polymer strength. Thus, the large raster width, and the subsequent reduction in the number of bonded raster edges, benefits the tensile strength.

2.2.8. Raster/layer thickness

Raster/layer thickness is defined by the vertical distance from the nozzle outlet to the printing bed/previous layer. The thickness is related directly to the interaction of the layers that reflects the tensile strength. Current research findings can be categorized into two groups. The first group found that a high number of interfaces reduces tensile strength. Thus, the high raster thickness decreased the number of layers minimising the interface and improving the strength. The effect is limited to only neat polymers, as shown in [22, 31, 73]. By contrast, another group claimed that a low raster thickness could compress layers together. Hence, achieving good compaction reduces porosity between raster and increases the interlayer bonding strength. This increases the mechanical properties, not only the tensile strength but also the flexural and shear strength. The effect can be widely seen in neat thermoplastics, short and continuous fibre reinforced thermoplastics as mentioned in [11, 12, 25, 35, 51, 52, 56, 62]. In continuous fibre reinforcement, produced by feeding the fibres to the polymeric matrix melted pool in the nozzle (the co-extrusion method for continuous fibre reinforcement printing described in Section 2.3.2.1), high raster thickness produces a reduction in the fibre content by an increase in the matrix covering a fibre that leads to a decrease in strength [62]. Figure 2.13 shows the relationship between tensile strength and raster thickness (the solid line represents neat polymer and the dash-dot line is the short fibre reinforced thermoplastic). There are both upward and downward trends, however, the

average trend is a decrease in tensile strength when the thickness increases.

From a manufacturing point of view, a high thickness produces a better temperature gradient which reduces the part distortion [22, 31] whilst low thickness can cause edge warping [66]. The high thickness exhibited a rough “staircase-like” pattern surface because of the imperfect fusion, this decreases overall finished sample accuracy [25, 82]. The raster thickness relates to manufacturing efficiency, setting low thickness uses more material and time, increasing the cost of products. Normally, the first layer thickness is defined to be slightly lower than the other layers, in order to apply high compaction force and ensure good bed adhesion.

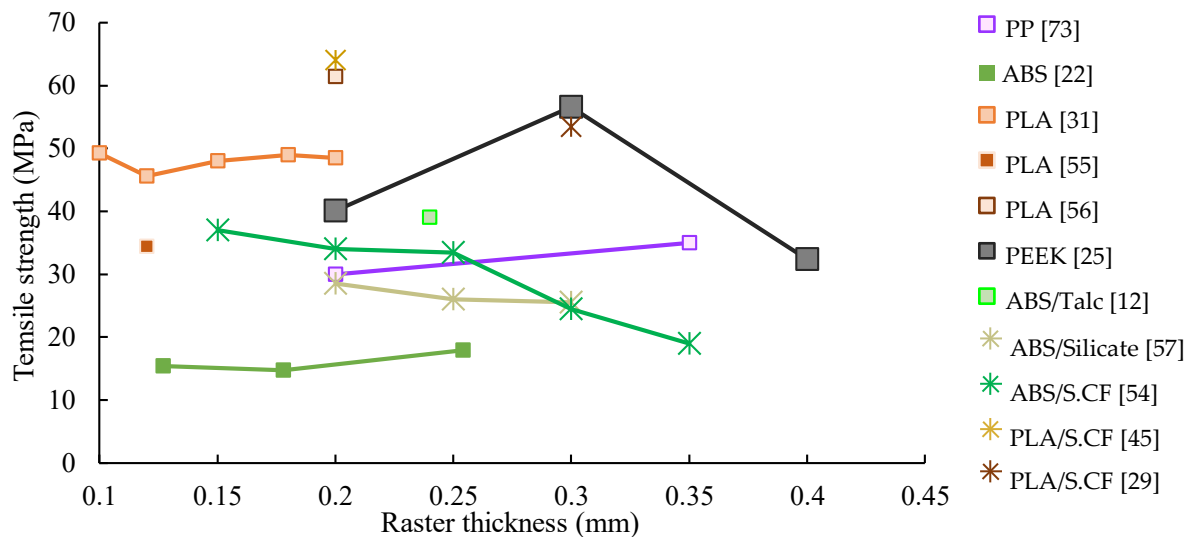


Figure 2.13 Tensile strength at the various raster/layer thickness of neat thermoplastics and short fibre reinforced thermoplastics, most of the findings show a modest reduction in strength when the thickness increases (the information is shown in Tables 2.2-2.4 along with all printing parameters used in the study).

2.2.9. Contour numbers

By default, commercial FDM machines always generate outer shells (Figure 2.9) to ensure good surface finishing and reduce stress concentrations at the end of the raster. The contour always runs concentrically around the part, so part of the contour always lies in the load direction despite any pre-defined (inner structure) raster angle. It can be

implied that the number of contours affects tensile properties. A high number of contours increases the material laid in the load direction, increasing the tensile strength and stiffness but decreasing the elongation of the raster [16, 31, 39]. The number of contour lines (NC) can be defined as the product of two times the number of longitudinal rasters per layer ($2n_c$), to take into account both specimen edges, and the number of layers (n), as shown in Equation (2.4) [83].

$$NC = 2n_cn_l \quad (2.4)$$

According to this equation, the contour has a high influence on the tensile properties compared to other printing parameters, *e.g.* printing orientation (“flat” and “on-edge”) or a small different raster angle. Samples with the same number of contours, but different orientations or raster angles show similar tensile properties.

2.2.10. Infill volume (% infill)

This parameter refers to the amount of material used to fill space inside the contours. The infill material is deposited within the outer contour according to various patterns, *e.g.* rectangular, triangle, honeycomb, zigzag, or line with several raster angles, described in Section 2.2.9. The G-code generator can adjust the volume content of the infill from 20-100% to change the amount of material used in the inner structure. A high % infill increases the amount of material in the part and consequently its net density. Carneiro *et al.* [73] suggested that denser parts always have high tensile strength and stiffness because of the high amount of material available to carry the load. De Toro *et al.* [84] confirmed the state by printing nylon reinforced with 20 wt% S.CF with 100% and 60% infill and testing their properties. The 100% infill shows approximately a three-fold improvement in tensile strength and stiffness from 60%. Yasa and Ersoy [85] observed that the change in infill percentage from 50 to 75% of the commercial Markforged chopped fibre (Onyx) increases the tensile stiffness by about 6%. They continued to study the infill percentage effect on toughness and found that the increase

of infill from 75% to 100% resulted in a two-fold toughness improvement, but the improvement is insignificant when the shift from 50% to 75% infill [86]. However, the high amount of infill requires a high amount of material and time to complete the part, causing high manufacturing costs [31, 87]. By contrast, a low % infill offers high accuracy. Nazan *et al.* [66] found that at low % infill, the rasters showed better heat diffusion than the high-density part, reducing the warping of the part.

2.2.11. Nozzle geometry

Typically, the nozzle tip diameter for commercial neat thermoplastic 3D printing filament (1.5-2.85 mm in diameter) is 0.4 mm. The available nozzle diameters range from 0.1 to 0.5 mm depending on the accuracy requirement and material viscosity. The Markforged continuous fibre reinforced nylon filament, 0.35 mm filament diameter, is printed by a 0.9 mm nozzle diameter with a filleted outlet edge. The edge fillet is expected to guide the continuous fibre and promote its placement on the bed. In the dual-nozzle Markforged printer, the nozzles used for neat thermoplastic (0.4 mm diameter) and continuous fibre reinforced thermoplastic filament (0.9 mm diameter), are shown in Figure 2.14.

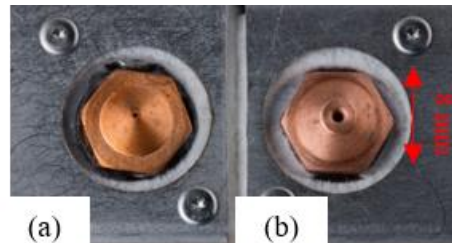


Figure 2.14 Nozzles for Markforged dual-nozzle 3D printer: (a) neat thermoplastic 0.4 mm diameter nozzle; (b) nylon continuous fibre 0.9 mm diameter nozzle [88].

Normally, the convergent nozzle is divided into three stages: large inlet, convergence zone, and small outlet shown in Figure 2.15(a). The pressure-drop depends on the dimensions of the large inlet section (the conical section) and the small outlet section. A test of feeding PLA filament through a convergent nozzle by Sukindar *et al.* [89] detected

a large pressure-drop at the small outlet diameter that caused a poor surface finish of the printed part. Yet, the high pressure-drop offered a consistent material flow that increased the accuracy of the printing. The printed geometric error, calculated from conical angular and outlet diameters (Figure 2.15(b)) using Equation (2.5), showed that the larger nozzle diameter created a higher geometric error than the smaller nozzle diameter. The nozzle diameter also links to extrusion time or fabrication time calculated with the combination of feed rate (FR), the part volume (V), and total layer thickness (ΣL) using Equation (2.6). According to this, the small diameter requires longer times to complete the part. Sukindar *et al.* [89] also claimed that the optimum nozzle diameter, providing an appropriate pressure-drop to maximize accuracy and minimize geometrical error, was 0.3 mm. To ensure the consistency of the printed part, Geng *et al.* [24] suggested that printing with a small nozzle diameter at high speed and feed rate could maintain the same amount of deposited materials during the printing. The effect of nozzle outlet geometry was also investigated by Papon *et al.* [76, 90] using carbon nanofibre/PLA polymer. Three nozzle outlet shapes with the same cross-section area of 0.1257 mm² were studied in this research: square, star, and circle. According to the simulation, the star-shaped nozzle was predicted to deposit a smooth velocity gradient that reduced the swelling effect and provided a rectangular deposited raster cross-section. This could reduce the void formation from circular raster cross-section that has small contact between rasters. Figure 2.16 shows the different nozzle outlet geometry in the study reported by Papon *et al.* [76] and the simulated shape of the deposition at the different outlet geometry. Hence, nozzle shape and size should be considered for different materials to achieve good product properties as they cause different flow behaviour.

$$ERROR = \frac{R}{\sin\left(\frac{\beta}{2}\right)} - R \quad (2.5)$$

$$time_{extrusion} = \frac{V}{d \times FR \times \Sigma L} \quad (2.6)$$

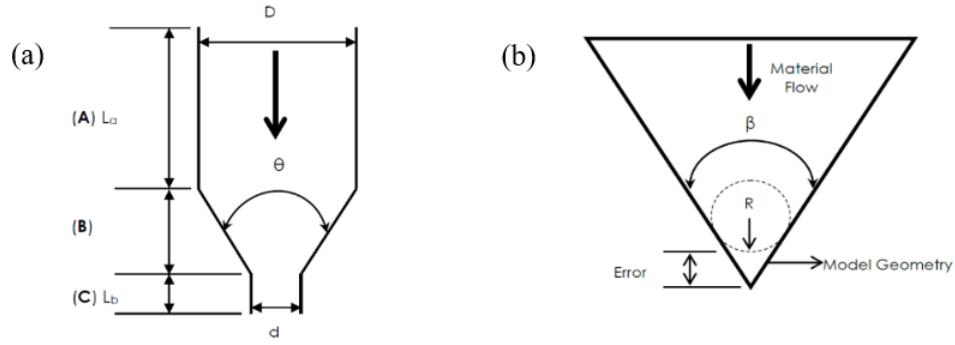


Figure 2.15. (a) Conical shape 3D printing nozzle dimension and area of pressure-drop from zone A (large inlet area), B (convergence area), and C (small outlet area); (b) parameters for error calculation of circular nozzle, in Equation (2.5), where R is the radius of the extrusion orifice and β is the angle of the modelled conical nozzle geometry using in the simulation [89].

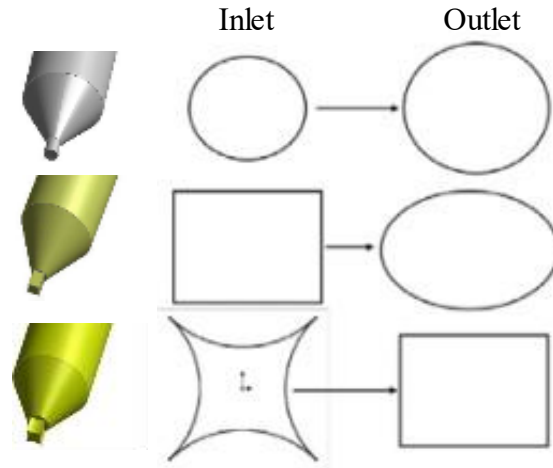


Figure 2.16. Investigation of the different nozzle outlet geometry: circular; square; and star on the deposition geometry at the outlet using ANSYS fluent computational fluid dynamic modelling studied by Papon *et al.* [76].

2.3. Material parameters

According to Figure 2.1, this section describes three types of materials used in the FDM process: (i) thermoplastic polymers as a matrix, (ii) fibres as a reinforcement, and (iii) additional materials as a sizing agent.

2.3.1. Matrix

In general, the FDM process uses thermoplastic polymers that can melt at relatively low temperatures and be re-shaped in a short time. Several thermoplastics, from the low

performing (*e.g.* polypropylene (PP), poly(acrylonitrile-butadiene-styrene) (ABS), poly(lactic acid) (PLA), polycarbonate (PC), polyamide (PA, nylon)) to the high performing (*e.g.* poly(ether ether ketone) (PEEK) or polyetherimide (PEI, ULTEM1000)) accordingly to their mechanical properties have been used with the FDM process. Among those materials, the most common thermoplastic used in FDM is PLA because of its low processing temperature, low shrinkage, and relatively high mechanical performance-to-cost ratio. Another “generic use” thermoplastic is ABS which has better thermal conductivity than PLA, but its high viscosity hinders the fusion of the printed raster and leads to porosity in the structure [47, 56]. Different classes of polyamide (*e.g.* PA6, PA12, PA66, *etc.*), also known as nylon, have high strengths compared to the first two thermoplastics but have poor layer adhesion and moisture absorption issues. PC is one of the high-performance thermoplastics, *e.g.* high strength, toughness, and hardness. Yet, it has high heat resistance that requires high printing temperature and makes it difficult to print [91]. PEEK and PEI are high-end thermoplastics which have high mechanical performance and require high process temperatures.

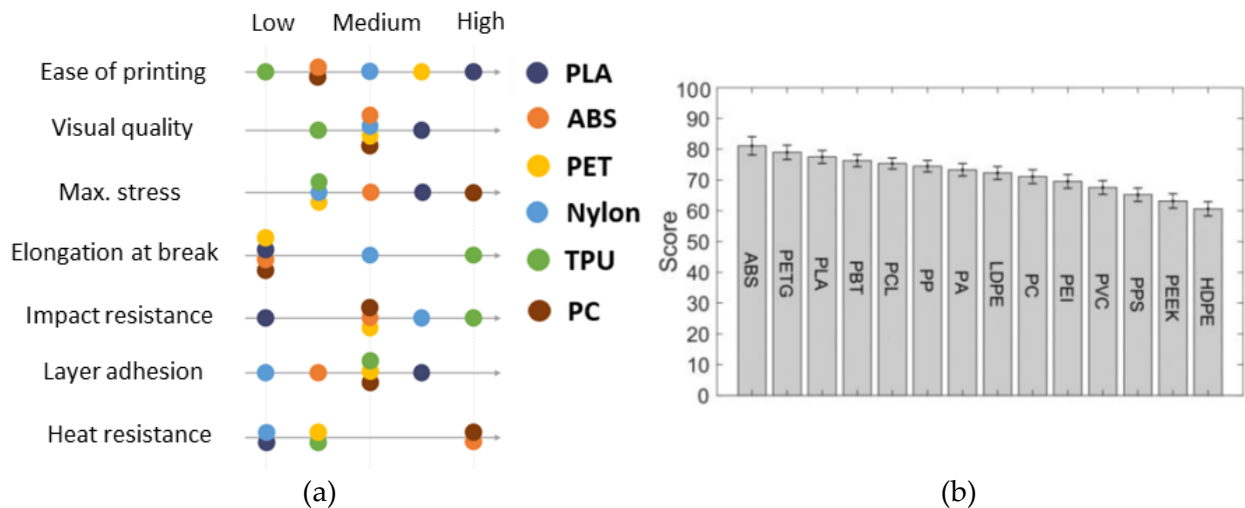


Figure 2.17 (a) Six polymers for 3D printer benchmarks according to a study from 3D Matter [92]; (b) sensitivity study of different thermoplastics for producing highly aligned discontinuous fibre thermoplastic 3D printing filament suggested by Blok *et al.* [47].

3D Matter [92] proposed a comparison of six low-to-medium performance

thermoplastics: PLA, ABS, poly(ethylene terephthalate) (PET), nylon, thermoplastic polyurethane (TPU, rubber-like material), and PC, for FDM process, shown in Figure 2.17(a), considering the printability, visual quality, strength, elongation at break, impact resistance, layer adhesion and heat resistance. It can be implied that the optimum thermoplastic in terms of manufacturability and mechanical performance is PLA which shows relatively high mechanical performance and high printability with good visual quality, although it has a low heat resistance leading to some issues in high-temperature applications and warping on the printing bed. Another full review of the possible thermoplastics used for highly aligned discontinuous fibre thermoplastic composite in the FDM filament was studied by Blok *et al.* [47]. This trade-off study considered several parameters, including process temperature, moulding temperature, cost, glass transition temperature, coefficient thermal expansion, thermal conductivity, shrinkage, printing ability, interfacial properties with carbon fibre, specific heat capacity, density, crystallinity, and strength. Each parameter has its weight score according to its suitability to produce composite FDM filament and then fabricate 3D printed products from the filament. Figure 2.17(b) shows that ABS is the most suitable matrix to combine with the highly aligned discontinuous fibre followed by poly(ethylene terephthalate glycol) (PETG) and PLA. This study procedure would benefit generally composite material developers and particularly the material selection in the next chapter to find a proper combination of polymer and reinforcement. The tensile stiffness and strength of neat thermoplastic as a filament gathered from manufacturers are listed in Table 2.1.

Focusing on the tensile strength and stiffness of polymers, the 3D printed parts (in the chequered pattern), gathered from the research papers shown in Table 2.2, always have lower strength and stiffness than the bulk polymers filament, before printing (bulk colour), gathered from various sources in Table 2.1, as seen in Figure 2.18. This is because of the instinct effect of layer-by-layer manufacturing that leaves porosities, poor inter-raster bonding and rough surface finishing in the printed structure.

Table 2.1 Tensile strength and stiffness of neat thermoplastic as a 3D printing filament gathered from various sources.

Material	Tensile Stiffness (GPa)			Tensile Strength (MPa)			Reference
	Min.	Max.	Average	Min.	Max.	Average	
PLA	2.3	4	2.9 ± 0.8	26.4	65	44.2 ± 14.2	[93-97]
ABS	1.1	7.6	3.1 ± 2.6	25	50	35.8 ± 10.1	[94, 98-101]
PP	0.2	1.75	1.1 ± 0.8	8.2	36	27.7 ± 11.0	[97, 102-104]
PC	1.94	2.28	2.1 ± 0.2	57	76.4	67.7 ± 7.3	[97, 105-108]
Nylon	0.4	1.7	1.2 ± 0.6	32	51	43.1 ± 7.9	[100, 109-113]
PEI	2.77	3.3	3.1 ± 0.3	64	85	78.8 ± 10.0	[100, 114-116]
PEEK	3	4.3	3.9 ± 0.6	90	115	101.6 ± 10.8	[117-119]

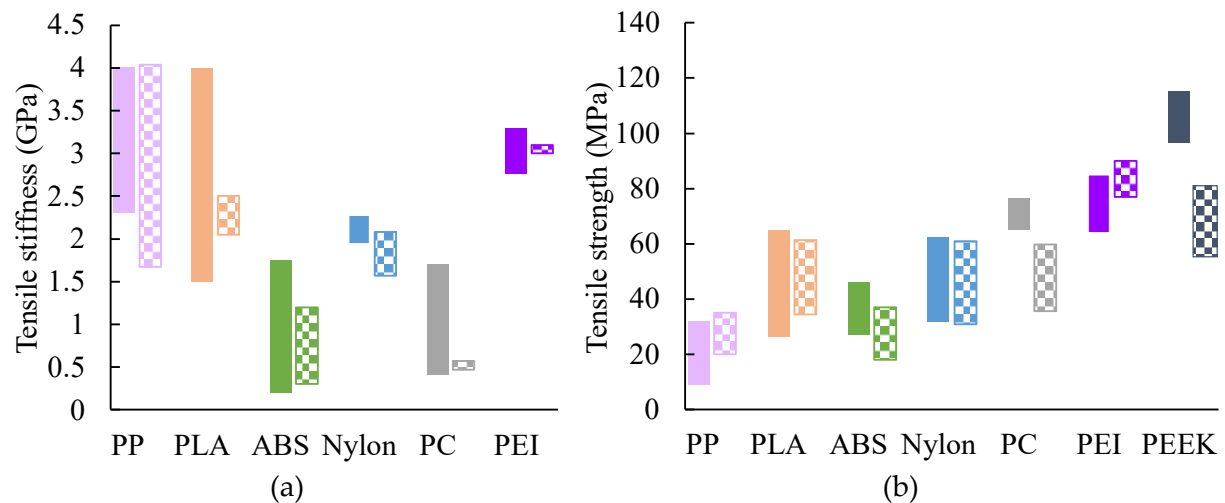


Figure 2.18 Range (minimum to maximum) of (a) tensile strength; (b) tensile stiffness of neat thermoplastics as a filament (bulk) according to the information and their reference in Table 2.1 and as-printed (chequered pattern) from Table 2.2.

2.3.2. Reinforcement

This section considers fibre reinforcement categorized according to the length of the fibre in the filament after the filament production (accounting for a fibre breakage during the process) including nano, short, discontinuous, and continuous. Nanofibres are defined as fibres with a diameter that is less than 1 μm and an aspect ratio (the ratio between length and width) greater than 50 [120]. Critical fibre length, defined as the

length that allows full load transfer from matrix to fibre, is used to classify short and discontinuous fibre. For lengths below the critical fibre length, the fibres are defined as short: the load cannot be fully transferred between the fibres through the matrix, and the failure is usually fibre pull-out or matrix failure. While for length above the critical length, the fibres are here defined as “discontinuous” and the composite material fails by fibre breakage as in continuous fibre composites. The main types of fibre reinforcement; GF, CF, and KF are mainly considered in this review.

The following subsections will discuss the process to add the reinforcement to the polymeric filament and describe the effects of fibre reinforcement on the polymeric filament and the printed part. Finally, the effects of reinforcement parameters, amount of fibre and fibre length, on the mechanical properties will be reviewed.

2.3.2.1. Fibre composite filament production

Most of the research in composite 3D printing used commercial fibre-reinforced filament produced by commercial manufacturers, *e.g.* Markforged, MakerBot [33] or Lulzbot TAZ [43], which have a fixed composition of each filament. Some researchers have produced their customized composite 3D printing filament so that the composition in the filament, *i.e.* matrix type, fibre type, fibre architecture, fibre length, the amount of fibre and sizing agents, can be tailored. To produce the customized composite filament, various filament-forming processes were designed. In this literature review, the filament production processes are divided accordingly to the fibre architecture, *i.e.* nano-, short, and continuous fibre mentioned above.

For nanofibre reinforcement, Shofner *et al.* [30] produced ABS reinforced with vapour-grown carbon fibres (VGCFs) by mixing both substances with a high shear rate in a Banbury mixer. Next, the melted composite was heated and pressed to form a sheet, then the sheet was granulated. Finally, the granules were melted and extruded using a single screw extruder and spooled manually to store the 1.7 mm constant diameter

filament.

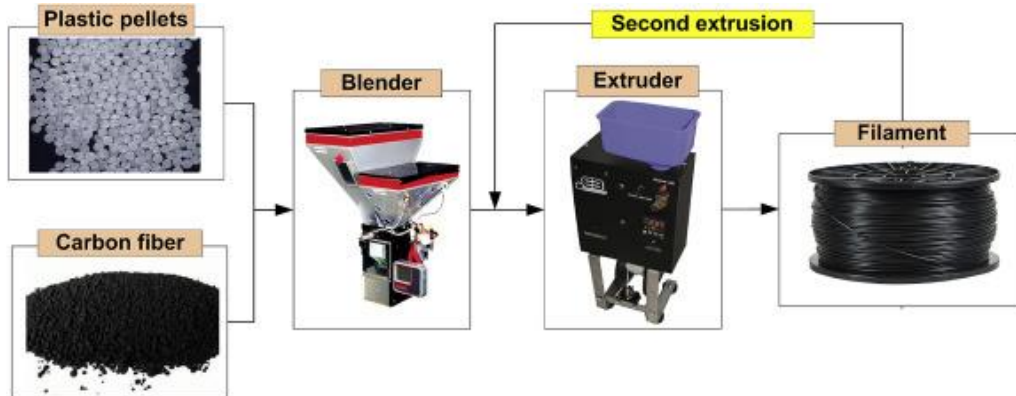


Figure 2.19 Short fibre FDM filament processing by mixing and extrusion used by Ning *et al.* [54].

For short fibre reinforcement, the fibre is combined with the polymeric matrix using a similar method as the nanofibers: mixing and extrusion. Before the fibre-matrix mixing process, it might be necessary to chop the commercially produced continuous fibre to an appropriate length for the mixing machine, typically between 1 to 3 mm, as described in [44, 45, 54]. The short or chopped fibres are usually blended with melted thermoplastic in a high-shear rate mixing machine or twin-screw extruder at high temperatures [19, 37, 90]. The molten composite could be cooled and chopped again into pellets ready to be fed to the final extrusion [19, 27], or fed directly to the final extrusion, usually a single screw extruder with a small circular die [44, 45]. The final circular cross-section filament diameters range from 1.5 to 2 mm, depending on the die size. After the extrusion, the filament is cooled to room temperature naturally or forcibly, *e.g.* using a cooling bath [27]. Finally, the constant cross-section diameter filaments are spooled in a suitable feedstock format at temperatures around 50°C to soften the polymer [27]. The short or discontinuous fibre-reinforced matrix filament feedstock can be printed using a general FDM machine without any extra equipment. An example of a brief procedure is shown in Figure 2.19. Fibre breakage always occurs during the mixing and extrusion, using a screw extruder, because of the high shear

stress during the compound process. For example, Sang *et al.* [27] showed fibre breakage from the initial 1-3 mm to an average of 0.13 mm after the process. Moreover, the similar process studied by Tekinalp *et al.* [45] and Love *et al.* [44] underlined the fibre breakage from the chopped 3.2 mm to less than 0.4 mm when using Brabender Intelli-Torque Plasti-Corder prep-mixer at speed of 60 rpm for 13 minutes and extruding to a plunger-type batch extrusion unit to make 1.75 mm diameter filament.

For continuous fibre reinforcement, there are two well-known methods to fabricate continuous fibre reinforcement. Markforged developed a pre-impregnated continuous fibre feedstock using nylon and various types of continuous fibres [11, 43, 121-123]. The filament is fabricated by applying tension to the fibre while passing it through a melted matrix pool. Then, the pre-impregnated composite filament, 0.35 mm in diameter, is spooled to be stored, similarly to neat polymeric filament feedstock. This filament can be printed *via* the Markforged dual-nozzle commercial 3D printer, shown in Figure 2.20(a), or a normal FDM machine with some modifications: a fibre cutter to finish the fibre extrusion and a specific filleted edge nozzle, as shown in Figure 2.14(b). In the Markforged dual-nozzle commercial 3D printer, the fibre cutter is attached away from the printing head to avoid adding the weight of the moving part. The fibre pre-impregnated filament is normally printed in combination with a neat thermoplastic layer to enhance the adhesion between layers or to the printing bed and fill the gap that the stiff fibre cannot fill, so the printer needs two separated nozzles, impregnated fibre and matrix nozzles, as shown in Figure 2.14, that separately fed the fibre and neat thermoplastic filaments. In recent research, there has been an introduction of a new material to replace the neat thermoplastic filament in the dual nozzle printer. This is called “Onyx”, a product from Markforged which uses nylon reinforced with short carbon fibres. According to Yang *et al.* [63] study, the Onyx filament has an average fibre length of around 0.12 mm with a fibre volume fraction of about 13%. In common with the neat nylon filament in the dual nozzle printer, the Onyx filament is normally printed

along with the pre-impregnated continuous carbon fibre [36, 124, 125]. The gaps filled with the short carbon fibre-nylon composite provide higher strength than the neat nylon.

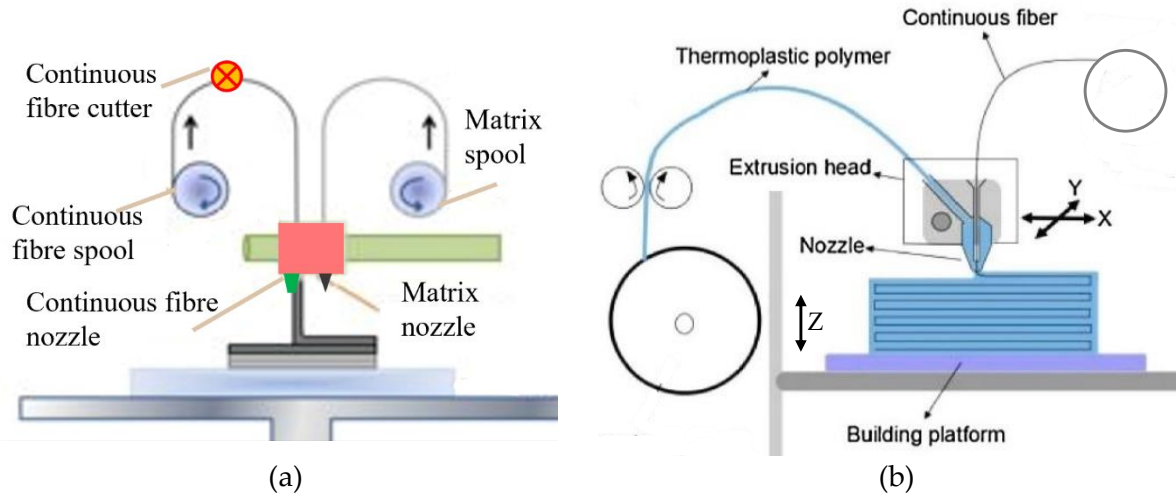


Figure 2.20 Schematic of (a) Markforged dual-nozzle printer for feeding separate impregnated fibre and thermoplastic matrix, modified from Pertuz-Comas *et al.* [123]; (b) customized co-extrusion continuous FDM process feeding fibre to the melted matrix in the melted pool [51].

The second procedure to print continuous fibre is the customized method developed by many researchers [51, 61, 126]. The main concept of customized continuous fibre printing is a co-extrusion method that feeds continuous dry fibre bundles to mix with the melted thermoplastic filament in the hot nozzle bath. The composite is extruded by the pressure difference between the inlet and outlet of the nozzle. The matrix used in the method is usually a normal neat thermoplastic 3D printing spool. Figure 2.20(b) shows the customized continuous 3D printing concept with the co-extrusion method using dry fibre and thermoplastic spool feeding to the hot nozzle and their deposition. The fibre content in the composite printing with this method depends on the fibre and matrix feed rate and printing speed *e.g.* feeding fibre at a higher speed than the matrix results in high fibre content, but poor fibre-matrix interface [51, 60, 61, 126]. Obviously, the co-extrusion method, compared to the former commercial pre-impregnation, shows poorer surface impregnation since, in the co-extrusion process, the impregnation takes

place in the heated nozzle without the possibility of in-situ quality control, while the quality of the pre-impregnated filament can be inspected in the production line.

2.3.2.2. Effect of reinforcement on 3D printing filament

Adding fibres to the 3D printing feedstock causes the formation of voids within the filament owing to the improper fibre-matrix interface. Zhang *et al.* [12] compared the filament cross-section of ABS, ABS/CNT (carbon nanotube reinforced ABS) and ABS/S.CF using scanning electron microscopy (SEM) imaging, as seen in Figure 2.21. It is obvious that the neat ABS filament (Figure 2.21(a)) has no inner void while voids are present in the composite material filament. According to Figure 2.21, ABS/S.CF filament clearly shows the largest void. The voids left in the initial filament may present as inner-raster voids in the printed part. Inner-raster voids are also found in the printed part of the Markforged containing continuous fibre filament because of the poor interfaces between fibre and matrix [121]. In the Markforged continuous fibre filament, it was observed that the fibres are distributed just on the edge of the filament leaving a large matrix-rich area in the middle of the cross-section [43, 127], as seen in Figure 2.21(f).

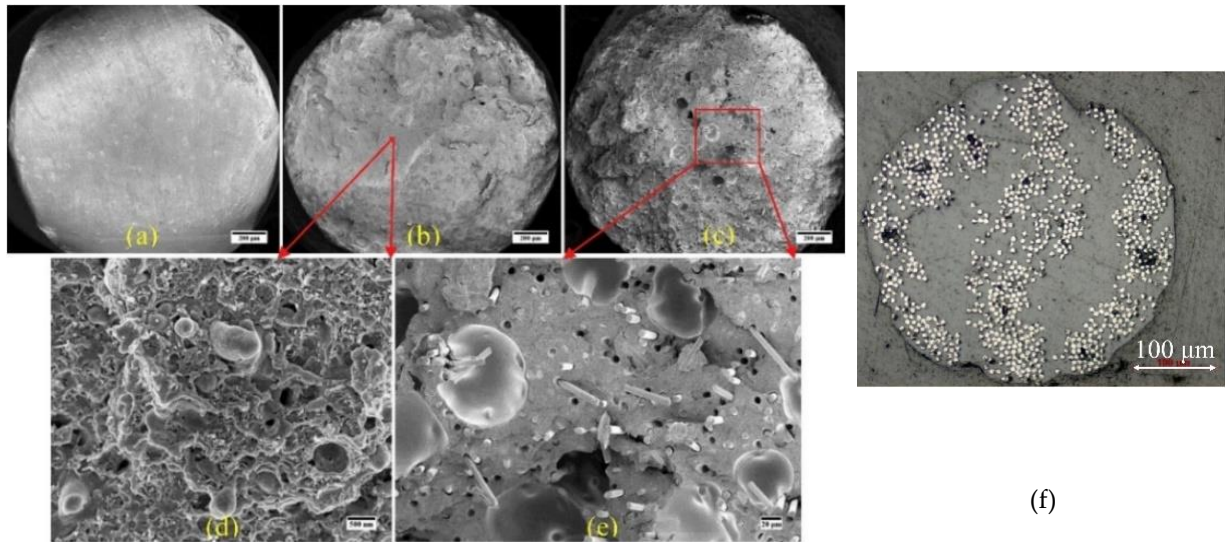


Figure 2.21. SEM images of the 3D printing filament with the different materials: (a) neat ABS; (b) ABS/CNT; (c) ABS/S.CF; (d) and (e) enlarging of the last two filaments from Zhang *et al.* [12]; (f) Markforged continuous fibre cross-section showing the large matrix-rich area in the middle of the cross-section from Blok *et al.* [43].

2.3.2.3. Effect of reinforcement on the 3D printed part

Considering the mesostructure of composite 3D printing parts, the fusion ability of the deposited rasters, the reinforcement increases heat diffusion of the thermoplastic and enhances the raster fusion. This causes a reduction in porosity between rasters, for example, glass fibres improved the thermal properties of poly(phenylene sulphide) (PPS) [59]. This result was emphasized in a mesostructured study of ABS and ABS/S.CF by Tekinalp *et al.* [45]. Figure 2.22 shows a polished cross-section of the printed ABS and ABS/S.CF with different fibre content from 10-30 wt% (chopped fibre length of 3.2 mm before filament production and broken to around 0.2-0.35 mm after the mixing and extrusion depending on the fibre content). It can be seen the triangular voids in printed neat ABS (Figure 2.22(a)) are larger than the ABS/S.CF parts Figure 2.22(b) to (d). Tekinalp *et al.* [45] suggested that the fibres decrease the die swelling phenomenon, so the cross section of the deposited raster is more rectangular than circular in shape. The fibre reinforcement also increases thermal conductivity which helps raster fusion and fills the rectangular voids.

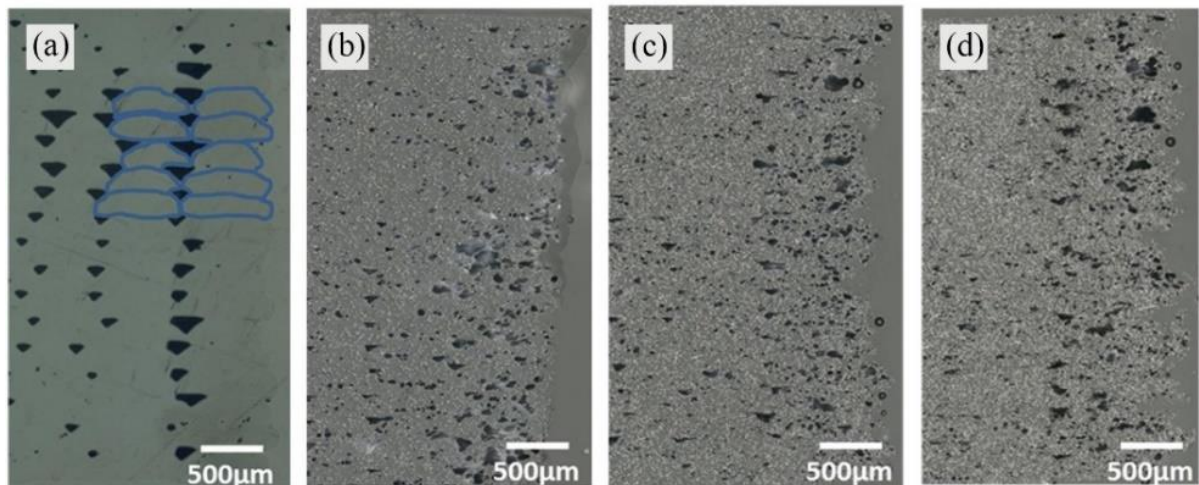


Figure 2.22. Micrograph cross-section of FDM printed part using (a) neat ABS; ABS/S.CF with (a) 10 wt%; (b) 20 wt%; (c) 30 wt%, manufactured by Tekinalp *et al.* [45].

Other articles suggested different results. Ivey *et al.* [20] found that the presence of the S.CF in PLA (commercial filament produced by 3DXMax CFR Carbon Fibre

Reinforcement PLA Filament, 3DXTech, Wyoming, MI, USA with 15 wt% of CF) increased the polymer viscosity and reduced melted flow flexibility. This hindered the flowability of the melted polymeric composite to fuse to the adjacent rasters, so the depositions were imperfectly fused. It left inter-raster voids in the structure. They also commented that the high viscosity at high fibre content might cause nozzle clogging and inconsistency melted flow, so the deposition was unsteady causing large voids in the structure. Duty *et al.* [69] mentioned that the short fibre reinforcement changed the flow field of the melted polymer and created a favourable nucleation site for bubble formation. Figure 2.23 shows the inter-raster voids and the ability to fuse between the rasters of ABS, ABS/CNT, and ABS/S.CF printed part when printing with 0° raster angle, from which it can be seen that large inter-raster voids are found in the fibre reinforced thermoplastic [12]. The inter-raster void depends directly on the percentage of the fibre filler as concluded by Sang *et al.* [27] and Blok *et al.* [43].

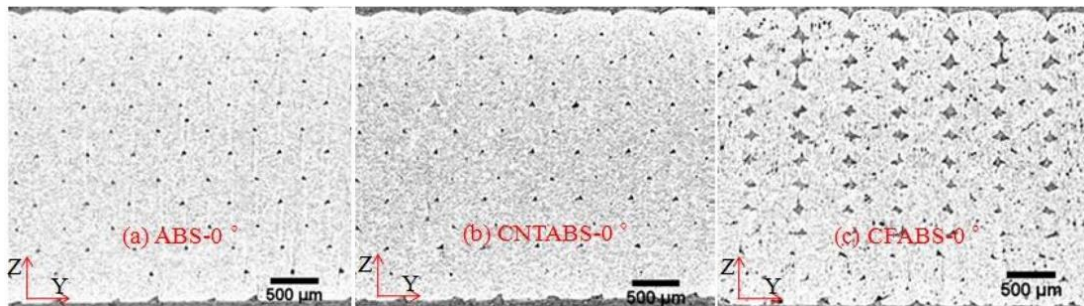


Figure 2.23. Cross-section of printed parts from (a) ABS; (b) ABS/CNT; (c) ABS/S.CF with 0° raster angle and the difference in the inter-raster void formation which shows larger voids in the fibre-reinforced specimen than the neat ABS and nanofibre samples observed by Zhang *et al.* [12].

The effect of fibre on the mesostructure of the FDM part is ambiguous (from Figure 2.22 and Figure 2.23). However, the latter effect, that the fibre reduces the raster fusion leading to inter-raster voids, was more extensively published than the improvement in mesostructure when adding fibres. This may depend on several variables such as fibre-matrix compatibility or sizing agent added to composites.

2.3.2.4. Effect of reinforcement on physical and chemical properties

The volume of crystalline structure within the polymer increases with the addition of fibre reinforcement. Sang *et al.* [27] stated that fibre reinforcement promoted the formation of crystalline structures from the amorphous phase by decreasing the crystallization temperature. Liao *et al.* [37] suggested that the presence of carbon fibre in nylon reduced nucleation-free energy and allowed the molecular chain to arrange into a crystallized phase because the fibre acted as an efficient nucleating agent for the crystallization.

The fibre reinforcement raises the degradation temperature of the polymer because it performs like a thermal stabilizer that absorbs heat [37]. This, however, has a very small influence on process temperatures especially T_m and T_g [27, 37].

The presence of fibres improves the thermal conductivity of the composite and the capabilities related directly to the fibre content [43]. The improvement in the thermal conductivity helps residual heat from the previously deposited raster to transfer to the recent deposition, increasing the inter-raster bonding and part strength. The better heat transfer of fibre-reinforced filament compared to neat thermoplastics, caused by the presence of fibres, reduces the thermal residual stress and local high-temperature points, so the weak points are eliminated [43, 59]. Furthermore, the presence of fibres decreases the coefficient of thermal expansion (CTE), preventing warping during fabrication and improving dimension accuracy [43, 128]. Owing to the random short fibre alignment in anisotropic fibre-reinforced thermoplastic, the direction and amount of conductivity cannot be controlled. To achieve a controllable conductive direction of short fibre composite, fibre alignment technology was introduced [129].

Different fibre architectures show different effects on polymeric matrix viscosity. Shofner *et al.* [30] reported that VGCFs have an insignificant effect on viscosity [30]. Sang *et al.* [27] claimed that short fibres increased the complex viscosity of the molten matrix

proportionally to their content. Ivey *et al.* [20] suggested that a large amount of short fibre reinforcement in the matrix might result in nozzle clogging, caused not only by the fibre entanglement but also by the lack of backpressure to push the melted filament through the nozzle. Considering short fibre reinforcement, the viscosity of PLA/S.CF is higher than short basalt fibre (BF), so the PLA/S.BF has higher printability than carbon fibre [27]. Moreover, Zhang *et al.* [12] claimed that short carbon fibre restricted flow during printing, thus the raster fusion was diminished resulting in inter-raster voids.

2.3.2.5. Effect of reinforcement on mechanical properties

Overall, the reinforcements aim to improve the mechanical performance of thermoplastics. Shofner *et al.* [30] investigated the effect of VGCFs on the mechanical performance of ABS in a static tensile test, according to ASTM D638, and through its dynamic properties, following a DMTA procedure. The findings indicated that the VGCFs increased tensile properties, 40% in tensile strength and 60% in tensile stiffness, and storage modulus of ABS. Gardner *et al.* [18] found that CNT yarn improved the strength of PEI, but it had less effect on the stiffness and strain to failure.

For short fibres, commercial short GF reinforced PP filament, *e.g.* Niroumand Polymer Company (Iran) used by Sodeifian *et al.* [23] and SOFTER used by Carneiro *et al.* [73], show improvements in strength and stiffness over neat PP. Short CFs increase the mechanical performance of the thermoplastic, especially in the load direction. The stiffness of the CF composite 3D printed parts clearly improves, as confirmed by many articles [20, 29, 54, 59], for example, 400% improvement from neat ABS when adding 13 wt% of CF with 3.2 mm long chopped fibre (before mixing and it is expected to be broken during the filament production) claimed by Love *et al.* [44]. The strength of the CF composite parts also increases, but less significantly than the stiffness [21, 54]. This might be because of the plastic-dominated failure. As detailed in Ferreira *et al.* [29], PLA carried most of the stress in PLA/S.CF composite (estimated fibre length of 60 μm after

filament production and printing) at the failure instead of the fibre reinforcement. The presence of fibre changes the material behaviour from ductile to more brittle with a reduction of the failure strain [20, 29]. By contrast, in the through-thickness direction, the presence of S.CF fibre, from the aforementioned study by Love *et al.* [44] diminishes through-thickness tensile strength. This is mainly because the through-thickness mechanical properties depend on the raster bonding strength and the fibre restricts interlayer bonding as mentioned above.

For continuous fibre reinforcement, the mechanical performance of the composite substantially increases due to the continuous nature of the fibre that can transfer load along the length. A good example is Matsuzaki *et al.* [60] who reported a PLA/C.CF co-extrusion 3D printed composite that showed a 600% improvement in tensile strength. Brenken *et al.* [53] claimed that the continuous fibre lifts the mechanical properties of the thermoplastic composite 3D printing material (continuous carbon fibre-nylon) to a level comparable to aluminium. The study of Zhou *et al.* [121] in flexural properties of the continuous fibre reinforcement produced by Markforged also showed an 11-fold improvement in flexural strength from neat nylon printed with the same procedure (395 MPa of continuous fibre compared to 32 MPa for neat nylon). Some articles [61, 122] applied the rule of mixture to describe the mechanical behaviour of continuous fibre printed materials. They mentioned that the mechanical properties of composite materials printed by FDM technology did not comply with the rule of mixture, being always lower than the ones theoretically predicted. This may be because of poor fibre-matrix interface, porosity (both inner and inter-raster voids) in the structure instinct in the layer-by-layer technology and the poor steering capability of the stiff continuous fibre creating defects in the part. Comparing the different types of continuous fibre including CF, GF, and KF produced by Markforged, CF shows higher mechanical properties in the tensile and flexural tests [11]. Although the continuous fibre composite material has high mechanical performance, the continuum of stiff fibre causes low

flexibility, this may result in manufacturing defects, *i.e.* fibre waviness. In the layer-by-layer deposition, the low flexibility fibre cannot fill a small radius leading to the fibreless area seen in Figure 2.24(a), compared to nylon/S.CF printed sample as a square shape produced by Lulzbot TAZ 6 printer (Figure 2.24(b)) [43]. The manufacturing defects, being weak areas, reduce the full performance of continuous fibre [11].

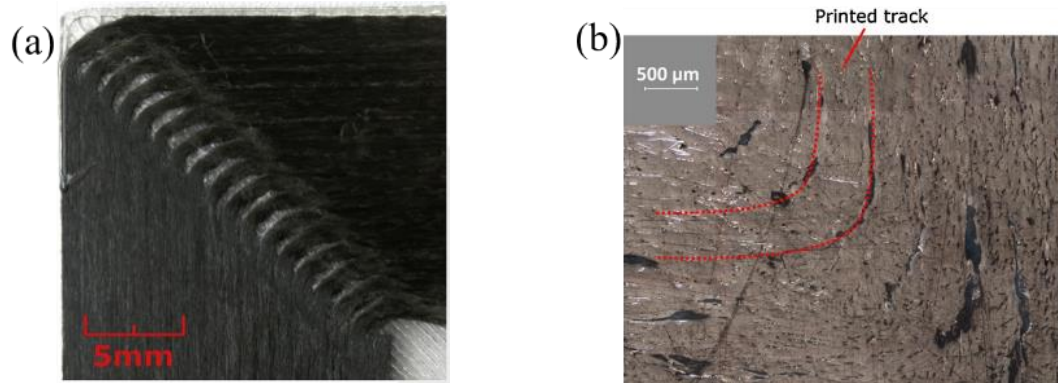


Figure 2.24. (a) Fibreless area inspected in continuous fibre printed parts; (b) small space between raster of short fibre printed part studied by Blok et al. [43].

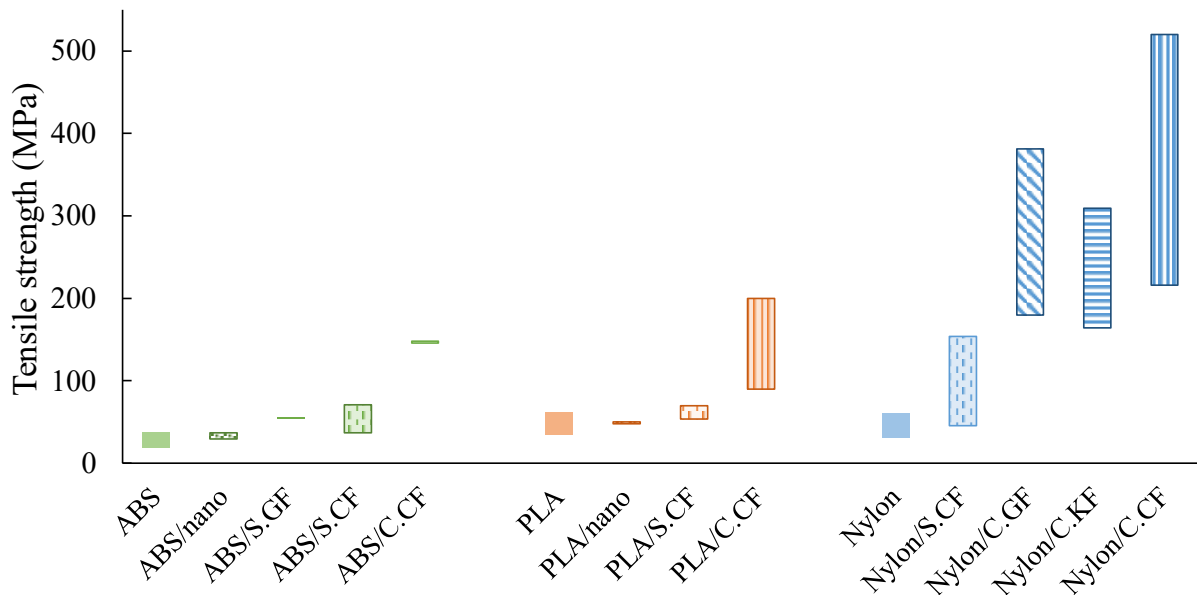


Figure 2.25. Tensile strength of several reinforcement types: CF, GF, and KF, and architectures: nano-, short, and continuous, with ABS, PLA, and nylon (the information is shown in Tables 2.2-2.4 along with all printing parameters used in the study).

Figure 2.25 plots the tensile strength in longitudinal fibre direction in different fibre

reinforcement formations from nano-, short to continuous fibre in ABS, PLA, and nylon against neat polymers. Nanofibre reinforcement strength is similar to neat thermoplastics. Short fibre reinforcement shows a moderate improvement with a slightly higher strength than the neat polymers. The continuous fibre reinforcement shows a substantial increase in tensile strength and the best reinforcement is the commercial continuous CF-nylon produced by Markforged which is 10 times stronger than neat nylon. Other customized continuous fibre reinforcement produced by some researchers using ABS and PLA shows an increase between 2- and 3-fold in tensile strength because of the poor interface and fibre wetting.

2.3.2.6. Effect of reinforcement on failure mechanisms

Fibre reinforcement changes the failure mechanism of the thermoplastic filament from ductile to brittle and causes the printed components to fail for various reasons. Most of the nano and short fibre reinforcement composites show pull-out failure because of (i) the fibre length is below the critical length, the load cannot fully transfer to fibres, and (ii) the poor fibre-matrix interface [21, 30, 36]. The effect of poor fibre-matrix adhesion was emphasised by Hofstätter *et al.* [130]. They observed in the micro-scale that the imperfectly round shape cross-section of fibre created gaps that were difficult to be filled by viscous matrix, leading to the poor interface. In this study, 40% of the fibres in the load direction were confirmed to have undergone pull-out. Liao *et al.* [37] observed that short fibres (15-20 mm before feedstock mixing and filament extrusion) act as a crack stopper, impeding the crack growth that meets the fibres perpendicularly even if intuitively that could have been considered a crack nucleation point being foreign objects in neat polymers.

In continuous fibre, the tensile load parallel to the fibre direction is fully transferred amongst fibres, until failure occurs, so the expected failure of continuous fibre is fibre breakage. However, other failure modes were detected in 3D-printed continuous fibre,

especially for those manufactured with the customized co-extrusion printing method. A mixed-mode failure of fibre breakage and fibre pull-out, due to imperfect wetting in the nozzle and poor interfacial bonding, occurred in various continuous fibre specimens [13, 60, 61, 126].

Even though the impregnation of fibre-matrix in the commercial Markforged 3D printed filament with continuous fibre is expected to be better than the customized co-extrusion methods, failures of CF Markforged 3D printed part under tensile load, observed by Chacón *et al.* [11], were through extensive fibre pull-out and minor fibre breakage due to improper coating and poor interfacial bonding. They mentioned that the thermoplastic coated the outer surface of the fibre bundle while the internal fibres were hardly infiltrated, so the fibre-matrix adhesion was relatively low compared to vacuum-assisted thermosetting fibre impregnation. The research also found that a similar failure occurred in GF and KF, except that the CF specimen broke perpendicular to the load direction, but the others broke at several locations, in the centre of the specimen and close to end tabs, perpendicularly to the load direction and then the crack ran parallel to the load. Figure 2.26 shows fibre breakage on the rupture surfaces of the tensile testing specimen with different types of continuous fibre reinforcement: CF, GF, and KF, from Chacón *et al.* [11] article. Al Abadi *et al.* [122] conducted a failure prediction using a finite element software, Abaqus, with Hashin's damage initiation theory observing that the initial damage in CF coupons was matrix tensile damage caused by tensile and shear stresses, while GF and KF initially failed by the fibre tensile damage. Those failure modes were confirmed by their experiment. A poor fibre-matrix interface results in matrix failure, rather than fibre failure common in conventional composites, leading to a reduction in strength. This causes low confidence in using thermoplastic 3D printing techniques for structural applications. The improvement of the fibre-matrix interfacial strength in thermoplastic composites should be studied to increase the final product strength.

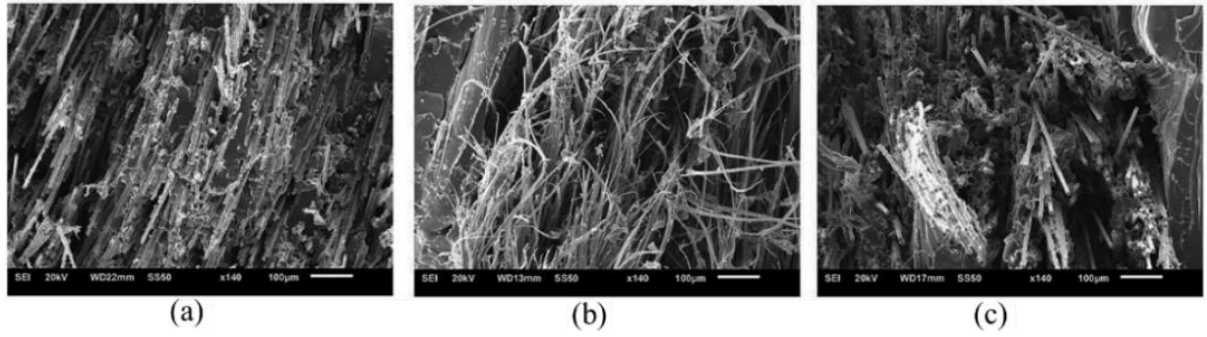


Figure 2.26. SEM images showing details of fibre breakage on the rupture surface of the tensile samples with different fibres: (a) C.CF; (b) C.KF; (c) C.GF at 140x magnification, as observed by Chacón *et. al* [11].

2.3.2.7. Effect of fibre length on composite performance

The critical fibre length is the length that determines load resistance ability. It can be calculated using Equation (2.7) [48] where S_c is the critical fibre length aspect ratio, σ_f is the tensile strength of fibre, τ_i is the shear strength or the shear yielding stress of the interface or the frictional shear stress at the interface, l_c is the critical fibre length and d_f is the fibre diameter.

$$S_c = \frac{\sigma_f}{2\tau_i} = \frac{l_c}{d_f} \quad (2.7)$$

A fibre length greater than the critical fibre length allows full load transfer to fibres causing a fibre-dominated failure. In contrast, if the length is below the critical length, the applied load cannot be fully transferred through the matrix from fibre to fibre, leading to matrix failure and fibre pull-out (slippage between fibre and matrix). Normally, for the carbon fibre-epoxy case, the critical fibre length is 0.45 mm.

Ideally, the long fibre shows better mechanical performance than the short fibre [27, 46]. Ning *et al.* [54] showed that a fibre length of 0.15 mm showed higher tensile strength and stiffness than 0.1 mm. As detailed in Section 2.3.2.1 above, the short and discontinuous fibre breakage during the filament-forming processes, *i.e.* fibre-matrix mixing and extrusion, leads to a fibre length reduction in the produced feedstock. Sang

et al. [27] observed that the initial chopped 1-3 mm fibre can be broken down to less than 0.13 mm after the mixing extrusion filament production. The fibre length in this process has a reverse relationship with the percentage of fibre in the composite. The high percentage of fibre shows more fibre breakage which reduces the fibre length. This is because of the higher contact between fibres at the high concentration during mixing. Figure 2.27 shows the reduction of fibre when the fibre content increases as proposed by Tekinalp *et al.* [45]. It can be implied that the highest percentage of fibre cannot achieve the highest strength and the optimized fibre content of short fibre in thermoplastic composite should obtain the best mechanical properties and minimum production cost. Moreover, fibre breakage was observed during the printing with a commercial nylon/S.CF [84]. With extremely short fibres (60 μm), Ferreira *et al.* [29] found poor matrix adhesion that may result in low interfacial strength and reduce the overall part strength.

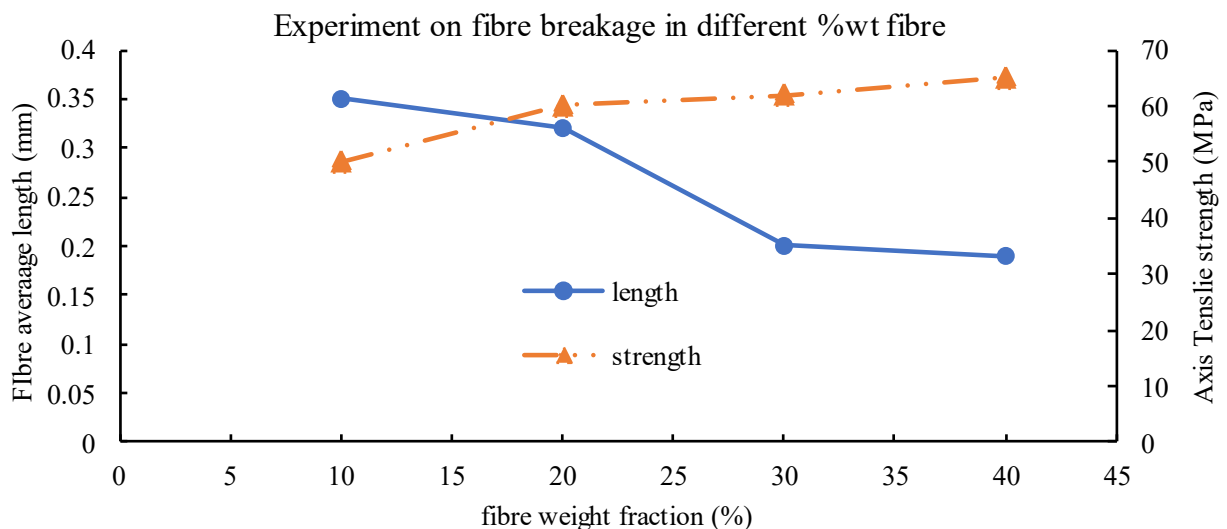


Figure 2.27. Fibre breakage at the high amount of randomly aligned fibre in the matrix resulted in minor strength improvement showing the optimized fibre volume fraction in ABS/S.CF filament, observed by Tekinalp *et al.* [45].

2.3.2.8. Effect of fibre content

Differences in fibre content, fibre volume fraction, or the amount of fibre filler in a composite, change the overall properties. A high fibre volume fraction is expected to be

beneficial to the properties. Nevertheless, a high fraction does not always reflect in mechanical performance improvement. In the nano-reinforcement case, the high content of nanofibre causes them to aggregate, reducing the printability of the filament; moreover, this has a double effect of creating a weak point in the matrix and subtracting reinforcement from the remaining material volume, reducing the part strength [21, 131]. A high-volume fraction of nanofibre increases the viscosity of the matrix causing a high surface tension of the raster leading to inter-raster voids [76].

The trend described above is also found in short-fibre reinforcement cases: the maximum strength and stiffness are not achieved at the highest fibre fraction. Ning *et al.* [54] suggested that the too-high content of short CF leads to high porosity that diminished the interfacial strength. Sang *et al.* [27] claimed that the fibre content, when excessive, also increased viscosity, reducing the printability of the composite and causing nozzle clogging. Tekinalp *et al.* [45] found nozzle clogging when adding 40 wt% of CF in ABS.

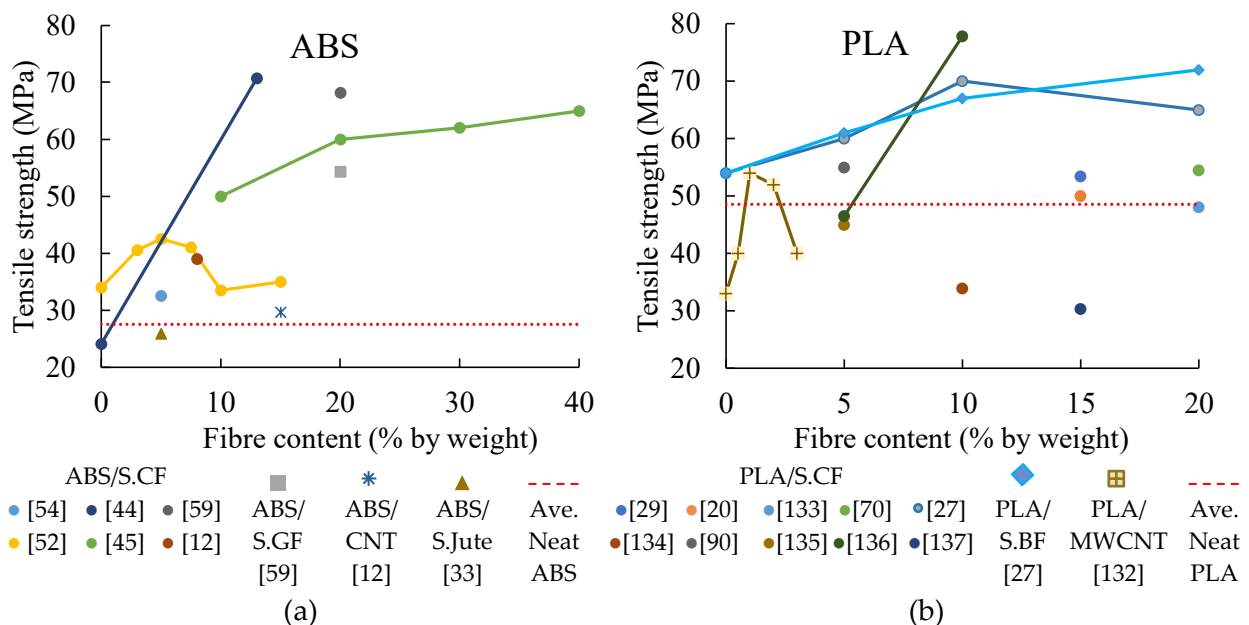


Figure 2.28. Tensile strength of composite FDM parts with different percentages of short fibre reinforcements in (a) ABS; (b) PLA with the average neat thermoplastics (as printed) strength shown in the red line (the information was gathered from several studies from Table 2.2-2.4).

Figure 2.28(a) and (b) show the tensile strength development from neat ABS and PLA when nano- and short fibres are added. The average 3D printed neat polymers strength (ABS and PLA), obtained from articles concluded in Figure 2.18, is presented as a red dash line as a baseline. This also shows the performance reduction at the too-high fibre content. In the through-thickness direction, the properties decrease with the fibre content, this is because of an increase in the viscosity that induces interlayer porosity [59].

A study by Silva *et al.* [26] adjusted the fibre content by selecting different fibre yarn types (1K and 3K) that changed the fibre volume fraction from 3.4 vol% to 11.73 vol%. With the customized co-extrusion printing for continuous, the fibre content is adjusted by controlling the fibre and matrix feed rate, printing speed, raster thickness and raster width. As detailed by Tian *et al.* [51], the fibre content decreased with an increase in the feed rate of the polymeric filament to the melted pool, raster thickness, and raster width. This is because the same amount of fibre is covered by a higher amount of the matrix when increasing the mentioned printing parameters.

2.3.2.9. Fibre alignment during the FDM process

The printing path can be predefined to control fibre orientation [13]. Generally, the majority of short fibres are aligned following the nozzle movement, while there are a few fibres laid perpendicular to the nozzle movement direction [21, 29, 45, 63]. This effect can be seen in both straight-line and turning-radius printing paths [53]. Considering the streamline in the convergence zone of the nozzle shown in Figure 2.15(a), a velocity gradient is generated in the flow direction, resulting in higher shear stress in the flow direction. The fibres are forced to align in the flow direction to reduce the flow resistance [37]. Hence, the fibre orientation could be estimated from the velocity and velocity gradient of the deposition using a fibre orientation tensor [53, 63, 128, 138]. During the printing, the re-melting of the previously deposited raster due to

the next raster deposition disturbed the fibre orientation; the fibres were more oriented at the middle of the extrusion line and showed more random orientation at the outer surface [130]. It can be inferred that the FDM process enhances fibre alignment, especially for short fibre reinforcement, along the nozzle movement direction, so the relationship of the printing path and alignment should be investigated further to improve the product performance.

2.3.3. Additional materials

Additional material or sizing agents are chemical substrates added to matrix or fibre to improve the performance of composite materials. The presence of hydrated magnesium silicate (Talc, $\text{Mg}_3\text{Si}_4\text{O}_{10}(\text{OH})_2$) in PLA leads to an increase in melting and degradation temperature while reducing T_g [55]. In composite materials, sizing agents aim mainly to improve the interfacial strength between fibre and matrix. Linear low-density polyethylene (LLDPE) was added to ABS/C.GF filament to increase the ductility of the composite and hydrogenated Buna-N (an elastomer) was added to increase the compatibility of the composite to LLDPE. Plasticizers and compatibilizers in the composite could improve the strength of the part [19]. Maleic anhydride polyolefin (POE-g-MA) was added to PP/S.CF composite to increase the elasticity and flexibility of the brittle composite, but an increase in POE-g-MA led to a decrease in tensile strength and more fibre pull-out failure, possibly because of degradation in the interactions between the functional groups on MA and hydroxyl group on GF [23]. BF, a poor surface interface natural fibre, was treated with a silane coupling agent (3-aminopropyl triethoxysilane, KH550, $\text{NH}_2\text{CH}_2\text{CH}_2\text{CH}_2\text{Si}(\text{OC}_2\text{H}_5)_3$) Aladdin reagent to improve the fibre-matrix adhesion [27]. In customized co-extrusion continuous carbon fibre 3D printing, Li *et al.* [126] suggested a surface modification of the carbon fibre bundle to improve interfacial strength according to the process shown in Figure 2.29. However, those examples of surface treatment methods and sizing agents are not always compatible with all polymers and reinforcements, so the proper additional material and

method need to be investigated to achieve the best combination for specific composite materials.

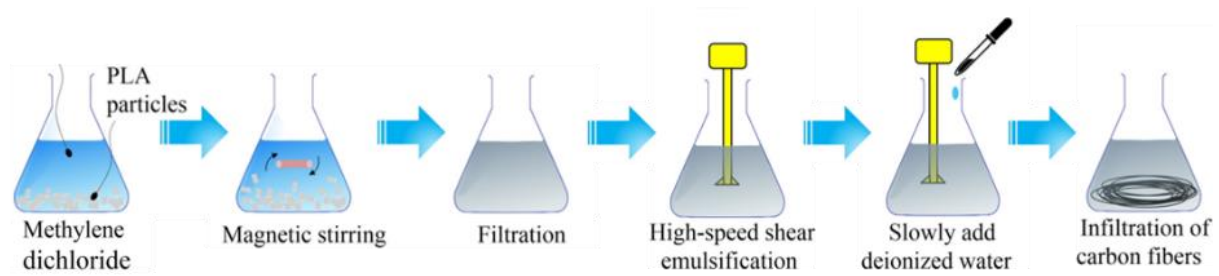


Figure 2.29 Surface modification of continuous carbon fibre and PLA, proposed by Li *et al.* [126].

2.4. Chapter discussion

Parameters	Printing parameter	Remark	Material parameter	Remark
	Printing speed	↓ minimized the manufacturing time	Matrix materials	- high-end polymers ⇒ high process temp.
	Material feed rate	⊕ synchronize with speed and temperature	Reinforcement materials	- carbon fibre reinforcement
	Nozzle temperature	⊕ relatively high ($T_g < T_{NT} < T_{5\%}$)	Fibre length	Continuous best mechanical performance poor formability
	Bed temperature	⊕ minimize warpage and maximize dimension control		Short best formability low performance
	Building orientation	- preferable “flat” and “on -edge”		Nano- non-effective on mechanical properties
	Raster angle	- neat + single raster : 0° - neat + crisscrossing raster : $[\pm 45^\circ]$ Fibre: only 0°	Fibre content	⊕ high content ⇒ breakage ⊖ low content ⇒ no improvement
	Raster distance	↓ overlap bonding / required materials & time	Additional materials	⊕ increase interfacial strength
	Raster thickness	- neat plastic – not clear ↓ fibre reinforced – promote compaction	Sizing agents	⊕ proper chemicals
	Infill volume	↑ dense part / required materials & time	Surface treatment	⊕ help fibre-matrix compatibility
	Contours number	↑ required materials & time		

Properties

Mechanical properties

High tensile strength

Thermal properties

High crystalline structure

Physical Properties

High dimension accuracy
Good surface finishing
Low (inter-raster) void

Legend

↓ is to minimize ↑ is to maximize

⊕ is to optimize - is unclear

Figure 2.30 Printing and material parameters, that can be assigned to the FDM process to high tensile strength and the outgrowths from the setting such as crystalline structure, low porosity, and surface finishing.

According to the review, FDM, layer-by-layer manufacturing, allows for the fabrication of complex geometries within a short time, but the part quality depends significantly on the exact combination of printing parameters and the materials used in the process.

The focused printing parameters in this review have shown that the highest tensile strength can be generally achieved by maximising the number of contours and percentage of infilled material while minimising the printing speed and the raster distance (air gap) and optimizing the nozzle and bed temperature. Thermoplastics, the material used in the general FDM process, have low mechanical performance compared to thermosetting or metals, so the neat thermoplastic FDM products are limited to low-performance applications. The fibre reinforcement with different architectures and fibre content is a mechanical performance improvement. Long and continuous fibre offers the highest performance improvement because of their load-transferring ability. The short fibre reinforcement shows a lower mechanical performance improvement than the continuous, but it has high flexibility and formability. Although the addition of fibres improves the overall performance, it degrades the internal structure of the filament because of the poor fibre-matrix interface. Moreover, the fibre hinders the printed raster fusion, leading to poor inter-raster bonding and porous structure in the printed part. The microstructure interface can be solved by surface treatment procedures such as adding sizing and the poor inter-raster fusion can be minimized by optimizing the printing parameters. Figure 2.30 proposes an overview of the process, both printing and material, parameters, that allow for achieving the highest tensile strength and other properties improvement.

2.5. Chapter conclusion

Among the gathered articles, there are several studies on the mechanical performance improvement of FDM products, both on the printing parameters and the composite printing, but there are still several research gaps in the use of fibre as a reinforcement to thermoplastic in FDM applications. Although the continuous fibre shows the best strength improvement, it creates defects, *i.e.* fibre-free areas and fibre waviness, because of their poor formability. The short fibre reinforcement offering similar formability to the neat thermoplastic provides an insignificant

increase in mechanical performance. Hence, an optimized fibre architecture with high formability and mechanical properties, such as highly aligned discontinuous fibre, which can use a fibre longer than the critical fibre length plus the good fibre alignment, has rarely been considered as a reinforcement for the 3D printing thermoplastic. In this thesis, the aligned discontinuous fibre used for the reinforcement is produced with the HiPerDiF technology described in Chapter 1. The challenge of using HiPerDiF fibre to produce 3D printing filament is the available filament production processes, reviewed above, that may be inappropriate to produce discontinuous aligned fibre-reinforced thermoplastic filaments. This is because the blending-mixing used with short fibre would break the fibre and demolish the alignment; while the pultrusion through a resin bath for impregnation, used to manufacture continuous fibre filaments, is impossible because the pulling force would tear the discontinuous fibre preform apart. A new method should be developed to preserve an appropriate fibre length and alignment which are the two main characteristics of the HiPerDiF. Apart from the mechanical properties gained from the long discontinuous fibre and the alignment, the HiPerDiF fibre is claimed to help with the formability of the reinforcement during printing. It should enhance the complex geometry fabrication with a high degree of manufacturing freedom in the 3D printing process, but again there are very few publications that consider the printing of discontinuous aligned fibre thermoplastic using FDM. The printing of pre-impregnated continuous fibre should be the most similar case for the printing technique and initial printing parameter trial as it also needs to steer the long-stiff fibre.

2.6. List of the available literature on FDM

After the review of the quoted articles, the summary of the method to print the FDM materials, both printing and material parameters, are concluded in Table 2.2-2.4 which is organised according to the composition of the filament: neat thermoplastic, short/discontinuous fibre, and continuous fibre, respectively.

Table 2.2 Summary of parametric study in neat thermoplastic of the FDM process.

Study	Material Parameters				Printing Parameters							Tensile properties		
	Polymer	Reinforcement			Print speed (mm/min)	Nozzle temp. (°C)	Bed Temp. (°C)	Build orientation F, E, Z	Raster angle (degree)	Raster thickness (mm)	Infill volume (%)	Contour (lines)	Stiffness (GPa)	Ultimate Strength (MPa)
		Material	Length (mm)	Diameter (μm)										
[73]	PP				3600	165	room		45, 0, 90, [±45], [0/90]	0.2, 0.35	20, 60, 100		0.3-1.2	10-35
[22]	ABS							F	[0/90], [15/75], [30/60], [±45]	0.127, 0.178, 0.254				9.95-18.09
[34]	ABS							F	0, 45, 90	0.127, 0.330				4.01-34.61
[83]	ABS							F, E	±45	0.25		1, 4, 7, 10	1.81-2.11	23.9-29.7
[68]	ABS							F, E, Z	0, 30, 45, 60, 90	0.253			1.9-2.5	19-37
[74]	ABS				1800	250	120		[0/90], [30/60], [±45], [75/15]	0.5		1		28-35
[32]	ABS					235	105	F, E, Z	[0/90], [±45]	0.1			1.96-2.05	30.0-32.8

Table 2.2 *Cont.*

Study	Material Parameters				Printing Parameters							Tensile properties		
	Polymer	Reinforcement												
		Material	Length (mm)	Diameter (µm)	Content (by wt%)	Print speed (mm/min)	Nozzle temp. (°C)	Bed Temp. (°C)	Build orientation F, E, Z	Raster angle (degree)	Raster thickness (mm)	Infill volume (%)	Contour (lines)	Stiffness (GPa)
[12]	ABS				3600, 4800, 6000				0, [±45], 90	0.18, 0.24, 0.3			1.95-2.44	22.31-27.69
[36]	ABS							F	[±45]	0.25			1.89-2.18	21.5-28.8
[59]	ABS					250	95						2.3-2.41	31.2-34
[55]	PLA				2100-2700	210	50		[0/90]	0.12	100		2.66-3.74	28.37-34.43
[56]	PLA				2700, 3600, 6000, 9000	200, 210, 220, 230		E	0, 45, 90	0.1, 0.2, 0.3, 0.4			3.96-4.04	46.24-61.42
[31]	PLA				3600	205	60	F	0, 18, 45, 72, 90	0.1,0.12,0.15,0.18,0.2	100	2, 3, 4, 5, 6	2.79-3.49	37.62-53.59
[20]	PLA				1800 ^{1st} 2100 ^{rest}	200	85		[0/90]	0.1	100	2	3.37	59.3
[76]	PLA				1200	220	110		[±45/90/0] _s	0.4	100		1.67	45
[134]	PLA				1800-5400	190-230	40-50		0	0.2	100		3.47	46.67
[139]	PLA				2400-5400	195-230		E	0, 45,90	0.1-0.3	100		1.52-2.25	22-55
[140]	PLA				2400	210-230	60	E	0-90		20-100		1.50-2.44	20-54.4
[141]	PLA				3000	210	70	E	0,45,90	0.1-0.3	100		4.73	26.75-47.3
[142]	PLA				1800	200	50		45	0.1-0.2	20-50		0.73-1.34	27.6-48.9
[143]	PLA								[0/90],[±45]	0.2-0.4	100		3.2-3.4	48.5-60.4
[29]	PLA				3000	190	70	F	0,90		100		3.4	54.7

Table 2.2 *Cont.*

Study	Material Parameters				Printing Parameters								Tensile properties	
	Polymer	Reinforcement			Print speed (mm/min)	Nozzle temp. (°C)	Bed Temp. (°C)	Build orientation F, E, Z	Raster angle (degree)	Raster thickness (mm)	Infill volume (%)	Contour (lines)	Stiffness (GPa)	Ultimate Strength (MPa)
		Material	Length (mm)	Diameter (µm)										
[144]	PLA				2400-5400	215		E	0-90	0.1-0.3			1.52-2.23	23.78-55.86
[145]	PLA								0,45,90				1.24-1.52	31.1-38.7
[137]	PLA				1200	190-240	40	F	[0/90], [30/60], [±45], [75/15]	0.1	100	12	2.12-2.62	28.71-35.66
[10]	PLA					240	90			0.08-0.64	20-80		2.35	1.18-25.41
[136]	PLA				1200	230	60		0,90	0.2	100		0.61-0.63	48-54.5
[146]	Nylon								concentric, 0				0.53	61
[11]	Nylon					274		F, E	0	0.1, 0.125, 0.2	100		0.41-0.47	27.2-30.9
[32]	PC					345	145	F, E, Z	[0/90], [30/60], [±45], [75/15]				1.62-2	30.4-43.5
[72]	PC					300		F	0, 15, 30, 45, 60, 75, 90	0.267			1.35-2.08	16.89-59.77
[67]	PC							F, E, Z	[0/90]	0.508			1.18-1.57	20.6-35.7
[75]	PC					345	140		[0/90], [30/60], [±45]	0.432-0.508			1.5-1.83	45-55
[25]	PEEK					334		F	0, 30, 45	0.2, 0.3, 0.4		2		32.4-56.6
[131]	PEEK					405		F	[±45]	0.2	100		3	81
[39]	PEI							F	0, 90			1, 5		26-77
[18]	PEI					375	162		0				3	90

Table 2.3 Summary of parametric study in nano/short fibre thermoplastic FDM process.

Study	Material Parameters					Printing Parameters								Tensile properties	
	Polymer	Reinforcement				Print speed (mm/min)	Nozzle temp. (°C)	Bed Temp. (°C)	Build orientation F, E, Z	Raster angle (degree)	Raster thickness (mm)	Infill volume (%)	Contour (lines)	Stiffness (GPa)	Ultimate Strength (MPa)
		Material	Length (mm)	Diameter (µm)	Content (by wt%)										
[73]	PP	GF			30	480	185			[±45]	0.2	100		1.9	40
[23]	PP	GF					240	30			0.1, 0.4	100		0.25-0.4	20-32
[54]	ABS	CF	0.15 ,0.1	7.2	3 - 15	1200 ^{1st} 1500 ^{rest}	230			[±45]	0.2	100		2-2.6	34-44
[52]	ABS	CF			5	15, 20, 25, 30, 35	200, 210, 220, 230, 240	80	F	[±45], [0/90]	0.15, 0.2, 0.25, 0.3, 0.35	100	3	0.6-1.1	18-37
[45]	ABS	CF	<0.4		10 - 40		205				0.2			2-14	30-65
[44]	ABS	CF	<0.4		13		220							1.52-8.91	7.0- 70.69
[69]	ABS	CF	1		20	3048	250			0, 90				2.13-11.92	10.27-66.18
[59]	ABS	CF	<3		13, 20		250	95						8.18-11.94	53.3-66.4
[12]	ABS	CF			8	3600, 4800, 6000				0,[±45], 90	0.18, 0.24, 0.3			2.19-5.89	13.74-39.05
[19]	ABS	GF					250	60	F, Z						24-58 kg*
[69]	ABS	GF	1		20	3048	250			0, 90				2.48-5.65	15.30-54.33
[59]	ABS	GF	<3		20		250	95						5.67	54.4
[33]	ABS	Jute			5	3300	230				0.27			0.871-1.543	12.9-25.9
[33]	ABS	Nano TiO ₂			5	3300	230				0.27			1.355-1.708	18.4-32.2

Table 2.3 *Cont.*

Study	Material Parameters					Printing Parameters							Tensile properties		
	Polymer	Reinforcement				Print speed (mm/min)	Nozzle temp. (°C)	Bed Temp. (°C)	Build orientation F, E, Z	Raster angle (degree)	Raster thickness (mm)	Infill volume (%)	Contour (lines)	Stiffness (GPa)	Ultimate Strength (MPa)
		Material	Length (mm)	Diameter (μm)	Content (by wt%)										
[12]	ABS	CNTCF			15	3600, 4800, 6000				0, [±45], 90	0.18, 0.24, 0.4			2.01-2.52	21.46-29.64
[30]	ABS	VGCFs	0.1	0.1	10										37
[29]	PLA	CF			15	3000	190	70		0,90	0.3	100		7.54	53.4
[27]	PLA	CF	0.131	7	5,10,20	1200 ^{1st} 3600 ^{rest}	210	60		[±45]	0.1	100		3.4-7.4	60-70
[20]	PLA	CF	0.125	7.4	15	1800 ^{1st} 2100 ^{rest}	200	85		0/90	0.1	100	2	5.68	55.2
[134]	PLA	CF			10	1800-3000	210-240							1.6	34.2
[137]	PLA	CF	0.06		15	1200	190-240	40	F	[±45]	0.1	100		3.6	30.35
[10]	PLA	CF					240	90		[0/90], [±45]	0.08-0.64	20-80	2	2.35	25.41
[133]	PLA	CF	.015-0.03	6.105	20	3600	230	72		45	0.1-0.3	25-100	2	0.55-1.45	16.56-48.06
[70]	PLA	CF	0.15-0.2	7	20	1200-3600	190-230		F,E,Z		0.1-0.3				20-54.5
[90]	PLA	CF	0.15	7.2		1200	200	80			0.4	100		2.75	55
[136]	PLA	CF	0.15-0.2		5,10	1200	230	60	F,Z		0.2	100		0.96 -2.02	54.1-81.2
[135]	PLA	CNT			1,5,10	3600	220		F	[0/90], [±45]	0.2	100		3.8-4.2	35-45
[27]	PLA	BF	0.13	12	5 - 20	1200 ^{1st} 3600 ^{rest}	210	60		[±45]	0.1	100		3-5.5	61-70
[21]	PLA	MWCNT			14.3									~3-3.5	40-50

Table 2.3 *Cont.*

Study	Material Parameters					Printing Parameters							Tensile properties		
	Polymer	Reinforcement													
		Material	Length (mm)	Diameter (μm)	Content (by wt%)	Print speed (mm/min)	Nozzle temp. (°C)	Bed Temp. (°C)	Build orientation F, E, Z	Raster angle (degree)	Raster thickness (mm)	Infill volume (%)	Contour (lines)	Stiffness (GPa)	Ultimate Strength (MPa)
[76]	PLA	nano CF	0.0005	0.05	0.5 - 2	1200	220	110		[±45/45/90/0] _s	0.4	100		1.822	41-48
[43]	nylon	micro CF	0.1		6		260		F		0.2			1.85	33.5
[21]	nylon	CF	0.13		14.3									~1-2	45.5
[26]	nylon	CF	0.05-0.2	5	65	300	270	110			1			3.5	153.62
[37]	nylon	CF		6-7	2 - 10	1800	250	120		0		100		1-3.5	48-90
[36]	nylon	CF							F	[±45]	0.1			3.019	58.2
[125]	nylon Onyx	CF			30		275			[0/90]	0.125	100		1.59	64.2
[85]	nylon Onyx	CF								[0/90]	0.1	100		3.2	51
[59]	PPS	GF	<3		40		357	95						10.82	51.2
[69]	PPS	GF	1		40	3048	251			0, 90				10.82	51.2
[18]	PEI	CNT yarns					375	162		0				3	119
[131]	PEEK	MWCNT			3-10		405-450	100	F	[±45]	0.2	100		3.4-3.8	51-101

Table 2.4 Summary of parametric study in continuous fibre thermoplastic FDM process.

Study	Material Parameters				Printing Parameters								Tensile properties	
	Polymer	Reinforcement			Print speed (mm/min)	Nozzle temp. (°C)	Bed Temp. (°C)	Build orientation F, E, Z	Raster angle (degree)	Raster thickness (mm)	Infill volume (%)	Contour (lines)	Stiffness (GPa)	Ultimate Strength (MPa)
		Material	Length (mm)	Diameter (µm)										
[43]	nylon	CF		36.67	2.39 cm³/hr	260			0	0.125	100		62.5	968
[21]	nylon	CF		35.7					0				10	341
[121]	nylon	CF							0					
[11]	nylon	CF		350	2.4-32	274 (nylon) 232 (fibre)	F, E	0	0.125				7.6-51.7	96.6 - 436.7
[122]	nylon	CF		45					[±45]/0				37	360
[41]	nylon	CF				265 (nylon) 270 (fibre)		concentrict, 0	0.125	50				235.5 - 404.3
[42]	nylon	CF		30-35					0.125				15-35.7	128 - 520
[146]	nylon	CF		350	13.59	263	NO	concentrict, 0	0.125				7.73	216
[124]	Onyx	CF		350	38-41	270 ^{Onyx} 250 ^{CF}		[0,±45,90], [± 45]	0.125	100			71.7-80.4	597-768
[11]	nylon	GF		300	4-34	273 (nylon) 232 (fibre)	F, E	0	0.1				3.7 - 19.6	113.4 - 381.2
[122]	nylon	GF		47.62					[±45]/[0/90]				6.4	180
[41]	nylon	GF				266 (nylon) 270 (fibre)		concentrict, 0	0.1	50				302.6 - 372.1
[146]	nylon	GF		300	10-13	263	NO	concentrict, 0	0.1				3.12-3.75	194 - 206

Table 2.4 *cont.*

Study	Material Parameters				Printing Parameters								Tensile properties	
	Polymer	Reinforcement			Print speed (mm/min)	Nozzle temp. (°C)	Bed Temp. (°C)	Build orientation F, E, Z	Raster angle (degree)	Raster thickness (mm)	Infill volume (%)	Contour (lines)	Stiffness (GPa)	Ultimate Strength (MPa)
		Material	Length (mm)	Diameter (µm)										
[11]	nylon	KF		300	3.2-29	275 (nylon) 232 (fibre)		F, E	0	0.1			5.2 - 25.5	55.8 - 235.6
[122]	nylon	KF			42.1				[±45]/[0/90]				8.7	170
[122]	nylon	KF			42.1				[±45]/[0/90]				8.7	170
[41]	nylon	KF				267 (nylon) 270 (fibre)			concentric, 0	0.1	50			259.7 - 309.14
[146]	nylon	KF		12	8.6-10.8	263	NO		concentric, 0	0.1			3.61-4.37	150 - 164
[60]	PLA	CF			9.3	60	210	80	0				20	200
[126]	PLA	CF			<42.92									91
[51]	PLA	CF			34.93	100, 200, 300, 400, 500, 600	180, 190, 200, 210, 220, 230, 240	NO		0.3, 0.4, 0.5, 0.6, 0.7, 0.8				
[147]	PLA	CF			24-35	300	220		0	0.25-0.4			39-61	481-650
[148]	PLA	CF			20.19		210		0	0.3			14.76	140
[61]	PLA	CF			1.45	100	210	80					5.8	90
[149]	PLA	CF					260	100	0					112

Table 2.4 *cont.*

Study	Material Parameters					Printing Parameters								Tensile properties	
	Polymer	Reinforcement				Print speed (mm/min)	Nozzle temp. (°C)	Bed Temp. (°C)	Build orientation F, E, Z	Raster angle (degree)	Raster thickness (mm)	Infill volume (%)	Contour (lines)	Stiffness (GPa)	Ultimate Strength (MPa)
		Material	Length (mm)	Diameter (µm)	Content (by wt%)										
[150]	PLA	CF		7	36.3	300	215			0	0.5			8.28	61.4
[60]	PLA	Jute			7.11	60	210	80		0				5	50
[62]	PLA	KF			13.11	100	210	NO			0.1-0.3			7.42	73.54
[151]	PLA	KF		400	6.54 vol%						0.8		4	3.29	104.64
[148]	PLA	KF			8.07									2.6	125.22
[13]	ABS	CF			10	600	230	90			0.5			4.18	147

Chapter 3 Manual Moulding Filament

This chapter aims to study the feasibility of forming a DcAFF 3D printing filament from ADFRC, produced with the HiPerDiF technology and impregnated with PLA. At this stage, this study deploys manual moulding, which is a pragmatic interim solution given its low manufacturing complexity and minimal investment requirement. Then, the printability of the produced circular filaments will be investigated. Finally, the tensile properties of the batch-produced DcAFF filament will be benchmarked to commercially available 3D printing materials.

This chapter was constructed based on the work published in *Additive Manufacturing* in 2021 under the title of “Batch production and fused filament fabrication of highly aligned discontinuous fibre thermoplastic filaments” [2]. The whole article and the testing result were prepared by N.K. and amended by all the authors.

N. Krajangsawasdi, M. L. Longana, I. Hamerton, B. K. Woods, and D. S. Ivanov, "Batch production and fused filament fabrication of highly aligned discontinuous fibre thermoplastic filaments," *Additive Manufacturing*, vol. 48, p. 102359, 2021. DOI: 10.1016/j.addma.2021.102359.

3.1. Chapter introduction

The HiPerDiF ADFRCs are initially produced in the form of thin tape. One of the main challenges with printing ADFRC is the creation of a circular cross-section filament that would be suitable for a generic FDM machine. The literature review in Chapter 2 showed that the conventional filament manufacturing techniques are not appropriate for the dry fibre preforms produced with the HiPerDiF technology. Blending/mixing used with short fibre composites would break the fibres and undo the careful fibre alignment created by the ADFRC process; while the other option (used to manufacture continuous fibre reinforced filaments) of pultruding the fibres through a resin bath for impregnation is impossible because the pulling force would tear the discontinuous fibre preform apart. Thus, a new bespoke filament-forming process must be developed for the DcAFF filament to minimise fibre breakage and maintain fibre orientation.

In this chapter, a manual moulding method was used for the first filament-forming feasibility study to reshape the HiPerDiF-PLA tape into a DcAFF circular cross-section filament. In the beginning, the mould designed by Blok [50] was examined, before a new mould was designed to address the issues with the original mould, *i.e.* the voids trapped in the filament and low filament quality. After a satisfactory moulded filament had been achieved with an optimized mould, the printability of the produced filament was tested under different printing parameters: deposition speed, process temperature, and layer thickness. As a result, a set of printing parameters offering a good deposition was proposed. Then, the physical and mechanical properties of the produced material at each manufacturing stage were studied. Finally, the performance of a component produced with the DcAFF filament was compared with the data available in the literature. This placed the results in a wider context and paved a clear route forward to improve the production rate and performance of the DcAFF filament.

3.2. Materials properties

Poly(L-lactic acid) (PLA), a common FDM material, was chosen for this preliminary study as a proof-of-concept matrix due to its high printability, well-known mechanical and thermo-chemical characteristics and low cost, as mentioned in Chapter 2. The PLA used in this study is a commercial 3D printing transparent PLA filament, supplied by 3D4Makers B.V. [152]. The filament has a melting temperature between 145°C and 160°C.

The fibres used to produce the HiPerDiF preform are commercial 3-mm chopped C124 carbon fibre with a fibre diameter of 7 µm supplied by Toho Tenax GmbH. According to the calculation of the critical fibre length of PLA/S.CF mentioned by Blok *et al.* [47], the critical fibre length is between 0.8-1.38 mm depending on the interfacial shear strength of PLA-carbon fibre, around 11-19 MPa, reported by Wan *et al.* [153]. The selected fibre length, 3 mm, is chosen to be comfortably above the mentioned fibre critical length. The raw material properties: PLA filament and carbon fibre, are shown in Table 3.1.

Table 3.1 Physical and mechanical properties of PLA filament and carbon fibre.

Material	Density (g/cm ³)	Tensile modulus (GPa)	Tensile strength (MPa)
PLA filament [154]	1.24	3.86	144
C124 carbon fibre [155]	1.82	225	4344

3.3. Manual filament forming manufacturing

The forming process to obtain a circular cross-section DcAFF 3D printing composite filament starting from discontinuous fibres and PLA tape is summarised in Figure 3.1. The process can be broken into four main stages:

3.3.1. Stage (A): preparation of fibre and matrix

Dry HiPerDiF preforms were prepared using the HiPerDiF machine as described in Chapter 1 (Figure 1.2). The fibres were suspended in water at the calculated concentration, 0.001–0.003% of the fibre in volume, and processed through HiPerDiF to obtain an aligned discontinuous fibre preform. The PLA was initially printed,

using a RepRap Prusa i3 MK3S 3D printer, into a thin film of approximately 0.1 mm in thickness, 13 mm in width, and 200 mm in length.

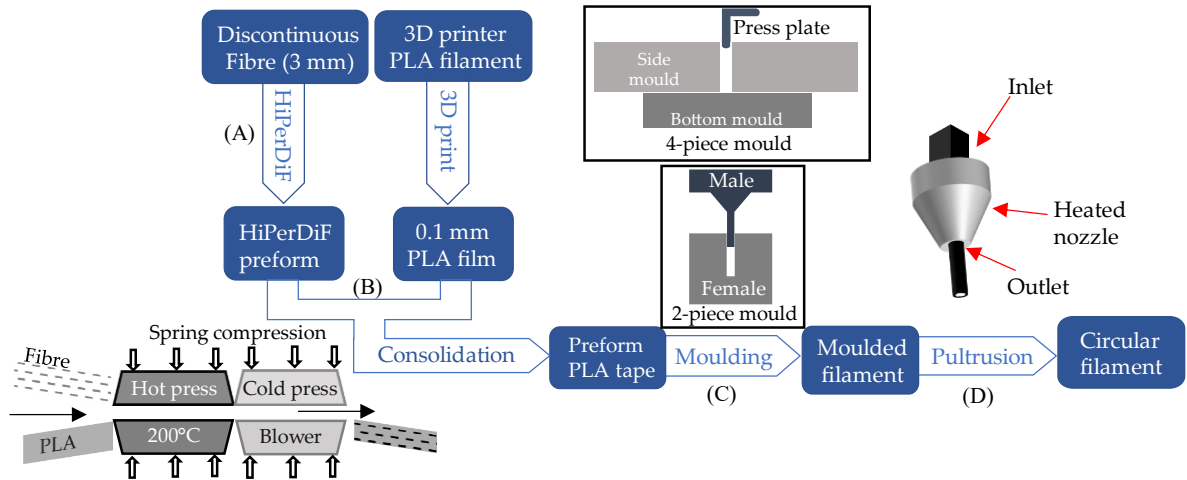


Figure 3.1 Summarized manual moulding method to produce a circular-shaped DcAFF filament from stages (A) preparation of discontinuous fibre (HiPerDiF) and PLA matrix; (B) consolidation of HiPerDiF-PLA; (C) manual moulding; (D) pultrusion.

3.3.2. Stage (B): consolidation

HiPerDiF preform was placed on top of the printed PLA film on a guiding slot and then they were fed into a custom-built consolidation module, shown in Figure 3.1 stage (B). There are two stages in the consolidation process: a hot press at about 210°C, with approximately 1 bar pressure for about 25 seconds, followed by a cooling section under the same pressure, as described by Blok *et al.* [47]. These parameters were found in processing trials as those that offered a better tape mechanical performance compared to other temperature and pressure ranges. After the preform was impregnated with the PLA film, the excess PLA tape, occurring due to the transverse shear flow of the matrix, was trimmed, resulting in a tape measuring a width of 5 mm and a thickness of 0.2 mm; the cross-section of the tape and all of the following produced materials were prepared, polished and inspected with the method (microscope) described in Appendix A. Figure 3.2 shows the current HiPerDiF-PLA impregnated tape. It was observed that there was a greater concentration of fibres (seen as white dots) on the upper surface of the preform. This is because the preform was placed on top of the PLA tape and the pressure is not

high enough to cause diffusion of the fibres into the lower surface.

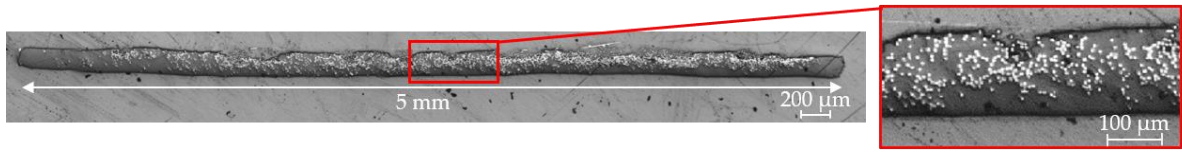


Figure 3.2. Cross-section of 5 mm wide HiPerDiF-PLA tape.

3.3.3. Stage (C): manual moulding

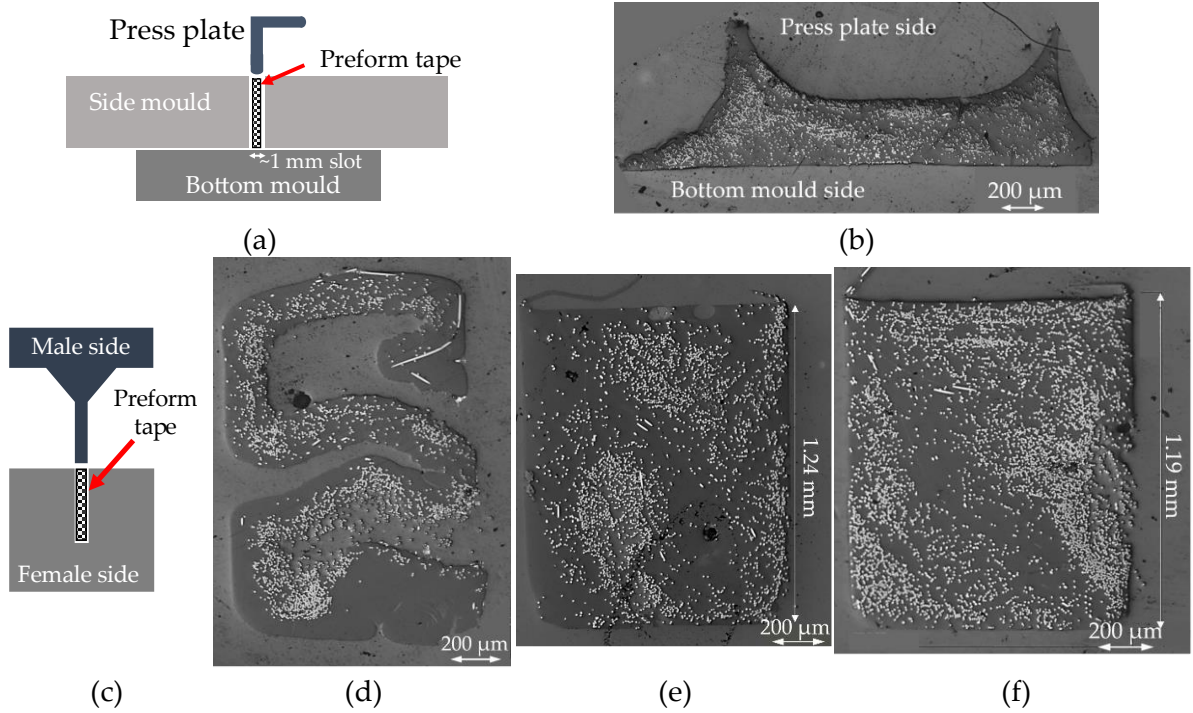


Figure 3.3. (a) Schematic of the 4-piece mould including three aluminium blocks and a press plate with a preform tape inside; (b) cross-section of the moulded filament after moulding with the 4-piece mould; (c) schematic of the 2-piece mould designed with a perfect sharp machined corner shape of the female and male mould; (d) cross-section of the moulded filament with the 2-piece mould under 150°C and 2 MPa condition showing folding tape without thermoplastic fusion; (e) and (f) cross-section of the moulded filament with the 2-piece mould under 200°C and 1 MPa condition at different positions: 120 mm and 240 mm.

In Figure 3.1 stage (C), the tapes were reshaped using two different small-channel moulds; the first mould, from Blok's study [50], was made from three assembled aluminium blocks and using an off-the-shelf L-shape aluminium extrusion to compress the tape, shown schematically in Figure 3.3(a), called a "4-piece mould". The HiPerDiF-PLA tapes were placed in the mould that was then heated to 250°C in an oven for an hour. Next, the L-shape bar was inserted into the channel to press the

heated tape and change the flat shape into the moulded shape, as shown in Figure 3.3(b). The moulded filament has a flat side, corresponding to the flat end of the channel, and a material overflow side, caused by the L-shape press plate filleted edges. Moreover, some material also flowed into the channels created between the bottom mould and the filleted corners of the side mould blocks.

The uncontrolled material overflow into the slot and the high aspect ratio of the moulded part may induce voids inside the filament during the next pultrusion stage to form a circular cross-section filament. To reduce this uncontrollable phenomenon, the mould was re-designed to produce a controlled square or rectangular moulded shape under compression pressure and heat. The modified mould was designed and precisely machined into two pieces: a female slot mould with perfect 90° corners at the bottom and a male mould with a perfectly flat end, as illustrated in Figure 3.3(c) and called the “2-piece mould”. The temperature and pressure of the moulding process were investigated to find the lowest temperature and pressure in order to identify the minimal energy needed to produce the filament. In this case, the pressure is calculated from the mass of the metal placed on the mould and the area of the slot. At the lowest temperature (150°C) and pressure around 2 MPa (8 kg per 40 mm²), the tape cannot reshape to a proper square shape. Figure 3.3(d) shows an improper moulded cross-section shape which presents a folding of the thin tape without thermoplastic fusion. This will lead to void formation in the filament. The desired cross-section was achieved at 200°C and 1 MPa (4 kg per 40 mm²) condition, while higher temperatures yielded similar results and tended to degrade the thermoplastic. Examples of the cross-section of moulded filament at 12 and 24 cm along the length of a moulded filament under 200°C and 1 MPa condition are shown in Figure 3.3(e) and (f). It can be seen that the moulded filament cross-section has an almost sharp square shape with very limited material overflow: there are almost no voids in the cross-section and the fibres are more evenly distributed. Although the bottom corners are curved and do not conform perfectly to the 90° corners, this may in fact be beneficial during further stages of the process which form a circular

filament. There are tiny overflows at the top corner because of the small gap between the female and male mould that is necessary for mould insertion. This overflow is expected to be eliminated during the pultrusion and will not trap voids in the same manner as the previous large overflow area. Fibre dispersion in this moulding technique is manipulated by the formation of folding due to compression, as seen in the improper fusion at low temperatures (Figure 3.3(d)).

3.3.4. Stage (D): pultrusion

The moulded filaments were pultruded through a series of circular cross-section brass nozzles, converging from 1.5 mm to 1.2 mm in diameter with steps of 0.1 mm at a temperature of 120-140°C to produce a circular cross-section filament. Initially, the moulded filaments produced from 4-piece mould filament could be smoothly pultruded until reaching a circular filament of 1.2 mm diameter and the cross-section at different positions of a filament were observed through polishing, as shown in Figure 3.4(a)-(c). It can be seen that the fibres disperse around the cross-section. The pale grey and black colours in the filaments represent voids filled and unfilled by the potting resin. The pale voids in the middle of the filament are believed to have become entrapped by the folding of overflow material in the 4-piece moulded filament (Figure 3.3(b)) and this is consistent with the assumption that the two overflow triangles on either side join to produce an asymmetric section, as seen in Figure 3.3(a)-(c).

With the 2-piece mould filament, the moulded filament processed was pultruded through a circular 1.2 mm diameter die at 120-140°C, to change the cross-section from square to circular. As the large void area was eliminated by the 2-piece mould, the final filament cross-section can be reduced to a diameter of 1.1 mm which still can be easily pultruded through a circular nozzle. Figure 3.4(d)-(f) shows the cross-section of the circular-shaped filament at different positions. Overall, the 2-piece moulded filament cross-section is almost circular at every position, although where the cross-section is slightly less than 1 mm², due to inconsistent tape impregnation

and excessive pressure during moulding, a square-shaped filament with a round corner is observed, as Figure 3.4(d). The imperfect circular-shaped filament may cause non-continuous extrusion during printing as the diameter variations impede correct material feeding. Owing to the uncontrollable folding of the tape during mould compaction, some cross-sections present non-uniform fibre distribution, as seen in Figure 3.4(f) where there is a higher fibre concentration on the right edge of the filament than in the centre. The phenomenon needs to be addressed if better damage tolerance of composite is required. Because of the short length of the mould (400 mm), it is necessary to bond multiple filaments end-to-end before the pultrusion process to produce a continuous filament that could be fed continuously to the printer.

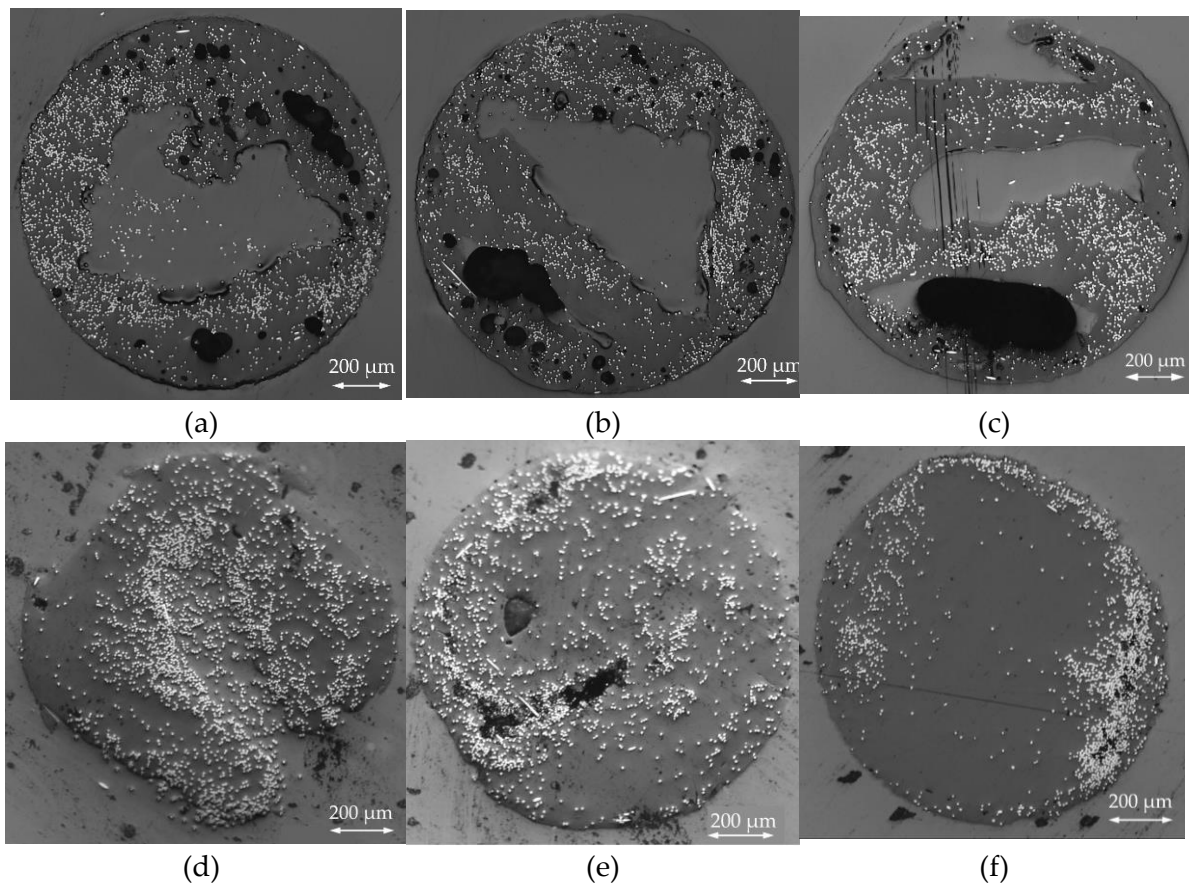


Figure 3.4. (a)-(c) cross-section microscopy of a 1.2 mm filament produced from the 4-piece mould filament at the different positions along the length; (d)-(e) cross-section microscopy of a 1.1 mm filament produced from 2-piece mould filament at the different positions along the length.

The information gained by comparing the two moulding techniques is important for the future development of a continuous process as it makes the first attempt to relate process parameters to internal morphology resulting from the re-shaping of the thin tape. Moreover, it was demonstrated that a well-designed mould can reduce the thickness-to-width ratio of the moulded filament close to 1-to-1. At the same time, the void formation during pultrusion can be reduced by minimizing the material overflow during moulding.

3.4. Filament characterisation

3.4.1. Thermogravimetric analysis of the HiPerDiF-PLA tape

Thermogravimetric analysis (TGA) was conducted on the HiPerDiF-PLA composite tape to identify the degradation temperature and establish a maximum processing temperature for this study. TGA was operated at a ramp rate (10°C/min) from room temperature to 800°C using a simultaneous thermal analysis (STA) instrument (Netzsch STA 449 F1 Jupiter [Netzsch-Gerätebau GmbH, Wolverhampton, UK]). STA result of the HiPerDiF-PLA sample is shown in Figure 3.5. The maximum temperature for this study is limited to a maximum of 250°C as there is no significant mass loss below this temperature.

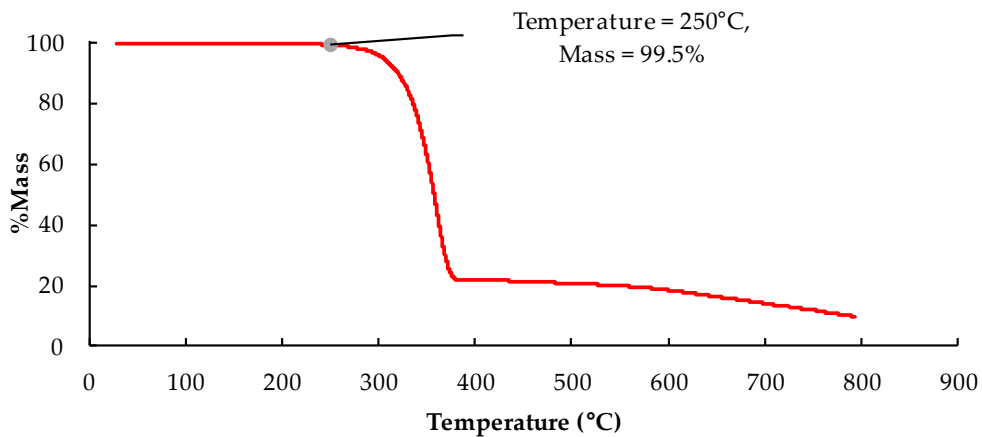


Figure 3.5. TGA result of a HiPerDiF-PLA composite material showing no degradation of a sample before 250°C as the mass loss around 0.5%, which is less than the 5% mass loss criterion, at 250°C.

3.4.2. Fibre alignment calculation with microscopic image method

In this preliminary study chapter, the degree of fibre alignment was calculated on a

burn-off technique and employing microscopic images, to compare their accuracy and ease of use.

3.4.3.1. Fibre content calculation using matrix burn-off method

The burn-off technique uses a special TGA programme that was developed to calculate fibre weight fraction in composite materials [156]. This method needs a TGA instrument, the same one used for the degradation test in Section 3.4.1, to measure the weight loss after reaching a predefined temperature. The sample was heated rapidly to 250°C with a 20°C/min ramp followed by a 10°C/min heating rate to 600°C and then held isothermally for 40 minutes. The heating programme (indicated by the dashed and dotted red line) and the TGA results of fibre, PLA, and DcAFF composite filaments are shown in Figure 3.7. There is no significant degradation of the fibre at 600°C and the average residue from pure PLA is 0.9%. The filaments tested using the programme show around 16-19% residual mass. The fibre weight fraction (f_f) is the difference between the residual mass and the PLA residual percentage, so the fibre fraction of the filament is approximately 15-18 wt%. The fibre weight fraction can be converted to fibre volume fraction (V_f) and compared to the image method using Equation (3.1)

$$V_F = f_F \frac{D_C}{D_F} \quad (3.1)$$

where D_C is composite density by measurement and D_F is fibre density. The void volume (V_V) also calculated from the TGA result using Equations (3.2) and (3.3):

$$V_V = \frac{100(T_D - D_C)}{T_D} \quad (3.2)$$

$$T_D = \frac{100}{\frac{R}{D} + \frac{r}{D_F}} \quad (3.3)$$

where R is the percentage of resin by weight, r is the percentage of fibre by weight that is the result of the TGA and D is the resin density.

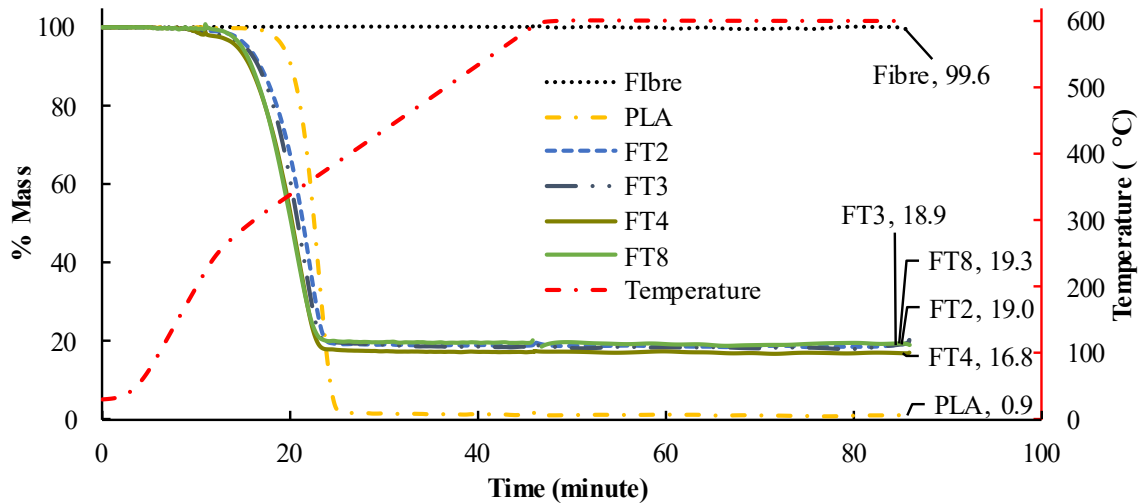


Figure 3.7. Special TGA programme, using Netzsch STA 449 F1 Jupiter, to investigate fibre weight fraction by considering residual fibre content after matrix burn-off including fibre, PLA and DcAFF filament with the temperature profile (red). The FT indicates the filament produced from the 4-piece moulding method and the numbers is the different filaments in the tensile testing below.

3.4.3.2. Fibre content calculation using the microscopic image method

Fibre content can be calculated with a cross-section microscopic image by a separation of the different colour shades, with white representing fibre, grey PLA matrix, and black or pale grey as voids in the cross-sectional area. The percentage of the white area in the cross-section is computed. The percentage shows the volume of fibre in the cross-section. The colour shade difference is identified by the threshold adjustment using ImageJ software. Figure 3.8 illustrates an example of threshold adjustment to identify the amounts of white dots in the total cross-sectional area (in the yellow envelope) of a circular filament, as shown in Figure 3.4(b).

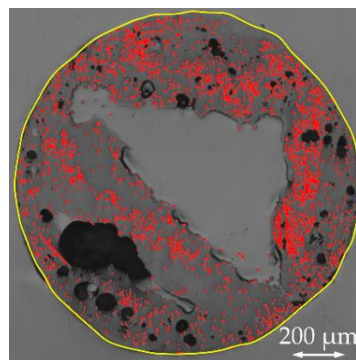


Figure 3.8. Threshold adjustment to identify fibre in the cross-section of filament in Figure 3.4(b) showing the fibre, red highlighted colour, is 8.1% of the total area in the yellow circle.

The fibre content by volume calculated from the matrix burn-off method is the direct calculation procedure that measures the actual weight of fibres, but it is a time and resource-consuming process. This fibre volume calculation neglected the void volume in the sample (assuming $V_v = 0$), so the calculated fibre volume content from the TGA burn-off technique presented in Table 3.2 are overestimated and the actual fibre volume content should be slightly lower. The microscopic image can be produced and analysed easily, but it analyses only one section along the length. Thus, the image method is an indirect measurement and has lower reliability compared to the burn-off method which needs to be verified. The result from the microscopic image method of several circular filaments produced from the 4-piece mould is compared to the result from the burn-off method in Table 3.2 to verify the reliability of the microscopic method.

Table 3.2 Comparison of fibre content by volume of the same filament batch at the different positions along the length calculated with microscopic image over the polished cross section area and TGA burn-off methods over a certain length (~10-30 mg).

Sample	FT2	FT3	FT4	FT8
Microscopic image	9.5	7.5	8.8	8.1
Burn-off	13.1	13.0	11.4	13.3
%difference	27.4	42.3	22.8	39.1

The difference between the two methods is relatively large and variable. Although the microscopic method can reduce the calculation resource, *i.e.* special machine, and save processing time in the heating stage, it may be an inaccurate method to measure the fibre content due to the low resolution of the small fibre diameter on the filament diameter and can be used only for fibre comparison between batches. It is recommended that the fibre content should be calculated using the matrix burn-off technique, but this can provide only the fibre weight content and cannot reveal the void content. Hence, the void content still needs to be calculated following the microscopic image method. Owing to the limited resources, time, and access to the TGA instrument, the fibre and void content of the materials produced in this chapter were estimated roughly based on the microscopic method. The fibre content used

for a comparison to the following chapter will be the result of the matrix burn-off.

3.4.4. Filament mechanical performance

To investigate the mechanical performance of filaments produced from the 4-piece and 2-piece moulds, tensile testing was used to compare the improvement after the reduction of voids by the newly designed mould. The specimens were prepared by cutting 100-mm long sections from the circular filament, and 20-mm long fibreglass end-tabs were attached at both ends of the samples leaving a gauge length of 60 mm, as shown in Figure 3.9, with the assistance of a thick double side sticky tape on the circular sample. Repeated measurements of specimens' dimensions were taken along the gauge length by a micrometre for cross-section area calculation. The fibre alignment and fibre content in this chapter were calculated based on the microscopic image method presented in Sections 3.4.2 and 3.4.3.2. A servo-electric tensile testing machine (Shimadzu, Japan) with a 1 kN load cell operated at a cross-head displacement speed of 1 mm/min was used. The strain was measured using a video extensometer (Imetrum, UK). The outliers in tensile stiffness and strength results were eliminated using the "Modified Thompson Tau Test" [157] and the specimens that broke in end-tabs were discarded from strength calculation. This procedure allowed to calculate the mechanical properties of the filaments averaging over 7 and 14 samples for the 4-piece and 2-piece moulds, respectively.

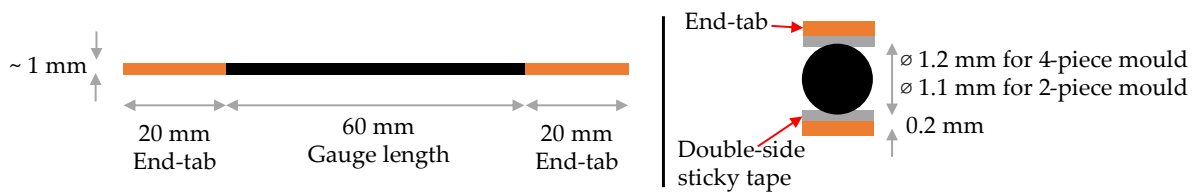


Figure 3.9. Schematic of circular filament specimen produced from moulded filament with 4-piece and 2-piece mould and the end-tab position in top and side view.

The properties of 4-piece and 2-piece moulded filament and the improvement achieved from the mould design are shown in Table 3.3. The fibre alignment, measured according to Section 3.4.2, shows that the 2-piece mould has a slightly lower percentage of fibres aligned within $\pm 10^\circ$ than the 4-piece mould. This may be

a result of the restriction in the 2-piece mould that offers no space for the molten material to flow creating backpressure so the fibres cannot freely move perpendicularly to the compression force. However, the majority of fibres in the 2-piece moulded filament are still aligned in the longitudinal direction. An obvious change between circular filament produced from 4-piece and 2-piece mould is the reduction in the total cross-section area. The circular filaments produced from the 2-piece mould square shape filament have a smaller cross-section area than the 4-piece mould one because of the lower void content trapped in the circular filament after the pultrusion. The void content substantially decreases from above 30 vol% to below 10 vol%, according to the void calculation across the cross-section microscopic image method presented in Section 3.4.3. As the reduction of the overall cross-section area, there is an increase in the fibre content by volume calculated as a fraction of the total cross-section area. Although there are several improvements in the physical properties when using the 2-piece mould, the mechanical properties of both groups are practically almost the same when considering the average values and standard deviation, as can be seen in the plot of Figure 3.10, especially the tensile strength. The similarity in strength is because both groups have a similar failure mode as fibre pull-out dominated by the fibre-matrix interface. There is a small increase in the tensile stiffness of the 2-piece filament due to the mass reduction of the voids.

Table 3.3 Properties comparison of circular cross-section filament produced from moulded filament with the 4-piece and 2-piece mould.

	4-piece mould	2-piece mould	% difference
Alignment (% in $\pm 10^\circ$)	79.4	70.4	-11.3%
Cross-section area (mm ²)	1.21 \pm 0.03	0.87 \pm 0.10	-28.1%
Fibre content (vol%)	7.7 \pm 0.7	8.6 \pm 2.0	+9.4%
Void content (vol%)	33.9 \pm 3.9	9.6 \pm 9.2	-71.7%
Tensile stiffness (GPa)	16 \pm 1	18 \pm 2	+10%
Tensile strength (MPa)	163 \pm 42	170 \pm 81	+5%

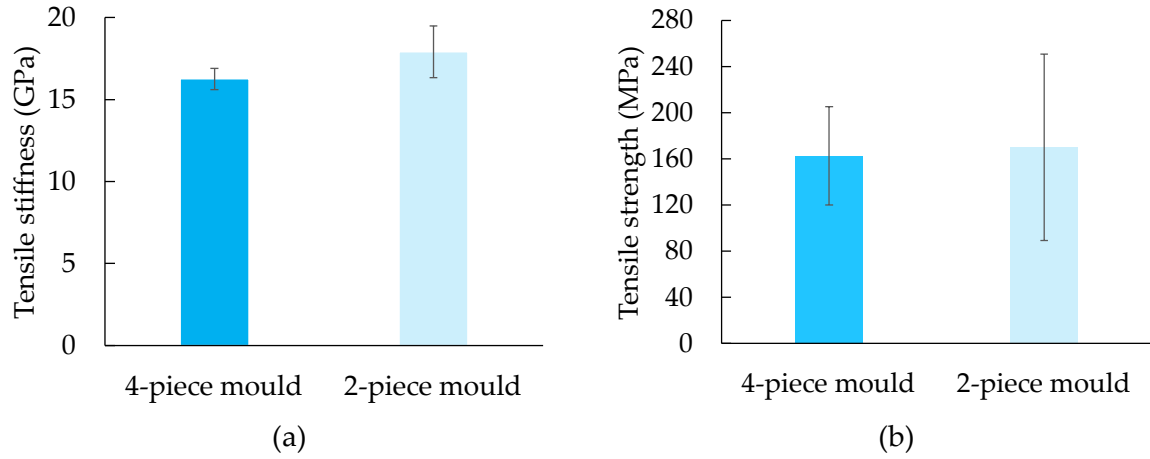


Figure 3.10. Comparison of (a) stiffness and (b) strength of circular filament produced from moulded filament with the 4-piece and 2-piece mould.

3.5. Printing parameter study

3.5.1. Parametric selection

The printability of the produced filament was studied using a Creality Ender 3 commercial 3D printer. The printing nozzle was specifically designed for the DcAFF filament and inspired by the filleted edge nozzle used in the Markforged continuous fibre printer and the flat face nozzle [158]. The customized nozzle drawing and the machined brass nozzle used in the printing process are shown in Figure 3.11. The bed temperature was kept constant in this chapter at 60°C as the lower bound temperature mentioned in Section 2.2.4, Figure 2.5. The investigated printing parameters are deposition speed (S), processing temperature (T), and layer thickness (L). The process temperature was chosen from the literature featuring PLA and fibre-reinforced PLA printing, Figure 2.4. Consequently, a low boundary temperature (210°C) was selected to ensure that the filament would be sufficiently softened during extrusion, while the upper bound was limited to 250°C, which is the limit of the degradation onset temperature of the HiPerDiF-PLA composite tape according to the TGA data presented in Section 3.4.1. To enhance the filament placement, the use of a low range of deposition speeds for printing continuous fibre filaments, as summarised from the literature review in Chapter 2, is preferable and so the speed was set in the range of 300-900 mm/min. The layer thickness was set to be lower than the diameter of the filament (1.2 mm) to press the filament on the printing bed; the

tested layer thickness is between 0.4 mm and 0.8 mm. The test matrix is shown in Table 3.4. The printing path was defined in a G-code to be a 100 mm long straight raster. At the end of printing, the filament feeder was reversed to cut the filament and finish printing.

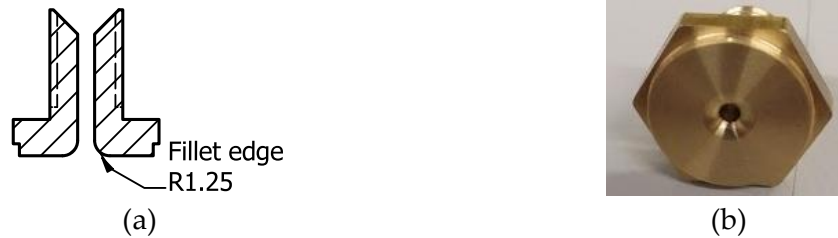


Figure 3.11. (a) Drawing of the designed nozzle with a 1.4 mm diameter and 1.25 mm fillet radius; (b) brass nozzle used in the printing process.

Table 3.4 Testing parameters and their levels in the printing trial.

Parameters	Symbol	Low	Medium	High
Process temperature (°C)	T	210	230	250
Deposition speed (mm/min)	S	300	600	900
Layer thickness (mm)	L	0.4	0.6	0.8

3.5.2. Set-up printing trial with 4-piece moulded 1.2-mm circular filament

This set-up printing trial was performed using the 4-piece mould circular filament to investigate the effect of printing parameters, mentioned in Table 3.4, and then scope the possible parameters used for the produced filament. There are three repeated prints for each test case. The printing results are shown in Figure 3.12.

Deposition at a speed of 900 mm/min resulted in a wavy raster because the material was not sufficiently softened within the nozzle resulting in a large deviation from the desired path (Figure 3.12(a)). During deposition at higher speeds, the raster tended to curl, possibly due to locked-in thermal stresses dominating the adhesion to the printing bed. In contrast, the lower speeds, 300 or 600 mm/min, provided good bed adhesion and produced straighter rasters, as shown in Figure 3.12(b). In this case, the lowest deposition speed (300 mm/min) is the most favourable, but it is time-consuming. Hence, also the medium speed (at 600 mm/min) was selected for subsequent tests, and the high speed of 900 mm/min was discarded.

The low process temperature generates a smooth surface, as seen in Figure 3.12(c). At the higher process temperatures, 230°C and 250°C, the polymer was in a fully molten state that allowed fibres migration and reorientation, resulting in a partial loss of their longitudinal alignment. Fibre misalignment resulted in fuzzy and stray fibres that blocked the nozzle. Besides, the raster printed with high temperature shows a ‘fuzzy’ surface, as seen in Figure 3.12(d1) with the high magnification in Figure 3.12(d2). The high and medium process temperatures (at 230°C and 250°C) were discarded as they led to nozzle clogging and fuzzy fibre on the surface of the deposited rasters, whereas 210°C was deemed optimal.

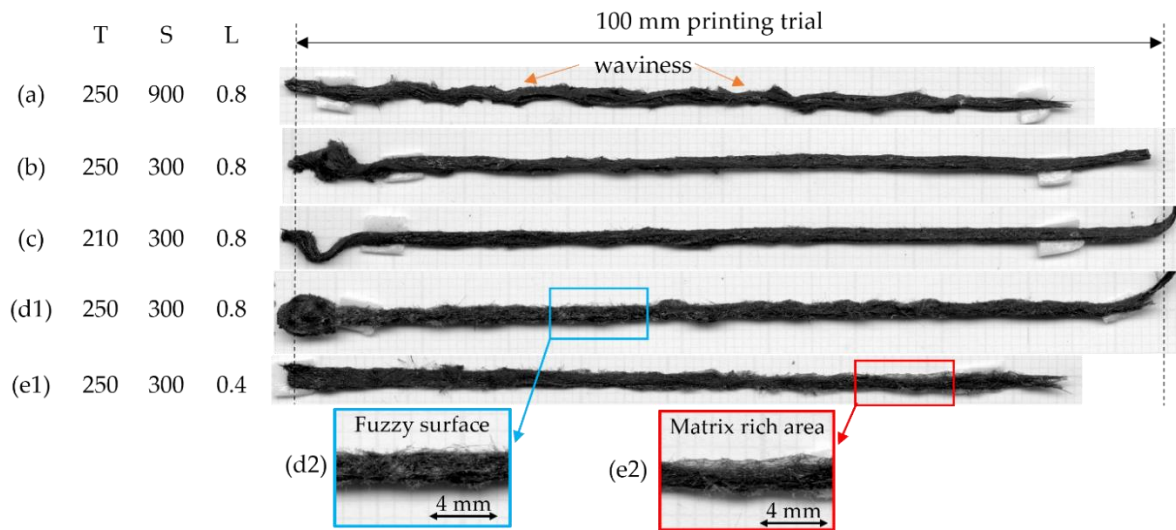


Figure 3.12. Set-up printing trial with single raster at different conditions for comparison: (a) high deposition speed; (b) low deposition speed; (c) low process temperature; (d1) high process temperature with the fuzzy fibre surface; (d2) high magnification of the fuzzy fibre surface when printing at high process temperature; (e1) low layer thickness with the matrix-rich area; (e2) high magnification at the matrix rich area when printing at low layer thickness.

Layer thickness is controlled by the nozzle height from the printing bed defined in the G-code. Printing at a low layer thickness (0.4 mm) caused a flat raster that sticks well to the printing bed, but the low layer thickness generates a high compression force that sometimes promotes lateral matrix flow causing matrix-rich areas at the sides of the raster, as seen in Figure 3.12(e1) with the high magnification in Figure

3.12(e2). The material overflow is difficult to control and it may change the expected raster width. Printing at the high layer thickness, 0.8 mm, provides insufficient compression forced to push the filament against the printed bed. This sometimes leads to poor adhesion of the raster to the printing bed, preventing proper deposition. The medium layer thickness (0.6 mm) was the most suitable because it gives a good bed adhesion and no matrix-rich area. However, the 0.4-mm thickness was kept for the next experimental trial because it provides good bed adhesion. Only the sample with a 0.8-mm thickness was discarded.

3.5.3. Refined printing trial with 2-piece moulded 1.1-mm circular filament
A further printing trial using three different conditions distilled from the parametric study result in Section 3.5.2 was performed using the 1.1-mm-diameter filament produced with the 2-piece mould. The refined parameters of the three conditions are shown in Table 3.5.

Table 3.5 Printing trial with refined conditions.

Condition	Process temperature (°C)	Deposition speed (mm/min)	Layer thickness (mm)
Raster-1	210	300	0.4
Raster-2	210	300	0.6
Raster-3	210	600	0.6

The 3D printer with the nozzle replacement was the same as the one described in Section 3.5.1. There are 12 repeated prints for each condition in order to confirm the repeatability. Figure 3.13 shows examples of printing trials resulting from each condition and their cross-section.

At the low-speed conditions (Raster-1 and Raster-2), the printing shows a good raster adhesion to the printing bed, especially at the low layer thickness (Raster-1). Yet, when printing under high-speed conditions, the deposition tended to curl and leave the printing bed. The rasters printed with the Raster-1 condition are flatter compared to the Raster-2 condition because of the lower layer thickness, but the low thickness

(Raster-1) leads to lateral matrix flow and the formation of matrix-rich areas, as seen on the edges of the raster in Figure 3.13(a1) and the matrix with low fibre content on both sides, as seen in the cross-section microscopy in Figure 3.13(a2). This is a result of an excess compression pressure applied by the motion of the nozzle. Although the low thicknesses provided a good bed adhesion, it sometimes caused the raster to be severed, leading to discontinuous printing. Printing at the highest speed, as the Raster-3 condition, results in wavy rasters (Figure 3.13(c1)) and poor bed adhesion as it is difficult for the raster to adhere to the bed, as shown by the rough lower surface in Figure 3.13(c2). The most favourable manufacturing condition is Raster-2 because the defined thickness of 0.6 mm does not cause matrix-rich areas at the sides of the raster and the raster still shows enough adhesion on the bed, Figure 3.13(b1) and (b2). Besides, the lower speed slowly deposits the raster on the printing bed. This is better in terms of bed adhesion and raster orientation than the higher speed.

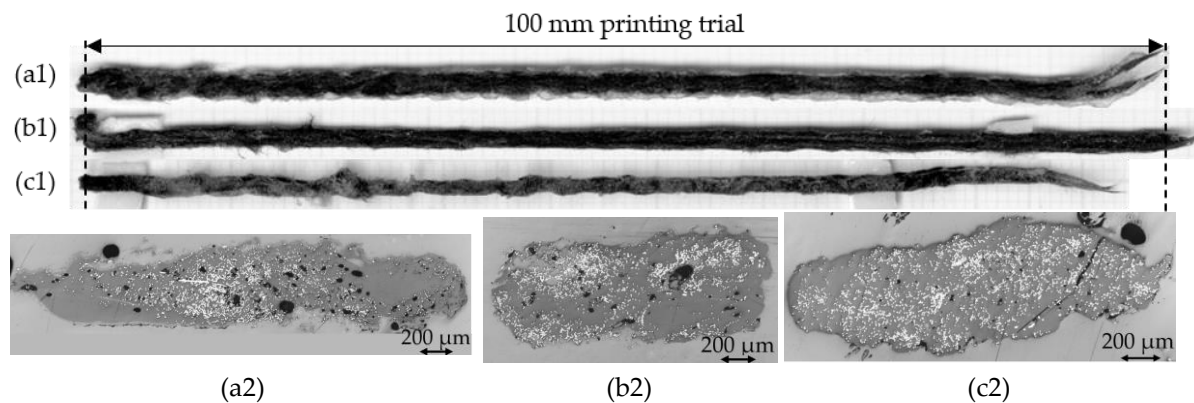


Figure 3.13. Examples of the printing trial at different conditions from the top view printing with conditions: (a1) Raster-1; (b1) Raster-2; (c1) Raster-3, and cross-section of the printing in conditions: (a2) Raster-1; (b2) Raster-2; (c2) Raster-3.

3.5.4. Single-layer printing trial

To examine full-layer properties, a one-layer rectangular shape of 100 mm x 10 mm was fabricated using the Raster-2 condition with a 1.3 mm raster distance (80% expected width to allow for overlaps between rasters). The printed path was designed as a spiralling print starting from the outside contour to the inside, as shown in Figure 3.14(a). Figure 3.14(b) and (c) show the rectangle part on the top and

side attached to the printing bed, respectively. Although the deposition along the straight section performed well following the desired path, the deviations were observed at the corner and the short side of the rectangle instead of a sharp 90° corner. The flat heated nozzle dragged on the top surface during printing motion, so the top surface is flatter and the material fused better than the side attached to the printing bed. This can be seen as the raster path of Figure 3.14(c). The improper fusion of raster showing on the side attached to the printing bed causes poor raster bonding that may lead to a premature failure of the single-layer printing. The poor fusion defect could likely be reduced through optimisation of the raster distance or tuning printing speed and temperature.

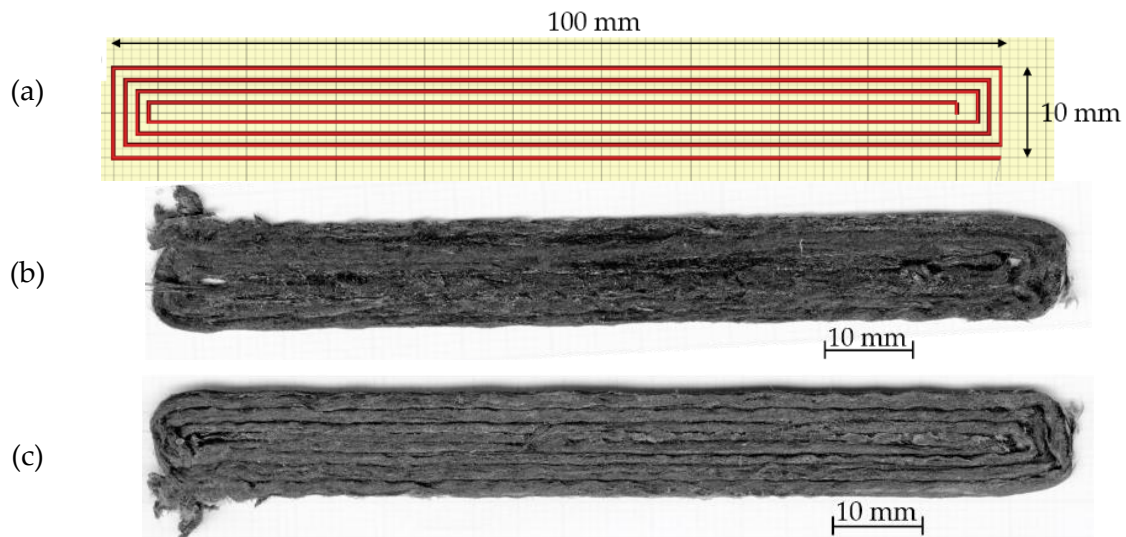


Figure 3.14. (a) Printing path of a rectangular shape with one layer; the rectangle printed part on (b) top surface; (c) side attached to the printing bed surface.

3.6. Mechanical performance investigation

3.6.1. Comparison of the different stages of filament manufacturing

To investigate the effect of the filament manufacturing process on the tensile properties using the same tensile testing and measurement procedure of the single filament described above in Section 3.4.4, the DcAFF material produced with the 2-piece mould was tested at the different stages of the manufacturing process listed below:

- square shape moulded filament produced with the 2-piece mould, called

“moulded” (11 samples);

- circular filament after pultrusion called “filament” (14 samples);
- single raster printing trial with different conditions called Raster-1, Raster-2, Raster-3 as defined in Section 3.5.3 (12 samples on each group);
- single layer printing trial as rectangular shape using Raster-2 condition (Section 3.5.4) called “1-Layer” (5 samples).

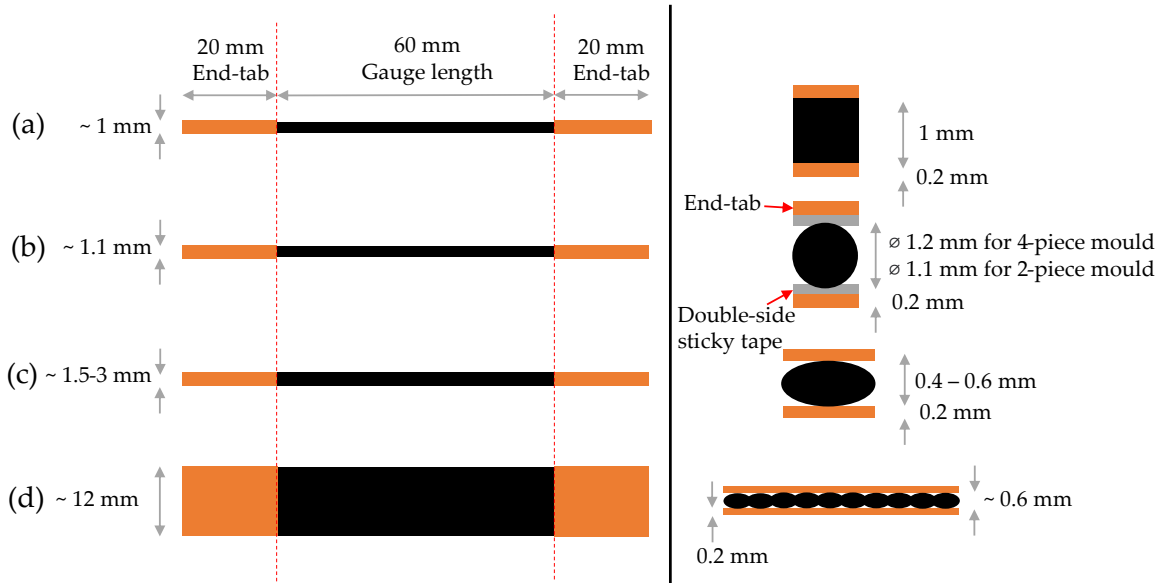


Figure 3.15. Schematic of tensile specimens with the end-tab position in top and side view: (a) moulded; (b) filament; (c) printed single raster; (d) printed single layer.

There are two different types of specimens in this tensile testing. The first type is a single 100 mm long “line” of the material cut from the square moulded bar, the circular filaments, and the single raster printed in Section 3.5.3. The second type is the full layer printed as a rectangular part with the procedure described in Section 3.5.4 (Figure 3.14). 20-mm fibreglass end tabs were attached at both ends of the samples leaving a gauge length of 60 mm. The specimens’ schematics and dimensions are illustrated in Figure 3.15. The pre-impregnated HiPerDiF-PLA tape properties obtained by Blok *et al.* [47] are included in the comparison as the initial formation of the material before moulding.

Table 3.6 Tensile properties result from DcAFF at different stages with the HiPerDiF-PLA tape.

Stage	Area (mm ²)	Fibre content (vol%)	Tensile stiffness (GPa)	Tensile strength (MPa)
Tape [47]	N/A	12.5	24 ± 4	275 ± 30
Moulded	0.99 ± 0.13	8.9 ± 2.1	18 ± 3	223 ± 31
Filament	0.87 ± 0.10	8.6 ± 2.0	18 ± 2	188 ± 67
Raster-1	1.11 ± 0.12	8.2 ± 1.4	14 ± 3	109 ± 46
Raster-2	1.04 ± 0.12	7.5 ± 1.6	15 ± 3	126 ± 21
Raster-3	1.06 ± 0.11	7.0 ± 1.6	12 ± 3	85 ± 34
M. 1-Layer	8.07 ± 0.45	N/A	14 ± 2	104 ± 32

The statically analysed result, cross-section area, fibre content, tensile stiffness and strength, after the elimination of outliers summarised in Table 3.6. The envelopes generated by the tensile stress-strain curves of the different sample groups are presented in Figure 3.16 and the tensile strength and stiffness of each stage are illustrated in Figure 3.17(a) and (b), respectively. Overall, the cross-section area of the filament at each stage remains constant at about 1 mm², with no statically significant difference; however, the aspect ratio of the cross section is changed by the printing process due to the constraint of the defined nozzle height/layer thickness, especially at low layer thickness (Raster-1 condition) that applied high compaction force causing also the matrix-rich areas at the sides of the raster and large unreinforced area. The fibre content of the produced samples in every stage ranges from around 6-10 vol% (according to the microscopic image measurement, Section 3.4.3.2) which is slightly lower than the HiPerDiF-PLA tape fibre content investigated by Blok *et al.* [47] (12.5 vol%). The tensile properties reduce after each processing step as the moulded bar has the highest performance among the tested materials, but it is lower than the tape. It can be inferred that the processing may induce defects, *e.g.* voids or fibre breakage, to the filament, especially during the printing stage which is difficult to control. Comparing the printing conditions, they show statistically the same, but the Raster-2 condition seems slightly superior performance to other printing conditions in this test. This is because in the Raster-1 condition, the low layer thickness, has unreinforced matrix-rich areas, as described

in Section 3.5.3. and shown in Figure 3.13(a1), which may have a detrimental effect, particularly when damage accumulation is concerned. The Raster-3 condition uses high speed which gives insufficient time for adhering to the substrate, as the raster tends to leave the printing bed. The poor adhesion to the printing bed resulted in poor fibre orientation and may cause voids in the raster during printing with Raster-3 condition. The single-layer rectangle shows slightly lower properties compared to the single-raster Raster-2 condition. This may be because of the poor inter-raster fusion shown by the initial inter-raster breakage parallel to the load direction during the test. The raster distance needs to be re-considered to improve the inter-raster fusion.

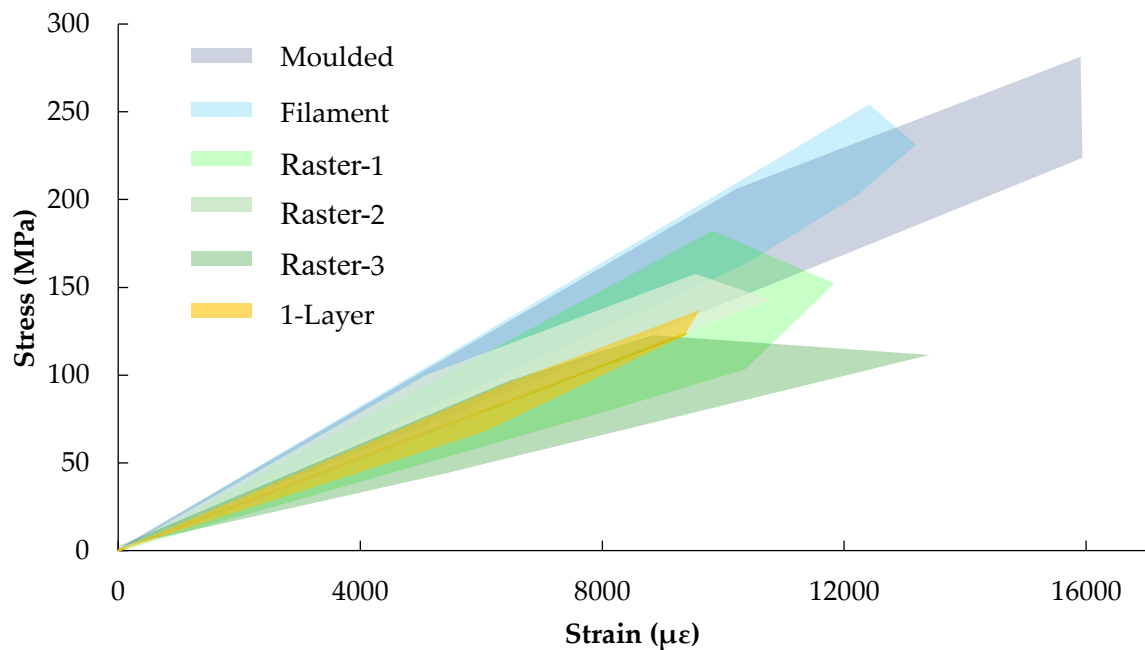


Figure 3.16. Stress-strain data clouds of the tested samples presented as the range of the curve for moulded, filament, printing single layer with Raster-1, Raster-2 (M.1-Raster), Raster-3 condition, and single layer printing.

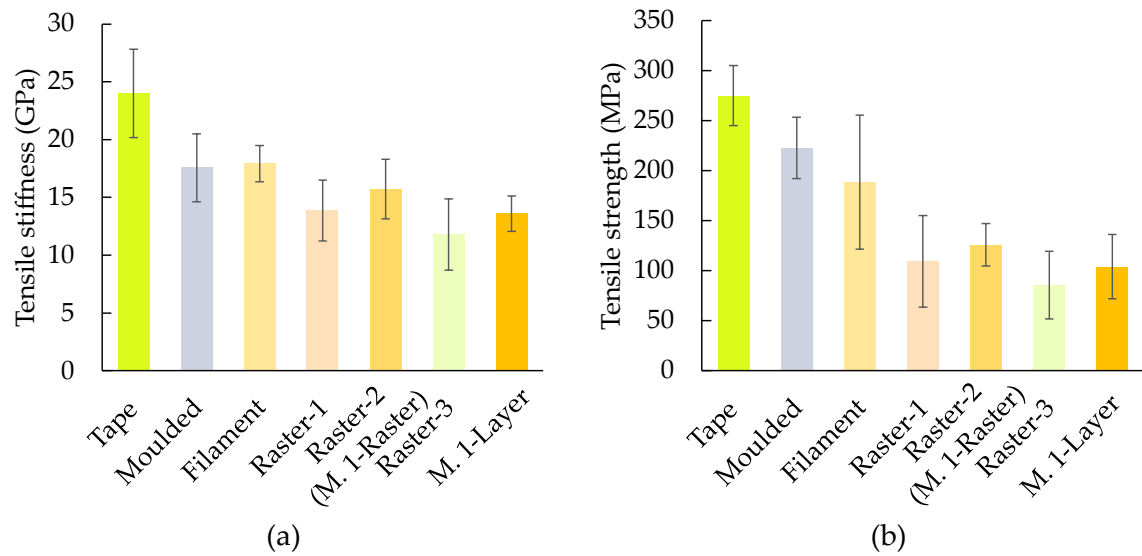


Figure 3.17. Comparison of tensile (a) stiffness and (b) strength between DcAFF material at different manufacturing stages from original HiPerDiF-PLA tape [47], moulded, circular filament, single raster printed with Raster-1, Raster-2 (M.1-Raster), Raster-3 condition, and single layer printed with Raster-2 condition (M. 1-Layer).

3.6.2. Failure mechanism during tensile testing

The failure of specimens at different stages of the development from moulded, filament, printed rasters (Raster-1, Raster-2, Raster-3), and the full layer printing (M. 1-Layer) are shown in Figure 3.18.

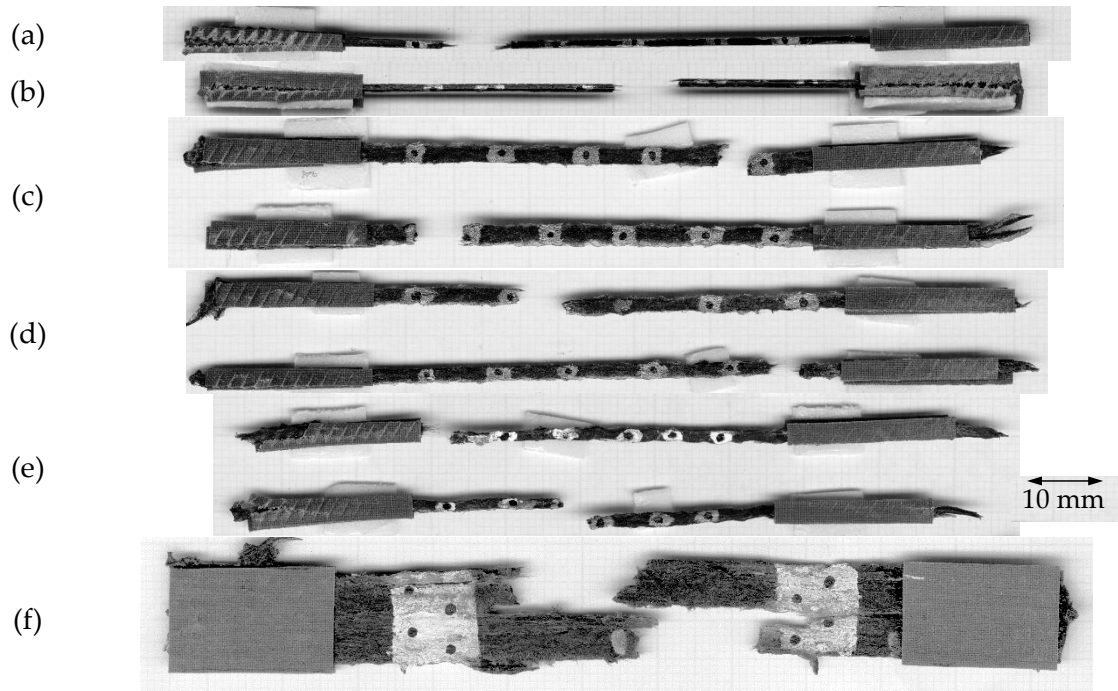


Figure 3.18 Failed samples for each stage of filament development: (a) moulded; (b) filament; (c) Raster-1; (d) Raster-2; (e) Raster-3; and (f) full layer printing (M. 1-Layer).

The expected failure during tensile testing of the discontinuous fibre composites is fibre breakage. Fibres that are shorter than the initial length (3 mm) and the rough fibre breakage surface were observed by scanning electron microscope (SEM) shown in Figure 3.19. However, the dominating failure mechanism, as can be deduced by analysing micrographs of failure surfaces, is fibre pull-out. The evidence of that is the fibre-diameter-size holes (Figure 3.19). The pull-out might occur because of improper fibre-matrix interface bonding due to the lack of fibre surface treatment in this study.

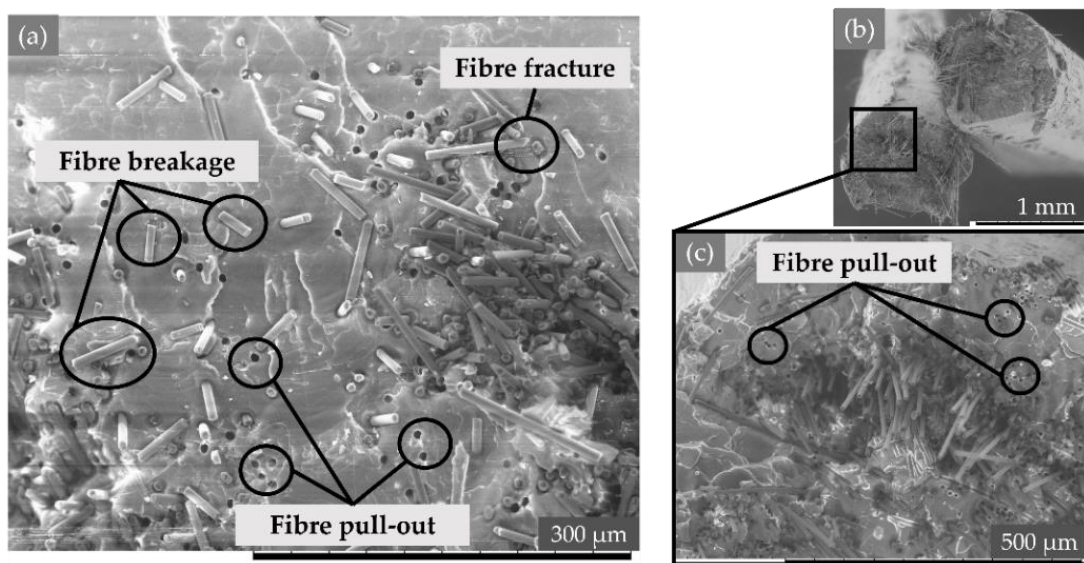


Figure 3.19. SEM images of fibre pull-out failure with fibre-sized holes on the breakage surface investigated in a circular filament after tensile breakage and their high magnification to indicate the pull-out holes.

Apart from the two major failure modes, there are also some peculiar mechanisms. Some filaments have poor fibre dispersion leading to fibre bundles that are not fully impregnated by the matrix. This causes dry fibres in the centre of the bundle which can be easily pulled out under tensile load, as seen in Figure 3.20(a). Even if voids are minimized by the 2-piece designed mould, some imperfect compression in the mould and pultrusion process created occasional voids inside the filament that present themselves as large cavities, as seen on the breaking surface in Figure 3.20(b). The large void reduces the load-bearing area leading to breakage. The joint position to increase the filament length for printing, as described in Section 3.3.4 (stage D) is

the weakest point of the filament because of the low strength of thermoplastic-to-thermoplastic bonding, so some filaments fail at the joint position without fibre pull-out or breakage. Figure 3.20(c) shows a clear-cut surface without evidence of fibres connecting across the fracture surfaces. Those failures that arise from manufacturing defects reduce the tensile strength of the material.

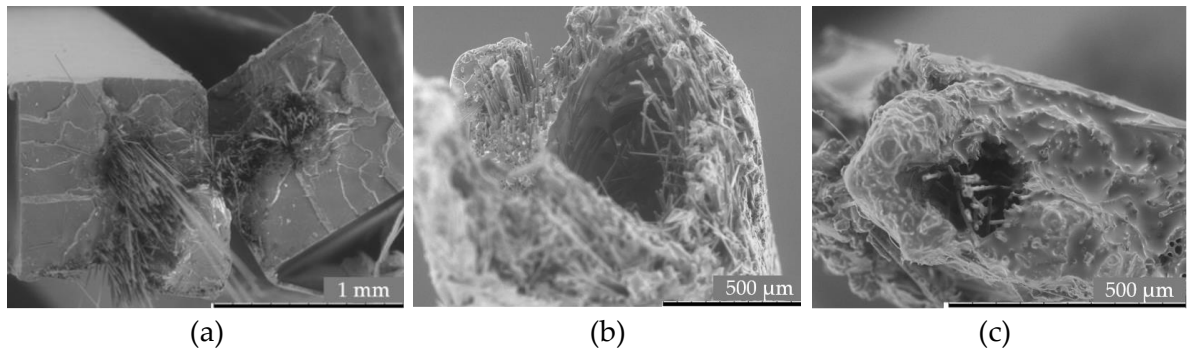


Figure 3.20. SEM images of (a) a moulded filament with a bundle of fibre in the middle that was pulled out under tensile load; (b) a circular filament with a large hole in the middle that leads to failure; (c) a printing part with Raster-3 condition fails at the filament bonding position leaving with clean failure surface without fibre pull-out holes or fibre failure on the surface.

3.6.3. Properties comparison to other 3D printing composites

In Figure 3.21, the tensile properties of the DcAFF printed as the single layer with a rectangular shape (Section 3.5.4) were plotted against other PLA [10, 20, 29, 31, 55, 56, 134, 137, 139-145], PLA-short carbon fibre (PLA/S.CF) [20, 27, 29, 70, 90, 132-137, 159], PLA-continuous carbon fibre (PLA/C.CF) [60, 61, 126, 148-150] from the literature. The DcAFF single-layer printed part has significantly better mechanical performance compared to the PLA and PLA/S.CF. In addition, the stiffness of the DcAFF is higher than the average of the PLA/C.CF manufactured by co-extrusion of fibre-matrix in the heated nozzle before printing: in this case the difficulties in controlling the impregnation results in the poor fibre-matrix interface [1, 60, 61]. The strength of the DcAFF is comparable to the PLA continuous carbon fibre. This can be indicated that the discontinuous fibres longer than the critical length have a similar load-transferring ability to the continuous one.

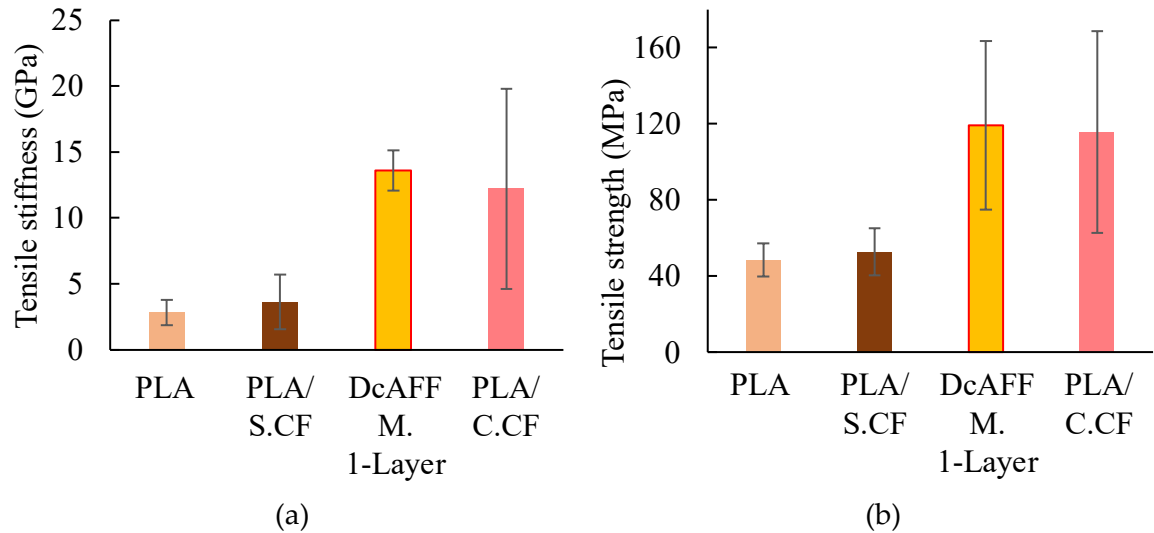


Figure 3.21. Comparison of (a) tensile stiffness; (b) tensile strength between the DcAFF printed as single-layer rectangular part and other composite 3D printing from publications: PLA [10, 20, 29, 31, 55, 56, 134, 137, 139-145], PLA-short carbon fibre (PLA/S.CF) [20, 27, 29, 70, 90, 132-137, 159], PLA-continuous carbon fibre (PLA/C.CF) [60, 61, 126, 148-150].

3.7. Chapter conclusion

This preliminary study chapter proposed a filament-forming method using a simple and low production rate manual moulding process to show the feasibility of producing DcAFF filament from HiPerDiF-PLA tape. Then, the printability and the mechanical properties of the produced filament were studied. Some of the key findings can be concluded below:

- The thin HiPerDiF-PLA tape, achieved from the HiPerDiF alignment machine and impregnation process, can be re-shaped to a square shape by a manual moulding technique. Although the first moulding technique using off-the-shelf materials to make the 4-piece mould from the previous design caused large voids in the circular shaped filament, the more optimised designed 2-piece mould, with adequate heat and pressure, offers a nearly perfect square shape moulded cross-section leading to a lower void content final circular shaped filament. After pultrusion through a circular die of 1.1 mm in diameter, the filament is ready to be used in a general 3D printer.
- The printability of the produced filament was investigated by a single raster

printing trial with three printing parameters: deposition speed, processing temperature and layer thickness. The proper printing condition, that can feed the material and lay on the printing bed properly with the lowest dimensional fault and no composite degradation, was recommended for the 1.1-mm diameter filament produced from the 2-piece mould.

- Then, a full-layer printing trial was conducted as a spiralling rectangular shape with the suggested printing condition. Then, it was tested under the tensile testing standard. Although the full-layer printed part showed slightly lower tensile properties than other formats, *i.e.* moulded or pultruded filament, due to the poor inter-raster strength, the DcAFF single-layer printed part shows an outstanding mechanical performance, *i.e.* higher tensile stiffness and strength than other PLA composites in 3D printing technology including the continuous fibre one.
- Although this preliminary chapter shows the first successful production, printing and performance of the DcAFF, the manual moulding filament production technique, which is time-, energy- and labour-consuming, with less than a meter per hour production rate, prevents the novel filament from scale-up to print larger or more complex geometry and finally commercialising the DcAFF filament. Thanks to this good mechanical performance of the DcAFF material, there is an inspiration to modify and improve the filament-forming process to be a continuous and automated process which can increase the production rate so that the higher amount of filament will allow to study other aspects of the material. With an automated continuous process, the DcAFF materials could gain some considerable benefits, in terms of steering capabilities, and enhance material properties.

Chapter 4 Automated Filament Forming Machine

The previous chapter proved the concept that DcAFF filaments of acceptable quality can be produced and showed the requirements for such a process. However, at that stage, the moulding process was manual and labour-intensive. A more continuous and automated process based on a bespoke filament-forming machine designed, built, and tested is the subject of this chapter. The scale and relative consistency of the process allowed for the production of sufficient quantities of material to print a series of single-layer specimens and assess the basic tensile properties of the produced composites. Subsequently, open-hole tensile tests with a curvilinear printing path were trialled to show the capability of the printing DcAFF and explore the potential benefits of using the ADFRC as a filament.

The details of creating the automated filament-forming machine, the printing of the new filament type, and the mechanical performance of the printed part presented in this chapter were published in *Materials* in 2022 under the title of “Open Hole Tension of 3D Printed Aligned Discontinuous Composites” [3]. The whole article and the testing result were prepared by N.K. and amended by all authors.

N. Krajangsawasdi, I. Hamerton, B. K. S. Woods, D. S. Ivanov, and M. L. Longana, "Open Hole Tension of 3D Printed Aligned Discontinuous Composites," *Materials*, vol. 15, no. 23, p. 8698, 2022. DOI: 10.3390/ma15238698.

The DcAFF filament fibre alignment angle measurement section (Section 4.3.2) is a part of the work published in *Composite part B: Engineering* in 2023 under the title of “DcAFF (Discontinuous Aligned Fibre Filament) – Investigation of Mechanical Properties of Multilayer Composites from 3D Printing” [4]. This characterisation is a collaboration work with μ -VIS X-ray Imaging Centre, University of Southampton. N.K. analysed the test result and prepared the whole article.

4.1. Chapter introduction

In the successful manual filament forming described in the previous chapter, a thin HiPerDiF-PLA tape was re-shaped by compression in a 2-piece, male and female, metallic mould under high temperature and finally pultruded to a 1.1 mm diameter circular cross-section suitable to be fed to a general 3D printer. The fine circular cross-section filament offers the possibility to manufacture more complex geometries with fewer defects than flat tape. Although the DcAFF printed part shows a significant improvement in the tensile properties comparable to those of PLA/C.CF with providing much greater potential in terms of fibre steering, one of the limitations of the first manufacturing method is that the filament-forming was performed manually, which is time-, energy-, and labour-consuming and can only batch-produce a few centimetres of filament per hour. This is not sufficient for the printing of large parts or commercialisation.

A new industrially scalable filament forming method, designed to continuously produce the DcAFF filament, was developed from the 2-piece moulding concept to compress the thin tape in the small slot to form a square-like cross section. The invented filament-forming method is designed to reshape the tape without breaking the fibre length and keeping the fibre alignment while running at a high production rate with a continuous process, called now DcAFF semi-automated filament-forming machine, and will be described in this chapter. After the fine-tuning and testing of the new machine, the DcAFF filament was mass-produced for physical and mechanical testing. With the DcAFF machine, the filament production rate increased from a metre per hour (using manual moulding) to a half metre per minute. This allows the fabrication of more structural geometries than the straight rasters printed in Chapter 3. In this chapter, only single-layer parts were considered due to the limitation of the HiPerDiF tape produced with the lab-scale machine. At first, simple rectangular specimens were fabricated to characterise the tensile mechanical properties with a higher number of samples than in Chapter 3. Moreover, a more complex geometry, *i.e.* curvilinear printing, was printed to investigate the steering

potential of the material around tight radii during fabrication and evaluate the mechanical behaviour changes caused by steering the filament to produce an open-hole specimen instead of cutting the fibre as per conventional material subtraction methods. The curvilinear, 3D-printed open-hole samples will be benchmarked against a subtractive manufacturing process using a similar geometry: straight samples with the same material system, original width and thickness HiPerDiF tapes manually laid and consolidated in an oven, where an open hole is obtained by an extra machining step, *i.e.* punching. Post-printing consolidation was also considered to show the potential for improving mechanical properties after the printing process.

Thanks to the collaboration with the μ -VIS X-ray Imaging Centre, University of Southampton, under an NXCT grant, the fibre alignment of the produced material at each stage of the filament-forming process, from the tape, square and the final circular filament, can be calculated precisely in this chapter obtaining a more representative evaluation of the whole fibre structure than the microscopic image method, mentioned in Section 3.4.2.

4.2. Materials and filament forming method

The raw materials, carbon fibre and PLA, are the same as presented in Section 3.2 in the previous chapter. The HiPerDiF preform and PLA thin tape were prepared, with the HiPerDiF process and 3D printing, and impregnated to composite thin tape with a nominal 0.2 mm \times 5 mm cross section using the same method in Section 3.3.1 (stage A). To increase the fibre content of the filament, which should result in mechanical properties improvement, the pump speed of the fibre-water suspension nozzle was increased from 70% to 90% and the conveyor belt speed was decreased from 60% to 40% from the previous process. This leads to a denser fibre preform and the fibre content will be presented later in the next section. According to the requirement of the production rate mentioned in the previous chapter, a new semi-automated continuous filament forming process was developed to enhance the production rate while retaining the quality of the filament.

4.2.1. Roller compaction machine

To replace the manual moulding method in Chapter 3 (Figure 3.1 stage (C)), the tape was formed by feeding it through a matching pair of heated rollers, as shown in Figure 4.1, where the rollers were designed to interface with each other through a slot and rim profile which leaves a square-shaped gap (approximately 1 mm × 1 mm) when fully meshed for the formed filament. Owing to the circular cross-section of these rollers, the film experiences a progressive, gradual reduction in width as it is fed through the counter-rotating rollers. The roller moulding concept was adapted from the metal rolling process used to form metal profiles. The rollers were machined with an aluminium shaft of 50 mm in diameter with corresponding male and female shapes at the compression point. The rollers were coated with a release agent, LOCTITE® Frekote 770-NC, before each production to prevent the material from sticking to the metal rollers. Both rollers were heated with cartridge heaters that were inserted into the axis of the rollers. The temperature of both rollers is set just below the melting point of the HiPerDiF-PLA material, around 130 °C, to allow the material to soften and fuse, but not melt, which helps prevent tearing. The rotation of the rollers was driven by stepper motors with a controlled tuneable linear speed between 200-500 mm per minute.

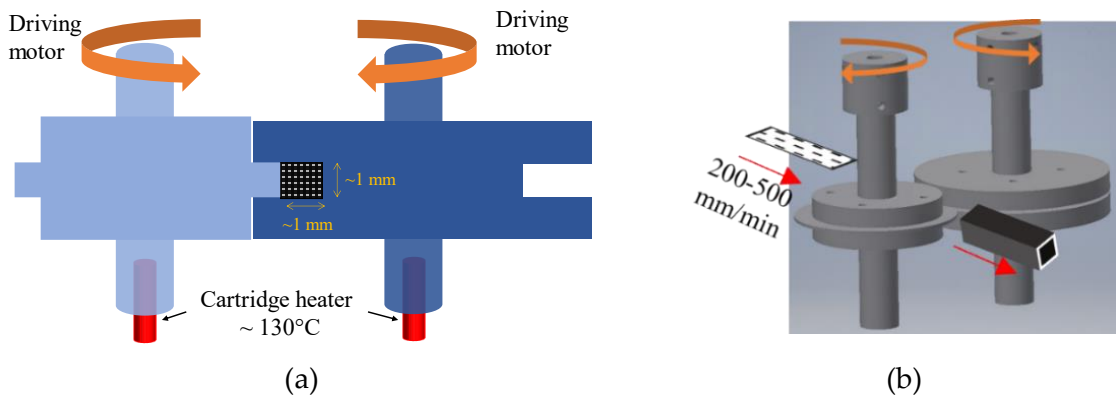


Figure 4.1 (a) Concept of male and female roller compaction module with motor driving and cartridge heater temperature control that can produce a square-like cross section filament; (b) 3D sketch of the rollers.

After leaving the rollers, the now square filament is also pulled by an additional motor and traction drive system. The linear pulling speed is synchronized to the

roller speed to avoid any net changes in the length of the filament. Microscopy images of the cross sections of various filaments following passage through the moulding rollers are shown in Figure 4.2.

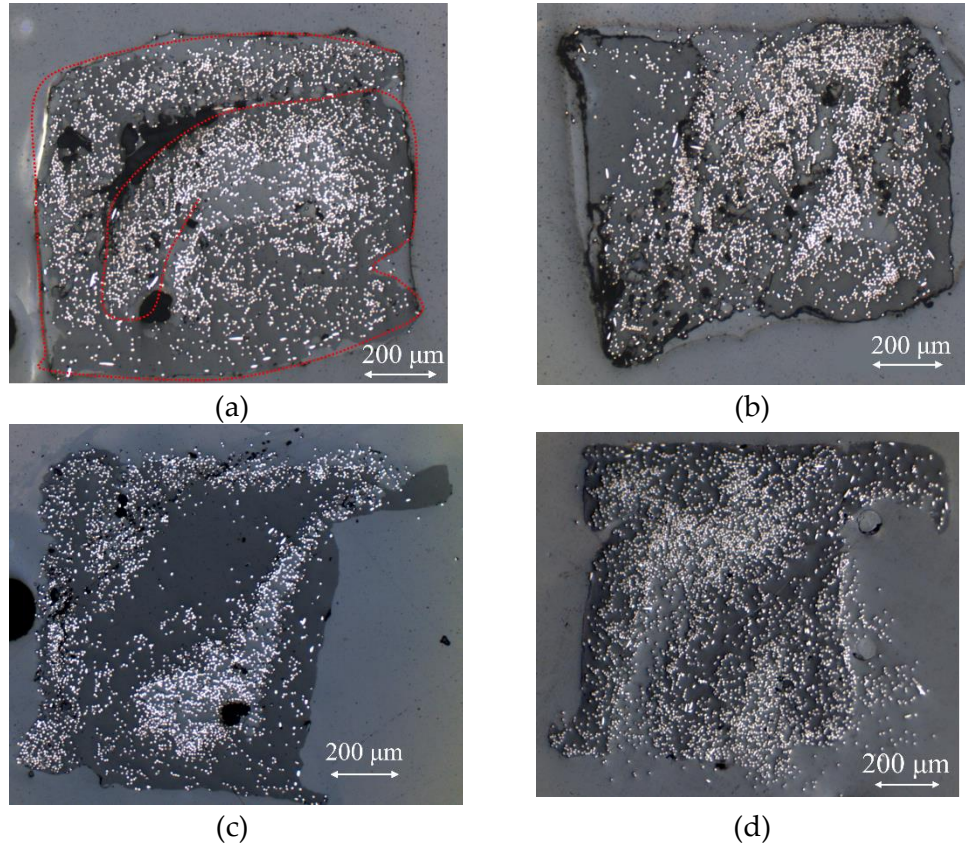


Figure 4.2. Square filament after passing through the rollers: (a) folding of tape with poor bonding; (b) microvoids in the filament ; (c) - (d) material overflow at the corners.

When the gap between the rollers is too wide, the tape is folded and not well homogenised, presenting a curved shape with a large void area of imperfect fusion that is difficult to eliminate at the next step, Figure 4.2(a), or some microvoids which are more acceptable than a single large void as it can be removed by the next pultrusion, Figure 4.2(b). If in the initial setup, the two rollers are too close, then material overflows, created by the small gaps between the male and female rollers, are produced and present themselves as flanges on the corners of the square shape Figure 4.2(c) and (d). These flanges are perhaps preferable to the inner voids as they could potentially be reduced by manufacturing the male and female rollers to higher dimensional tolerances. Microvoids and flange imperfections, as seen in Figure

4.2(b), (c), and (d), are acceptable at this stage, as a further step allows to minimize them and mitigate their effect on the filament properties.

4.2.2. Movable nozzle pultrusion

To shape the filament cross section to circular, the square filament (with imperfections) was pultruded through a specifically designed moveable nozzle. The moveable nozzle was designed as two mirror parts that can be assembled into a convergent nozzle (Figure 4.3(a), (b)) with a conical hole with a bore tapering from 1.4 mm to 1 mm. The two-side blocks are compressed with springs to ensure that they are always in contact during the process and form a circular filament while they can move slightly to allow large overflows to pass through. The nozzle was heated to 130°C to soften the matrix and allow the reshaping of the filament into an almost circular cross-section, as shown in Figure 4.3(c). If the material overflow is compressed this causes an improper fusion of the matrix, as shown in Figure 4.3(d). Both figures show an imperfect circular shape caused by the joining between the two sides of the half-circle.

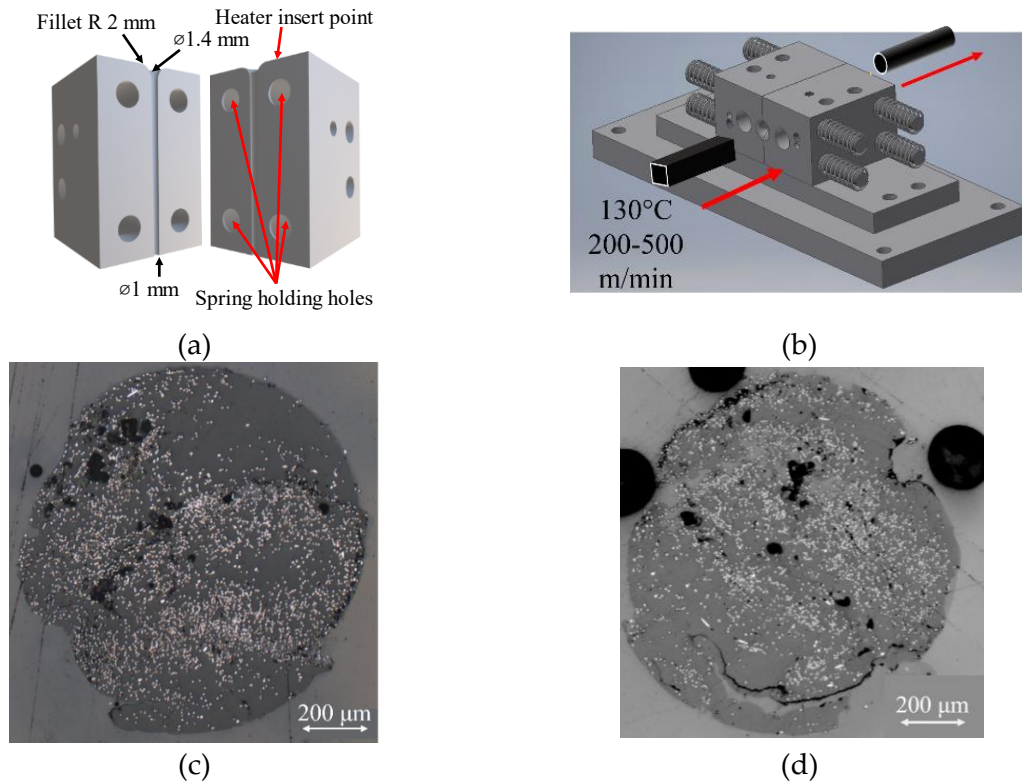


Figure 4.3. (a) - (b) A schematic of a two-side assembly convergent nozzle before and after assembly; (c) - (d) circular filament after passing through the two-side convergent nozzle.

To refine the shape and improve surface finishing, the filament was finally pultruded through a straight drilled PTFE polymer nozzle with a diameter of 1 mm and a length of 8 mm, Figure 4.4(a), at the temperature of 130°C. This also applies a compression force due to the thermal stress in the heated nozzle resulting in lower voids and better surface finishing as demonstrated by the highly circular cross-sections shown in Figure 4.4(b). The fibre distribution in the cross section cannot be controlled with this filament-forming procedure leading to inhomogeneities in the filament. However, this non-uniform fibre distribution is also found in commercial 3D printing composite filaments [43, 160].

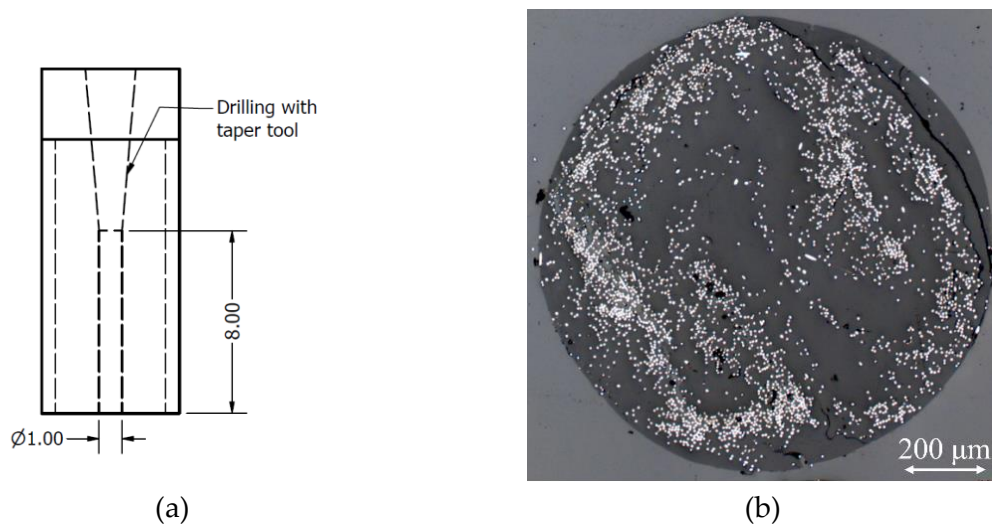


Figure 4.4 (a) The cross section of final pultrusion nozzle; (b) the final perfect circular cross section filament.

4.3. Filament characterisation

4.3.1. Fibre content investigation in filament

Because of the new DcAFF machine setting for the higher fibre content, the fibre content needs to be re-checked. Owing to the higher accuracy of the matrix burn-off method than the microscopic method, the same TGA programme, detailed in Section 3.4.3.1, was performed on the new batch of the DcAFF filament. The TGA machine was changed from the one in Chapter 3 to the TGA Q500 V20 (TA Instruments, USA). According to the TGA results in Figure 4.5, after the dwelling, the mass loss in the fibre is around 0.9% and the PLA residual mass is negligible. The residual mass percentage after the matrix burn-off procedure of the composite needs to be

increased by the fibre mass loss (0.9%) to represent the initial fibre weight content in the filament. The fibre weight fraction ranges from 28-33 wt%, equivalent to a fibre volume fraction between 21-25 vol%. This accounts for about 2-fold higher than the fibre content of the material in Chapter 3.

From the literature [45], it was observed that in a short (<0.3 mm) randomly oriented fibre composite filament, a fibre content above 40% by weight caused nozzle clogging during printing; however, the DcAFF filament, made of highly aligned 3 mm long fibres, is expected to experience less clogging, due to the lower fibre content aided by a better alignment.

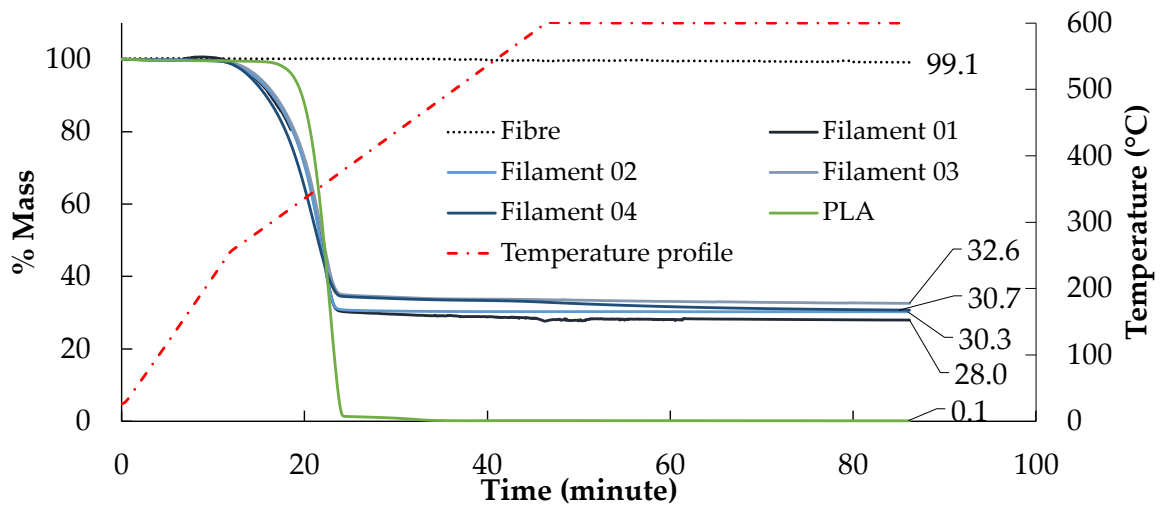


Figure 4.5 Special TGA programme, using TGA Q500 V20, to investigate fibre weight fraction by considering residual fibre content after matrix burn-off showing the fibre, DcAFF (HiPerDiF-PLA) composite, and PLA with the temperature profile (red line).

4.3.2. DcAFF filament fibre alignment angle measurement

In Chapter 3, the alignment was measured from a single microscopic image of the specimen cross-section. Assuming that the single fibre cross-section is perfectly perpendicular to the 0° direction, perfectly aligned fibres will appear perfectly circular, but the misaligned ones will present an elliptical cross-section. The size of the elliptical shape, major and minor axes, were calculated and converted into the misalignment angle from the longitudinal axis *via* a trigonometric method. This method is cumbersome and allows the researcher to measure only a few cross-

sections along the whole filament length, making it relatively unrepresentative and inaccurate. There are some methods to calculate fibre alignment in the literature, especially the series of HiPerDiF fibre alignment studies. There is a technique used to measure the HiPerDiF tape fibre alignment based on the image analysis of a polished in-plane surface. The method can evaluate only the in-plane fibre orientation of the through-thickness polished surface [48]. This is not suitable for the three-dimensional shape of the filament produced in this work. To measure the fibre alignment throughout the whole filament length, a higher-fidelity method is required. Microfocus X-ray computed tomography (μ CT) is a suitable tool to analyse the whole structure of the material. It can separate the different materials (different densities), in this case, fibre, matrix, and voids, to different greyscale and reconstruct a 3D image of the whole specimen. In a previous study [49], HiPerDiF tape fibre orientation was analysed with μ CT scanning and the scanned images were processed using VoxTex software [161] developed at KU Leuven originally designed for the analysis of textile architectures. In this study, the orientation was analysed with commercial software, AVIZO with its extension X-Fibre, which can detect fibre or tube-like structures and calculate the orientation of each tube with respect to a defined set of coordinates [63].

The DcAFF material was scanned using a Zeiss 160 kVp Versa 510 μ CT scanner. The source voltage was set at 80 kVp and 7 W power, 2401 projections were acquired with a 3-second exposure time per projection over a 360° rotation of the tomography stage, using a 4× magnification optics module. The source-to-object and object-to-detector distances were 24 mm and 16.4 mm, respectively, resulting in a 2 μ m reconstructed voxel size. This resolution permitted to resolve individual fibres, 7 μ m in diameter. Each μ CT acquisition consisted of four vertically overlapping scans to obtain a 3 mm \times 3 mm \times 12 mm field of view that could cover more than a whole fibre length (3 mm). The same length of the sample has been analysed through the three stages of the filament-forming process: tape, square-like filament, and circular filament to show the development of the fibre orientation during the filament-

forming process. After scanning, the 3D images were analysed in AVIZO using the X-Fibre extension. First, the composite material was segmented to separate fibre and matrix depending on the grey scale of the scanned images, then a cylinder correlation module was applied to the stacked image to find the cylindrical volumes, supposed to be fibres. After that, the fibre tracing was applied to the cylinder correlation data to convert the traced cylinder into position and orientation data of each fibre by tracing the centre line of the cylinder. The orientation was calculated in reference to the axis shown in Figure 4.6(a). In this analysis, the interesting value is the fibre orientation angle θ which is the deviation angle from the longitudinal axis. However, two cylindrically-shaped volumes of similar grey scales can be present in the scanned volume: real fibres, and, especially on the edge of the specimen, long cylindrical “channels” of the matrix, denoted here as “fibre-like matrix artefacts”. To avoid misinterpretation, the “fibre-like matrix artefacts” had to be filtered out from the tracing data accordingly to the following assumptions:

- Short fibres are rigid, no fibres with pronounced curvature can be presented in the scanned material;
- For the cylindrical shape filament (square or circular), there is a limit of fibre misalignment dictated by the size of the filament: in this case, the 1 mm x1 mm square-like filament diameter can provide room for 3-mm long fibre to deviate from the longitudinal axis no more than 28°;
- Fibre length limitation from the 3-mm input fibre:
 - The fibre cannot be extended: the maximum admissible fibre length is 3.5 mm;
 - The fibres are not broken during the process: the minimum admissible fibre length is 2.5 mm.

The traced cylindrical volumes were filtered retaining those with a length between 2.5-3.5 mm which is the fibre following the given assumptions. The fibre length range assumptions were confirmed with FASEP system (IDM Systems, Darmstadt,

Germany) [162], an image-processing fibre length measurement. Fibres extracted from a dry HiPerDiF preform around 0.5 g were dispersed in deionised water to be photographed through a flatbed scanner on the FASEP machine. To avoid the fibre agglomeration that can lead to a long processing time and some errors, the fibre-water suspension was diluted for several steps with the deionised water until reaching 0.02-0.04 g/L before putting the solution in a petri dish for the scanner. After the scanning, the image was analysed by separating the single fibre from clusters or dust and the software is able to break up complex fibre clusters into single fibres by tracking the intersection and end points of each fibre. Then, the fibre length was automatically measured using a straight-fibre algorithm by FASEP software. The fibre length distribution after the HiPerDiF process, in Figure 4.6(b), confirms the assumption of fibre length distribution between 2.5-3.5 mm by showing the majority of the fibres are around 3 mm. Owing to the image processing method, the very low and high fibre lengths could be the noise, (non-fibre voxels of similar grey scale) from the measurement system.

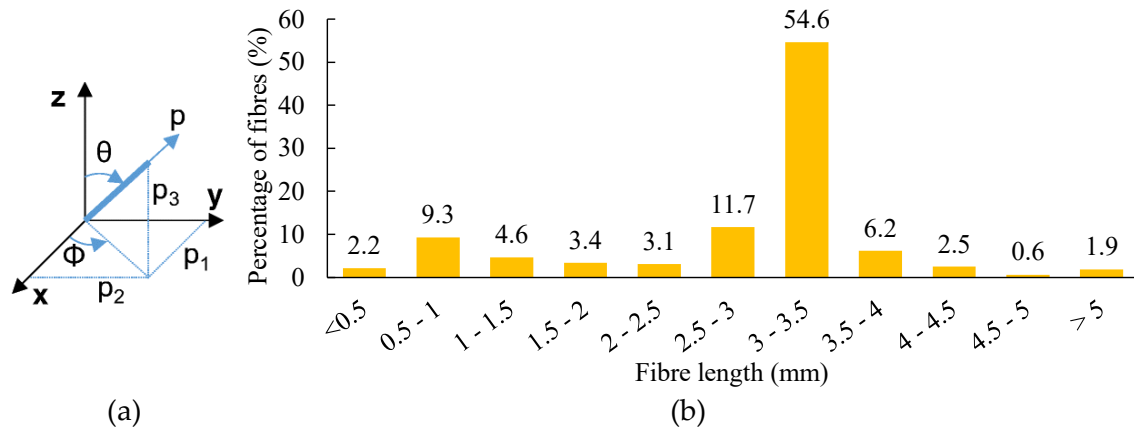


Figure 4.6 (a) Reference axis to calculate the fibre orientation; (b) FASEP fibre length measurement distribution of fibres processed from the HiPerDiF 3G machine.

The percentage of the number of fibres that deviated from the longitudinal axis (θ) was plotted in three histograms as a function of θ , for the different filament formats: tape (Figure 4.7(b)), square-like filament (Figure 4.8(b)), and final pultruded circular filament (Figure 4.9(b)). According to those three histograms, most of the fibres are aligned within the range of 0° - 15° . Overall, the amount of perfectly aligned fibres (0°

-1°) is lower than that of slightly misaligned ones (2-5°). The tape format, Figure 4.7, may have a slightly higher misalignment because of the lesser geometrical constraint of the thin and wide tape, wider than the fibre length, so the aligned 3-mm fibres on the tape surface can be easily deviated by the impregnation and forming process. This is shown by the misaligned fibre on the tape surface in Figure 4.7(a). However, the misalignment is significantly reduced due to the filament-forming process that helps to force the fibres to align in one direction by compressing the tape into a constrained cross section, 1 mm x 1 mm, so the 3-mm-long fibre cannot deviate out of this boundary. In the square-like filament, the majority of fibres are well-aligned and the amount of fibres more than 15° out of alignment is just 2%. The higher amount of aligned fibre can be seen in the 3D rendered image of the square filament, Figure 4.8(a). After the final pultrusion, the fibre orientation shows insignificant changes from the previous stage. The cross-section transformation after pultrusion into the circular filament is more uniform in shape and the surface of the circular one (Figure 4.9(a)) is smoother than the square filament. The alignment level of each stage of the filament-forming, as calculated by the amount of the fibre aligned within 10°, is presented in Table 4.1. The current HiPerDiF tape shows a fibre alignment similar to that of the previous study with the same HiPerDiF machine (2nd generation machine) measured with μ CT scanning and analysed with VoxTex software [49], *i.e.* 67% of fibre aligned within $\pm 10^\circ$. The filament-forming process provides a significant alignment improvement with about 90% of the fibre within 10°.

Table 4.1 Fibre alignment comparison over the development of DcAFF from tape to square-like and finally circular cross-section filament.

Format	Alignment (within 10°)
Tape	64%
Square-like filament	89%
Circular filament	88%

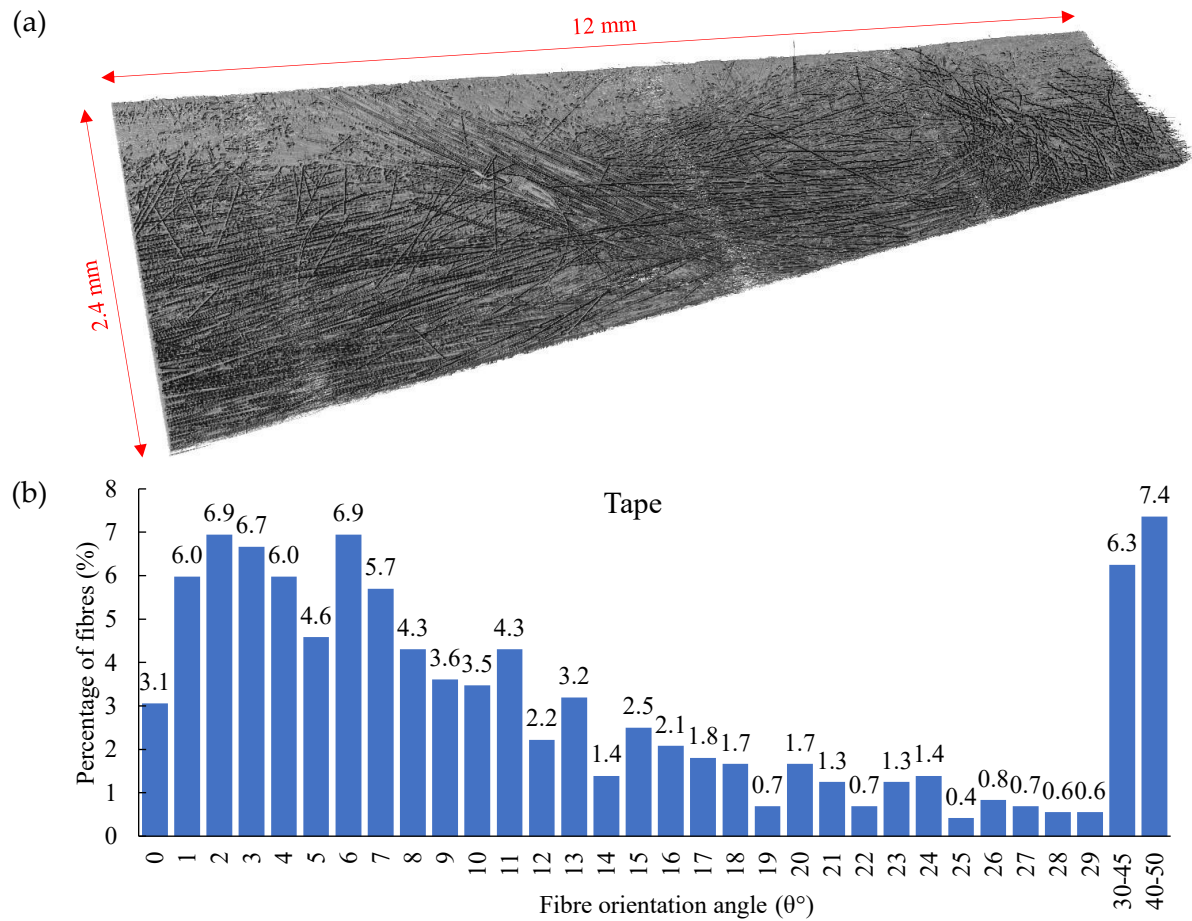


Figure 4.7 (a) 3D modelling of the μ CT scanned image for cropped tape (2.4 mm wide); (b) fibre orientation angle distribution deviation from the longitudinal axis of the tape.

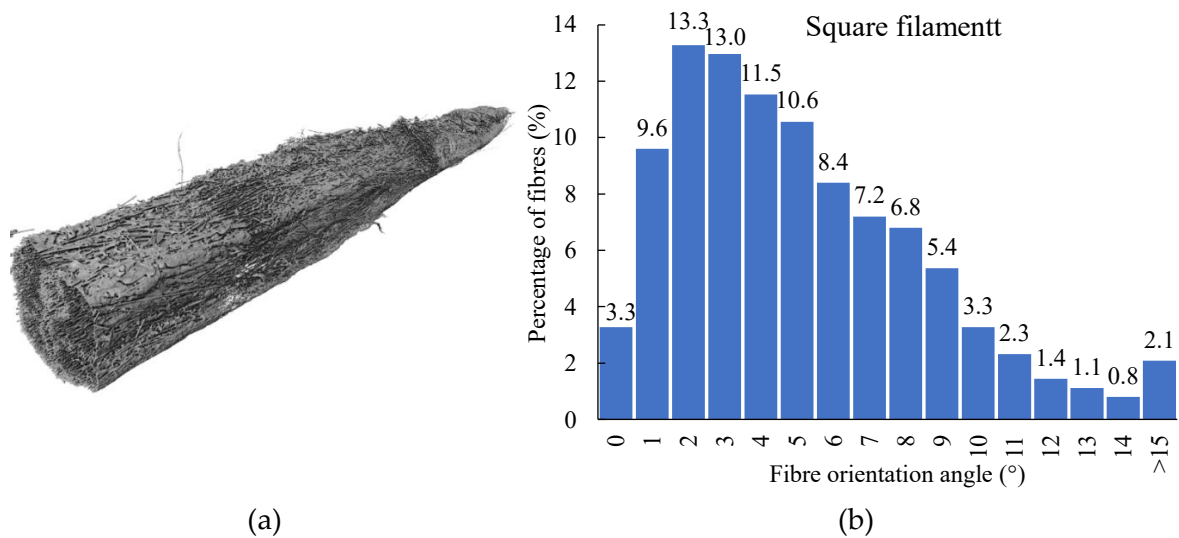


Figure 4.8 (a) 3D modelling of the μ CT scanned image for square-like filament; (b) fibre orientation angle distribution deviation from the longitudinal axis of the square-like filament.

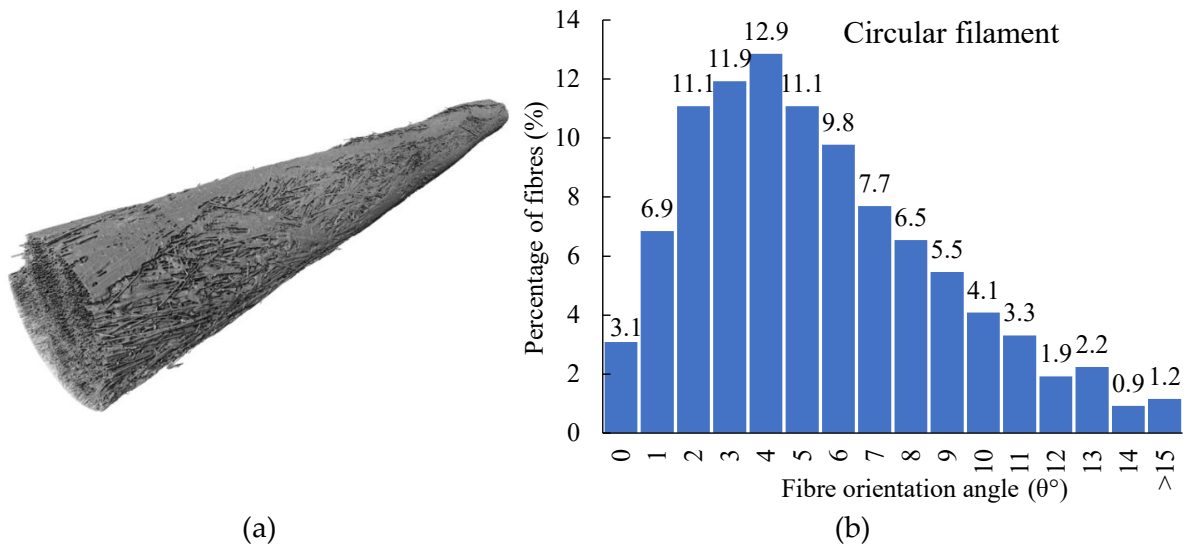


Figure 4.9 (a) 3D modelling of the μ CT scanned image for final pultruded circular filament; (b) fibre orientation angle distribution deviation from the longitudinal axis of the circular filament.

4.4. Tensile properties characterisation

4.4.1. Single-layer tensile specimen preparation

The tensile specimen is often produced using a simple 2D rectangular shape. However, for the single small rectangular specimens (as presented in Chapter 3), that requires steering around a very tight corner, *i.e.* 90° turning, when the head reverses the print direction, as can be seen in Figure 3.14. The many tight turns make the precise duplication of replicate samples difficult to achieve. Combined with the large number of samples required for the tensile testing, a new printing path for uniaxial single-layer tensile samples was designed to reduce the total number of raster turns in each specimen, while also producing more samples per print. The printing path was programmed as a single layer of 100 mm x 100 mm square spiral, with an empty centre, to produce four samples of 100 mm x 10 mm in one printing, as shown in Figure 4.10(a). The printing was performed with the same 3D printer used in Chapter 3 with the same bespoke nozzle. The printing set-up conditions were similar to the suggested condition in Chapter 3, *e.g.* nozzle temperature 210°C, bed temperature 80°C, and speed synchronized to feed rate of 300 mm/min. However, the set layer thickness was reduced to 0.4 mm due to the smaller filament cross section (1 mm

diameter) and the intention to increase the bed adhesion. While the raster distance was increased from 1.3 to 1.6 mm to compensate for the now excessive overlap between rasters caused by the reduction of the thickness (and subsequent increase in raster width). The bed temperature was increased to the higher bound of the PLA material (Section 2.2.4), from 60°C to 80°C, with the intention of promoting better bed adhesion. Figure 4.10(b) shows a picture of the 'as printed' square specimen and a detail of the corner region. The printed rasters are well laid following the defined printing path, but some interruption of the feed resulted in empty areas, even if the printing was continued at almost the same point as the stopping position. The linear section to produce the tensile specimen is straight following the path, but a perfect sharp 90° turn could not be achieved at the corners as the poor bed adhesion of the filament to the printing bed makes the sudden change of direction problematic [163]. The impregnated fibre presented on the surface is the result of high fibre volume fraction and imperfect fibre distribution. There are some fuzzy fibres that deviated from the printing path because of the fibre movement under the compaction nozzle.

Inspired by the post-consolidation of a commercial 3D printed continuous carbon fibre from 9T Labs [164] that provides mechanical properties improvement by the elimination of the voids and an increase in inter-raster adhesion, a group of samples was separated and then thermal consolidated under a vacuum pressure (1 bar) in an oven at 200°C for 1 hour, which in this work will be referred to as 'consolidated' specimens. This will allow for improved inter-raster fusion and allow for comparison of the improvement due to post-printing consolidation and exploration of the material mechanical performance limitation. The post-printing consolidated parts show smoother surfaces caused by the fusion of the rasters and accumulations of material on the edges, as can be seen in the comparison between the high magnification images of Figure 4.10(c) and (d). However, the inter-raster bonding can still be observed on the surface. Since the filament was already compacted by the modified nozzle during printing, the thickness reduction of the single-layer part due to the consolidation is relatively small, around 10%, and caused mainly by the

removal of microvoids.

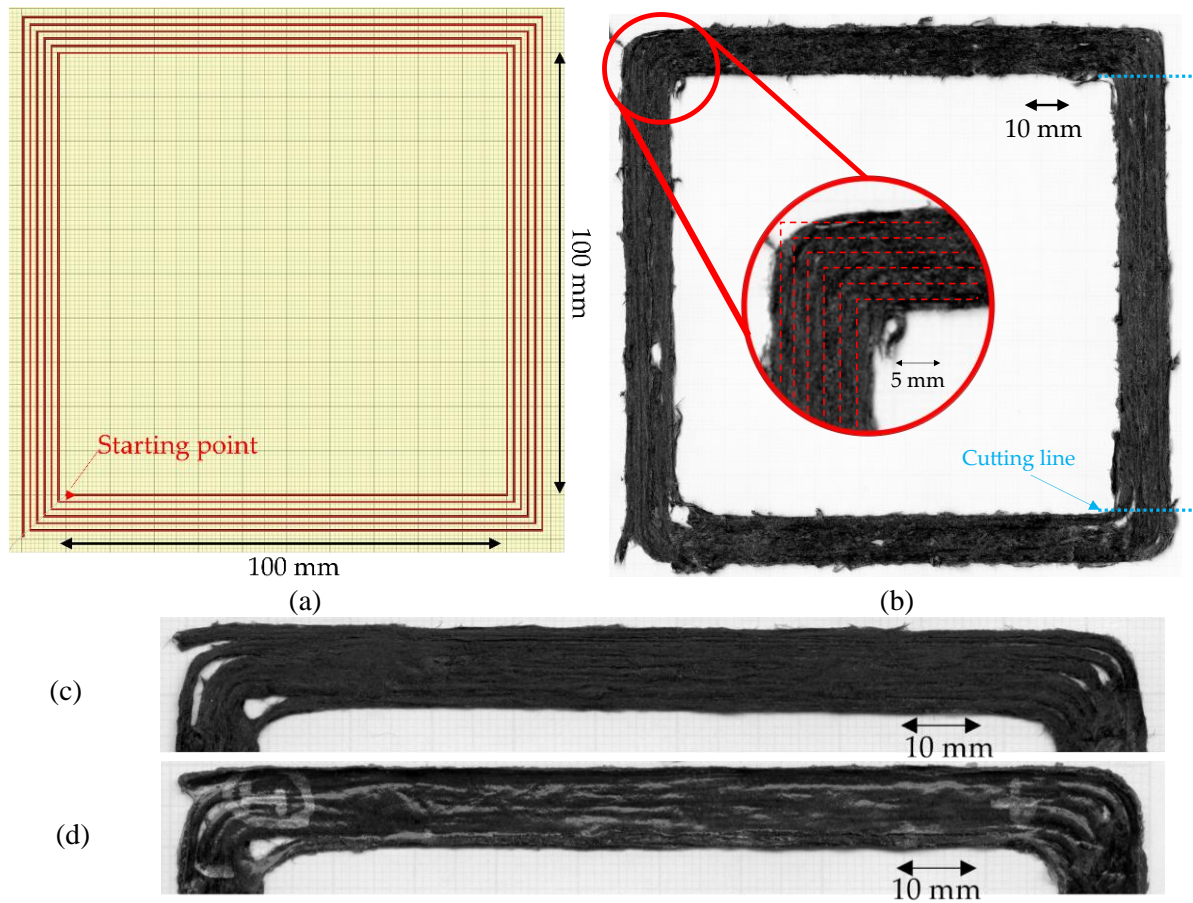


Figure 4.10 (a) Printing path of large square shape with 90° sharp turning corners to produce four tensile samples starting from inside; (b) top surface of the sharp corner printed part with a zoom-in of a corner [163]; (c) high magnification of the large square as printed; (d) high magnification of the same large square printed after post-printing consolidation.

To produce a uniaxial 10 mm x 100 mm tensile specimen from both 'as printed' and 'consolidated', their corners were discarded to avoid inconsistency of the printing by cutting at the transition from flat to a curved path, as shown as the cutting line in Figure 4.10(b), with a metal hack saw to make four tensile specimens. Finally, 20 mm fibreglass end tabs were attached at both ends of the 10 mm x 100 mm specimens leaving a 60 mm gauge length, similar to Figure 3.15(d). There are five large square printed parts, so a total of 20 specimens were fabricated for the as-printed testing. While there are two large square post-printing consolidated parts resulting in eight specimens of the consolidated one.

4.4.2. Tensile testing and result

The testing machine, strain measurement and testing procedure are the same as described in Section 3.4.4 with a higher load cell capacity, *i.e.* 10 kN. In Table 4.2, the current DcAFF printed part, 'as printed' and 'consolidated' are compared to the previous HiPerDiF-PLA studies: (a) the properties of the DcAFF single-layer part printed from the filament using the manual moulding technique (DcAFF M. 1-Layer) in Chapter 3 and (b) HiPerDiF-PLA the thin tape obtained from the consolidation machine [47]. In this chapter, the fibre content was calculated based on the matrix burn-off method. The tensile properties of the current part are significantly increased from the previous 3D printed part, with the manually moulded DcAFF filament. The mechanical properties improvement from the previous printing should be the result of a two-fold increase in fibre content. When comparing the DcAFF to the thin tape HiPerDiF-PLA format obtained from the consolidation machine [47], the DcAFF part presents a comparable tensile stiffness, while the strength is significantly lower. The difference in the tensile strength between the tape and printed formats is attributable to an undesirable failure mode triggered by poor raster-to-raster fusion in the printed part resulting in an initial breakage parallel to the load direction (Figure 4.11(a)). The better load-bearing ability correlates with the localised fibre rupture rather than the delamination failure mode manifested in the breakage perpendicular to the loading direction, Figure 4.11(b). Post-printing consolidation improves tensile properties, especially tensile stiffness, because of the reduction of the microvoids in the part and the better sintering of the rasters similar to the consolidation result suggested by 9T Labs and observed by Grieder *et al.* [164]. The average tensile strength of the consolidated one is higher than the as-printed one, this difference is however statistically insignificant when accounting for the large standard deviation of both groups: in both cases, the undesired failure mode, *i.e.* inter-raster breakage, is observed. The inter-raster bonding is still the weak point in both groups as shown by the presence of seamlines between the adjacent rasters instead of a homogeneous part. Some of the consolidated ones failed similarly to the 'as printed' specimens,

parallel to the printed raster, in Figure 4.11(c). However, post-printing consolidation with heat and pressure could still be considered as an option to improve the physical and mechanical properties of the DcAFF filaments after printing for simple shape parts without internal cavities.

Table 4.2 Tensile properties comparison of the current DcAFF samples to the previous studies.

Specimen format	Fibre weight fraction	Tensile stiffness (GPa)	Tensile strength (MPa)
DcAFF “as-printed” (A. 1-Layer)	28-30%	19 ± 3	132 ± 21
DcAFF “consolidated”	28-30%	24 ± 2	151 ± 29
Tape [47]	17.3%	24 ± 4	274 ± 31
M. 1-Layer (Chapter 3)	16-19%	14 ± 2	104 ± 32

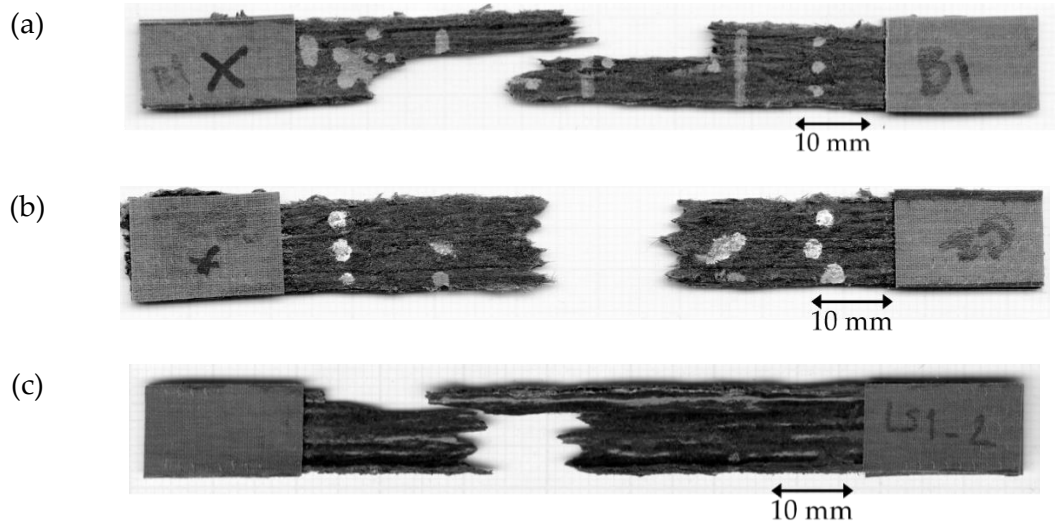


Figure 4.11. Breakage sample of tensile sample: (a) inter-raster failure parallel to the load direction; (b) favourable failure perpendicular to the load direction showing the load transfer to the fibre direction; (c) breakage of the post-printing consolidated sample showing the breakage, parallel to the raster direction.

4.4.3. Comparison of the DcAFF to literature (considering fibre content)

For a fair comparison of the DcAFF 3D printed part performance with other available 3D printing materials from literature, the tensile stiffness and strength of the DcAFF produced from the semi-automated filament forming machine and printed in a single layer (DcAFF A. 1-Layer) were plotted against the DcAFF single-layer printed from the manual moulding filament in Chapter 3 (DcAFF M. 1-Layer), other PLA

[20, 29, 31, 56, 71, 134, 137, 144, 145], PLA-short carbon fibre (PLA-S.CF) [20, 27, 29, 70, 132-134, 137, 159] and PLA-continuous carbon fibre (PLA-C.CF) [60, 61, 126, 149, 150] were plotted against their weight fibre content gathering from the literature. In Figure 4.12, both stiffness and strength versus fibre weight content plots show that the properties of the current printed DcAFF are superior to all of the PLA/S.CF composite 3D printed parts and most of the PLA/C.CF 3D printed parts even if the PLA/C.CF have higher fibre content than the DcAFF. This may be the result of the fibres that are longer than the fibre critical length plus the alignment. This again confirms the high tensile performance, comparable to continuous fibre, achieved by using discontinuous aligned fibre to reinforce a thermoplastic matrix.

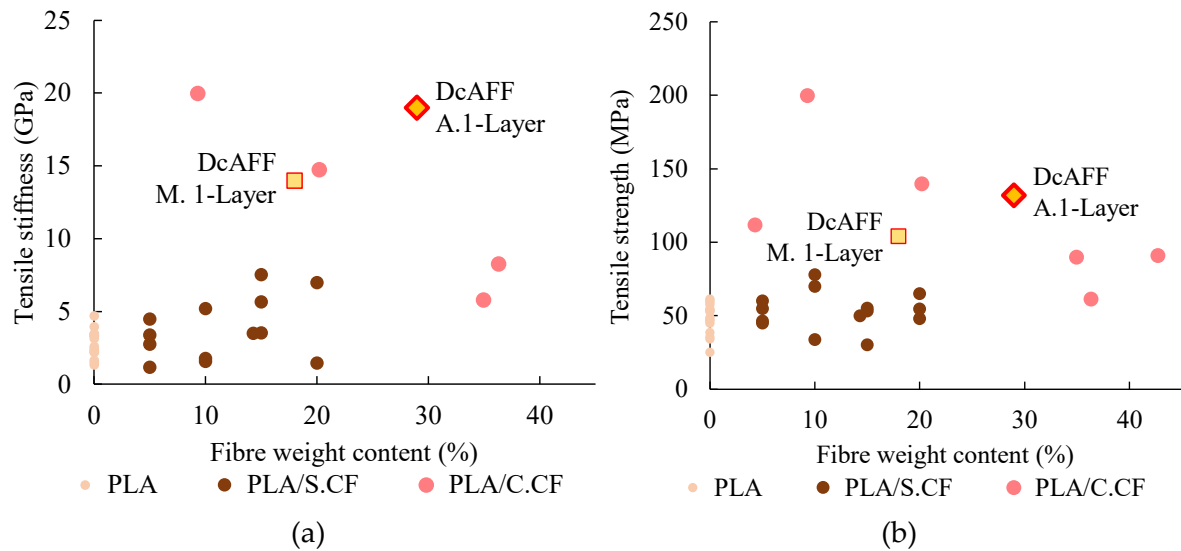


Figure 4.12. Comparison of (a) tensile stiffness; (b) tensile strength between the DcAFF printed as single layer 3D printed part, “DcAFF A. 1-Layer”, (20 tested specimens), the DcAFF printed with manually moulding filament from Chapter 3, “DcAFF M.1-Layer”, (5 specimens) and other composite 3D printing from publications: PLA [10, 20, 29, 31, 55, 56, 134, 137, 139-145] (Table 2.2), PLA-short carbon fibre (PLA/S.CF) [20, 27, 29, 70, 90, 132-137, 159] (Table 2.3), PLA-continuous carbon fibre (PLA/C.CF) [60, 61, 126, 148-150] (Table 2.4), plotting against their fibre weight content.

4.5. Open-hole testing

FDM allows for the manufacture of specimens where the fibre orientation can follow the load path, for example, the raster could be placed around an open hole to reduce

stress concentrations [31, 40, 71, 132, 165-167]. There are several 3D printing studies about the customized printing path to reduce the stress concentration around a hole. An optimized printing path, called Curvilinear Variable Stiffness (CVS), inspired by considering fluid flow around a circular obstacle, showed a significant strength improvement compared to a unidirectional composite straight fibre printing path with a drilled hole [168]. Concentric ring printing to the hole shape is another potential option that is known to reduce stress concentration [165, 169]. This section is the first demonstration of the complex part printing of DcAFF and the benefit of bulking the tape into the fine-diameter filament for 3D printing, instead of using a thin tape for automated fibre placement technologies [170] that is suitable for only large radius steering. The open-hole 3D-printed part with the designed curvilinear path will be compared to the conventional tape layup open hole manufactured by material subtraction methods.

4.5.1. Open-hole specimen fabrication

Open-hole samples were fabricated using two different methods: 3D printing with a curvilinear path and hand layup of unidirectional tapes with heat-pressure consolidation plus hole punching. Two different curvilinear deposition paths were considered. One set of printed specimens was consolidated under vacuum pressure in an oven to replicate the tape layup process with the heat-compaction process. In total, four sets of specimens were tested: 10-curvature printing (10C), 4-curvature printing (4C), 4-curvature printing with post-printing consolidation (4C-Oven), and tape hand layup with heat-compaction forming (Tape). There are four samples in each group in the testing.

4.5.1.1. Open-hole printing

To study the load-bearing behaviour of the different printing paths, the G-code was set to print the curvilinear specimen in two different ways: steering 10 rasters around the hole and keeping one straight-continuous line on each edge (known here as 10C), Figure 4.13(a1); and steering only four rasters around the hole and keeping eight

straight-continuous linear lines (4C), Figure 4.13(b1).

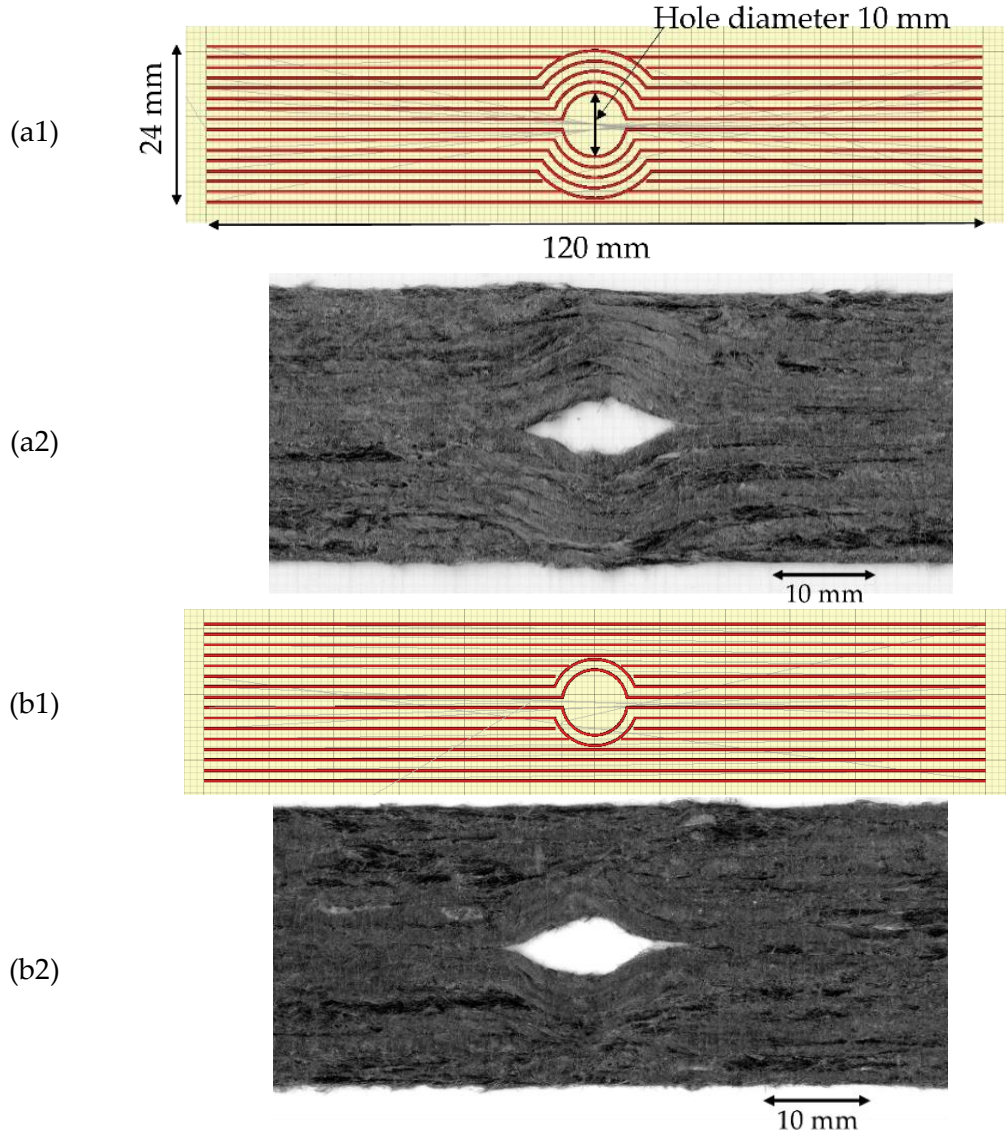


Figure 4.13. (a1) and (b1) Designed curvilinear 3D printing path for 10- and 4-curvature samples; (a2) and (b2) high magnification at the curvature hole of 10- and 4-curvature samples on the bottom side (attached to the printing bed) [163].

These paths were deposited in a single layer with the same printing condition as the large square tensile specimen mentioned in the previous tensile testing section. The finished parts of the 10C and 4C paths are shown in Figure 4.13(a2) and (b2), respectively. The hole was defined by the printing path as perfectly circular with a diameter of 10 mm, however, the circular hole cannot be achieved due to the poor adhesion between the printing bed and the deposited raster. At the sudden turning point from the linear to curvature, the raster cannot be held on the bed while the

nozzle moves upwards and sideways. This motion drags the filament, producing an eye-shaped hole rather than the one defined by the desired half-circular path. The measured hole dimension, in the direction perpendicular to the load, is around 5-6 mm.

4.5.1.2. Post-printing consolidation of the printed part

For a further study inspired by the thermal consolidation process carried out in the tensile testing, four of the 4C printed parts were consolidated in a vacuum bag (1 bar) at a temperature of 200°C for 1 hour, those specimens are identified as 4C-Oven. This post-printing consolidation aimed at obtaining better raster bonding and reaching a performance similar to the oven-consolidated lay-up, as described below. To prevent the shape-changing of the printed part, especially the hole, cork tape was used as a dam around the specimen and inside the hole. The changes in the sample surface between the printed and the consolidated specimens with a smoother surface and well-joined rasters can be seen in Figure 4.14(a) and (b). The hole shape does not change from the previous printed part, but there is material accumulation on the hole and sample edges, as the matrix cannot flow over the cork, leading to thicker edges. The overall raster direction does not change with the post-printing consolidation. The thickness reduction after the consolidation is approximately 20%, from an average of 0.60 ± 0.043 to 0.48 ± 0.023 mm

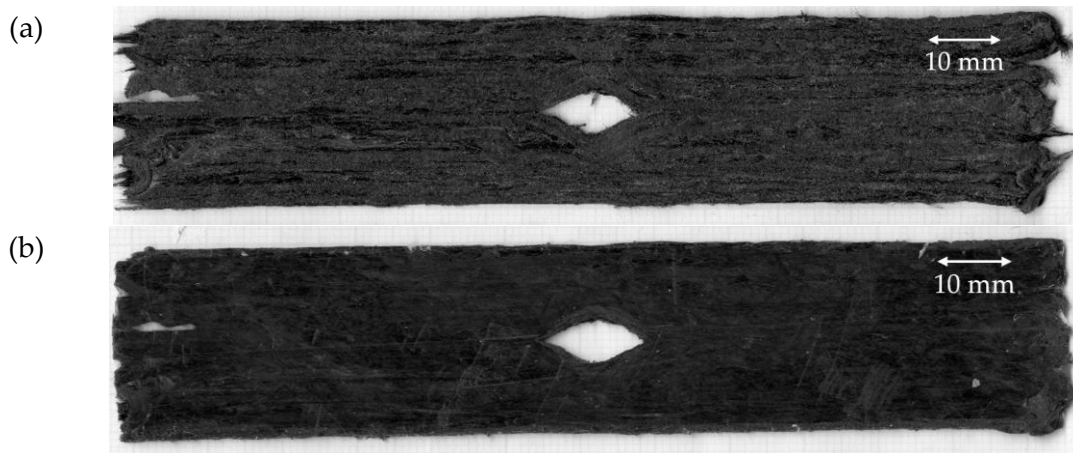


Figure 4.14. (a) 4-curvature printed part before post-printing consolidation; (b) the sample after the consolidation under heat and pressure (4C-Oven) showing a smoother surface and better raster fusion.

4.5.1.3. Open-hole layup

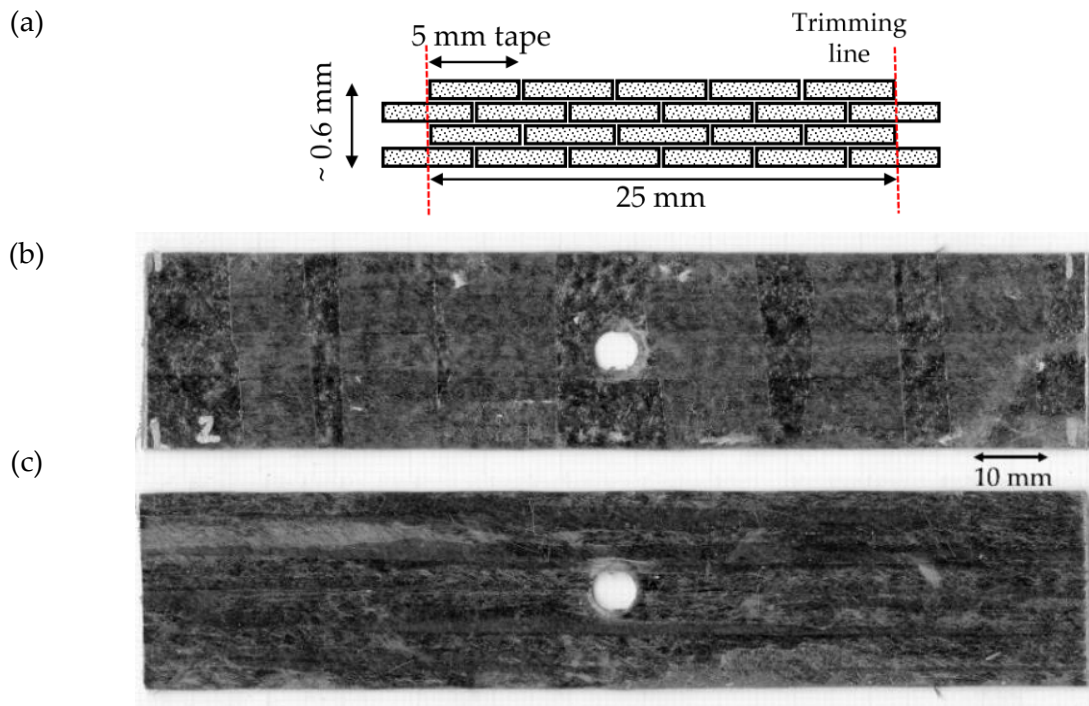


Figure 4.15. (a) Stacking sequence of the layup sample showing four layers with trimming lines to make a 25 mm wide sample; an example of a layup part with a cutting hole using a hollow punching tool: (b) top surface and (c) lower surface (surface attached to the metallic mould) [163].

Open-hole layup samples were built by placing the initial HiPerDiF tape, 5-mm-wide, side-by-side and staggered through the thickness to obtain the desired width and thickness. The tape used in this stage is the same production batch of the filament in the previous section, so the fibre volume fraction is in a similar range. In this case, there are four layers of tape as the thickness of the original tape is between 0.1 and 0.2 mm and the aim was to achieve a total thickness of ~0.6 mm. Figure 4.15(a) shows the cross section of the stacking sequence with the half-width overlap of six and five tapes on each layer [163]. The produced laminate was compressed and heated using the same pressure, temperature and duration of the post-printing consolidation of the printed one as described in the previous section to ensure the fusion of the PLA composite. The achieved consolidated thickness is between 0.6 and 0.7 mm. The layup edges were trimmed with a knife, where the first and third layers protrude from the other layers, to achieve a 25-mm-wide sample. Finally, the hole

was cut with a 6-mm-diameter hollow punching tool with a hammer. The punching is expected to produce a straight-cut hole rather than a spinning cutting of the drill as the specimen is a thin panel. The hole size was selected to be equivalent to the size of the holes of the printed samples measured perpendicularly to the longitudinal direction. The top and lower surfaces of the lay-up specimen are shown in Figure 4.15(b) and (c), respectively. The lower surface is smoother than the top surface, as it is an imprint of the tool in which the composite is laid up, however, some dry areas, corresponding to dry patches in the composite tapes, can be observed. The average measured thickness of the layup after the oven processing is 0.70 ± 0.046 mm.

4.5.2. Open-hole testing method

There are four groups of the tested sample: 10C, 4C, 4C-Oven and tape layup, and each group has four samples. The samples' width and thickness at the position of the hole were measured for stress calculation. The hole size was measured from the scanned image of the sample at the widest position of the hole. The cross-section area used to calculate the strength is the specimen thickness multiplied by the difference between the specimen width and hole diameter. The samples were tested using the same testing machine and procedure as the tensile tests described in Section 4.4.2. The strain was measured *via* digital image correlation (DIC) to obtain the strain map during loading. The DIC parameters are illustrated in Table 4.3.

Table 4.3 DIC technique parameters.

Software	Davis10.1.2	Image resolution	2056 x 2418 pixel
Camera & Lens	M-lite & 35 mm	Field of view	78.95 mm x 95.27 mm
Correlation mode	Sum of Difference	Frame rate	1 image per second
Subset size	21x21 pixel (0.8 mm x 0.8 mm)	Strain resolution	$7.56 \times 10^{-4} \epsilon$
Step size	2 pixel (0.076 mm)	Scale factor	26.04 pixel/mm

4.5.3. Open-hole testing result

The strengths of each sample group are shown in Figure 4.16(a). There is a significant OPH strength difference between the only printed parts (10C and 4C) and the post-

printing consolidation part (both 4C-Oven and tape layup). The post-printing consolidation strengthens the inter-raster bonding showing an increase in the OPH strength. The stress-strain curve of a sample from each tested group is shown in Figure 4.16(b). This also shows the different mechanical behaviour between the post-printing consolidated parts, which show a linear behaviour with a sudden failure of the whole structure, and the ‘as printed’ specimens, which display a highly non-linear behaviour with a gradual load drop after the initial failure caused by the separation between the curvilinear rasters while the remaining structure still carried the further load. The failure samples in each case are shown in Figure 4.17.

The strain maps obtained at the highest load in each sample, marked in Figure 4.16(b), in longitudinal, transverse and in-plane shear achieved from DIC are plotted in Figure 4.18 - 4.20, respectively.

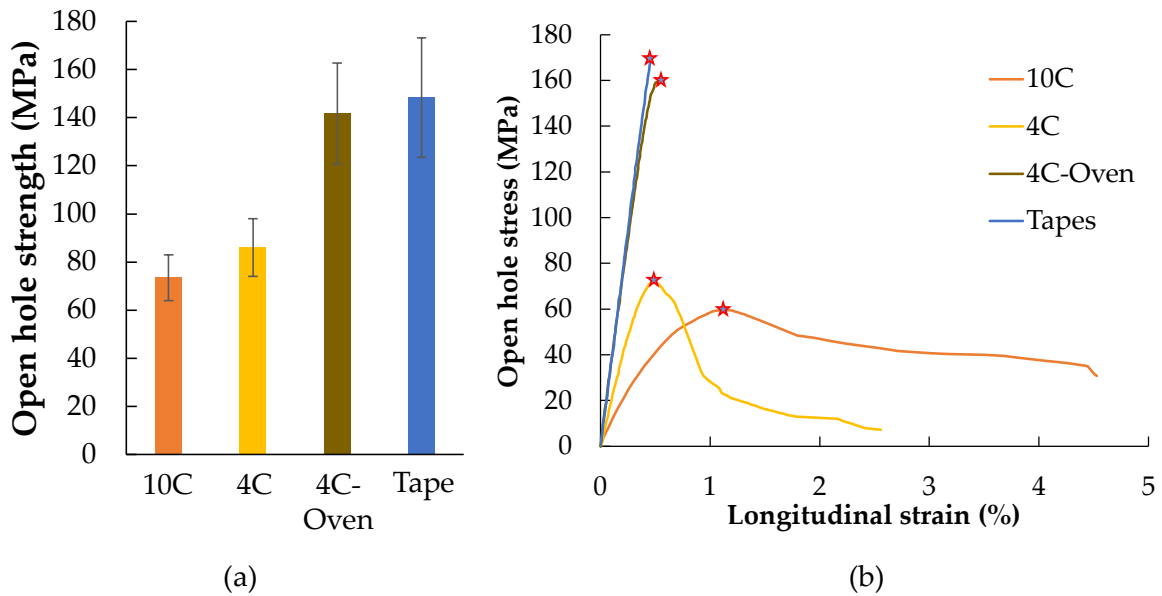


Figure 4.16. (a) Open-hole strength of different sample types; (b) open-hole stress *versus* average longitudinal strain curves of each sample type showing different failure behaviours.

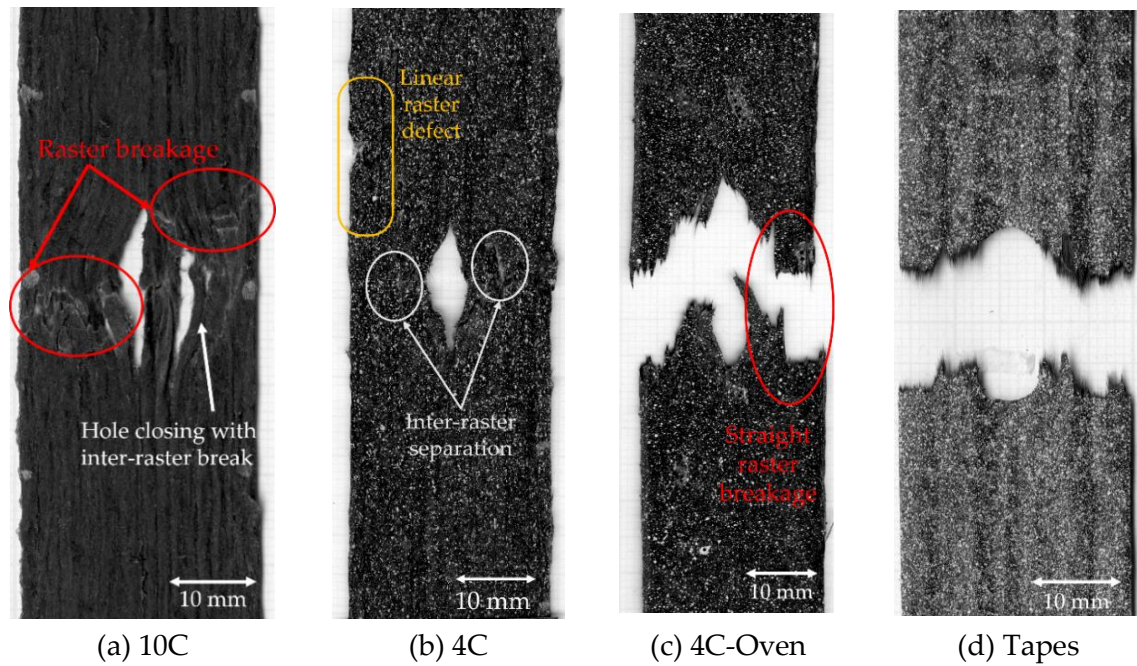


Figure 4.17. Breakage of the open-hole samples: (a) 10C showing hole closing by the inter-raster separation following raster breakage [163]; (b) 4C showing the raster separations with defect at the linear line that occurs before the breakage of the raster at the curvature area; (c) 4C-Oven showing the catastrophic failure in the rasters perpendicular to the load direction; (d) tape lay-up showing breakage perpendicular to the fibre/load direction at the middle of the hole [163].

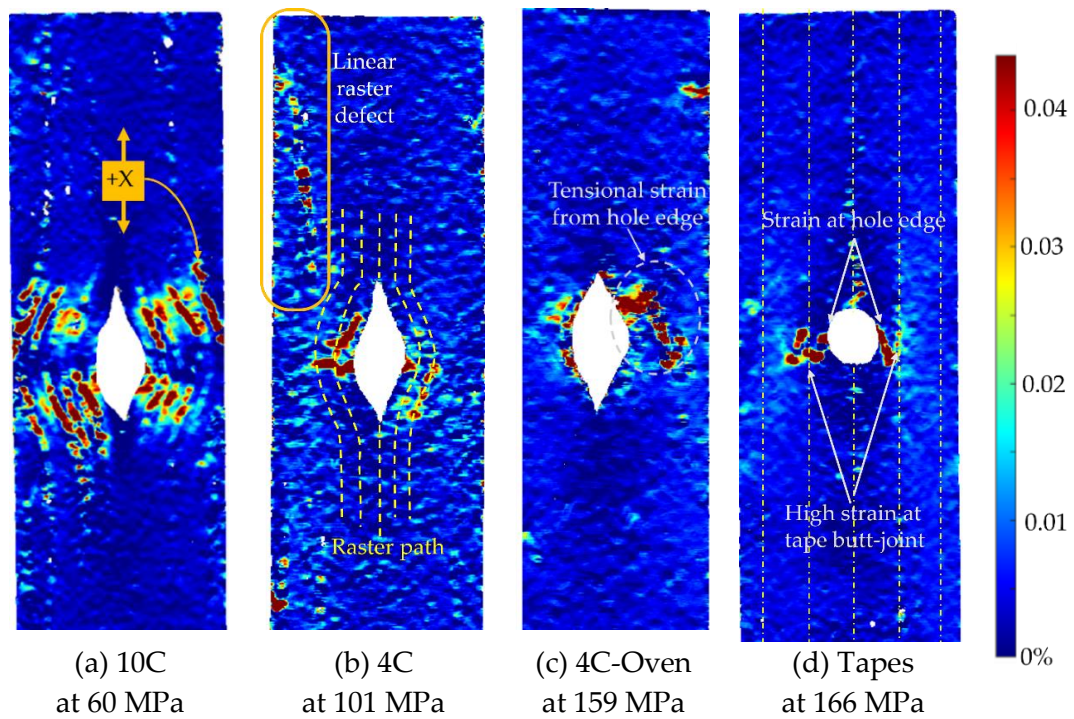


Figure 4.18. DIC analysis of longitudinal strain (ϵ_x) at the maximum load of each sample in different types: (a) printed 10C; (b) 4C; (c) 4C-Oven (post-printing consolidated part); (d) tape (lay-up part with a punched hole).

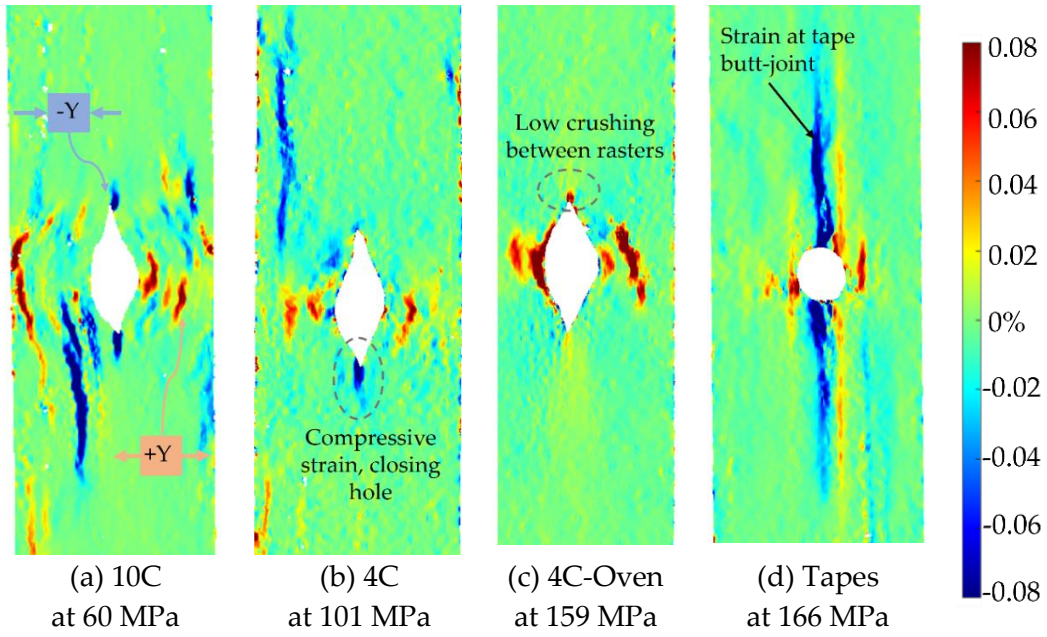


Figure 4.19. DIC analysis of transverse strain (ϵ_y) at the maximum load of each sample in different types: (a) printed 10C; (b) 4C; (c) 4C-Oven (post-printing consolidated part); (d) tape (lay-up part with a punched hole).

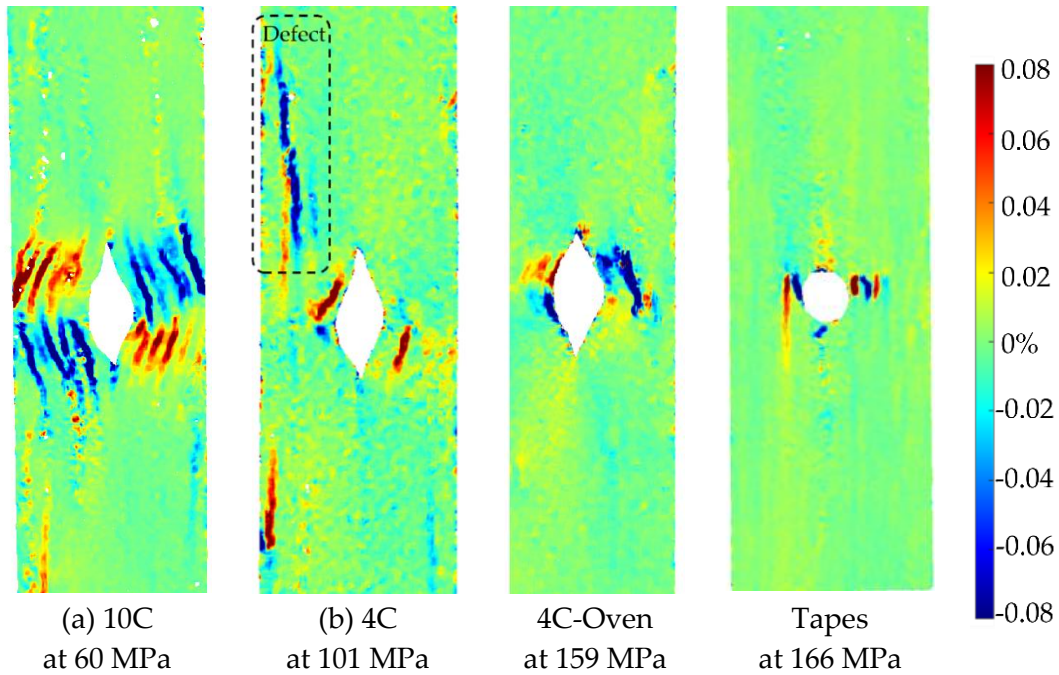


Figure 4.20. DIC analysis of in-plane shear strain (ϵ_{xy}) at the maximum load of each sample in different types: (a) printed 10C; (b) 4C; (c) 4C-Oven (post-printing consolidated part); (d) tape (lay-up part with a punched hole).

10C samples show the lowest average open hole strength according to Figure 4.16(a). This is because it has the greatest number of curvilinear rasters that have a lower load-bearing capacity than linear rasters. It also results in the highest non-linear

behaviour and shows a large deformation at failure, as seen in Figure 4.16(b). The longitudinal strain map of the 10C, Figure 4.18(a), shows that the tensile strain is concentrated in the inter-raster region around the curvilinear area. The tensile load in the longitudinal direction converts into compression in the transverse strain which is shown as a high compressive strain near the sharp corner of the elliptical shape, Figure 4.19(a). The primary strain of 10C is the shear strain (Figure 4.20(a)) which tends to separate the joint between rasters in correspondence with the curvilinear path in the 45° direction, which is weaker than the longitudinal raster direction. After the initial inter-raster failure, the printed rasters still stay connected, as seen in Figure 4.17(a), this behaviour may benefit some applications that require a non-linear, high strain capable behaviour rather than a high strength with a catastrophic failure.

4C sample has a lower number of curvilinear rasters than 10C which, in turn, means a greater number of linear rasters. This leads to higher open hole strength, Figure 4.16(a), and lower non-linearity than 10C, Figure 4.16(b), presented as the stress drops significantly after the maximum load. According to the strain map, the strain also accumulates around the curvilinear rasters showing the separation between them. The strain map of a 4C sample in all directions (Figure 4.18(b), Figure 4.19(b) and Figure 4.20(b)) also shows the high strain at the edge of the sample in correspondence to the linear rasters. This looks greater than the longitudinal strain near the curvature (Figure 4.18(b)). This may be a result of a printing defect. This leads to a weak point in the linear raster and a failure at the edge, as seen in Figure 4.17(b), rather than only curvilinear raster separations.

After the consolidation, the 4C-Oven samples have a significant increase in the open hole strength from around 80 MPa to 140 MPa, Figure 4.16(a). This is a similar level to the conventional tape layup sample. However, the post-printing consolidated part still shows a small non-linearity and a small plateau before the failure (Figure 4.16 (b)). Thanks to the welding of the rasters, due to consolidation, the inter-raster

separation is clearly reduced. The initial strain concentration moves from the inter-raster around the curvilinear area to the area near the edge of the hole and the fracture starts from this point before breaking the whole sample across the hole area, Figure 4.17(c). The separation of the rasters at the sharp corner of the eye shape is no longer present, showing a compressive strain at the sharp corner, Figure 4.19(c), rather than the tensile strain between rasters presented in the printed 4C. However, there is a high strain concentration in the longitudinal direction at the inter-raster bonding as clearly seen in Figure 4.19(c) because this is one of the weakest points, but this point also offers the non-linear behaviour, as mentioned above.

The tape layup with heat-compaction forming shows the highest open hole strength in this experiment, Figure 4.16(a). The strength is at a similar level to the 4C-Oven one, this confirms that the consolidation strengthens the raster bonding. Moreover, there is no non-linearity in this sample, as seen in Figure 4.16(b). The sample suddenly fails after the maximum load is reached, as seen in Figure 4.17(d). Instead of symmetric strain distribution around the hole, there are several small high-strain spots around the hole edges, as shown in Figure 4.18(d). This may be because of the different behaviour of the discontinuous fibre and the imperfect bonding on the butt-joint between tapes as shown by the strain concentration as the vertical lines parallel to the tape edges, as seen in Figure 4.19(d). The high compressive strain in the transverse direction should be the result of the butting line between two tapes that move against each other.

4.6. Chapter conclusion

In this chapter, a new filament-forming method was invented to continuously reshape HiPerDiF-PLA tape into DcAFF circular cross-section filaments suitable for 3D printing and replace the previous labour-and-time-intensive manual moulding method. The faster and easier filament-forming process here offers an opportunity to print more samples than in the previous chapter and perform a study of the DcAFF printability. The key findings and conclusion drawn from this chapter are

listed below:

- The concept of the 2-piece manual moulding has been converted to a semi-automated machine using two small slot compaction rollers. The thin impregnated tape passed through the well-adjusted gap between two rollers presented a promising square-like shape cross section. Then, the well-compressed square-like filament was pultruded through a series of nozzles leading to a good quality smooth surface circular 1-mm diameter 3D printing filament. The production rate was increased from a meter per hour with the manual process to a half meter per minute with the semi-automated machine. The DcAFF machine also increases the fibre alignment with almost 90% of fibre aligned in the longitudinal direction after reshaping from thin tape to circular filament.
- In tensile testing, the single-layer part printed with the DcAFF filament produced with the new forming method again presented superior tensile properties to other 3D-printed PLA composites even with a lower fibre content of DcAFF. This shows the potential of the produced filament to be used as a commercial filament.
- The open hole with curvilinear was chosen for the printability testing and revealing the actual benefit of using DcAFF as a filament instead of thin tape. Although the curvilinear printing of the filament shows some discrepancy between the desired and the deposited raster, the open hole with the curvilinear path has a different behaviour under tensile load to the layup with a material subtraction. The curvilinear open hole 3D printed sample changes the stress concentration from at the hole edges to the inter-raster separation. This resulted in a change of failure mechanism from brittle breakage that occurred in the layup with post-printing consolidation to the more progressive failure mode by breaking at the inter-raster bonding around the curvature. After the initial inter-raster failure, the rasters still stayed connected and carried the load for a while before its completed failure. This will be beneficial to applications that require

non-catastrophic failure.

- Despite the faster filament production rate, the limitation of the HiPerDiF preform produced with the lab scale machine leads to a limited amount of DcAFF filament. This resulted in the investigation of those mechanical properties in this chapter only on the single-layer 3D printing which presents only the behaviour of the in-plane adjacent raster. To enable large-scale filament production, the HiPerDiF pre-impregnated tape needs to be produced in a faster, more continuous and more efficient method. Thanks to the development of the HiPerDiF machine to a larger lab scale, ready for the industrially upgraded scale, more aspects of the DcAFF material will be studied in the next chapter. The multilayer printing must be investigated to complete the actual properties (with the through-thickness) of the 3D printed material and properties. The printing accuracy needs to be addressed to eliminate the discrepancy seen in curvilinear or complex geometry printing.

Chapter 5 Multilayer Printing

Following the development of the previous chapter, where the feasibility of printing DcAFF filaments has been demonstrated in single-layer trials, the printing of multilayer composites is explored here. The extension of the previous assessment is essential to examine the role of the newly formed interfaces on the performance of the composite. The mechanical properties of the multilayer part will be studied through tensile, short beam shear (SBS), and open-hole (OPH) tensile testing. These performances will be compared to those of the single-layer part obtained in the previous chapter and literature data.

The detail of the filament characterisation and the multilayer DcAFF printed properties part were constructed with some parts of the work published in *Composite part B: Engineering* in 2023 under the title of “DcAFF (Discontinuous Aligned Fibre Filament) – Investigation of Mechanical Properties of Multilayer Composites from 3D Printing” [4]. The whole article and the testing result were prepared by N.K. and amended by all authors.

N. Krajangsawasdi *et al.*, "DcAFF (Discontinuous Aligned Fibre Filament)– Investigation of mechanical properties of multilayer composites from 3D printing," *Composites Part B: Engineering*, vol. 264, p. 110903, 2023. DOI: 10.1016/j.compositesb.2023.110903.

5.1. Chapter introduction

In Chapters 3 and 4, the HiPerDiF pre-impregnated tape was produced at a small production rate (less than a meter per minute) with the second-generation lab-scale HiPerDiF machine. This leads to a low amount of produced DcAFF filament even though the semi-automated machine was successfully developed. Therefore, the printing was limited to only single-layer parts. Thanks to the further development of the HiPerDiF technology, the third generation machine, called “HiPerDiF-3G”, which can produce a higher amount of HiPerDiF preform (metres per minute), was commissioned at National Composites Centre, UK. This allows to produce more DcAFF material at a faster rate offering an opportunity to study other aspects, *i.e.* more complex geometries and multilayer specimens, of its application and exploitation in 3D printing. Figure 5.1 shows the schematic of the HiPerDiF-3G machine including three modules: (i) the fibre-water mixing tank where the fibres are mixed to the calculated concentration, (ii) the alignment head where the fibres are sprayed to the alignment head, and (iii) the impregnation module where the dry preform is impregnated with the selected matrix.

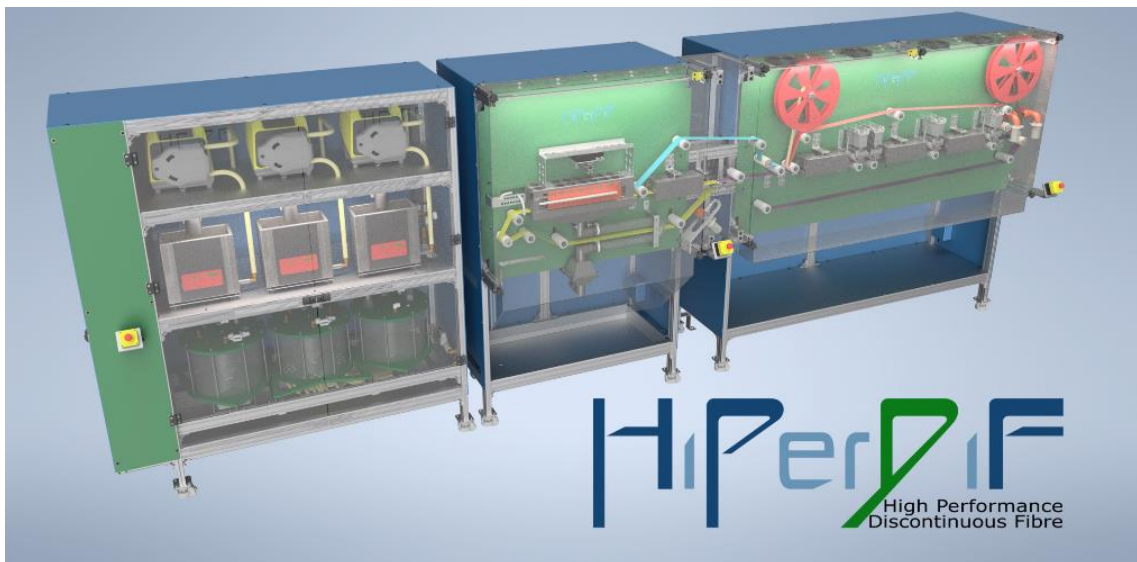


Figure 5.1 Schematic of the HiPerDiF-3G, larger-lab-scale, machine located at the National Composites Centre, UK (developed within EP/P027393/1, High Performance Discontinuous Fibre Composites - a sustainable route to the next generation of composites).

After the mass production of the DcAFF filament, the DcAFF was printed to

multilayer samples and then its mechanical performance was investigated using (i) multi-layer tensile testing, (ii) short beam shear testing (SBS) and (iii) multi-layer curvilinear open-hole tensile testing (compared with a multi-layer printed part with a hole obtained by drilling). The post-printing consolidation was considered with the expectation to improve the properties of the printed part even more than what was achieved from the single-layer printing in Chapter 4. The multilayer properties were compared to the single-layer part to show their difference.

5.2. DcAFF filament quality

5.2.1. DcAFF filament production

In this chapter, the carbon fibre reinforcement is the same Toho Tenax 3-mm chopped carbon fibre used in the past chapters. The PLA, matrix was changed to a commercial PLA (poly-L-lactic acid) film, supplied as a roll of 32-mm wide and 0.05-mm thick film by Goodfellow Cambridge Ltd [171]. In the current HiPerDiF-3G process, the fibre concentration in the suspension was 0.0004-0.0008% by volume and the belt speed was set at 5 mm/s. This will be a dry-aligned fibre preform with an areal weight of 26-30 g/m². After the HiPerDiF alignment process, the dry preform was merged with the PLA film with a series of rollers which apply pressure around 1 bar at 200°C to ensure the well-impregnated fibre preform with the PLA matrix. The 32-mm-wide composite tape was slit into approximately 7-mm-wide tapes. Then, the slit tape was reshaped into a 3D printing filament with the semi-automated filament-forming machine described in Chapter 4. The tape was firstly compressed into a square-like cross-section (Figure 5.2(a)) in the small gap between two counterrotating and interlocking aluminium rollers. Then, the square filament was pultruded through a series of nozzles and finally a 0.8 mm diameter PTFE one to produce a circular filament with a diameter of 0.8 mm (Figure 5.2(b)) that is ready to be used with a standard 3D printer.

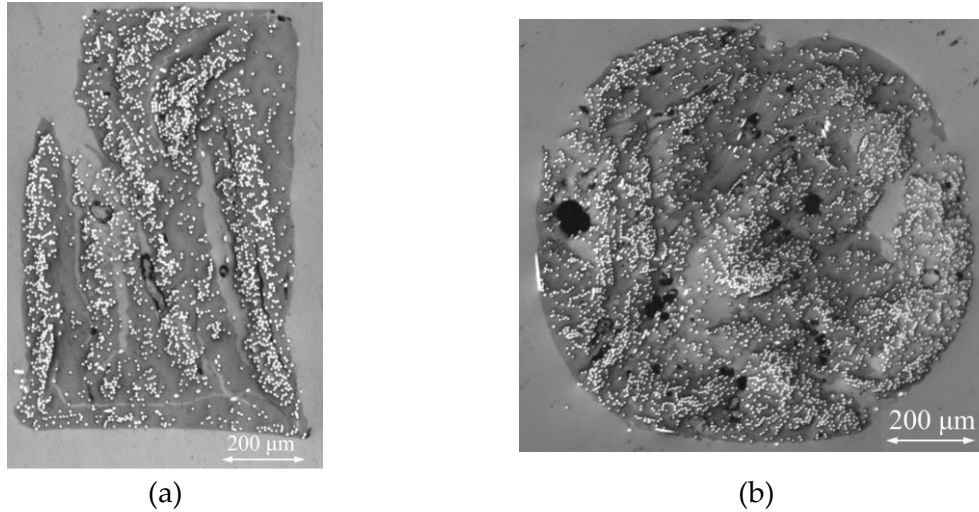


Figure 5.2 Cross-section microscopy of (a) square-like filament after the compression process in the DcAFF machine; (b) final circular filament ready to use in a 3D printer.

5.2.2. Fibre content investigation

The matrix burn-off procedure and TGA machine used in this test are the same as described in Section 3.4.3.1. The raw materials (*i.e.* dry fibre and PLA) were also tested beside the composites using the same programme to verify their residual mass after the dwelling stage. Figure 5.3 shows the result of the TGA programme. The amount of fibre burn-off is about 0.9% and the residual pure PLA after the process is relatively small around 0.3%. After accounting for those numbers, the fibre weight content of the current filament batch ranges between 22-30 wt% in different sections of the filament and the printed part. The fibre content depends on the quality of the alignment process that feeds the fibre to the alignment head and conveyer belt. The fibre content of the material produced with the HiPerDiF 3G was intentionally kept slightly lower than the one produced with the second-generation lab-scale machine (approximately 28-33 wt%) in Chapter 4 with the intention to increase the amount of matrix in the composite to improve the adhesion of the filament to the printing bed and adjacent rasters. The void (dark spots) on the cross-section can be estimated with the nominal diameter of filament in Figure 5.2(b) using the microscopic image method presented in Section 3.4.3 accounting for less than 5% void in the cross-section volume.

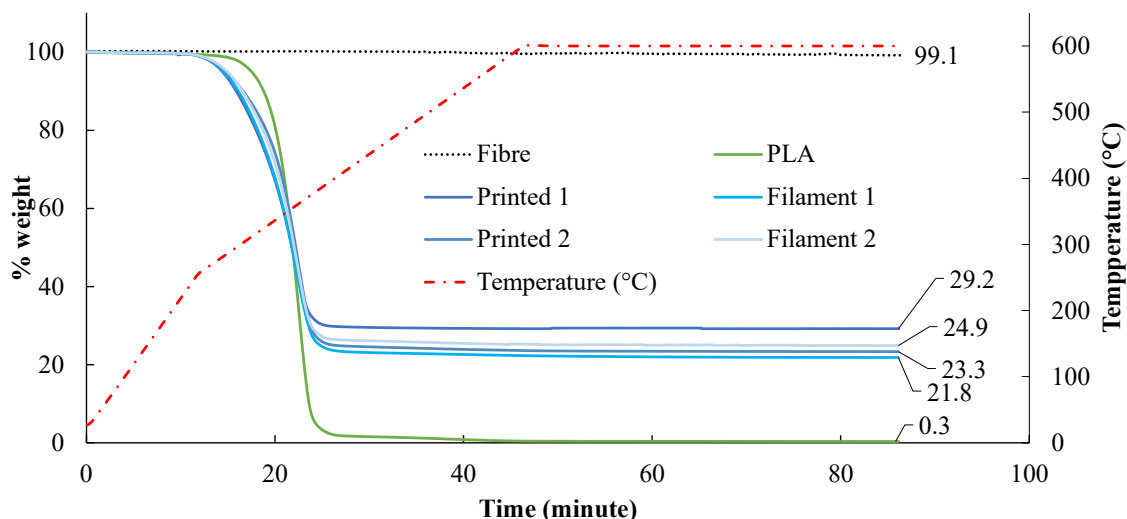


Figure 5.3 Special TGA programme, using TGA Q500 V20, to investigate fibre weight fraction by considering residual fibre content after matrix burn-off showing the fibre, four DcAFF composite specimens produced from the HiPerDiF-3G machine, and the current used PLA film with the temperature profile (red line).

5.3. Multilayer Tensile testing

5.3.1. Tensile specimen preparation and testing procedure

After the DcAFF material is formed into a circular cross-section and wound into a filament, it is ready to be printed into a defined shape. The commercial Ender3 3D printer with flat-end nozzle replacement, mentioned in Chapter 3, was used for sample fabrication. The printing conditions in this chapter were: nozzle temperature 210°C, bed temperature 80°C, speed and feed rate 300 mm/min, and set raster thickness 0.3 mm (slightly lower than in Chapter 4 due to the smaller diameter of filament). The nozzle height was reduced from Chapter 4 due to the finer diameter of the final extrusion to 0.8 mm. The raster distance was calculated based on the expected compacted area of the 0.8-mm-diameter filament with 0.3-mm raster thickness to the rectangular cross-section shape presenting about 1.6 mm raster distance. This printing condition will be used throughout the chapter.

The printing path for tensile specimens was designed to be a 100-mm long concentric path similar to the sample in Chapter 3 (Section 3.5.4), with four spiralling rasters for each layer, and built up to four layers. This is done *via* continuous printing by

moving the nozzle 0.3 mm upwards at the end of each layer. The printing of the following layer started immediately after, and the raster was placed on top of the previous layer. The printing path of the four layers is shown in Figure 5.4(a). The top and bottom surfaces of the tensile specimen printed following the defined path are shown in Figure 5.4(b). The discrepancy between the desired and deposited raster was observed again around the corner presenting as a blunt corner, similar to Figure 3.14. When investigating the cross-section of the specimen (Figure 5.4(c)), the imperfect bonding between the adjacent rasters can be seen, especially the top surface that has only one round of nozzle compaction. While better inter-raster bonding was observed on the bottom layer thanks to the four cycles of compaction by the nozzle. Although the nozzle is able to provide a certain degree of compaction, the bonding between layers is still imperfect, as shown by the presence of some interlayer voids – Figure 5.4(c). There were five as-printed specimens.

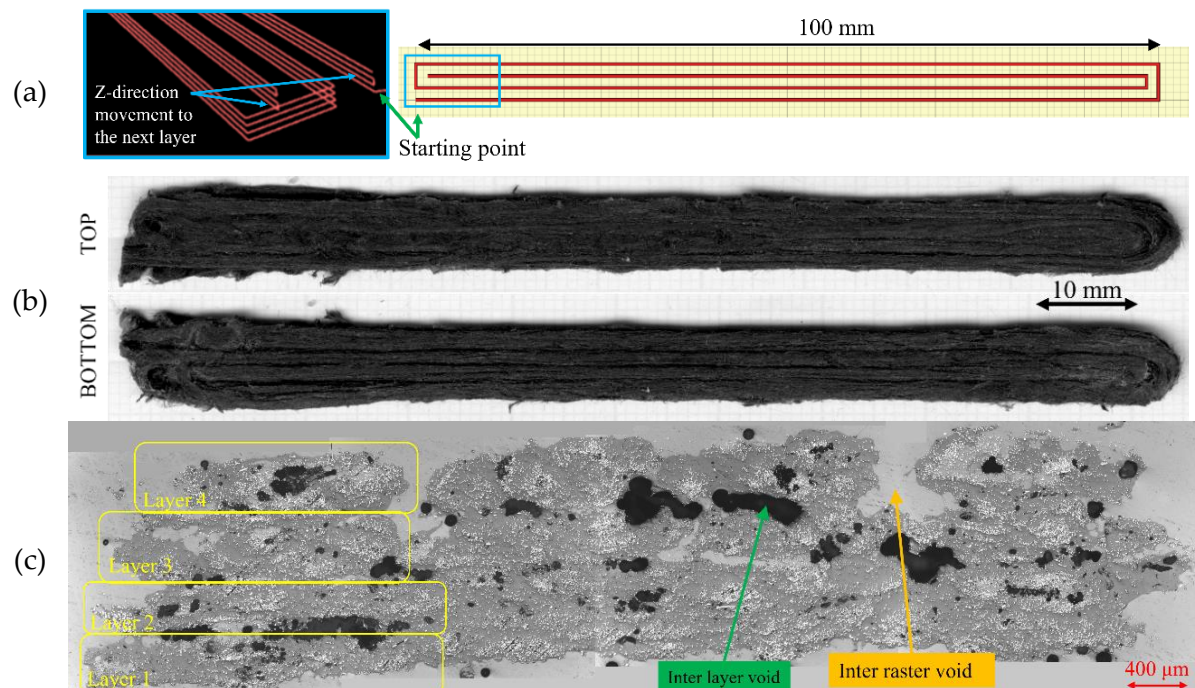


Figure 5.4 (a) Printing path for 4-layer stacking tensile specimen; (b) top and bottom surface of an as-printed 100-mm-long tensile specimen; (c) cross-section of the printed part showing four layers with four adjacent rasters on each layer.

As found in Chapter 4, the mechanical properties can be improved by post-printing consolidation. Another five printed tensile specimens were processed under similar

conditions to the consolidation in Section 4.4.1, under vacuum pressure in an open mould at 200°C for 1 hour. In the multilayer part, the consolidation significantly changes the sample morphology from the as-printed part by improving the contact between adjacent rasters and surface finishing, as seen in Figure 5.5(a). Moreover, the cross-section of the consolidated specimens is more uniform with fewer inter-raster voids than the as-printed part, as seen in the consolidated cross-section of Figure 5.5(b). To prevent material flow during the compaction, the specimens were placed in an open mould with a dam on the edges, this caused a slightly uneven cross-section with a higher thickness on the outer edges compared to the middle of the specimen.

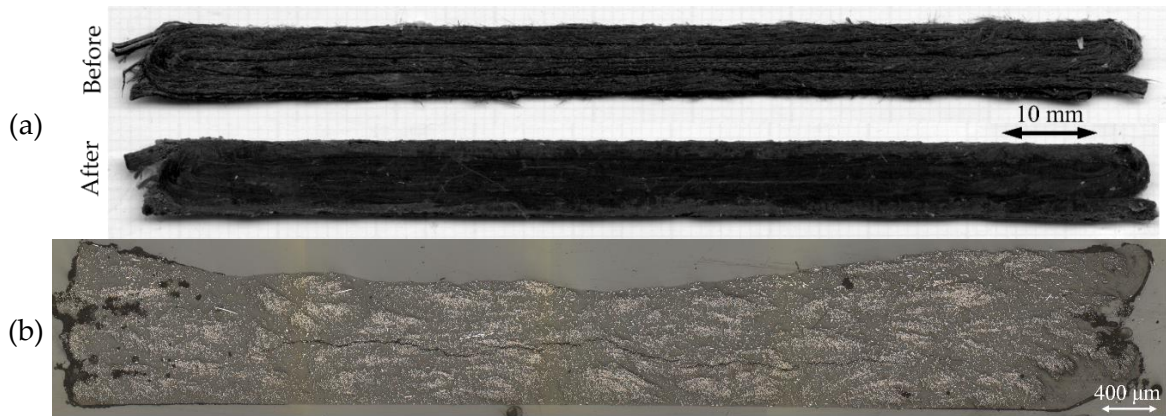


Figure 5.5 (a) Comparison of the tensile specimen before and after post-printing consolidation; (b) cross-section of the tensile specimen after post-printing consolidation (the cross-section microscopic image was taken after the tensile testing).

The width and thickness of the specimens were measured at five positions across the length with a calliper and a micrometre, respectively. The average width and thickness of the five as-printed specimens are 6.94 ± 0.074 and 1.48 ± 0.065 mm, respectively. The average dimension change due to the consolidation of the five consolidated specimens was recorded from the part before the consolidation as 7.02 ± 0.23 mm in width and 1.45 ± 0.12 mm in thickness to 7.53 ± 0.15 mm in width and 0.99 ± 0.21 mm in thickness after the consolidation. The consolidation reduces the thickness but increases the width of the specimen, so the average volume reduction is about 26% from the part before the consolidation, this could be attributed to the

removal of voids.

There are five samples in each testing case. The tensile samples were provided with 20-mm-long end-tabs at both ends leaving a 60-mm gauge length, similar to Figure 3.15(d). The testing machine, strain measurement and testing procedure are the same as described in Section 4.4.2.

5.3.2. Tensile testing result

The tensile testing result is presented as a stress-strain curve in Figure 5.6. The DcAFF shows a brittle behaviour under tensile load, as seen in the linear curve until the breakage. Unlike the small improvement observed in the single-layer consolidated part (in Chapter 4), the post-printing consolidation significantly increases the tensile properties of the multilayer 3D printed sample, *i.e.* stiffness from 27 GPa to 44 GPa (about 60%) and strength from 184 MPa (~1895 N failure load) to 268 MPa (~2000 N failure load), accounting for about 45% increase, as seen in Figure 5.7(a) and (b).

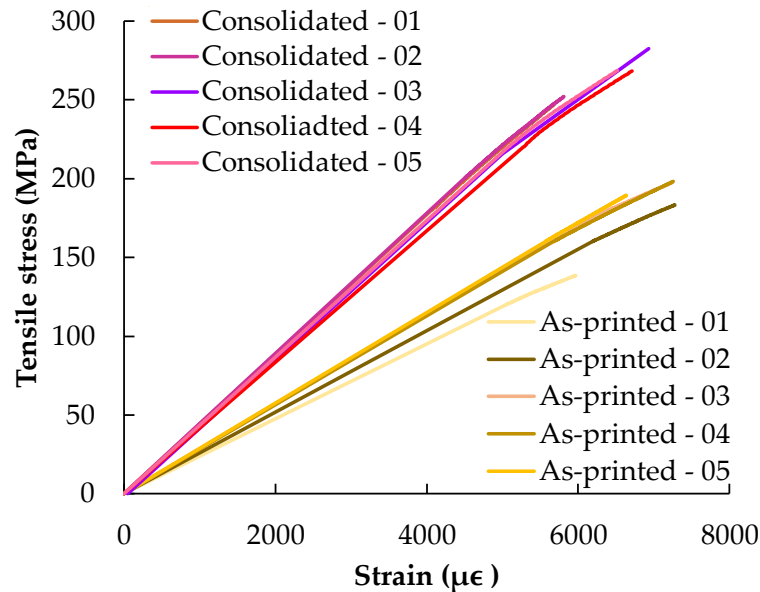


Figure 5.6 Tensile stress-strain curve of the as-printed and consolidated specimens.

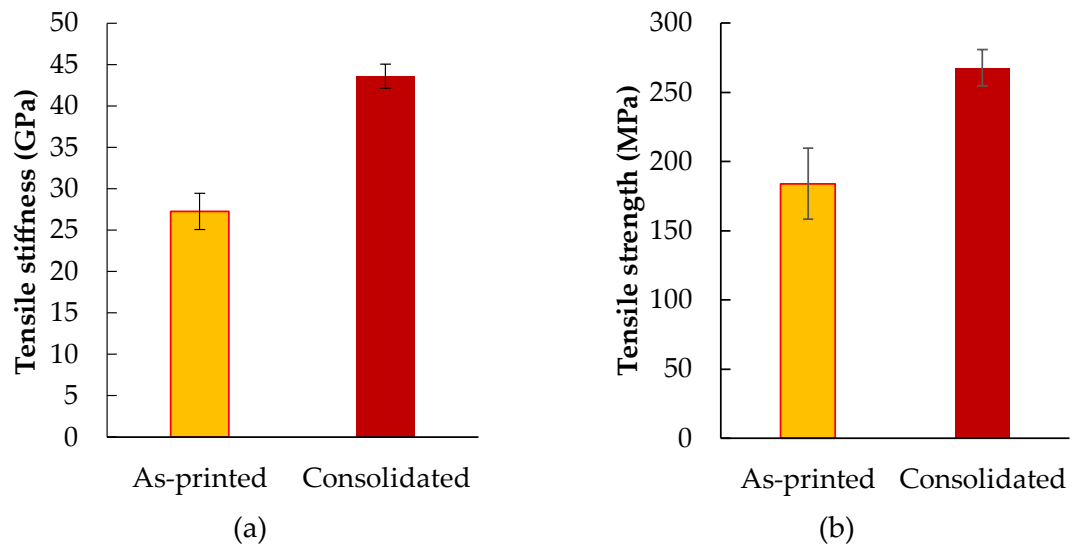


Figure 5.7 Comparison of as-printed and consolidated (under heat and pressure) tensile testing mechanical properties: (a) tensile stiffness; (b) tensile strength.

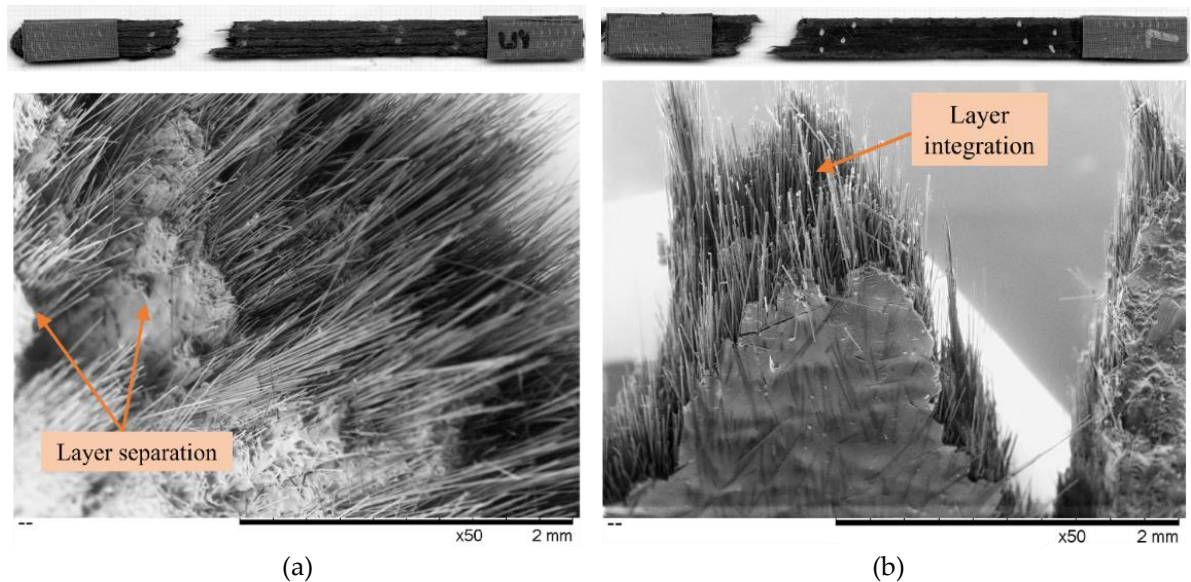


Figure 5.8 SEM image of tensile fracture surface: (a) as-printed; (b) post-printing consolidation.

According to the low increase in the failure load of the consolidated sample (only 5% from the as-printed), the property improvement is mainly the result of the cross-section area reduction from the elimination of the voids or other defects that improves the bonding between the raster/layer. SEM images in Figure 5.8 show the fracture surface of the tensile specimen with and without consolidation. In Figure 5.8(a), the as-printed specimen fracture surface presents a layer separation due to the poor bonding between layers; by contrast, the consolidated part, in Figure 5.8(b),

shows a united structure at the rupture surface. In both samples, there is no clear evidence of fibre breakage. The presence of “clean” fibres with no traces of resin on the fracture surface suggests that the major failure mechanism is fibre pull-out.

In Figure 5.9, the DcAFF as-printed part was compared to other 3D-printed tensile specimens from the literature, the collection of data, including the material used, fibre content, tensile stiffness and strength, can be seen in Table 2.2-2.4.

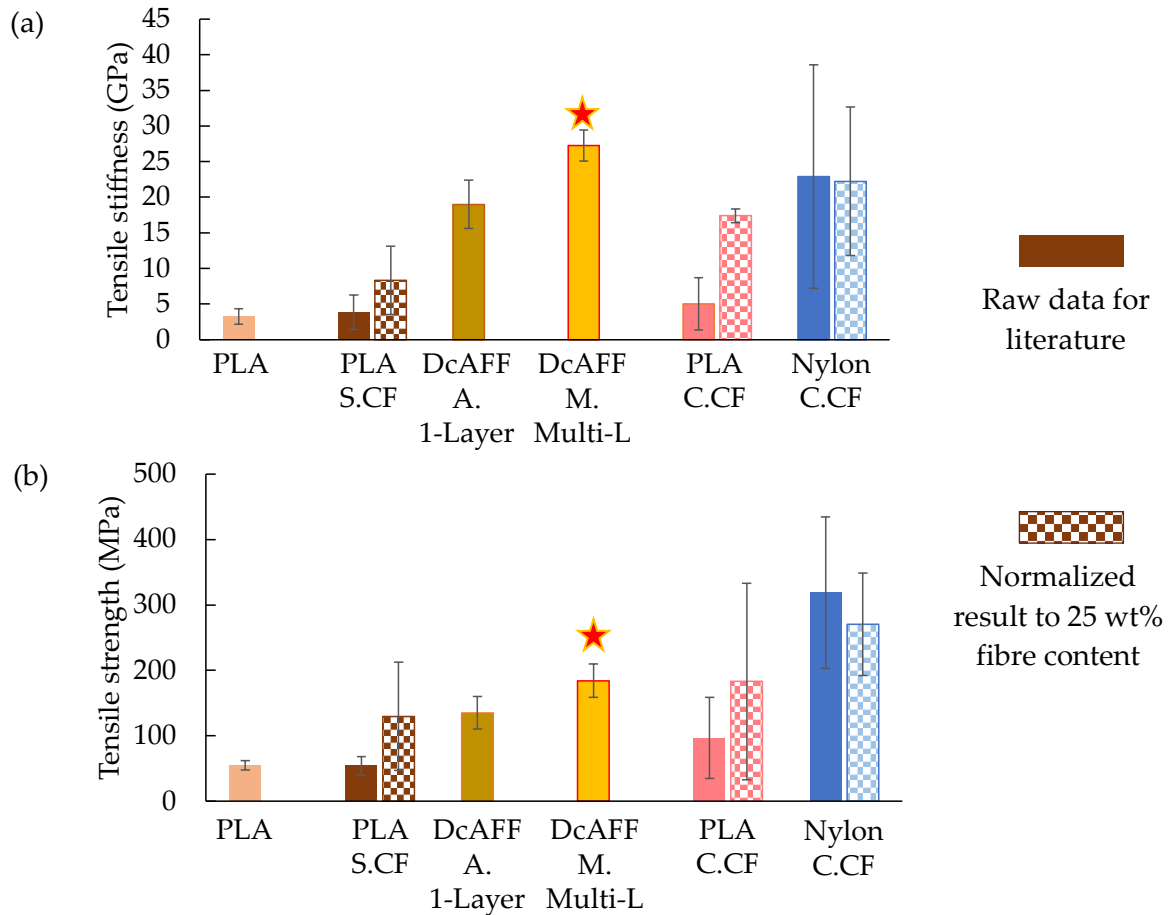


Figure 5.9 Comparison of tensile properties: (a) stiffness; (b) strength, between neat PLA [10, 15, 20, 29, 31, 55, 56, 134, 139, 143], short carbon fibre-PLA (PLA-S.CF) [20, 27, 29, 70, 132-134, 136, 137, 159], DcAFF as-printed single layer achieved from Chapter 4 (DcAFF A. 1-Layer), the current test DcAFF multiple layers as-printed indicated by a star “★” (DcAFF M. Multi. L), continuous carbon fibre-PLA (PLA-C.CF) [60, 61, 126, 149, 150] and continuous carbon fibre nylon (Nylon-C.CF) [11, 41, 122, 132, 146, 172-175], the whole composite sample was normalized with fibre weight content to 25 wt% as the average fibre content of the current DcAFF in the checked pattern bar according to the literature data in Table 2.2-2.4.

The multilayer DcAFF has significantly better mechanical properties than the neat PLA. In the reference studies reporting the results for reinforced filaments, the fibre content varied due to different manufacturing techniques. Short fibre composites showed consistently lower fibre volume fraction than DcAFF (5-20 wt%), and composites with continuous fibres can achieve higher volume fraction (up to 40-50 wt%). Owing to the difference in the fibre content in each study, the literature data were normalised with the average fibre weight content of the current DcAFF at 25 wt% (~18.6 vol%). When normalising the stress and stiffness from the literature to a fibre weight content of 25% using the rule of mixture, the strength of the short fibre composite increases up to the level of the DcAFF, this is because of the low fibre content in the short fibre composites, *i.e.* 5-20 wt%. However, on a practical level, it would be extremely difficult, if not impossible, to increase the short fibre content to 25 wt% since the randomly aligned short fibres will cause nozzle clogging during printing. The stiffness of DcAFF material is significantly higher than the short fibre because of the alignment and the 3-mm long longer fibre indicated by the fibre length measurement using FASEP and the μ CT scanned images mentioned in Section 4.3.2, which can carry and transfer the load better than fibres with lengths below 1 mm. When comparing the multilayer DcAFF (DcAFF A. Multi-L) to the single-layer 3D printed part (DcAFF A. 1-Layer), the multilayer printed material has higher stiffness and strength: this is the result of a better load-bearing capability given by more integrated rasters.

Comparing the multilayer DcAFF printed part to continuous fibre PLA composites which, on the contrary, have been scaled down, reveals that the DcAFF material has higher stiffness, whereas the strength of DcAFF is slightly lower after normalisation. It can be inferred that the fibres used in the HiPerDiF process, which are close to the critical fibre length, plus the high alignment, are sufficient to provide mechanical properties comparable to a continuous fibre composite. Furthermore, it is likely that the performance of the DcAFF filament can be improved further if the fibre content increases. Unlike the case of randomly aligned fibres, the fibre volume fraction of the

aligned fibre in the DcAFF can be boosted further towards the limit of the packing efficiency. This, in turn, offers a lower possibility for nozzle clogging, although this still requires some issues with the porosity of the filaments. Comparison of strengths is less straightforward as the performance of the matrix and fibre-matrix interface plays a more substantial role. The published results show the performance of the material with nylon matrix, whereas the current study operates with PLA. Owing to the high degree of hydrogen bonding present in nylon generally, and a specific treatment to improve fibre-matrix adhesion, the tensile strength of the nylon/C.CF from Markforged is superior to the current DcAFF.

5.4. Short beam shear testing (SBS)

To investigate the multilayer printed material properties, short beam shear testing was selected. The test was adopted from ASTM D2344 [176]. According to the layer-by-layer manufacturing method of FDM, the interlaminar shear strength of the 3D printed part is an important property, so there were several studies focused on the short beam shear behaviour of 3D printed materials [9, 10, 58, 90, 125, 177]. Moreover, heat treatments after 3D printing were also addressed in the literature to find the ultimate properties of the 3D printing part after the consolidation. The heat treatments can be performed from just above the glass transition temperature (70-80°C) to above the melting point (250°C) [90, 177]. Table 5.1 gathered the SBS strength with different material systems from the literature.

Table 5.1 Collection of 3D printed short beam shear (SBS) strength from literature.

Ref.	Material	SBS strength (MPa)	
		As-printed	Consolidated
[9]	Nylon-C.CF	43	-
[177]	Nylon-C.CF	25	27.8
[58]	Nylon-C.CF	32	-
[125]	Nylon-C.CF	40.9	-
[10]	PLA-S.CF	5.6	-
[90]	PLA-S.CF	15.38	-
[178]	PLA-S.CF/C.CF	8.81	-

5.4.1. SBS specimen preparation and testing procedure

According to the SBS specimen recommended size in ASTM D2344 [176], *i.e.* testing span-to-thickness is 4, width-to-thickness is 2 and length-to-thickness is 6. The testing span was first selected to be 10 mm leading to the required thickness of 2.5 mm (eight layers of 0.3-mm raster thickness), higher than the minimum specimen thickness of 2.0 mm prescribed by ASTM D2344 standard [176], and width of 4 mm (four adjacent rasters on each layer). This approach was also taken in the literature [125, 177, 179]. The specimen was built with the same concentric printing procedure and length as the tensile specimen with an addition of four more layers. The 100-mm long specimen was then cut into four of 20-mm long specimens with a hack saw. The cut-end was then deburred with a P1200 grid silicon carbide sandpaper and the dimensions of the specimens were measured. The average thickness and width are 2.51 ± 0.05 mm and 7.28 ± 0.22 mm, respectively.

A group of the 8-layer, 100-mm long specimens was post-printing consolidated at the same condition as the tensile samples (200°C for 1 hour under vacuum). Then, it was cut to the SBS size as specified by the standard. The top surface of the consolidated specimen (Figure 5.10(b1)), presents no visible raster lines and is smoother than the as-printed part (Figure 5.10(a1)). Voids in the specimen were removed after the consolidation, as shown by the comparison in Figure 5.10(a2) and (b2). Similar to the tensile specimens' case, the SBS specimens after consolidation are 1.99 ± 0.08 mm thick and 7.71 ± 0.31 mm wide (20.7% thinner and 5.9% wider than the as-printed).

There were six samples tested in each group. The SBS was tested with the three-point bending method. The span support was set at 10 mm. The support and loading nose diameters were 3 and 4 mm, respectively. The loading nose diameter was reduced from the size recommended in the ASTM D2344 standard [176] due to the short span limited by the span-to-thickness ratio used in this testing. This is expected to distribute the load around the contact points. The testing machine was the same

Shimadzu machine mentioned in Section 3.4.4 using the 10 kN load cell with the three-point bending fixture, as shown in Figure 5.11. The displacement and the load were recorded. According to ASTM D2344 standard [176], the testing was stopped when the displacement was larger than the thickness of the sample (2.5 mm) or the load drop-off was more than 30% of the maximum load. The short beam shear strength (F^{sbs}) was calculated from the maximum load (P_{max}) following Equation (5.1) where b and h are the width and thickness of the sample, respectively.

$$F^{sbs} = 0.75 \times \frac{P_{max}}{bxh} \quad (5.1)$$

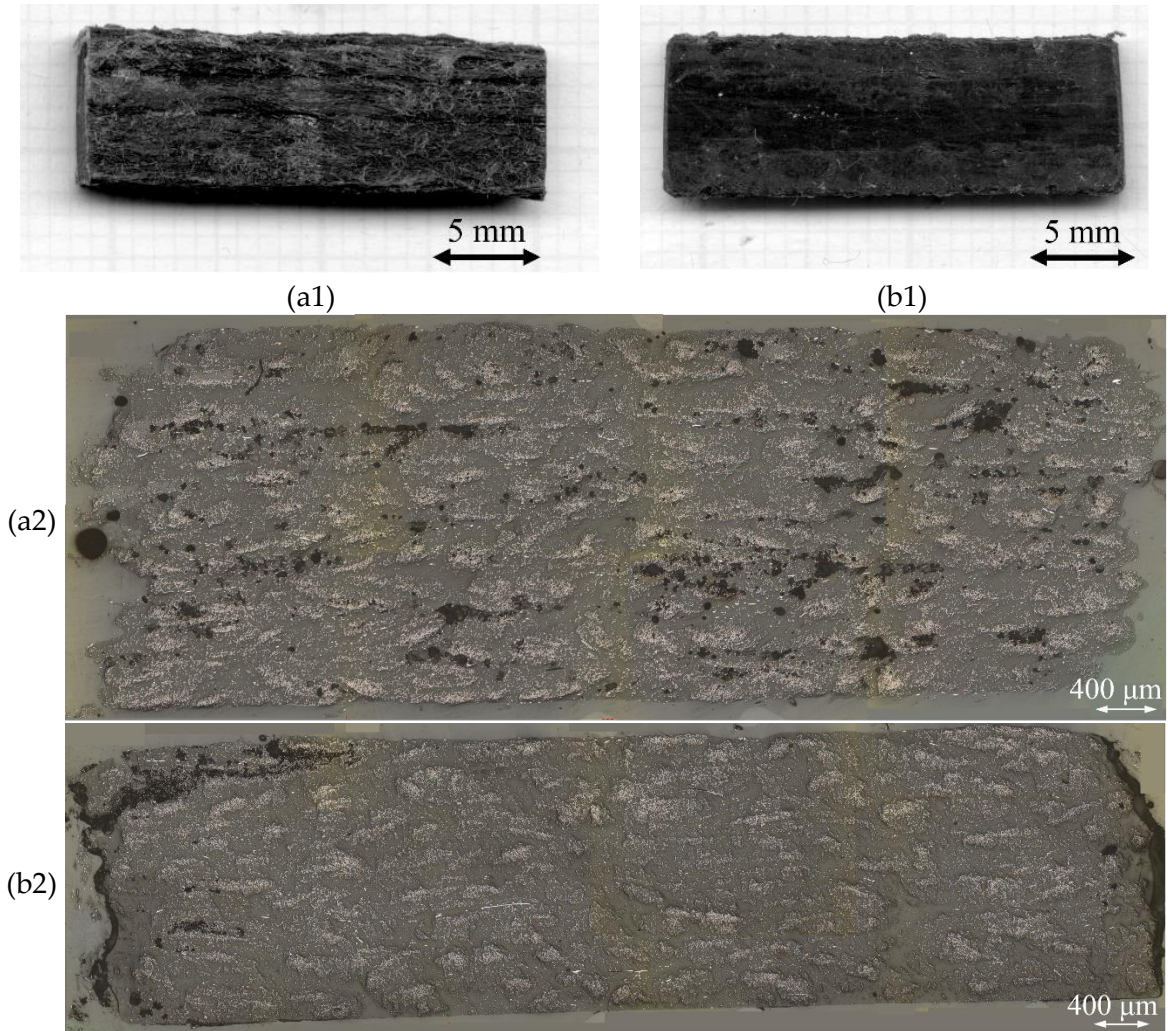


Figure 5.10 (a1)-(b1) Top view of SBS specimen: as-printed and post-printing consolidation; (a2)-(b2) cross-section of 8-layer printed specimen: as-printed and consolidated.

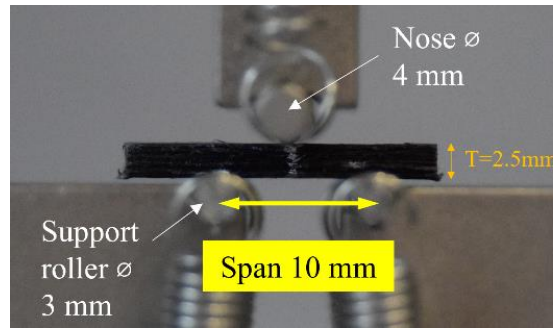


Figure 5.11 SBS test setup on the testing machine following the ASTM D2344.

5.4.2. SBS testing result

Plots between SBS stress calculated from the load response with Equation (5.1) *versus* displacement of SBS as-printed and post-printing consolidation specimens are shown in Figure 5.12(a) and (b), respectively. The average SBS strength result of the as-printed and consolidated specimens is presented in Table 5.2. It can be seen that the as-printed has slightly lower SBS strength than the consolidated one while the stress-displacement response curves of the as-printed and the consolidated part are remarkably different. The as-printed part displayed no load drop after the initial failure/maximum load. This may be caused by the inelastic deformation that can be seen in the failed sample: the sample deformed plastically under the bending load. The inelastic deformation can cause a tensional crack on the bottom surface or a compressive crack on the top surface, as shown in Figure 5.13(a). This plateau stress-displacement curve and the inelastic deformation behaviour were also found in the literature of 3D printed SBS testing [9, 177]. This inelastic failure may only be indicative of the general trends in the through-thickness behaviour of this material, but it cannot be interpreted as interlaminar shear strength. However, interlaminar failure is found in some failed samples, *e.g.* a partial interlaminar cracking on the side of a specimen Figure 5.13(b).

On the other hand, the post-printing consolidated sample shows a sudden load drop after reaching the maximum load before slightly increasing again until the test is stopped. This drop is a result of the brittle fracture of the compacted layers that causes the whole structure to fail at the same time. The failure of the post-printing

consolidated sample can be a compressive failure on the top surface (Figure 5.14(a)), tensile cracking on the bottom surface or layer separation (Figure 5.14(b)). The consolidation can reduce the single-layer separation that can be seen in the as-printed part and change the failure behaviour of the sample.

Table 5.2 SBS strength between as-printed and post-printing consolidated specimens.

Conditions	Short beam shear strength (MPa)
As-printed	20 ± 1
Consolidated	25 ± 2

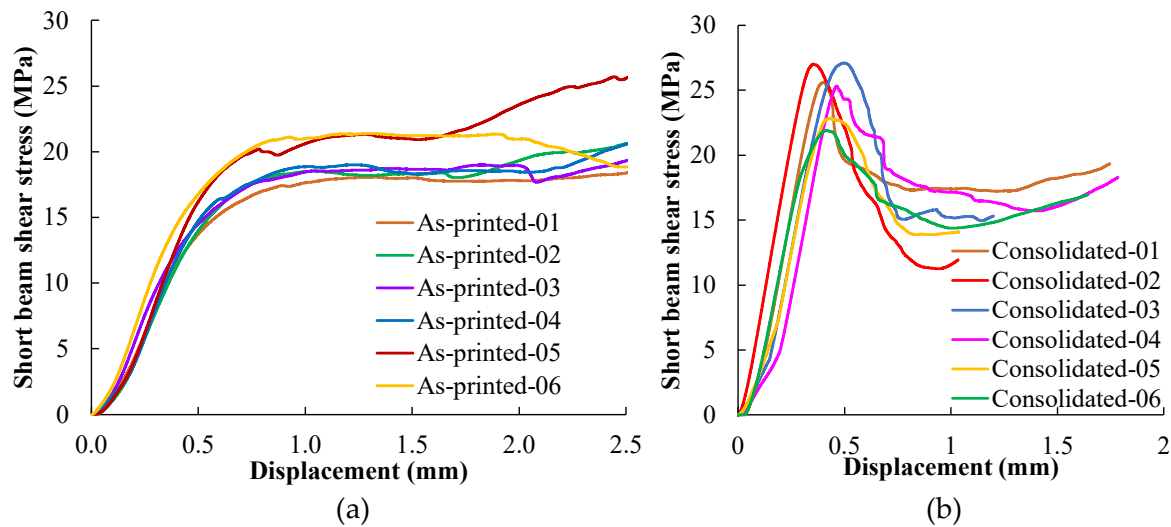


Figure 5.12 SBS stress *versus* displacement of the SBS testing: (a) as-printed; (b) post-printed consolidated sample.

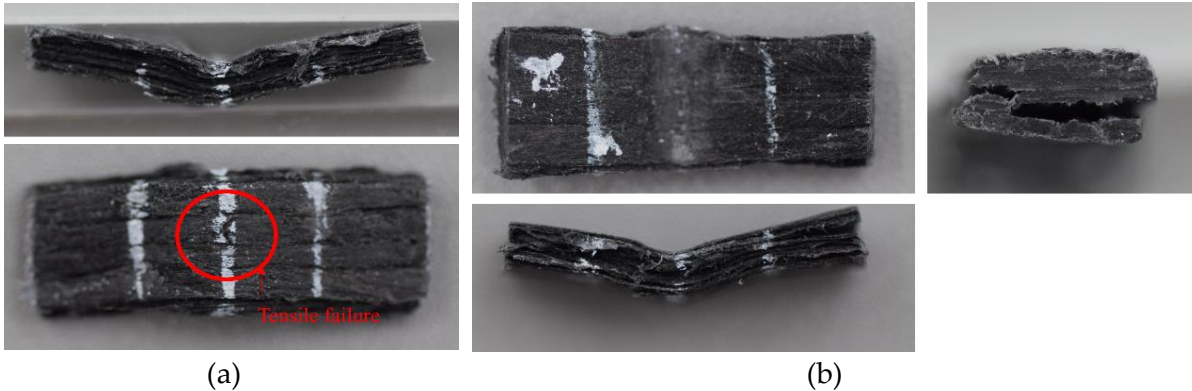


Figure 5.13 As-printed SBS failure sample: (a) tensile fracture on bottom side; (b) inelastic deformation with side layer separation.



Figure 5.14 Post-printed consolidated SBS failure sample: (a) compressive failure on the top surface; (b) mid-layer separation with the kink on the top surface.

The comparison of the as-printed DcAFF SBS strength to other composite 3D printed materials available in the literature (Table 5.1) is shown in Figure 5.15. The DcAFF material shows higher SBS strength than the short carbon fibre PLA-based materials. This should be the result of the long and aligned fibre in the HiPerDiF and the higher fibre content that strengthens the material, as seen in the tensile testing. DcAFF shows slightly lower properties compared to nylon/C.CF, *e.g.* Markforged. This is because of the different printing procedures of the Markforged which has dual nozzles feeding neat thermoplastic and impregnated fibre separately: the higher amount of thermoplastic on the outer specimen surfaces may enhance the raster fusion and increase the layer strength. Moreover, the continuous carbon fibre, the compatible fibre-nylon surface sizing, and the higher mechanical performance of nylon can also increase the strength of the material.

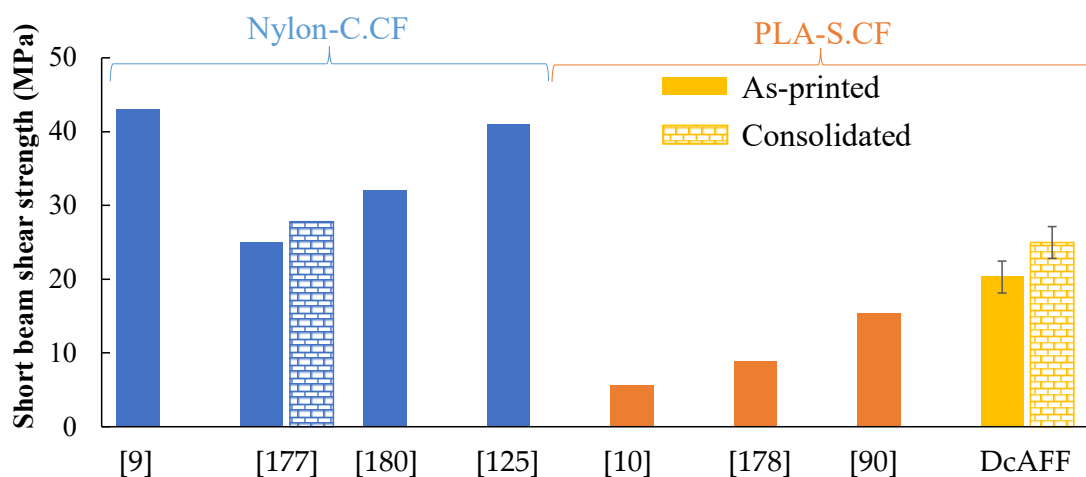


Figure 5.15 Comparison of the DcAFF SBS strength to other SBS testing in the literature of nylon-continuous carbon fibre reinforcement [9, 58, 125, 177] and PLA-short carbon fibre reinforcement [10, 90, 178].

5.5. Multilayer open-hole tensile testing

Open-hole tensile properties of the DcAFF were tested and compared to the single-layer part from Chapter 4. The aim of the testing is not only to examine the performance of raster bonds in the presence of stress concentration but to study the capacity of the steering of the new filaments for multilayer printing. In Chapter 4, it has been observed that the single-layer curvilinear 3D printed shape for open-hole tensile testing promoted a non-catastrophic failure, as the inter-raster breaks while the whole structure retained its continuity, this was not the case when the hole was obtained with a material subtraction method. As seen in the multilayer tensile testing in Section 5.3.2, multilayer 3D printing provides structural integrity that increases the overall mechanical performance of the part. Thus, the multilayer open-hole testing is expected to show some layer interaction that cannot be seen in the single layer. In this chapter, the open-hole sample was fabricated with a similar shape, curvilinear printing path, mentioned in Section 4.5.1 (Figure 4.12(b1) the 4C sample). The printing path was modified aiming to print the whole layer in one go without stopping by including curvilinear, short, and long linear rasters. The curvilinear printed path open-hole behaviour will be compared with a multilayer linear 3D printed specimen with a drilled hole in the middle. According to the claim from many papers [166, 168, 169], the curvilinear 3D printing path on the open-hole sample can provide composite steering with a higher fraction of continuous fibres aligned with the loading direction [166]. By contrast, the drilling will cut the fibre presenting a discontinuous load flow path. Hence, the curvilinear multilayer printed part is again expected to have a higher open-hole strength than the one where the hole has been obtained by drilling through continuously printed rasters.

5.5.1. Open-hole tensile specimen preparation and testing

5.5.1.1. Normal printing (OPH-N)

The curvilinear path was modified from the path in Chapter 4 to complete one layer without stopping. There are four curvilinear rasters with four free-end rasters on each quarter of the circle. The free-end-rasters, called short rasters, are extended to

attach to the circular curve to provide polymer adhesion. Eight straight rasters were built at the outer edge to strengthen the part. There are three superimposed layers of the same printing path. The curvilinear printing path and the printed sample are shown in Figure 5.16. The printed sample shows an eye-shape hole with a slightly smaller hole size than expected (~8 mm) due to the sliding of the raster on the printing bed as it is dragged by the nozzle during deposition. There are no important geometrical differences between the layers. The 3D printed part with the normal curvilinear, standard path, is called here “OPH-N”. There were four samples for this batch. The produced specimens' thickness and width were measured with a physical measurement, *i.e.* micrometre and calliper, while the hole size was measured *via* image processing of the scanned specimens. The average width, thickness and hole size were 25.87 ± 0.25 mm, 1.51 ± 0.11 mm and 6.25 ± 0.29 mm, respectively.

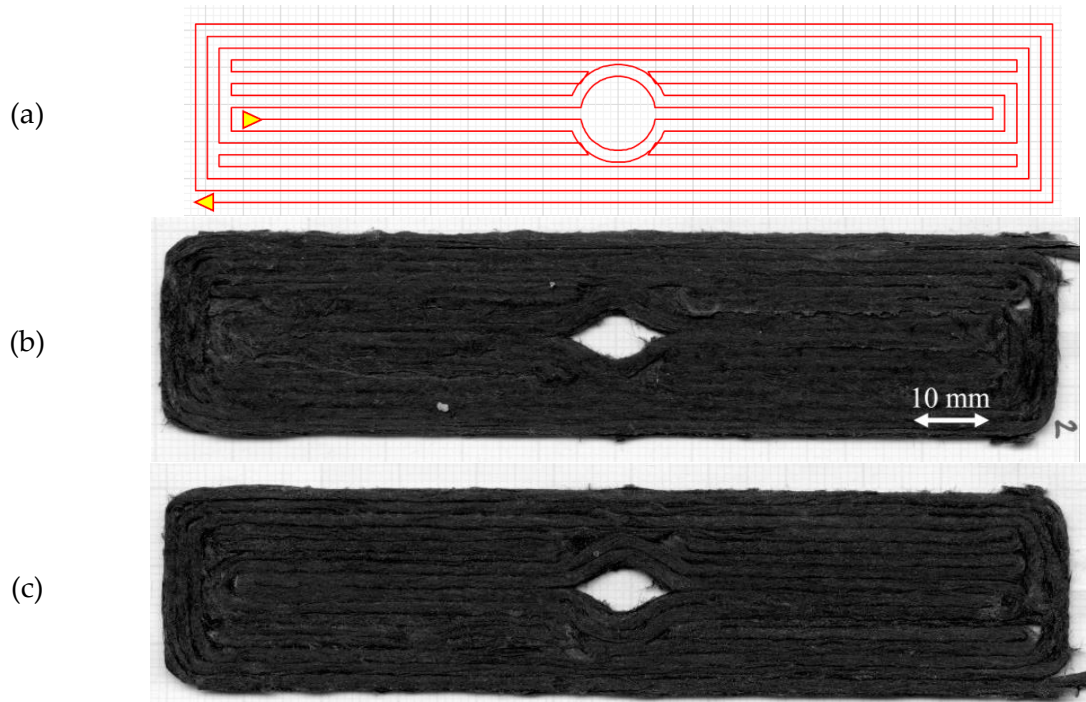


Figure 5.16 Normal curvilinear open-hole printing (OPH-N): (a) continuous printing path; (b) and (c) example of the printed sample on top and bottom (attached to bed) surface, respectively.

5.5.1.2. Modified printing path (OPH-M)

Owing to the poor hole shape, a modified path was introduced to improve the circularity of the hole and reduce the eye-shape effect. The movement of the raster

should be caused by the imperfect bonding between the deposited raster and the printing bed. This imperfect bonding may be because of the filleted nozzle that leaves a 2-mm gap between the centre of the nozzle (reference point) and the position where the flat-end filleted nozzle can provide full pressure onto the deposited raster to generate adhesion on the printing bed. The imperfect printing was expected to be cancelled out by modifying the printing path by moving the nozzle further inward towards the centre of the hole to provide more contact to the bed at the entry and exit of the circular section. The modified printing path is shown in Figure 5.17(a). The overshooting length is 2 mm according to the estimated gap of the filleted nozzle. The top and bottom surfaces of the printed part are shown in Figure 5.17(b) and (c).

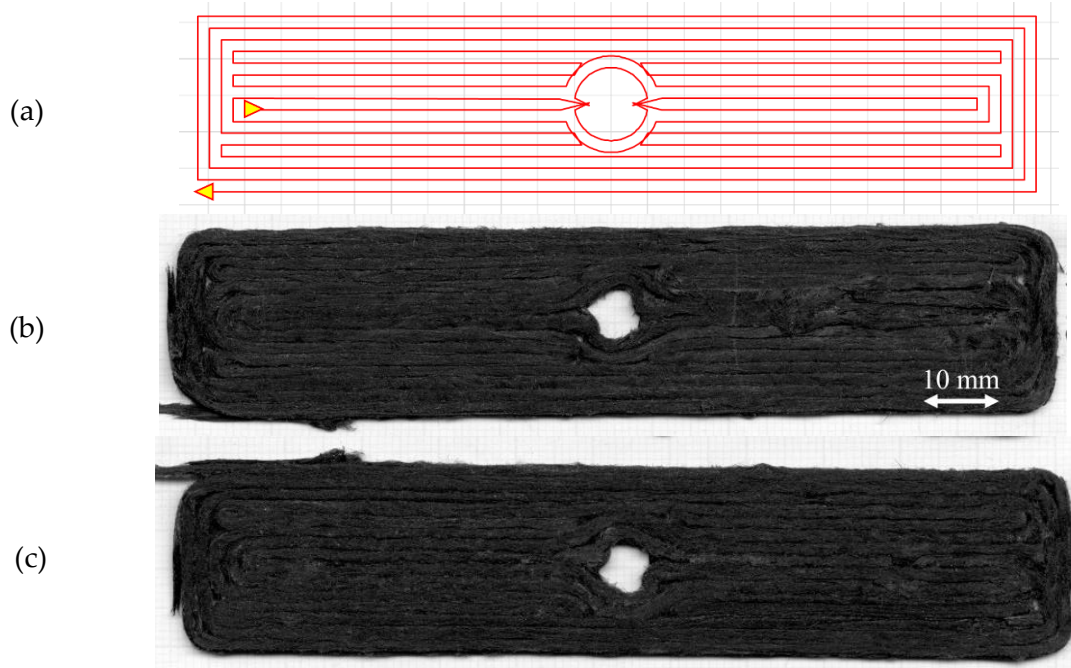


Figure 5.17 Modified curvilinear open-hole printing: (a) modified printing path with the overshooting inward through the centre of the hole; (b) and (c) example of the printed sample on top and bottom (attached to bed) surface.

The eye-shape corner at the attachment point disappears, but the hole is asymmetric due to the different behaviour between the movement at the entry and the exit of the circular section. This generates a sharp corner at the curvilinear entry, but a smooth curve at the exit due to the pulling on the raster because of the nozzle movement.

The hole size is still smaller than the expectation, but it is closer to a circular shape than normal printing. This open-hole printed part with the modified path will be called “OPH-M”. There were three samples in this batch. The average width, thickness, and hole size were 24.18 ± 0.17 mm, 1.42 ± 0.10 mm and 5.30 ± 0.97 mm, respectively.

5.5.1.3. Layup specimen with consolidation (OPH-D)

The 3D-printed open-hole will be benchmarked against the multilayer 3D printed with a drilled hole. The printing path is a concentric rectangular path, similar to the tensile specimen in Section 5.3.1, but this part has more rasters in the layer than the tensile specimen. There are 16 linear rasters on one layer with three superimposing layers. After the printing, the centre position was marked and the hole was obtained *via* drilling. A 6-mm diameter carbide drilling bit was used in this case. The cutting speed was set at 2000 rpm and the feed rate was 1 mm per min. The drilled sample is shown in Figure 5.18. The sample with a drilled hole will be called “OPH-D”. There were four samples in this batch. The width and thickness average across the sample were 26.03 ± 0.27 mm and 1.45 ± 0.08 mm, respectively. The hole size was precise at 6 mm.

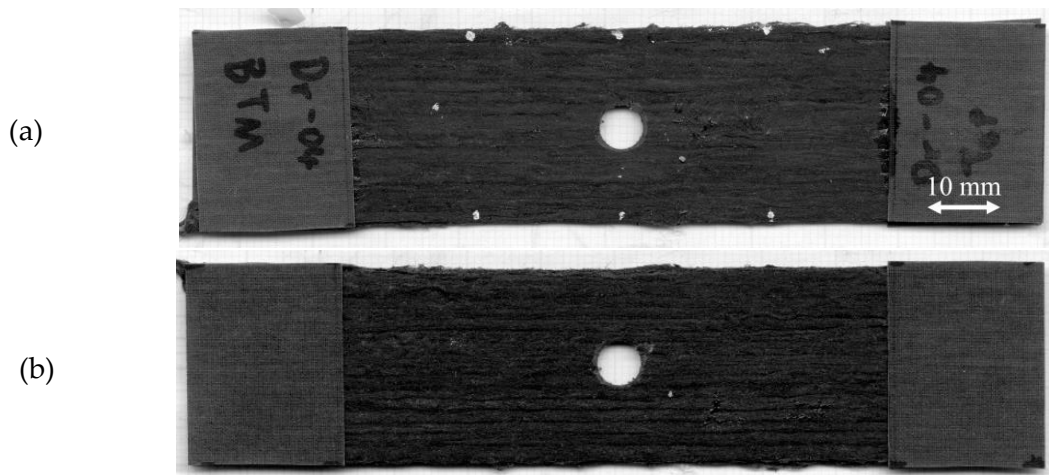


Figure 5.18 Drilled sample on three layers 3D printed part: (a) top side; (b) bottom (bed) side.

5.5.2. Open-hole tensile testing procedure

There are three testing cases: normal curvilinear printing (OPH-N), modified

curvilinear (OPH-M), and straight raster printed part with a drilled hole (OPH-D) with four samples for each testing case. All samples were completed with 20-mm long end tabs bonded to both ends. The tensile testing was performed with the same procedure and machine used for the tensile testing mentioned in Section 5.3.1. The strain was measured *via* digital image correlation (DIC) to obtain the strain map during loading. The DIC parameters are illustrated in

Table 5.3. The stress was calculated across the cross-section at the hole area and the presented strain was calculated along the longitudinal axis with the video extensometer feature of the DIC software.

Table 5.3 DIC technique parameters.

Software	Davis10.1.2	Image resolution	2466 x 2092 pixel
Camera & Lens	M-lite & 50 mm	Field of view	75.78 mm x 64.28mm
Correlation mode	Relative to first	Frame rate	1 image per second
Subset size	51 x 51 Pixel (1.6 mm x 1.6 mm)	Strain resolution	$2.33 \times 10^{-04} \epsilon$
Step size	2 pixel (0.061 mm)	Scale factor	32.54 pixel/mm

5.5.3. Open-hole tensile test result

The plot between open-hole stress, calculated across the hole section, *versus* the longitudinal strain of each specimen batch is presented in Figure 5.19(a)-(c). The stress-strain curve of the three groups is linear in the first part and the slope decreases near the maximum load. This is slightly different from the single-layer open-hole testing in Chapter 4: the multilayer has more linear behaviour than the single-layer one, and there is no load drop with increasing displacement. This may be because the multilayer, thicker cross-section, and good bonding between layers and rasters, allows to store more energy in the part. When the failure point is reached, the energy is released to the whole structure causing the whole part to fail rather than gradually sacrificing the weak inter-raster bonding as in the single layer open-hole part. The strength of the OPH-N multilayer is comparable with the single-layer 4-curvature samples (the similar printing path), around 80 MPa. The strength of the specimens printed with the standard path is slightly lower than those with the

modified one. This is because the modified path deposited slightly more material at the modified point than the standard printing. However, when comparing the three specimen groups shown in Figure 5.19(d), there are no statistical differences in the open-hole strength. The similar strength may be caused by the same amount of the continuous raster through the length of the specimen. There are four short linear rasters in the curvilinear part that are held to the other rasters by just the low-strength thermoplastic bonding. The number of short rasters is similar to the number of cut rasters due to the drill. Other printing procedures or post-printing processes may be considered to fill this gap, as seen in [166], and keep the number of continuous rasters as high as possible.

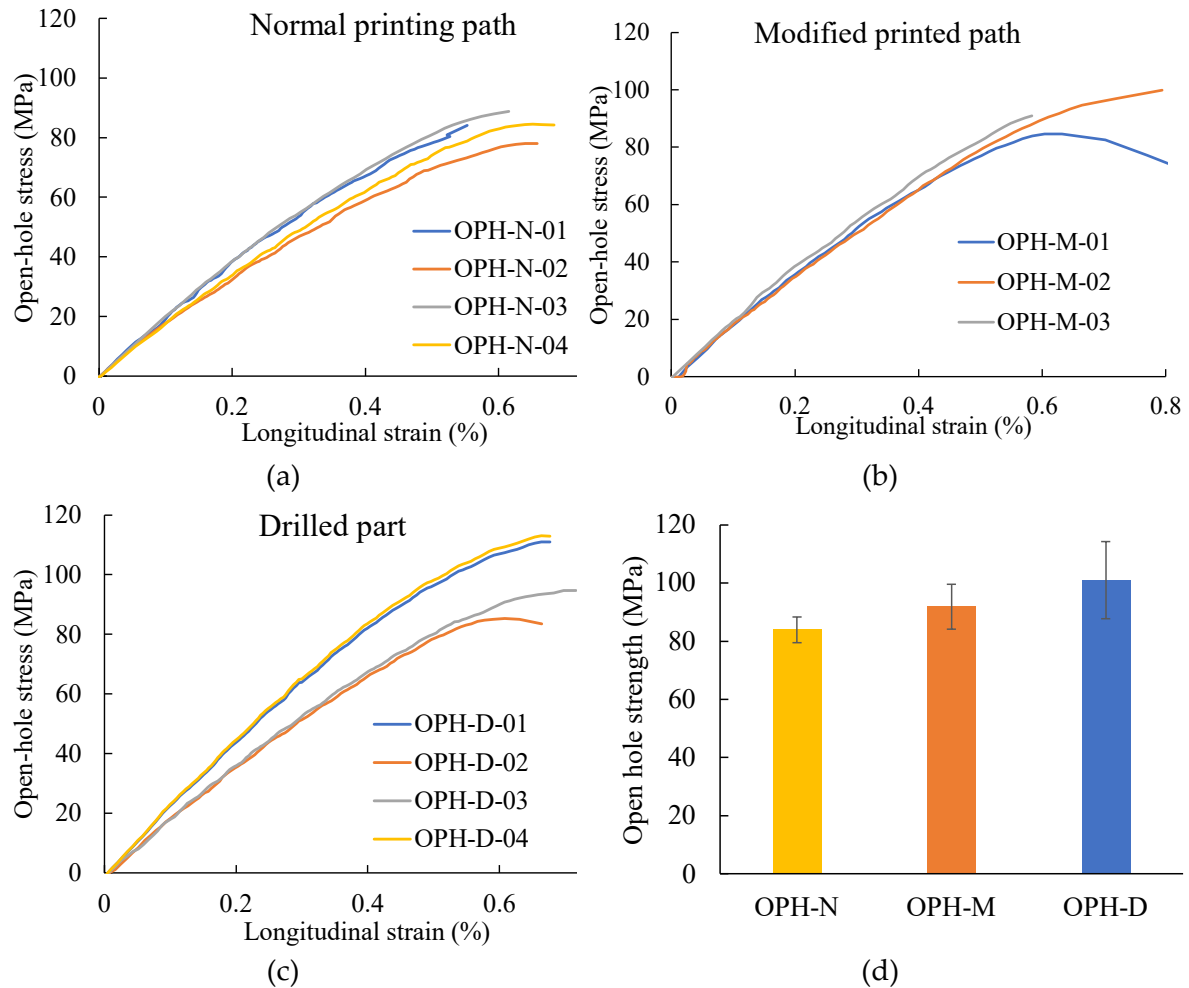


Figure 5.19 Open-hole tensile stress-strain curve of: (a) OPH-N; (b) OPH-M; (c) OPH-D; (d) open-hole strength comparison between three groups of the sample.

The local strain map at the maximum load of each sample of the three groups for longitudinal (ϵ_x), transverse (ϵ_y), and shear (ϵ_{xy}) strains are shown in Figure 5.20-5.22.

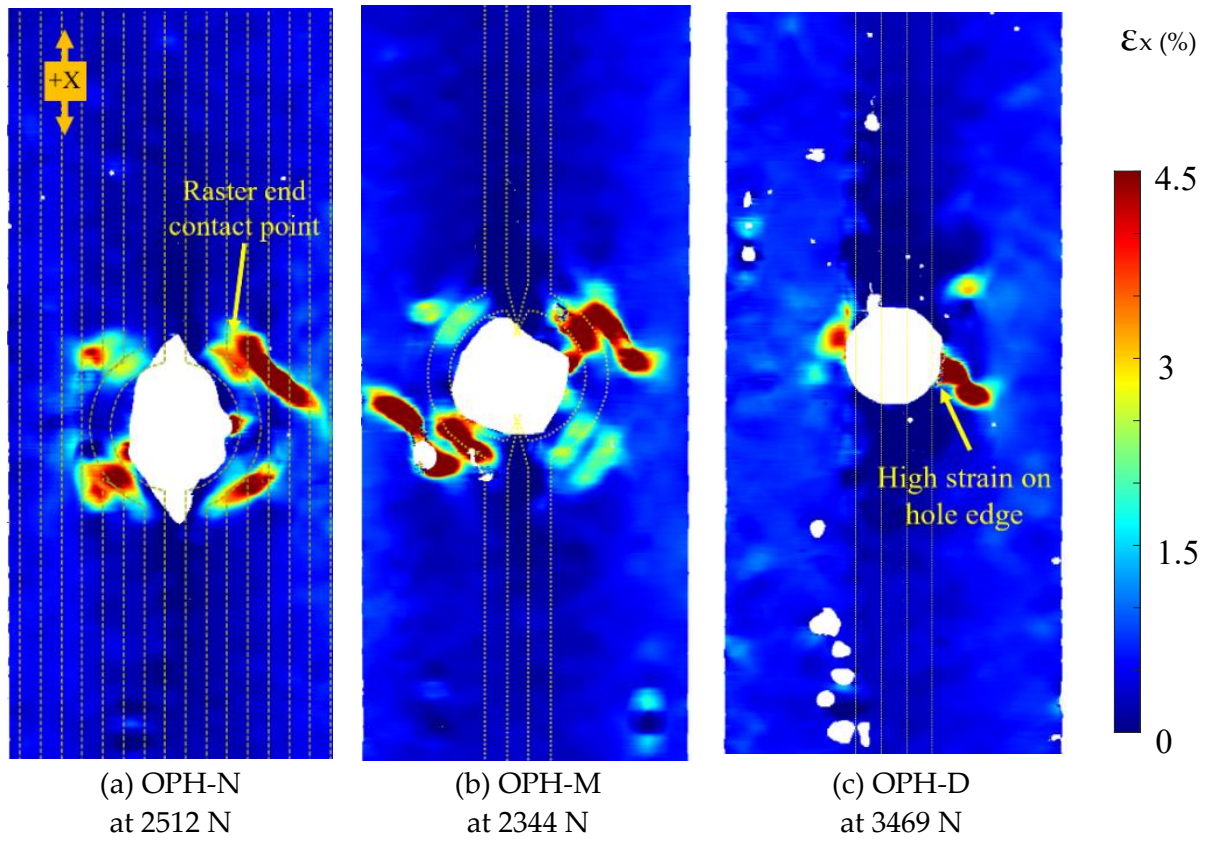


Figure 5.20 DIC strain map in longitudinal (ϵ_x) at the maximum load of each sample: (a) OPH-N; (b) OPH-M; (c) OPH-D.

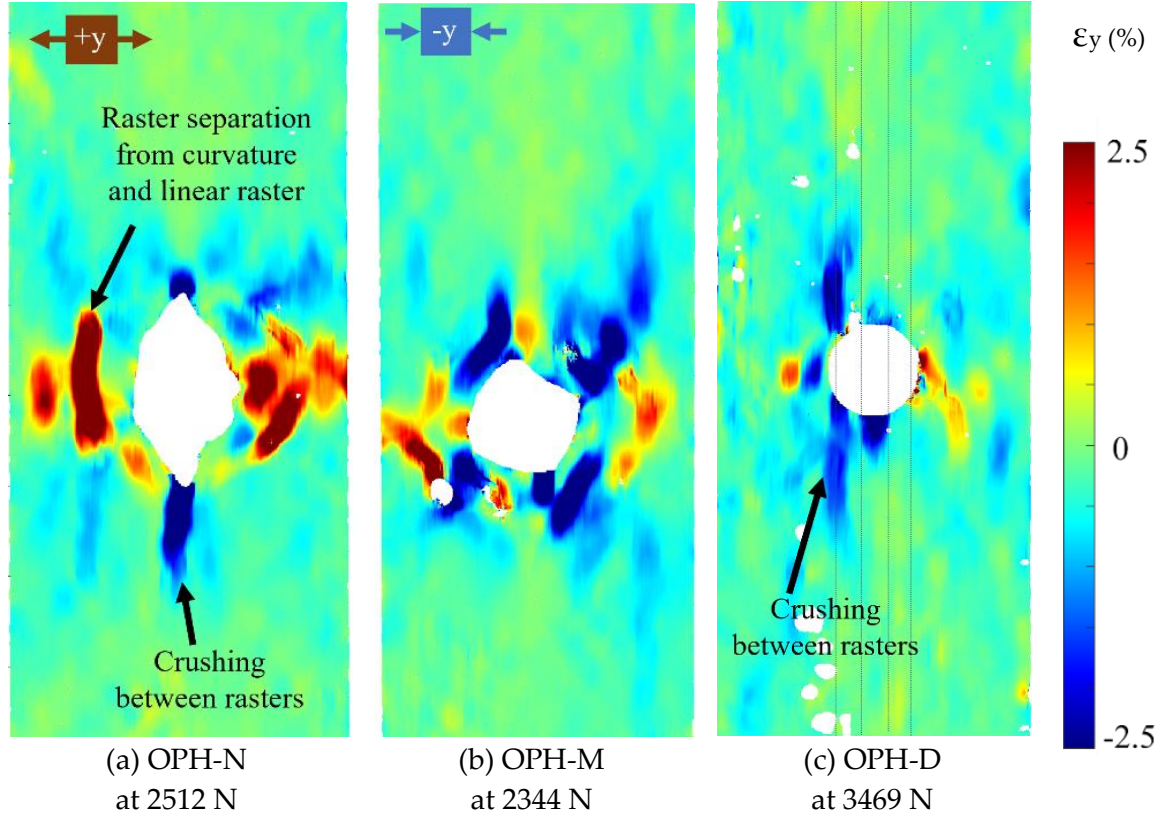


Figure 5.21 DIC strain map in transverse (ϵ_y) at the maximum load of each sample: (a) OPH-N; (b) OPH-M; (c) OPH-D.

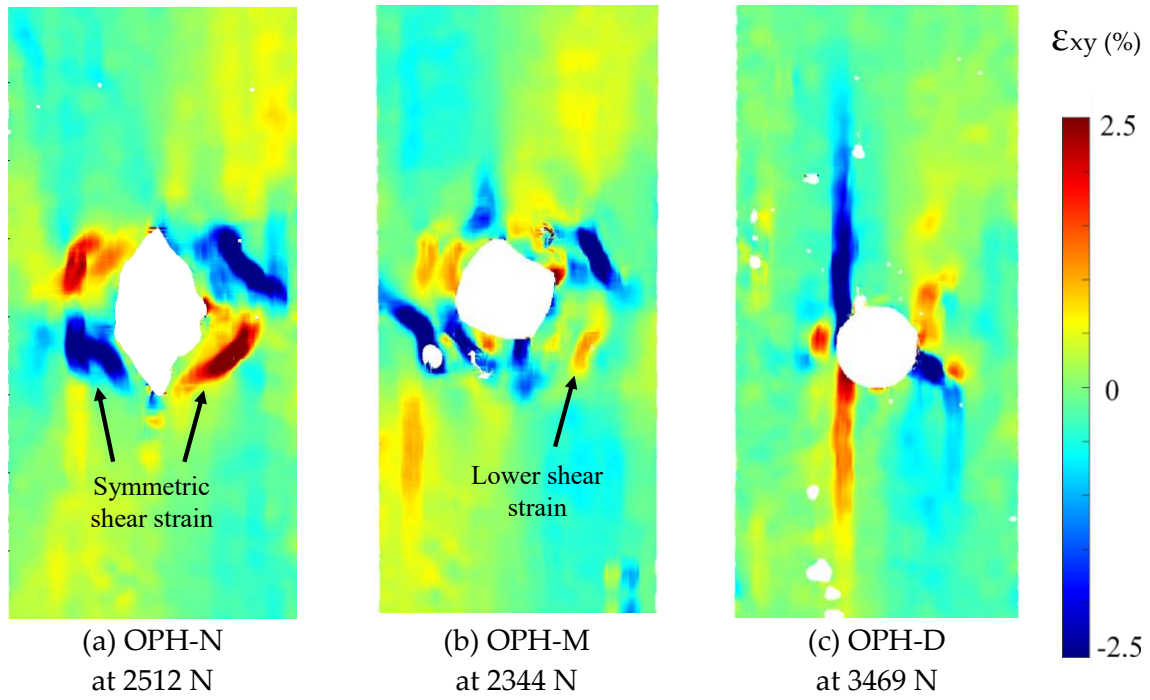


Figure 5.22 DIC shear (ϵ_{xy}) strain map at the maximum load of each sample: (a) OPH-N; (b) OPH-M; (c) OPH-D.

In the OPH-N sample, there is a high longitudinal tensile strain at the contact points between the short raster and the curvilinear section, in Figure 5.20(a). This is caused by the separation of the thermoplastic adhesion of the short rasters from the attached point on the curvilinear section. A separation between the curvilinear rasters is also found, but it is a lower longitudinal strain than the linear contact. This is because of the worse bonding at the short-raster-end contact point than at the side-by-side raster. In the transverse direction (ϵ_y), Figure 5.21(a) shows a high tensile strain on the hole side where the linear raster attaches to the curvilinear raster. As a result of the low contact area at that point, the linear raster tends to separate from the curvilinear section. There is also a compression strain between the two attached middle rasters at the sharp corner of the eye-shape hole caused by Poisson's ratio effect. In Figure 5.22(a), the OPH-N shows a symmetric shear strain between two halves of the hole caused by the separation of the short rasters from the curvilinear contact point.

In the modified path (OPH-M) sample, the longitudinal strain distribution, Figure 5.20(b), is asymmetrical around the hole. There is a high tensile strain on the

curvilinear entry side that has a higher bending angle than the exit which has higher curvature. The high bending angle accumulated high stress at the turning corner while the curvilinear section has less stress accumulation. This presents as the different strain map on the opposite quarter of the circle. A high compression strain in the transverse direction is observed in Figure 5.21(b) as a result of the tensile strain in the longitudinal direction. The short raster separation presents a high tensile strain in the transverse direction on the bottom left quarter. Unlike the OPH-N sample, the OPH-M, shear strain distribution is asymmetric, as seen in Figure 5.22 (b), presenting different strain distributions on each quarter of the hole, due to the asymmetric hole shape described above.

In the drilled sample (OPH-D), the longitudinal strain accumulated at the hole edge, as seen in Figure 5.20(c). This can be the cut of the raster that splits the rasters on the hole edge which is the weakest point in the part. In the transverse direction, the remarkable strain is the compression strain between the rasters on the left of the hole, as observed in Figure 5.21(c). This is the result of the high tensile strain in the longitudinal direction on the right of the hole that reflects the crushing on the left as a hinge point in the structure. At this high strain point, the rasters may have poor adhesion, or the drill cut through the raster reducing raster strength.

The failed samples, shown in Figure 5.23, comply with the strain map result. In the OPH-N sample, Figure 5.23(a), the crack started from the contact point of the short linear rasters and then it progressed through the diagonal direction producing a 45° failure on the opposite quarters due to the high shear strain, Figure 5.20(c). The breakage also ran through the curvilinear rasters after the initial failure. There is also a raster separation between the curvilinear rasters. In the OPH-M sample, the crack is similar to the OPH-N, but the final breakage is the linear breakage of the linear rasters, as seen in Figure 5.23(b). This is because the high strain progressed from the short raster contact point. The printed part can hold the structure together after the breakage. On the other hand, the drilled part (OPH-D) has a breakage through the

hole perpendicular to the load direction, as seen in Figure 5.23(c), especially on the right of the hole, according to the high tensile strain in the longitudinal direction presented in Figure 5.20(c).

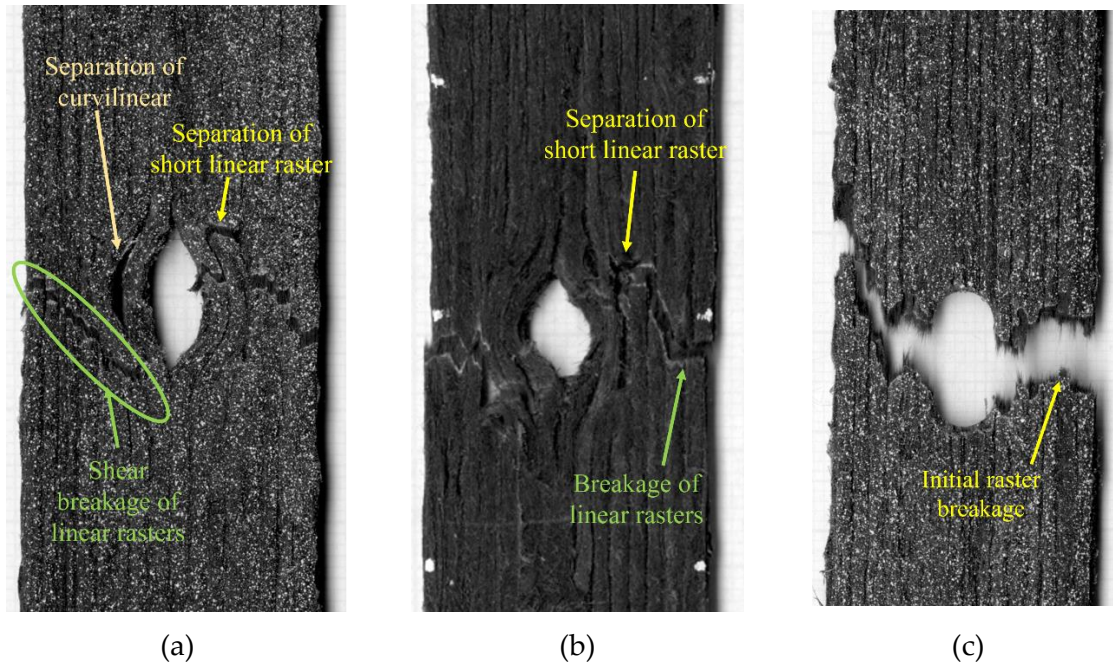


Figure 5.23 Open-hole tensile testing breakage sample: (a) OPH-N; (b) OPH-M; (c) OPH-D.

5.6. Chapter conclusion

In this chapter, other 3D printing aspects of DcAFF, especially the interaction between layers, were studied for the first time in this thesis. This is thanks to the development of the third-generation HiPerDiF machine that allows for a higher DcAFF production rate. Some key findings in this chapter are concluded below:

- The full-part multilayer printing enhanced the bonding between the adjacent rasters delivering structural integrity resulting in higher tensile properties compared to the single-layer printing in Chapter 4. Such integrity is achieved through layer nesting and filling the inter-raster space by the adjacent plies. Both the DcAFF single-layer and multilayer prints show higher tensile properties than other PLA-composite 3D printing studies, particularly the continuous fibre composites, even when normalised at the same fibre weight content. In addition, the stiffness of the DcAFF is at a similar level to the continuous carbon fibre Markforged 3D printed part. This is because of the alignment and the use of

discontinuous fibres that give properties comparable to those of continuous fibre. The tensile properties can be increased further with the post-printing consolidation under heat and pressure.

- The SBS testing was performed to show the interlayer properties of the material and the 3D-printed part. The layer properties again can be increased with the post-printing consolidation that compacted the layer structure. Although there is no clear evidence of the interlaminar failure at the middle surface due to the high ductility of the as-printed material, the DcAFF shows a superior SBS strength to other carbon fibre PLA 3D printed parts from the literature.
- The more complex structure printed part as the open-hole multilayer tensile printing was performed compared to the single-layer open-hole in Chapter 4. Although the curvilinear OPH printing part provides no significant strength improvement compared to the drilled sample, it shows a different failure behaviour as the structure retained its continuity and carried the load for a period after initial breakage similar to the behaviour of the single-layer OPH sample in Chapter 4.
- Overall, the three different mechanical tests of the full multilayer part printed with DcAFF show the DcAFF material properties and the potential to study further or scale up the DcAFF material to a commercialisation phase.
- One serious problem in this stage of the 3D printing filament development can be seen in the complex geometry printing, *i.e.* the open-hole samples. The deposited rasters deviated from the defined path creating an eye-shaped hole instead of a perfectly circular one. This poor printing accuracy causes an incorrect in-plane shape. The discrepancy may be the result of (i) the poor bed adhesion, (ii) the too-tight turning radius of the printing path for the stiff 3-mm-long fibre in the 1 mm diameter composite filament and (iii) the design of the nozzle with the filleted end. In the next chapter, several printing techniques will be introduced to increase the printing accuracy of DcAFF.

Chapter 6 Printing Accuracy Improvement

Accurate printing of DcAFF poses a challenge, especially for complex geometries, because: (i) there is a discrepancy between the path where the filament experiences the adhering pressure from the filleted nozzle and the nozzle path; and (ii) the rasters display poor adhesion to the printed bed after deposition, which causes the filament to be dragged when the printing direction changes. This chapter explains the implication of these phenomena on steering capabilities and examines the techniques for improving the accuracy of DcAFF printing that may be possible to apply to other continuous fibre printing.

The chapter on the printing accuracy improvement was composed using elements of the work published in *Materials* in 2023 under the title of “Steering Potential for Printing Highly Aligned Discontinuous Fibre Composite Filament” [5]. The conceptualisation of the printing path modification algorithm, obtained by adding compensation coordinates, was formed by N.K., D.N., B.W, M.L. and the code was constructed by D.N. while the experimental results were prepared by N.K. The whole paper was amended by all authors.

N. Krajangsawadi, D. H. Nguyen, I. Hamerton, B. K. Woods, D. S. Ivanov, and M. L. Longana, "Steering Potential for Printing Highly Aligned Discontinuous Fibre Composite Filament," *Materials*, vol. 16, no. 8, p. 3279, 2023. DOI: 10.3390/ma16083279.

6.1. Chapter introduction

Several studies have noted that the current FDM 3D printing procedure, which deposits the molten thermoplastic following the defined path convert directly from the CAD model, creates some geometrical inaccuracy [16, 24]. There is an intrinsic inaccuracy associated with 3D printing when the printed features exhibit a steep change in printing direction and when the radius of curvature of the printed path is comparable with the characteristic dimensions of filaments [181, 182]. In neat thermoplastic 3D printing, Ai *et al.* [183] suggested that imperfection in 3D printing can be caused by the shrinkage or crystallization of the polymer. These defects can be very small and visually undetectable. Furthermore, introducing fibre reinforcement to the thermoplastic reduces the printability of thermoplastic and the dimensional accuracy because of (i) the finite stiffness of fibres [43], and (ii) worse adhesion of the filament to the substrate. This is reflected by the fact that 3D printing of continuous fibre has a worse potential for steering on curved or angular trajectories compared to neat polymer and short fibre reinforced filaments [182]. The reinforced filaments are also prone to defects associated with the mechanical behaviour of the reinforcement, *i.e.* twisting and folding of filament, when printing tight radius curvatures [181, 184, 185].

The previous chapters, as well as the literature on relevant subjects, did not examine the printability of DcAFF in full. In Chapters 4 and 5, DcAFF was printed into an open-hole specimen with a defined curvilinear printing path combining straight-line printing with half circles. The printing accuracy was found to be relatively low: it can be seen in the curvilinear printing of 10-mm diameter, Figure 6.1(a), that the hole size (from the middle of the top and bottom rasters) is smaller than the desired path (10 mm) and the transition from linear to the circular path created a deviation from the programmed raster trajectory, giving an eye-shape to the hole. Although in Chapter 5, an empirical path modification was attempted by moving the nozzle further inward the circular radius to reduce the eye shape at the turning corner (Figure 6.1(b)), the hole remained asymmetrical (not circular as per design) due to

the nozzle dragging the printed raster. This highlights the need for further studies to improve printing geometry accuracy.

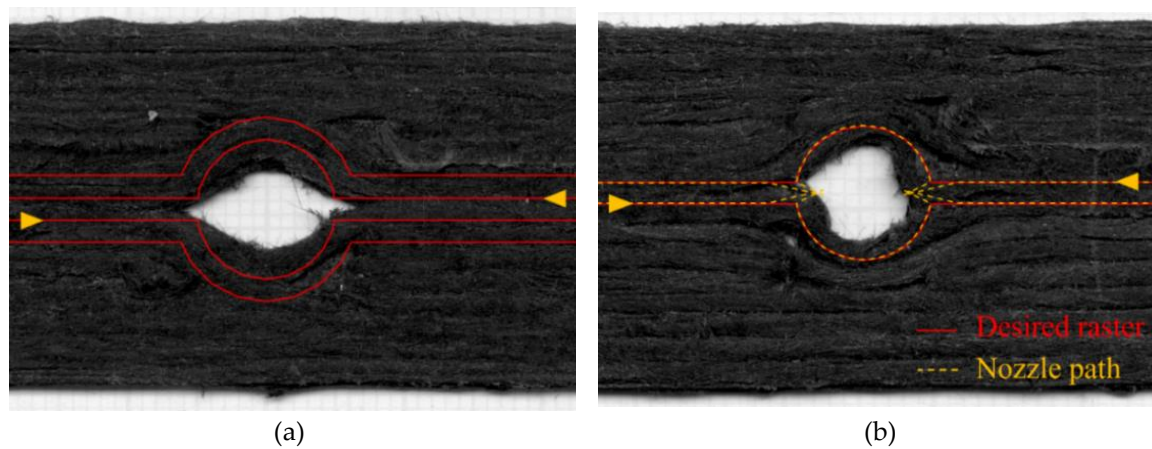


Figure 6.1 (a) Open hole printed part with normal curvilinear printing path; (b) open hole printed part with an empirical printing path modification (Chapter 5) by moving the nozzle further inwards.

In the literature, various mathematical models have been constructed to understand fibre printing defects and the deviation from the desired path. For instance, Matsuzaki *et al.* [181] studied the performance of continuous carbon fibre impregnated with ABS by printing a circular raster at different radii and found a twisting of fibre during steering resulting in a smaller radius than the defined path. Based on the experiments, they presented two mathematical models, twisting (where fibre twists and folds back around the curved steering) and path length difference (where the fibres overcome the bed adhesion and move from outside to inside the curvature), to explain the behaviour of the fibre printing and predict the actual printed radius when printing a circular path at different radii with stiff continuous fibre. With the advancement of automation technology, real-time monitoring and machine learning were introduced to 3D printing to detect the printing defect and modified the printing process, *e.g.* adjusting printing parameters or printing path, so that the printing accuracy and quality can be improved. With neat polymer printing, Delli and Chang [186] used a camera to capture the printing and detect the defects in the semi-finish part. Then, the images were analysed with a supervised machine learning method, support vector machine (SVM), to classify

the printing and discard them when the defect was detected. Instead of pausing to take a single shot image, Jin *et al.* [187] installed a real-time video camera to monitor the printing and then the images were fed to a model, a trained machine learning algorithm, to find the printing defect. If an issue is detected, *e.g.* over or under extrusion, there is a command to automatically and instantly adjust the printing parameters *e.g.* feed rate and layer thickness in the 3D printer controlling unit. This method is faster than human interaction. A similar idea was adapted to continuous fibre printing proposed by Lu *et al.* [188]. A high-resolution video camera was attached to the 3D printer for real-time defect detection, and then training and supervised deep learning was performed leading to closed-loop self-adjusting printing parameters to reduce defects, *i.e.* fibre misalignment and the abrasion between rasters.

This chapter aims to explore the routes for improving the printing accuracy of DcAFF material. In a first attempt, additional printing actions, *i.e.* the adjustment of the printing parameters, have been coded using a computer numerical control (CNC) programming language. In a second attempt, the initially desired raster has been modified using the instrumentarium of Proportional-Integral-Derivative (PID) control to compensate for the expected discrepancy between the desired and predicted paths. A PI controller was applied to generate a compensated printing path. The results of this modification will be benchmarked against nominal printing for the cases of the corner sections and a 10-mm diameter curvilinear open-hole sample.

6.2. Material and printing methodology

The DcAFF material used in this chapter is the same batch as the one in Chapter 5, produced with the HiPerDiF-3G machine and passed to the DcAFF machine to form the circular shape DcAFF filament. The filament has a nominal diameter of about 0.8 mm and the fibre content ranges between 20 and 30 wt%. The 3D printer, nozzle replacement, and printing setup are the same as those presented in Chapter 5: nozzle

temperature 210°C, bed temperature 80°C, nozzle moving speed and material feed rate 300 mm/min, set nozzle height 0.3 mm, raster gap 1.6 mm and using blue masking tape for the 3D printer to increase the bed adhesion.

6.3. Dimension accuracy study

The dimensional accuracy of the DcAFF filament was investigated by printing circles with different radii, from 5 to 20 mm with linear entry and exit. The nozzle path is defined incrementally, in a series of discrete linear steps following the circle contour. Representative results of the printed rasters are shown in Figure 6.2. It can be seen that the sharp change of path, such as at the entry and exit of the circular part, creates a triangular space between the entering and exiting rasters or fibre bridging between the circular and straight segments. In addition to these artefacts, the circle diameter (the centre of the raster is used for its measurements) is slightly smaller than the defined diameter, the difference ranges from ~4% in the large circular radius (20 mm) to 20% in the small radius (5 mm). The poor dimensional accuracy is caused by the nozzle geometry, the property of the filament, and the adhesive property between the filament and the substrate. The nozzle is filleted, which aims to offer a gentle direction change to the filament of being deposited from vertical in the nozzle to horizontal on the bed without breaking the fibres. Due to the limited stiffness of reinforced filament, this results in a small gap between the deposited material and the bed, as sketched in Figure 6.3, which will affect the adhesion of the deposited raster. The point of pressure applied by the nozzle is offset from the centre of the nozzle which follows the nozzle path. The location of the pressure application changes depending on the angle of the deposition and does not match the position where maximum adhesion needs to be achieved.

The second aspect of the problem is the behaviour of the deposited filament. To hold the filament in place, a sufficient adhesion bond must be formed. This requires longer processing times and higher pressure of the nozzle at the nip point. If the bonding is not fully formed, then bending stresses built in the reinforcements drive

the filament from the desired path.

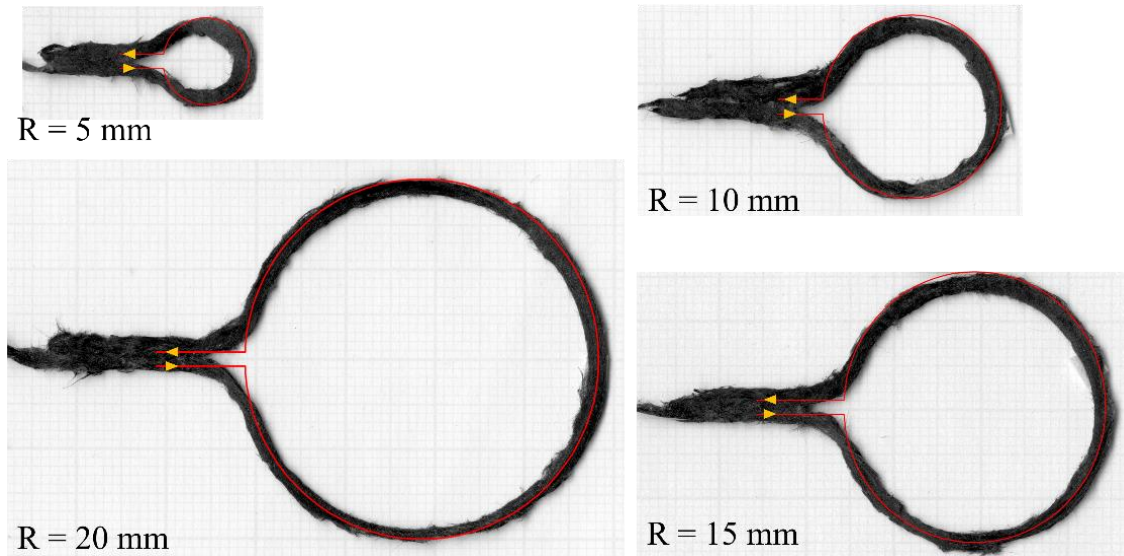


Figure 6.2 Deposited rasters at different radii from 5 - 20 mm presenting with the desired path (red line), same as the nozzle path, to show the dimension accuracy.

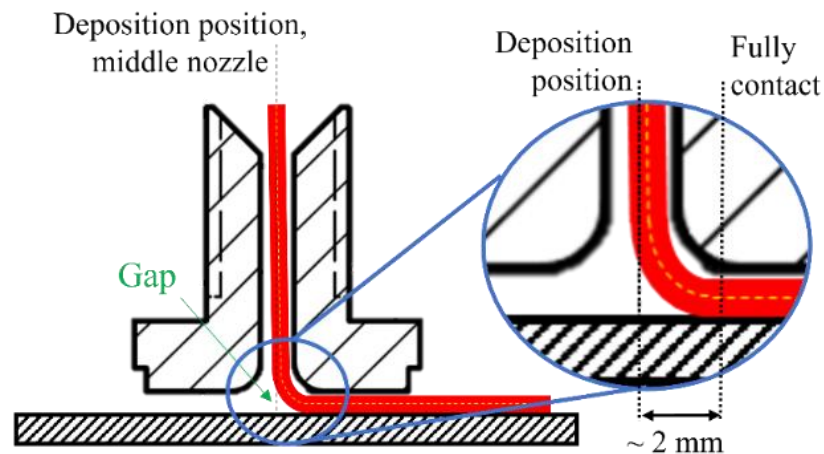


Figure 6.3 Gap between the filament and the bed because of the nozzle fillet end creating an offset of full contact position and the deviation of filament to the vertical middle line of the nozzle due to the smaller filament diameter than the nozzle diameter.

6.4. Printing modification by tuning printing parameters

As highlighted in the previous section, the location where the desired path and printed raster diverge the most in correspondence to the sharp direction change between the straight segment and the curved one. This can be simplified into a 90° turning point. This section will, therefore, focus only on sharp turning angles, and describes the first attempt to correct the poor printing at the 90° turning corner

without changing the nozzle path, in this case, the nozzle path coincides with the desired geometry. This will study only the modification of the printing parameters to build more adhesion to a specific point which is expected to reduce the gap created by a 90-degree corner turn. The desired raster and the nozzle path are the same as a 30 mm x 30 mm square with one loop raster. Generally speaking, there are three possible additional printing actions: (i) slow down in the vicinity of the corner to increase adhesion time; (ii) pause the movement at the corner; (iii) increase applied pressure by moving the nozzle downwards. It is possible to create combinations of these three actions in a single run, so the tested cases (shown in Table 6.1) are:

- P1: reduce the print speed from 300 mm/min to 200 mm/min at 5 mm before the corner and accelerate to 300 mm/min at 5 mm after the corner;
- P2: pause at the corner for 1 second before moving forward;
- P3: reduce the nozzle height (stamping) from 0.3 to 0.2 mm at the corner;
- P4: reduce nozzle height to 0.2 mm at 5 mm before the corner and rise back to 0.3mm at 5mm after the corner;
- P5: same as P4 plus reducing speed from 300 mm/min at 5 mm before the corner to 200 mm/min at the corner and rise back to 0.3 mm height at 5 mm after the corner with the increasing speed back to 300 mm/min.

Table 6.1 Printing parameter adjustment to tackle the 90° turning corner.

	Speed (mm/min)			Nozzle height (mm)		
	5 mm before	At corner	5 mm after	5 mm before	At corner	5 mm after
P1	300	200	300	0.3	0.3	0.3
P2	300	0 for 1 sec*	300	0.3	0.3	0.3
P3	300	300	300	0.3	0.3 → 0.2**	0.3
P4	300	300	300	0.3	0.2	0.3
P5	300	200	300	0.3	0.2	0.3

* Pause for 1 sec at the corner

** Stamping at the corner (reduce height 0.3 to 0.2 mm)

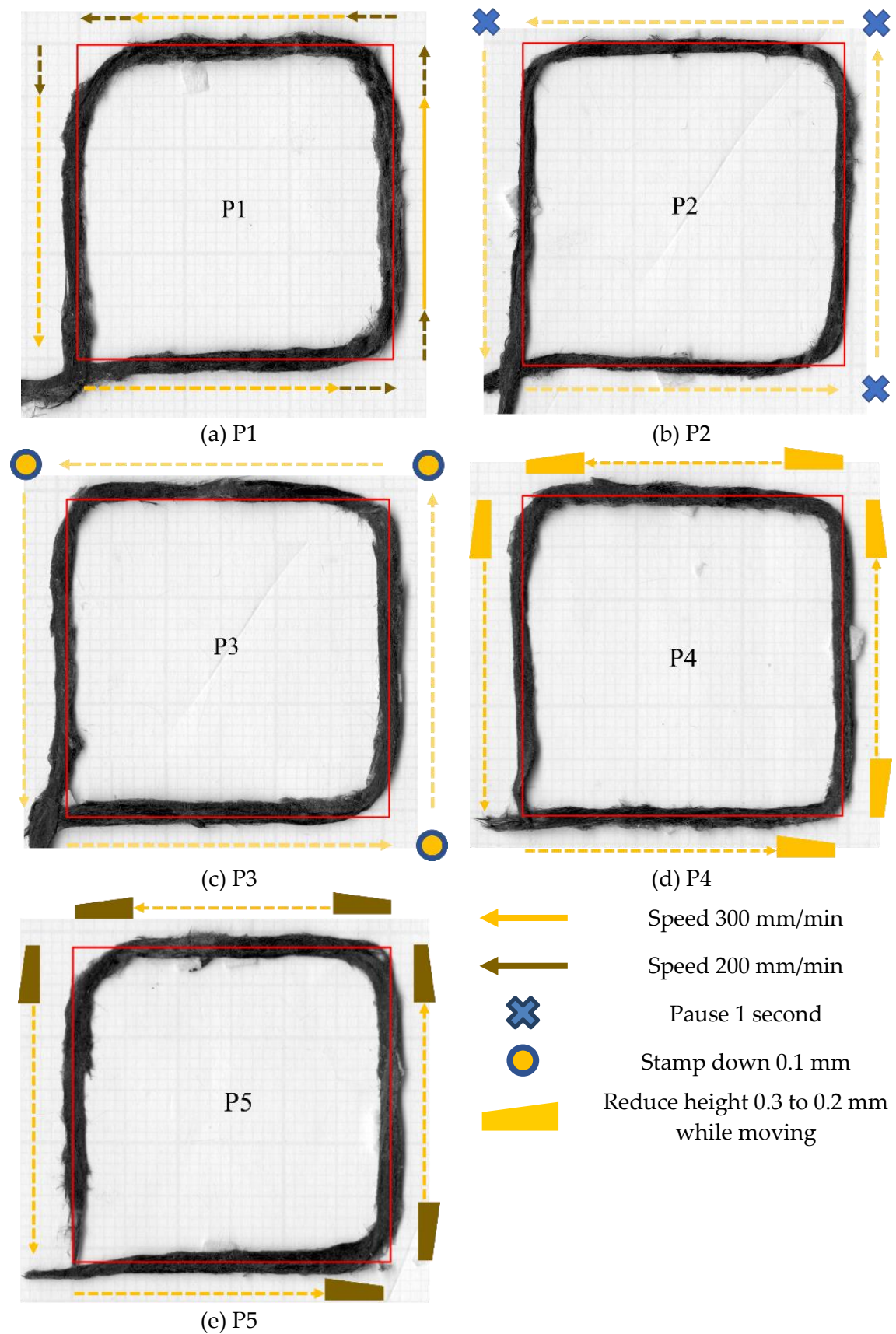


Figure 6.4 Additional machine actions to increase the printing accuracy following the P1 to P5 described above.

Figure 6.4 shows the rasters deposited using the modified actions. It is evident that none of the proposed modifications achieved the required adhesion to eliminate the fibre bridging at the corner. The important contributor to this is the lack of pressure in the centre of the filleted nozzle due to the gap described above (Figure 6.3). Irrespective of bonding time and applying pressure by the entire nozzle, the pressure at the nip point cannot be sufficiently built. That causes an imperfect bonding of the raster to the bed at the turning position: the unbonded deposited raster was dragged by the nozzle when it suddenly changed the printing direction. Hence, simple modifications of the printing parameters alone cannot provide good printing accuracy. A different method to reduce the corner gap by adjusting the nozzle path is needed.

6.5. Printing modification by adding compensation coordinates

6.5.1. Algorithm development

Section 6.3 has highlighted the challenges of printing along a defined path due to the discrepancy between the centre nozzle position (nozzle path) and the raster-surface contact point. Generally, the “(initially) desired path” is directly converted into the “nozzle path” by the G-code generator and then printed to obtain the “deposited raster”. Owing to the low deposition accuracy of the deposited raster, the nozzle path needs a compensation feature to correct the printing path for any turning angle.

The first step to build the compensation algorithm is to numerically model the nozzle-raster lag. It is noted that any step change in the nozzle travel direction requires some time for the raster to ‘catch up’ before they both travel in the same direction again. This relationship resembles a first-order lag, approximated by Equations (6.1) and (6.2):

$$\dot{x}_{predicted} = \tau(x_{nozzle} - x_{predicted}) \quad (6.1)$$

$$\dot{y}_{predicted} = \tau(y_{nozzle} - y_{predicted}) \quad (6.2)$$

where x_{nozzle} and y_{nozzle} are the x- and y-coordinate of the nozzle centre (in mm). Movement of the nozzle *via* x_{nozzle} and y_{nozzle} will result in the raster being printed

at locations with coordinate $x_{predicted}$ and $y_{predicted}$. Their time derivatives $\dot{x}_{predicted}$ ($\frac{dx_{predicted}}{dt}$) and $\dot{y}_{predicted}$ ($\frac{dy_{predicted}}{dt}$) represent the component of predicted velocity, and τ is an empirically-derived constant (in s^{-1}). The block-diagram representation of this first-order lag is shown in Figure 6.5(a). This simple approximation is only valid when the nozzle velocity is constant, which was kept at 5 mm/s in all experiments.

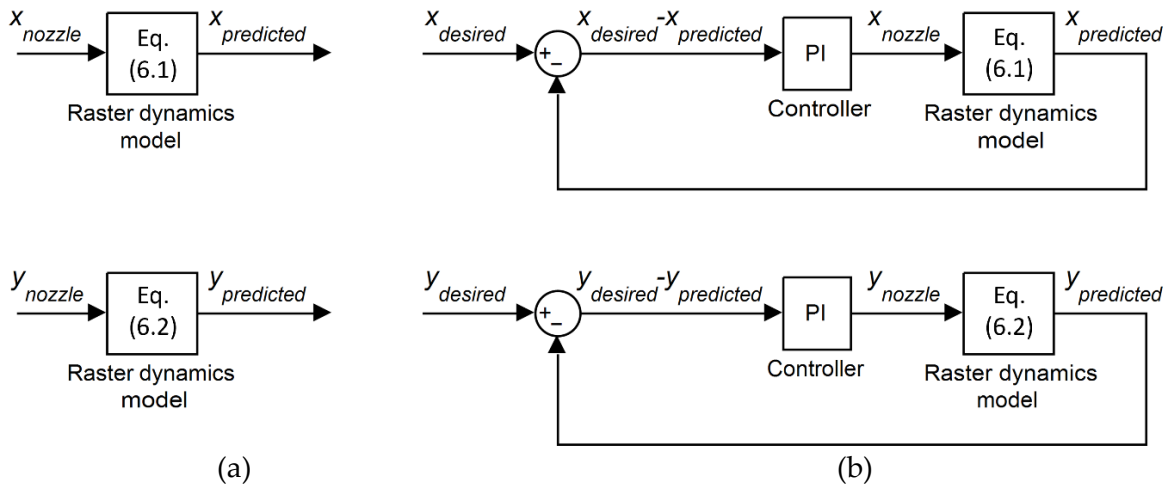


Figure 6.5 Schematic of the raster dynamics simulation (a) without; (b) with proportional and integral (PI) compensation.

The value of τ was empirically derived by comparing the predicted movement (Equations (6.1) and (6.2)) with the actual deposited paths in printing trials. Since the algorithm should be able to improve the accuracy for any turning angle, these trials are not only performed on the 90° turning case mentioned in the previous section, Figure 6.6(a), but also on other representative turning angles, represented by an acute angle (45° turning) and an obtuse one (135° turning), Figure 6.6(b). Then, numerical simulations were conducted with different values of τ until a good match between simulation and experimental results (Figure 6.6) was achieved. This approach results in $\tau = 1.25 s^{-1}$ that the predicted one matches to both 90° and 135° - 45° cases. Simulation result of the nozzle and predicted path based on Equations (6.1) and (6.2) using $\tau = 1.25 s^{-1}$ is shown in Figure 6.7(a) which can be seen that the predicted path are similar to the actual deposited in Figure 6.6.

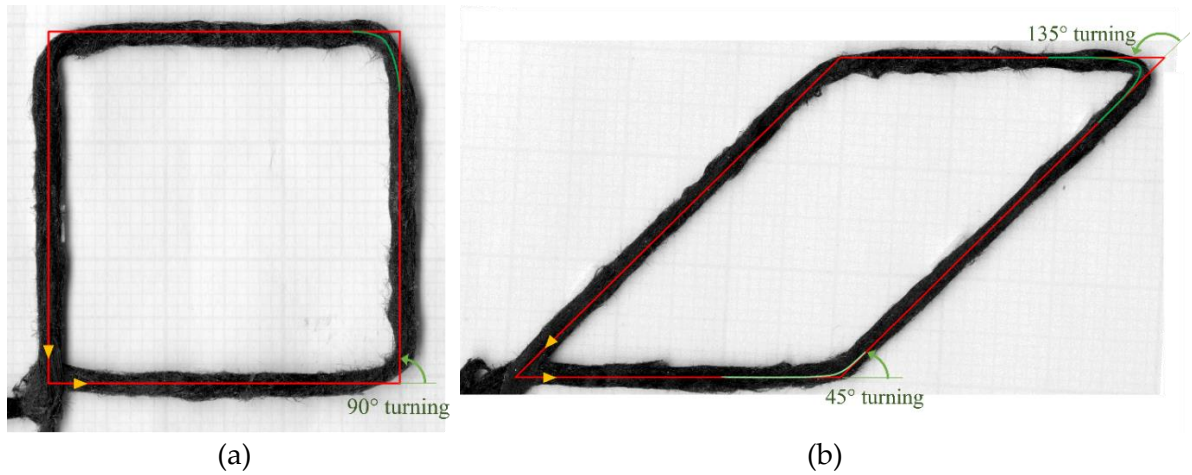


Figure 6.6 Preliminary shape study (before compensation): (a) 90° square; (b) parallelogram 135° - 45°.

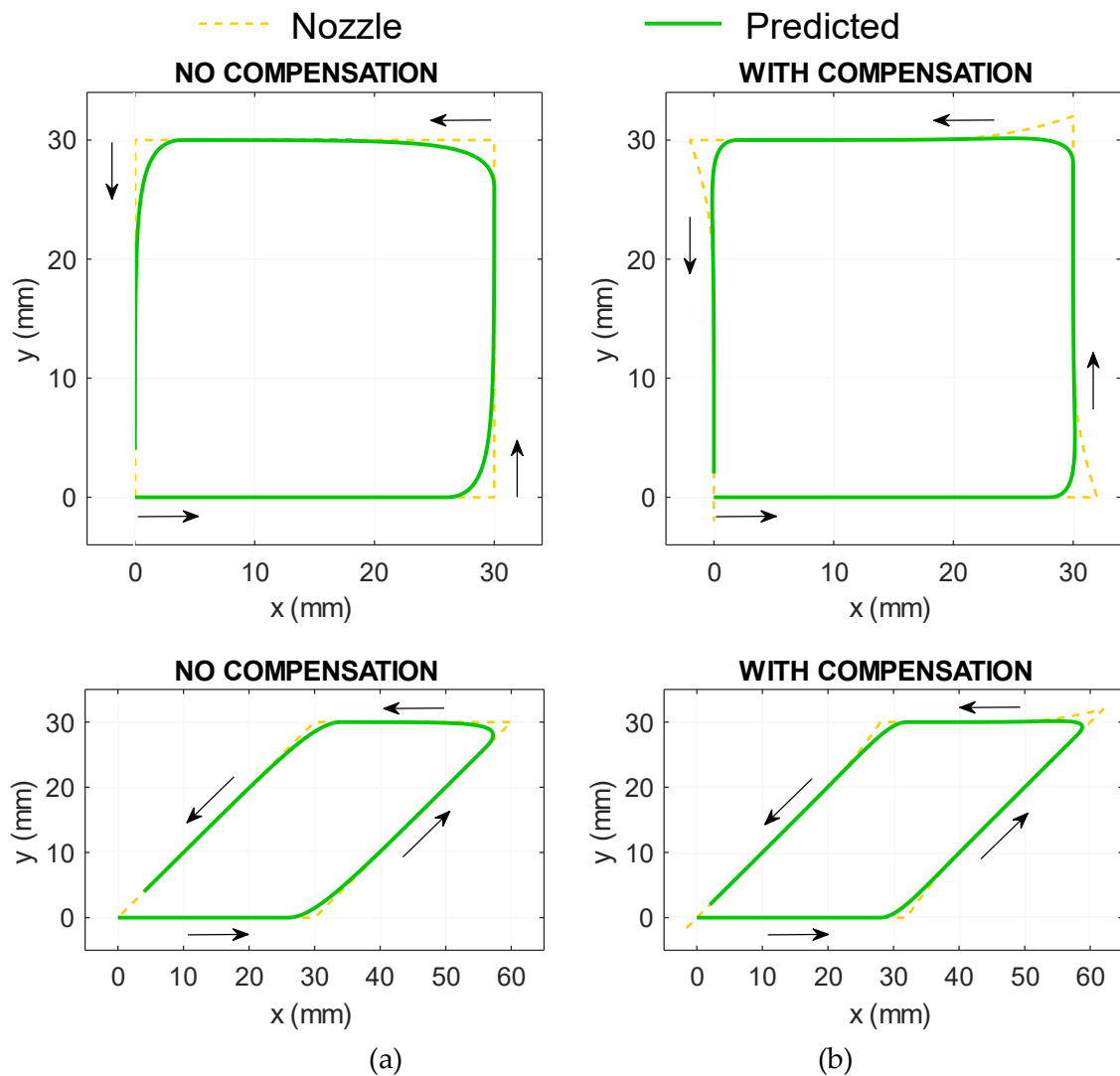


Figure 6.7 Simulated nozzle path (a) without; (b) with compensation showing with predicted raster path (the proportional and integral gains used by the PI controllers in (b) are $K_P = 1.5$ and $K_I = 2.5$).

With the nozzle-raster relationship identified, the next step is to derive a method to adjust the nozzle trajectory, so that the raster movement is more closely aligned with the ideal shape. A proportional-integral (PI) controller [189] is deployed to calculate the nozzle path, as shown in the closed feedback loop in Figure 6.5(b). The PI controller then calculates the necessary nozzle movement (x_{nozzle} and y_{nozzle}) while minimising the difference between the desired path ($x_{desired}$ and $y_{desired}$) and the predicted path. The mathematical description of this algorithm follows conventional PI controller principles, shown in Equations (6.3) and (6.4):

$$x_{nozzle} = (x_{desired} - x_{predicted})K_P + K_I \int (x_{desired} - x_{predicted})dt \quad (6.3)$$

$$y_{nozzle} = (y_{desired} - y_{predicted})K_P + K_I \int (y_{desired} - y_{predicted})dt \quad (6.4)$$

The coordinates (x_{nozzle} and y_{nozzle}) are updated in the iterative process until the desired path is achieved with sufficient accuracy. The two parameters of the PI controller are the proportional gain (K_P) and integral gain (K_I), both of which determine the trajectory of the compensated nozzle movement. The method to determine these gains is based on a similar fitting system, as described in the following section. When the convergence to the right nozzle path is achieved, the compensated nozzle path can be fed to the printer. The examples of compensated paths are shown in Figure 6.7(b).

6.5.2. Tuning the compensation algorithm

Experiments have indicated that optimum τ depends on the turning angle, although this value hovers around 1.25 s^{-1} (for the current deposition speed of 5 mm/s). Changing τ , in turn, affects the raster dynamics model, thereby requiring a different set of K_P and K_I to ensure accurate compensation. Identifying the relationship between τ , K_P , and K_I requires an extensive assessment that is beyond the scope of this paper, so some simplification has to be made. According to the visual inspection of the predicted raster from the generated PI-controlled software, it was found that increasing K_P beyond 1.5 provided negligible modification to the compensation path.

K_I , on the other hand, showed a significant influence on the compensated path. Therefore, it was decided to fix τ and K_P at 1.25 and 1.5, respectively, while K_I was determined empirically by running different numerical simulations of the compensated algorithm. Such an adjustment provides a pragmatic empirical solution and the demonstration of the compensation algorithm, though for arbitrary shapes these dependencies need to be explored with greater detail. These sets of nozzle trajectories were then verified in real experiments. The values of K_I that offered the best result (the print shape is closest to the desired shape) were then chosen.

The compensation algorithm was applied to the following two shapes printed following a spiralling trajectory made of three parallel rasters:

- A 30°-60° triangle that represents 90°-120°-150° turning.
- A parallelogram that represents 45° and 135° turning.

Figure 6.8(a) and Figure 6.9(a) show the spiralling triangle and parallelogram trajectories printed part without compensation, Figure 6.8(b)-(e) and Figure 6.9(b)-(e) are the printed parts with different K_I . The deposited raster is shown with the compensated nozzle path (yellow dotted line). The printing trials show that the magnitude of compensated overshooting is directly related to the K_I variable. Smaller K_I gives smaller compensated overshooting, and *vice versa*. In Figure 6.8(b), the K_I -1.5 print result is good with 90° turning, while the higher K_I creates longer overshooting which generates an extra curvature at the turning point. In Figure 6.8(d)-(e), The higher K_I , 2.5-3, works well with the large turning angle. The corners are filled-up, especially at the 120° turning (Figure 6.8(e)) better than using the low K_I -1.5, Figure 6.8(b), though there is some excess length on the sharp corner at 150° or 135° turning. At the 135° corner (small turning angle of 45°), the K_I 1.5-2 cases, (Figure 6.9(b)-(c)), performed well in terms of filling and building up the accurate corners. According to this visual observation, the high K_I values of 2.5-3 are suitable for the high turning angle and the low K_I of 1.5 is suitable for the low turning angle. The resulting relationship between the turning angle and PI gains is shown in Figure

6.10. By stitching each segment of the G-code from the previously generated paths, *i.e.* the best K_I for each turning angle, a printing test with variable K_I was performed, as seen in Figure 6.8(f) and Figure 6.9(f). These show a suitable compensation and a good match between the desired path and the deposited one.

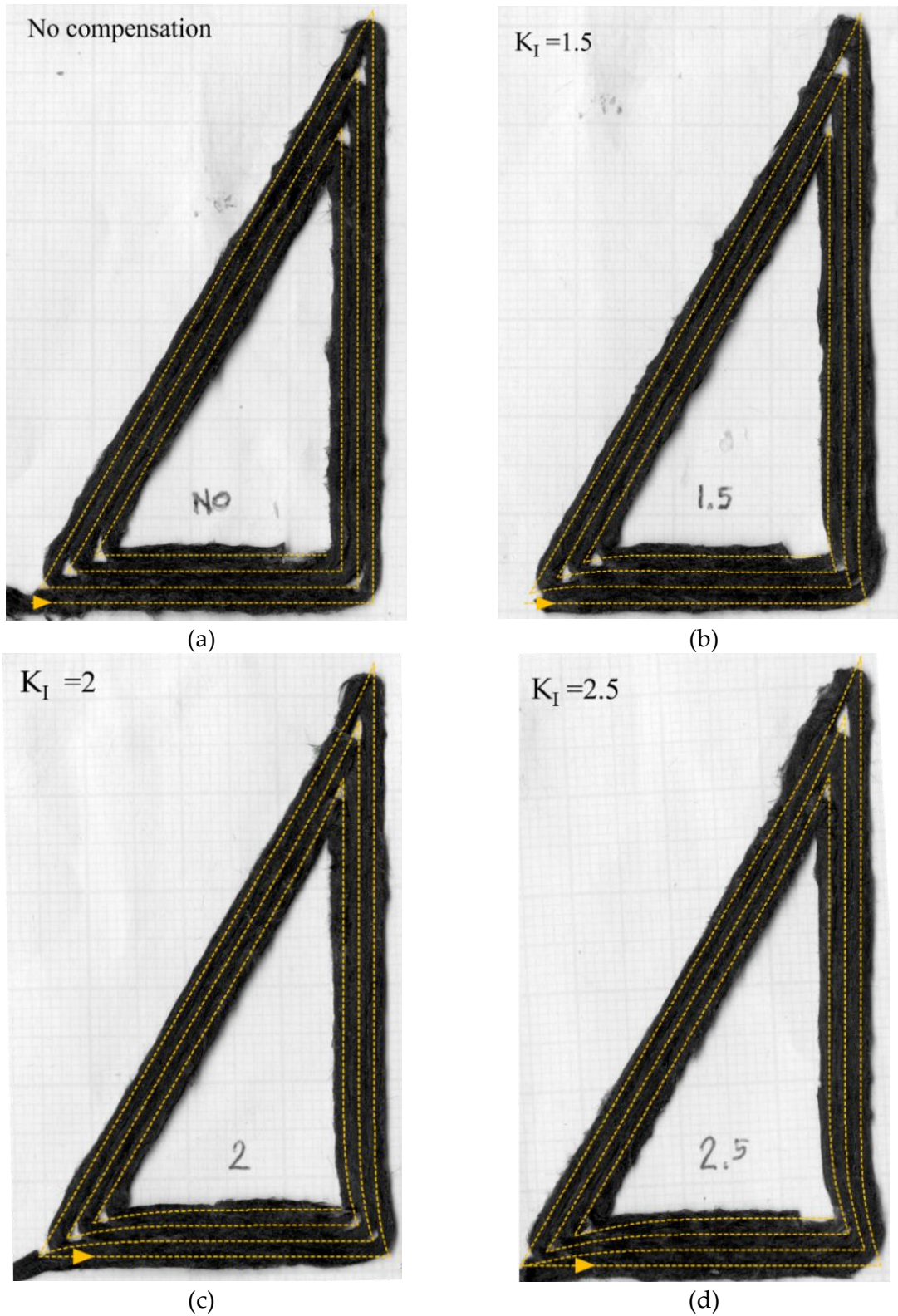
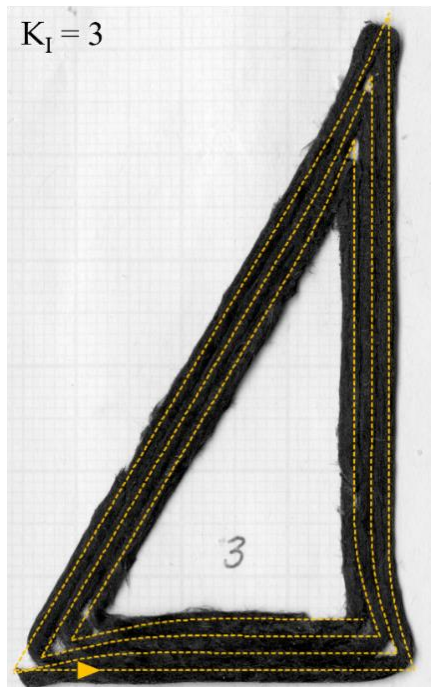


Figure 6.8 Cont.

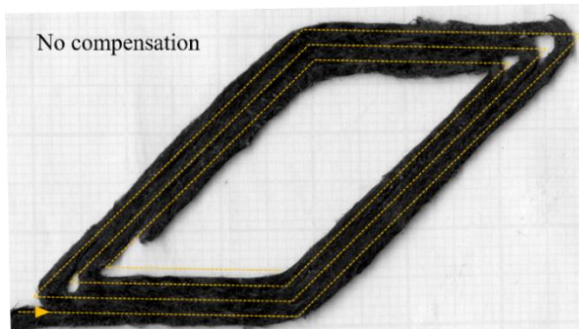


(e)

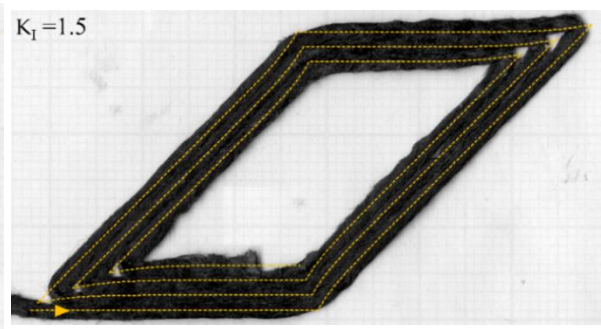


(f)

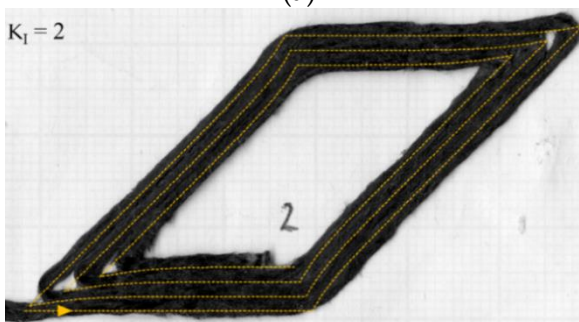
Figure 6.8 Triangle deposited rasters: (a) without compensation; (b)-(e) after path compensation with different levels of K_I from 1.5 to 3; (f) with varied K_I ($K_I=1.5$ at 90° , 2.5 at 120° , 3 at 150° turning angle).



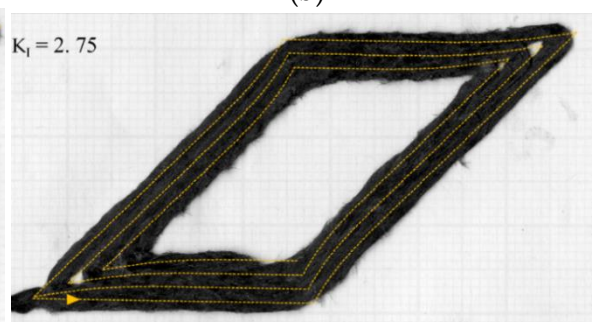
(a)



(b)



(c)



(d)

Figure 6.9 *Cont.*

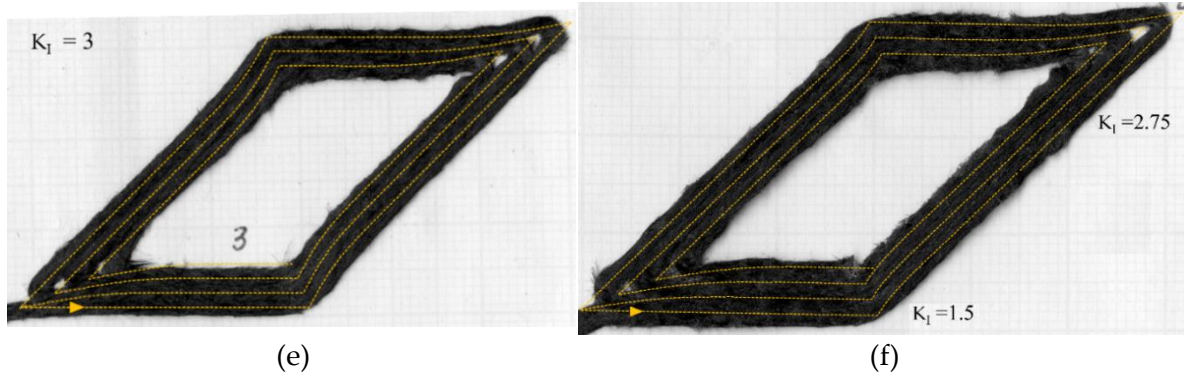


Figure 6.9 Parallelogram deposited rasters: (a) without compensation; (b)-(e) after path compensation with different levels of K_I from 1.5 to 3; (f) with varied K_I ($K_I = 1.5$ at 45° , 2.75 at 135° turning angle).

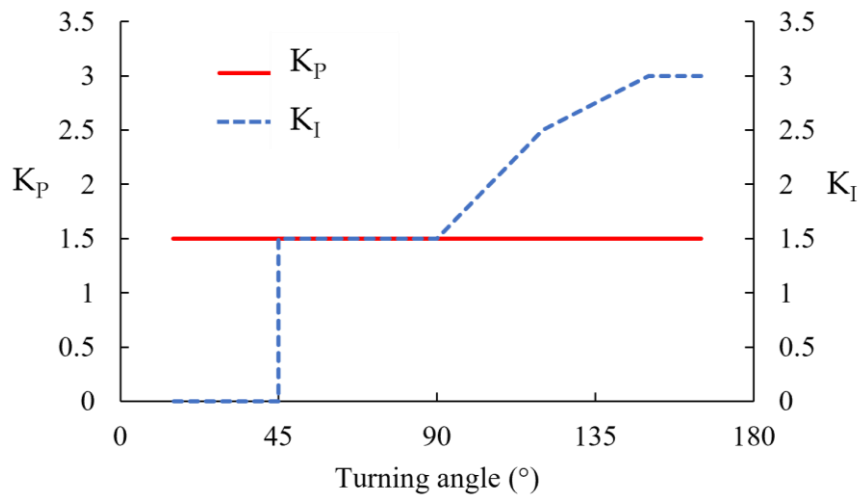


Figure 6.10 Controller gains, K_P and K_I , that are suitable for specific turning angles according to the experimental result

6.5.3. Path compensation of curvilinear printing

To resolve the steering problem, described in the introduction, the path compensation from the previous calculation was applied to the open-hole curvilinear geometry. The curvilinear desired path was approximated by a series of straight segments along the path and defined in cartesian coordinates. According to the relationship between the turning angle and the compensation controller gains (Figure 6.10), the most suitable controller gains are $K_P=1.5$ and $K_I=1.5$ for the curvilinear path which exhibits a turning angle between two adjacent segments less than 90° . In Figure 6.11, the compensation algorithm is applied to the open-hole 10 mm diameter (D10) desired raster (red) to create the compensated nozzle path

(yellow dotted). The compensation algorithm also predicts the printed raster (green) which appears slightly deviated from the centre of the circle.

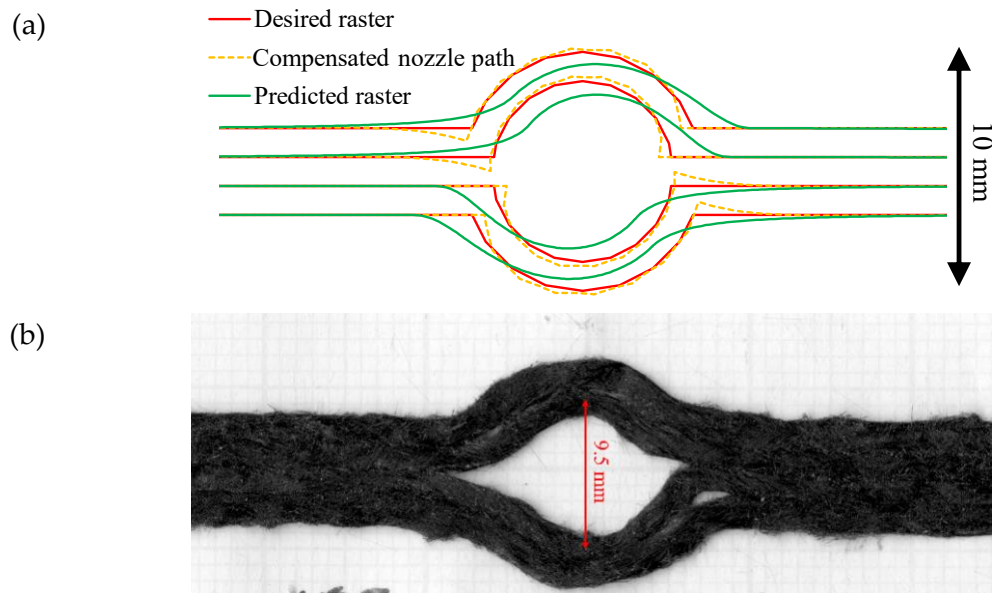


Figure 6.11 10-mm diameter curvilinear open hole part (D10): (a) coordinates of desired raster (red), compensated nozzle path (yellow dotted) and predicted raster (green); (b) deposited raster.

The compensated part has a circular diameter of about 9.5 mm (Figure 6.11(b)), which is closer to the desired path (10 mm) than the non-compensated one (Figure 6.1, diameter less than 9 mm). This can be implied that the compensation can slightly improve the curvilinear printing accuracy. However, it is still inaccurate in the hole diameter (middle of each raster) which is quite far off the desired raster. The compensated nozzle path is asymmetric between the entry and exit of the curvature. At the entry corner, the nozzle moves further inwards to the circle centre and dragged the raster in that direction resulting in a curved deposited raster at the corner similar to the non-compensated path. On the other hand, at the exit corner, the vertical (upwards/downwards) compensated movement of the nozzle can hold the raster at the desired position generating a sharp turning corner at the transition point. Due to the imperfect curvature shape seen in Figure 6.11(b), it can be implied that the curvature (5 mm radius) is too small, compared to the raster width (1.6 mm) and the filament diameter (0.8 mm), to provide geometrical accuracy. In addition, the length of the fibre (3 mm long) is comparable to the radius of curvature (5 mm)

and the filament diameter (0.8-1 mm) which significantly increases the in-plane bending stiffness of the filament.

The size limit is investigated further using larger diameters than 10 mm, such as 20 mm (D20) and 30 mm (D30). The deposited raster, D20 and D30, without compensation, are shown in Figure 6.12(a) and (b), respectively. The circle diameter of D20 and D30 is more accurate than the diameter measured on the 10-mm-diameter curvilinear, but the eye-shape issue at the corner still presents. This causes two noticeable gaps at the entry-exit corners that need to be filled with raster.

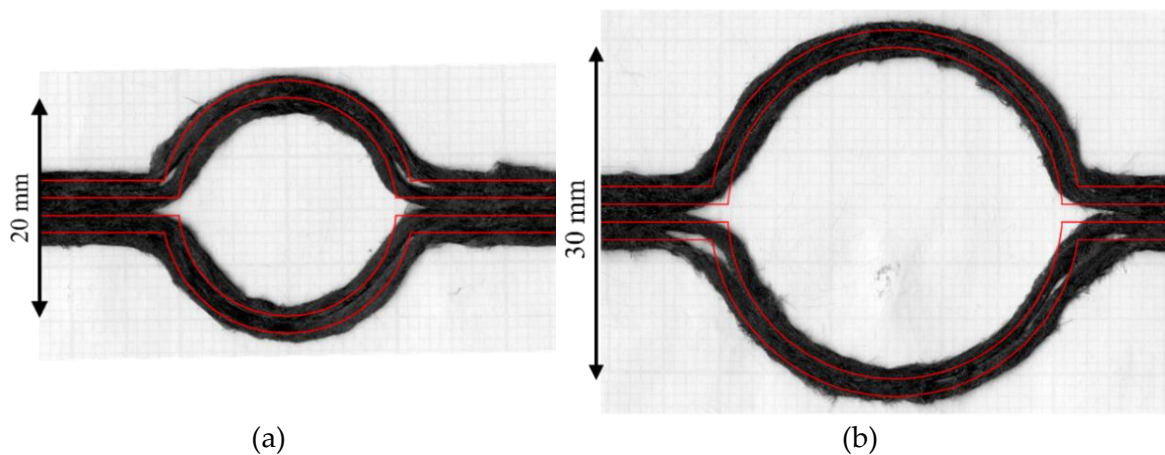


Figure 6.12 Curvilinear printed parts of (a) 20 mm; (b) 30 mm diameter without path compensation.

Using the proposed compensation algorithm, the new nozzle paths for D20 and D30 were generated, as seen in Figure 6.13(a1) and (b1). Figure 6.13(a2) and (b2) show that the hole dimension is very close to the as-designed dimensions, 19.6 and 29.7 mm, respectively, and the eye-shape effect at the corner is reduced. This deposition represents the desired path much better than the parts produced without compensation in Figure 6.12(a) and (b). At the transition, the top and bottom raster become closer to each other in the D20, this is slightly better in the larger diameter (D30). This may be caused by the larger curvature size allowing more nozzle travelling time that may create a better bed adhesion. The filling of the second raster is slightly better than with no compensation. The second raster corner is almost fully filled by the overshooting of the second raster.

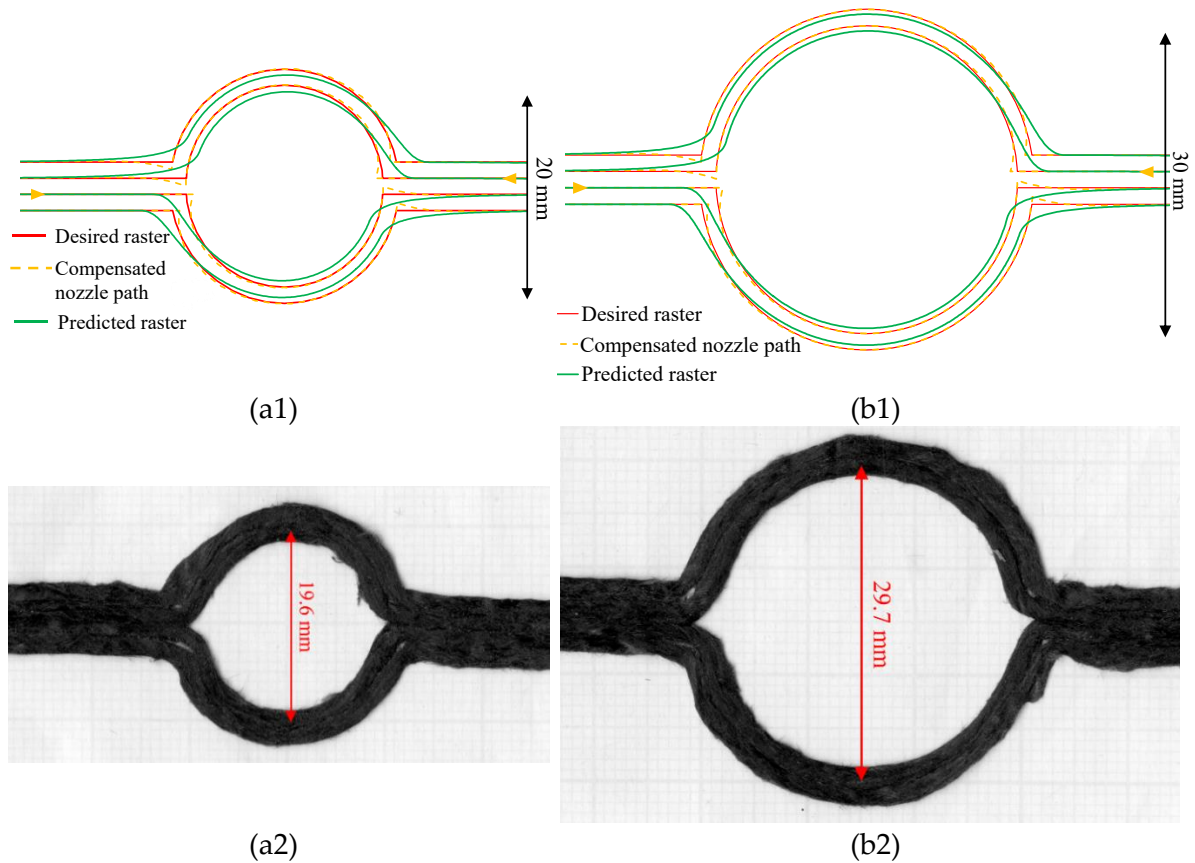


Figure 6.13 (a1) and (b1) Compensated path of 20 and 30 mm diameter circle calculated with the PI controller (yellow dotted) showing with the predicted printed path (green) and the desired raster (red); (a2) and (b2) curvilinear printed part of 20 mm and 30 mm diameter with the compensation.

To quantitatively show the improvement achieved by the algorithm, the compensation of curvilinear printing was further numerically analysed with error calculation between the deposited raster and the desired path using the root-means-square error (RMS) equation. This use of RMS for the evaluation of 3D printing errors was previously suggested by Sugiyama *et al.* [190] and Reich *et al.* [191]. In our case, the curvilinear deposited rasters were divided horizontally into 2.5 mm segments from the middle of the circle to 0.5 mm on the linear section at the entry and exit of the curvilinear path (another two segments before the entry and after the exit of the curvilinear path were added), as can be seen in the example of the 10-mm curvilinear path with compensation in Figure 6.14. On the divided lines, the intersection length of the vertical divided line on the deposited raster were measured (orange arrows line). The middle of the measured line was marked as the assessment points (yellow

points in Figure 6.14). There are 9, 13, and 17 assessment points on the single curvilinear raster for D10, D20, and D30 cases, respectively, according to the size of the part. With the image processing in ImageJ software, the vertical deviation from the desired raster (red line) to the calculation point on the deposited raster (yellow point) was measured. The deviation at different positions was recorded and converted to RMS values for the path deviation analysis. The RMS vertical deviation values were presented in Table 6.2. According to this table, the D10 curvilinear shows a minor accuracy improvement after the compensation. On the other hand, there is a strong reduction (with a factor of two) of error in the compensated D20 and D30. When normalised by the diameter of the circle, the RMS of D20 and D30 cases become similar. These metrics also show that the highest error is characteristic of higher curvatures. This confirms that there is a size limit for this compensation algorithm.

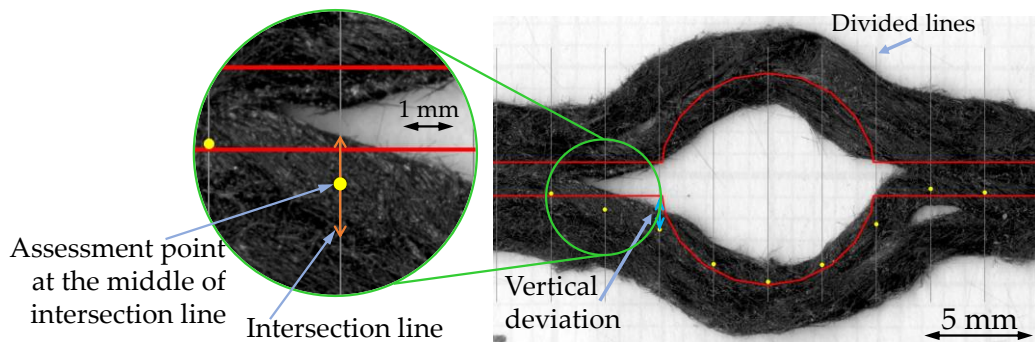


Figure 6.14 Example of the vertical deviation calculation of 10-mm compensated curvilinear part showing the assessment points (yellow point), at the middle of the intersection line between the divided line and the deposited raster, and the measured vertical deviation.

Table 6.2 RMS of vertical deviation measuring from the desired and the centre of the deposited raster.

Printing Diameter	Calculation points	Compensation		Normalized RMS by diameter	
		NO	YES	NO	YES
D10	9	0.76	0.73	0.076	0.073
D20	13	0.91	0.45	0.046	0.022
D30	17	1.28	0.64	0.043	0.021

6.6. Chapter conclusion

This chapter studied the printing accuracy of the novel DcAFF 3D printing material

and suggested a possible way to improve it. The key findings are summarised below:

- The printing accuracy was studied with circular shape printing and the result shows that the deposited rasters deviated from the defined path due to the nozzle design (filleted end) and insufficient bed adhesion. This caused dimensional inaccuracies such as slightly smaller circular diameters and poor turning corners.
- The first solution, *i.e.* the adjustment of machine parameters without changing the defined printing path, was insufficient to achieve sharp turning angles.
- A printing path compensation with a first-order lag relationship was used to calculate the path error, then a PI controller was added to generate a path compensation which presented itself as an overshooting of material deposition at the turning corners. This helps the raster to fully attach to the printed bed at the sharp turning corner.
- After the controller's gains were adjusted and matched to a specific turning angle, the compensation code was applied to the open-hole curvilinear case. Although this cannot give a good result in the 10 mm diameter circle, as it is too small for the 0.8-mm-diameter filament reinforced with 3-mm long fibres, the printing of larger diameter (20-30 mm diameter) curvilinear specimens offers a good indication that using the compensation algorithm as a feedforward tool to define the nozzle path could help to achieve complex shape with DcAFF or other discontinuous and continuous fibre reinforced filament.

Chapter 7 Overall Discussion

This chapter offers the general outlook on the original studies [50], the contribution of the current work, and the state-of-the-art studies reported in the literature. It attempts to revisit the key findings of the work presented here, identify their connections and comment on the current limitations. The three main areas of study: filament production, printing trials, and performance assessment, shown in Table 1.1, will be discussed to portray the context and potential for further development in each study area.

7.1. Production of DcAFF filament

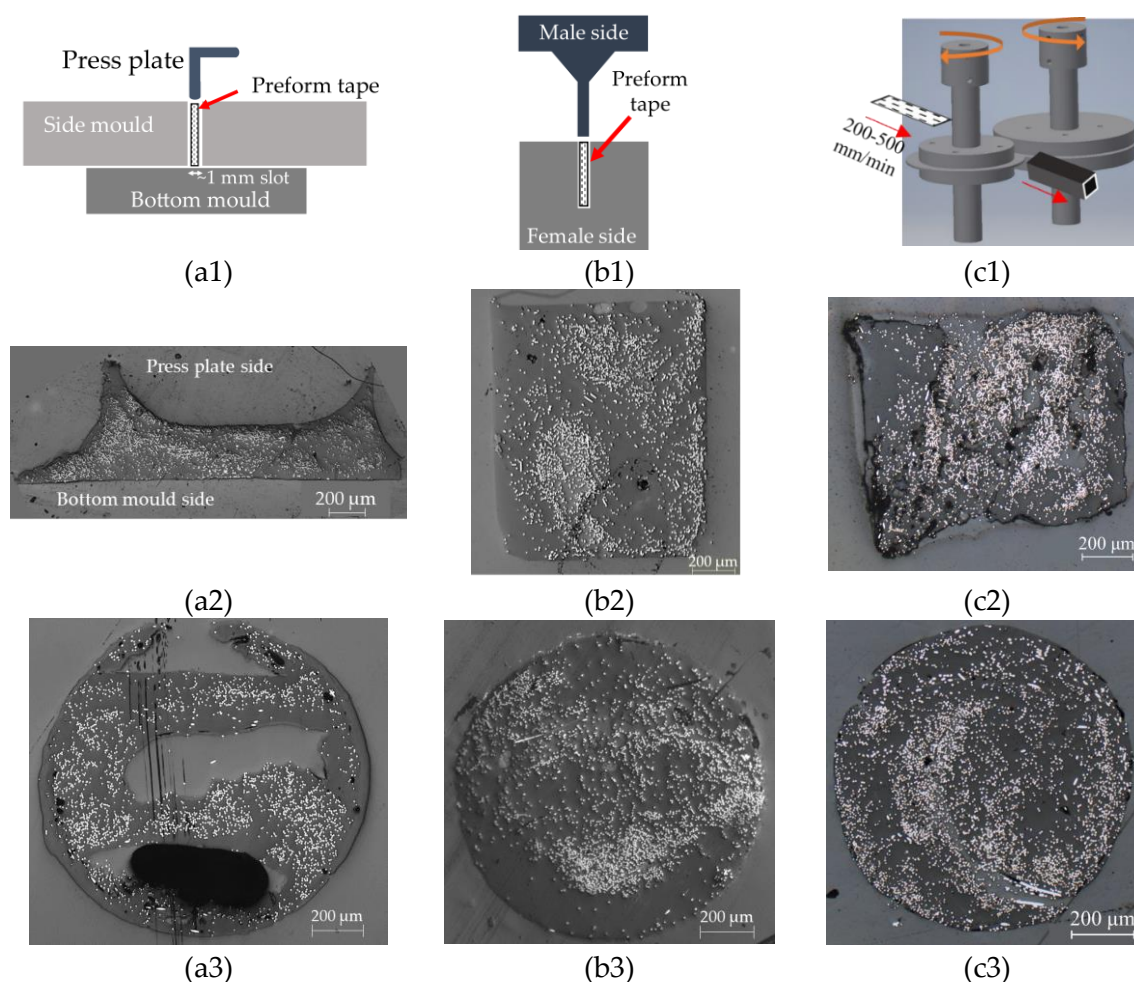


Figure 7.1 Development of DcAFF 3D printing material from the manual moulding with (a1) the first 4-piece mould to (b1) a single-slot simpler 2-piece mould and (c1) the semi-automated filament forming machine showing the compacted tape (square filament) (a2, b2, c2 according to the developed stages) and the final circular filament after the pultrusion of the compacted filament (a3, b3, c3 according to the developed stages).

As stated in the introduction, the main challenge of this thesis is to develop a method to produce aligned discontinuous fibre thermoplastic filament from the HiPerDiF preform tape while keeping the characteristics of HiPerDiF produced ADFRCs, *i.e.* a fibre length definable as “discontinuous” (3 mm long) and a high level of fibre alignment. The study of Blok et al [50] showed that the manual moulding technique using a 4-piece assemble aluminium mould (Figure 7.1(a1)) could reshape the cross-section of the pre-impregnated tape to a bulked and thick rectangular cross-section. This technique compressed the thin HiPerDiF tape in a small slot, where the tape was heated above the melting point. The compressed moulded filament, shown in Figure 7.1(a2), has a high aspect ratio and material overflow on the corners. After a hot pultrusion, this high aspect ratio and the material overflow in the moulded filament caused folding and joining of the rectangular sides that trap air in the structure causing a large central void, Figure 7.1(a3).

The second stage of the development was to design a proper mould that can produce a low aspect ratio or square cross-section filament after compression at a high temperature. The customized machined 2-piece mould with sharp 90° corners (as opposed to the rounded corners of the 4-piece mould) at the bottom female side and a perfectly flat end male side, seen in Figure 7.1(b1), produced a high potential compressed cross-section with little overflows and low aspect ratio, Figure 7.1(b2). This leads to a void-free pultruded circular cross-section filament at the end of the production, Figure 7.1(b3). However, the moulding technique using an oven to reach the required high temperature, approximately 250°C, is a time-, energy- and labour-consuming process with a production rate of less than a meter per hour. The filament production needed to be scaled up to a continuous and more automated process in order to produce more material for other aspects of the study and, finally, to allow for future commercialisation.

This, to the best of the author's knowledge, was the first time that an aligned discontinuous fibre composite filament for 3D printing was continuously produced

with an automated machine using the concept of two hot counter-rotating rollers shown in Figure 7.1(c1). With the fine-tuning of the roller gap, rotation speed and temperature, a promising square-like cross-section filament (Figure 7.1(c2)), presenting a low aspect ratio, void and material overflow, similar to the one achieved from the 2-piece moulding technique, was produced with a higher rate than the manual method, from a metre per hour to about a half-metre per minute. This leads to a similar quality of the pultruded filament in the final stage as the one pultruded from the 2-pieced moulded filament. When the HiPerDiF process was developed from the small lab-scale, 5-mm wide preform tape, to a larger-lab scale (third generation, 3G) machine, with 30-mm wide preform tape, the DcAFF filament was mass-produced and spooled up in a 3D printing feedstock filament ready to be fed to a general 3D printer. This filament-forming process, called DcAFF machine, has a high potential to be scaled up from a lab scale to an industrial machine.

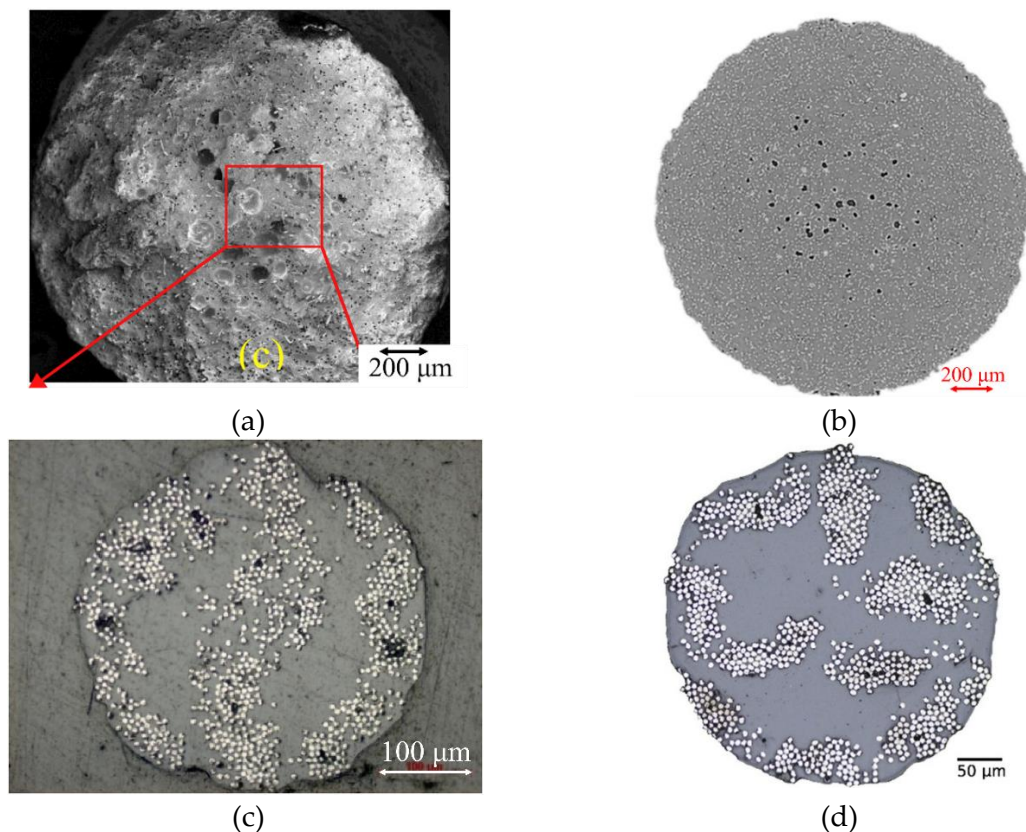


Figure 7.2 Available short fibre composite filament: (a) SEM image of ABS/S.CF 15 wt% achieved from [12] (Recalled from Figure 2.21(c)); (b) μ CT scanned image of commercial nylon/S.CF from Markforged achieved from [192]; (c) and (d) cross-section microscopy of Markforged nylon/C.CF achieved from [43] and [127], respectively.

Comparing the DcAFF machined filament cross-section (Figure 7.1(c3)) to the available composite 3D printing filament, the DcAFF filament has a fibre distribution and microvoids across the filament similar to the one observed in ABS/S.CF [12] (Figure 7.2(a)) or Onyx (nylon/S.CF by Markforged) [13, 192] (Figure 7.2(b)). In addition, the DcAFF has a better fibre distribution than the Markforged nylon/C.CF found in [43, 127] (Figure 7.2(c) and (d), respectively) in which those are distributed just around the edge of the cross-section.

There are some points to be considered for the design of the next, semi-industrial, iteration to form a circular cross-section DcAFF filament from thin HiPerDiF pre-impregnated tape: (i) using larger and higher precision machined rollers so that the gap between the two rollers is precise and the compressed filament cross-section is consistent, *i.e.* square shape without void and material overflow; (ii) using a higher efficiency heating method, *e.g.* laser or infrared heater, which consistently heats the tape to a finely controllable temperature instead of heating the entire rollers; (iii) a better rotational motor controller to synchronise and smooth the feed into and pull out of the rollers without tearing the filament apart.

Currently, the precursors for DcAFF filaments are the thin pre-impregnated thermoplastic HiPerDiF tapes. This material form necessitates the production methods to reform the high aspect ratio tape into a circular filament. As was shown in this thesis, the deployed method is prone to the entrapment of voids during the forming because:

- the extrusion had to be performed at a temperature lower than the melting point of the polymer to avoid the disintegration of the tape;
- the material tends to fold and the pressure applied by the nozzle is not sufficient to suppress the occurring voids (excessive pressure gradient may lead to backflow, nozzle clogging and filament disintegration);
- the extrusion of the continuous filaments relies on the backflow as the mechanism to increase the pressure in the nozzle. This however cannot be

utilised for DcAFF filaments as any backflow will impact the alignment of short fibres.

Hence, the next generation of approaches should address the issues with the initial material form, the bespoke nozzle design, and the tuned processing parameters. For instance, a better HiPerDiF format could deploy “intermingled fibre”, the combination of reinforced fibre, *i.e.* carbon fibre, with polymer fibre in a similar size (diameter and length) as the reinforced one. With this intermingled-aligned fibre format, it may be easier to reform/compress the particle-like structure than the solid thin tape into the low aspect ratio cross section or circular shape. This may result in less void creation compared to the folding of composite tapes as the flow length will be substantially reduced. Reforming the intermingled fibres may improve the alignment of the reinforced fibre better than the folding of the pre-impregnated tape in the rollers. A new filament forming method may be introduced to tackle the intermingled fibre preform, *e.g.* slightly bulking the intermingled fibres through a gradually converging nozzle while the thermoplastic fibres are solid. This approach is anticipated to result in improved fibre alignment, as compared to the conventional method of crushing and folding the thin tape in a roller. Following the bulking of the fibre preform to a lower aspect ratio, the subsequent melting of the thermoplastic during pultrusion through a circular nozzle is expected to facilitate further alignment of the reinforced fibre, by following the direction of the melt flow. Moreover, the reinforced fibre distribution in the composite should be more uniform than the pre-impregnated tape because the thermoplastic fibre can be distributed around the reinforcement fibres during the alignment stage preventing their clustering.

7.2. Printing

At each stage of filament production described above, the circular pultruded filament, ready for 3D printing, was fed to a general 3D printer for several printing trials. Creality Ender 3, a commercial 3D printer, was used in the whole study. The only modification made to prevent fibre breakage during printing was the

installation of a purposely designed nozzle, which can be easily done by the user. A nozzle that would be suitable for the discontinuous fibre filament was designed inspired by the continuous fibre printing nozzle used in the Markforged machine as seen in Figure 3.11.

7.2.1. Printing parameter trial

At first, the range of acceptable printing parameters was inspired by examples from the literature. The literature review conducted in Chapter 2, identified possible printing parameters for the DcAFF, such as the temperature range of the PLA printing, layer thickness and deposition speed synchronized with material feed rate (190-210°C for printing temperature and 80-90°C for bed temperature). These parameters were initially applied on single raster deposition in Chapter 3. After several printing trials, this set of parameters (Figure 3.13(b)) was further tuned. This allowed to print a straight raster with a good top surface finish. The established parameters comprised 210°C printing temperature, 80°C printing bed temperature, nozzle travelling speed equal to the material feed rate, *i.e.* 300 mm/min, and the application of a masking tape onto the printing bed to enhance adhesion. The low printing speed was found necessary to provide enough time to build good bed adhesion. Compared to neat polymer, the high fraction of fibre in the DcAFF creates challenges for reaching a good bond with the substrate as the effective viscosity of the filament is increased and hence flow and diffusion mechanisms are impeded.

For the initially produced 1.1-mm diameter filament, the layer thickness of 0.6 mm was selected from the printing trial. The raster distance was assigned as 1.3 mm which is smaller than the expected width (1.58 mm) calculated from the cross-section of the filament and the defined thickness. This was given with the intention to provide an overlap between rasters to improve the strength as mentioned in the literature. The single layer part printed with this large overlap (20%) presented a swell line at the inter-raster connection and high surface roughness. When the filament was pultruded to a smaller diameter, *i.e.* 0.8 mm, the nozzle height was

decreased to 0.3 mm as a proportion to the reduction of diameter and the intention to increase the bed adhesion. The calculated expected width is 1.68 mm, so the raster distance was set as 1.6 mm. This smaller overlap (~5% of the width), as used in the literature [74, 75], was chosen to prevent a swelling line from forming at the inter-raster area or a gap between adjacent rasters.

7.2.2. In-plane printing defect and mitigation

This section will show the development of the printing procedure for DcAFF to improve the printing accuracy and discuss the reason behind the modification of the printing path, which will differ from the desired path, to achieve accurate deposition. The discrepancy between the deposited raster and the nozzle path was observed when steering, particularly at the large turning angles ($>30^\circ$ from the initial direction). The problem is clearly described by the printed aerofoil outline shown in Figure 7.3 which shows constantly evolving path curvature. The printing path is the linear interpolation between a discrete set of points placed along the path. The printing started from the top surface at the trailing edge (small yellow arrow) passing the leading edge and ending again at the trailing edge on the lower surface. The top trajectory, A-B, has a small curvature evolution with a long recovery distance between the neighbouring points. This allows for achieving accurate deposition. While at the leading edge, B-D, there is a large direction change, especially at point C. This leads to a large discrepancy as can be seen around C-D. This required a long recovery distance until the deposited raster returned to the accurate deposition around point E. This required a long recovery distance until the deposited raster returned to the accurate deposition around point E.

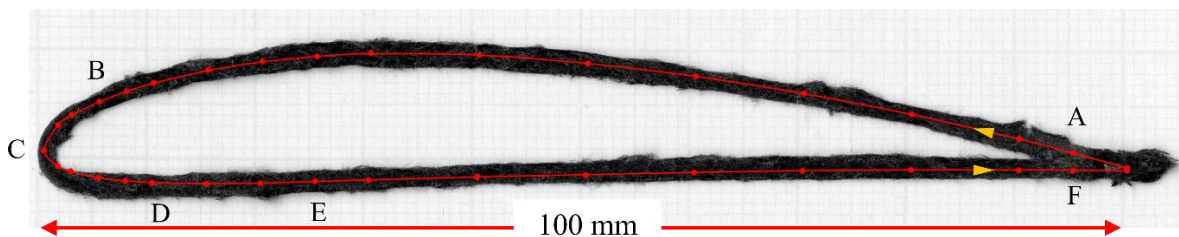


Figure 7.3 Aerofoil printing presenting different direction changes along the printing path and showing the deposition discrepancy, especially at the leading edge.

The discrepancy was highlighted when printing a 90° corner turning of a rectangular part. The deposited raster cannot form a sharp corner and the nozzle drags the deposited filament from the corners inwards. The deviation at the corner was clearly seen in the high fibre content deposited raster - Figure 7.4(a), as a blunt corner instead of a sharp 90° angle. This also created a printing difficulty due to the peeling of the deposited raster from the printing bed.

It is important to observe that the increase in fibre volume fraction results in more difficulties for steering. At the lower fibre content (~18-25 wt%), there was more bed adhesion, and the corner was formed better, as shown in Figure 7.4(b). The straight section almost reached the corner before the raster was dragged downwards at the turning and again when reaching the lower corner. This issue is manifested by the raster following an elliptical rather than a rectangular path. This sharp corner forming problem is also common in the printing of stiff continuous fibre (Markforged), as highlighted by many publications [43, 185, 193].

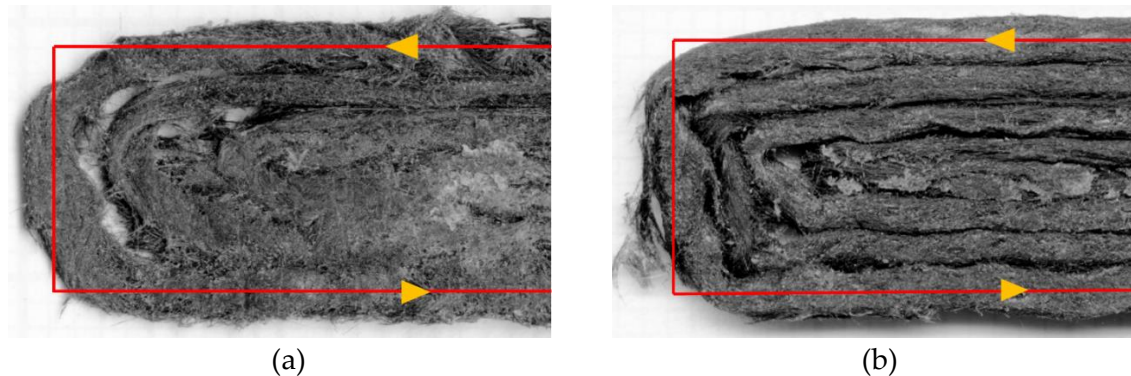


Figure 7.4 Corners of rectangular full layer printing expected to be used as a tensile specimen: (a) printing at high fibre content (28-32 wt%); (b) printing at lower fibre content (18-25 wt%).

Although the reduction of the fibre content can provide a better bed adhesion of the deposited material that retains the shape of the deposited raster, the deposition still deviated from the corner creating a poor deposition at the end of the rectangular printing. This leads to a new solution to fabricate a 90° corner by replacing the sharp corner (Figure 7.5(a)) with a small radius turning, a 3-mm radius, shown in Figure

7.5(b). The small radius corner deposited rasters tend to follow the defined nozzle path more than the sharp corner path, but there are some deviations, especially the sliding of the deposited raster inwards through the centre of the radius as a result of the nozzle movement that made the curvature smaller than the defined radius. Although this method is suitable for the large dimension printing used in Chapter 4, it is difficult for a small double turning, *e.g.* rectangular shape that has a short side smaller than 3 mm or a curvilinear path. Hence, this is not a practical solution.

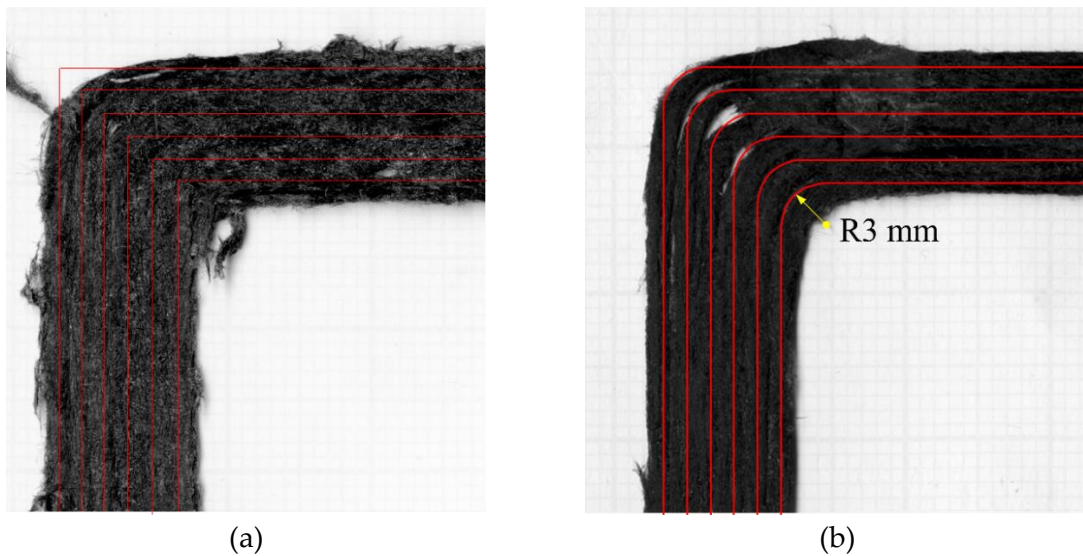


Figure 7.5 High magnification at a corner of a large square printing part: (a) with a sharp 90° corner; (b) a replacement of the sharp turning corner with a 3-mm radius fillet corner.

To solve the discrepancy problem, the deposition path defined in the G-code (nozzle path) might need to be different from the exact transposition of the desired shape into a path. It was hypothesised that the discrepancy may be the result of the nozzle shape. The schematic in Figure 7.6 shows the interaction between the nozzle and filament while printing a 90° angle with the designed filleted end nozzle. In Figure 7.6(a), from the side view, due to the smaller diameter of the filament than the nozzle, the filament in the nozzle is hanging and slightly inclined, so the filament always touches only one side wall of the nozzle opposite to the nozzle moving direction. The fillet allows the filament to gently change direction from vertical in the feeder to horizontal on the printing bed. Yet, this fillet created a small gap (~2 mm) between the centre of the nozzle which is the defined position from the G-code and the full

contact point where the flat nozzle can initially provide full pressure to the deposited raster to build bed adhesion. These issues in the nozzle design will have a small effect when printing along a linear path, but for the turning case, the filament cannot be made to change direction instantly at the turning point (Figure 7.6(a) top view). The filament will slightly change direction when the nozzle starts to move in a different direction, Figure 7.6(b), before it comes back to full contact at the lower side of the wall as presented in Figure 7.6(c). Because of the hanging of filament and the filleted nozzle that delays the full contact point, the deposited raster cannot build full adhesion on the printed bed and the printing inaccuracy is built up. Eventually, this leads to a curved turning corner. Since the fillet in the nozzle is necessary for fibre printing and cannot be eliminated, a new approach should be devised to solve this problem.

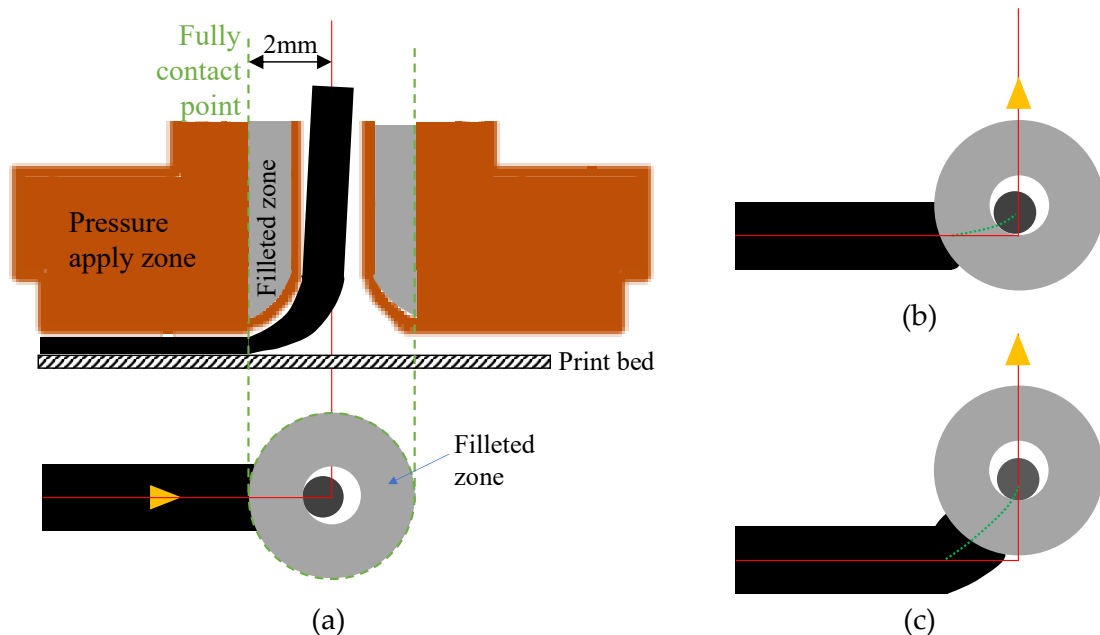


Figure 7.6 Action during printing 90° turning angle with filleted nozzle from (a) side view of the filament feeding to nozzle before deposition on the bed and top view of the deposition when reaching the 90° turning corner showing the misaligned of the filament centre and the nozzle centre (nozzle path); (b) top view of the deposition at the moment just after passing the 90° corner, the filament slightly recover back to the nozzle movement direction; (c) top view of the deposition when the filament fully reaching the nozzle movement and attached to the lower side nozzle wall while the nozzle moving up presenting a blunt corner deposition.

Owing to the 2-mm gap between the centre of the nozzle and the full contact point on the flat end, the idea to add an overshooting feature at the turning point to allow the filament providing full contact with the bed before turning was introduced. The initial idea was tested with a 90° turning square by printing an additional 45° line after reaching the corner before returning to the same corner point and continuing the printing until reaching another corner, Figure 7.7(a). This idea provided extra material to build a sharp corner. Hence, it was adopted to solve the problem found in the complex shape open hole printing with a 10-mm hole diameter curvilinear path presented in Chapters 4-5. Initially, in Chapter 5, an additional path was empirically added at the transition from straight segment to curvature, as shown in Figure 7.7(b), which was called the modified curvilinear open-hole printing path.

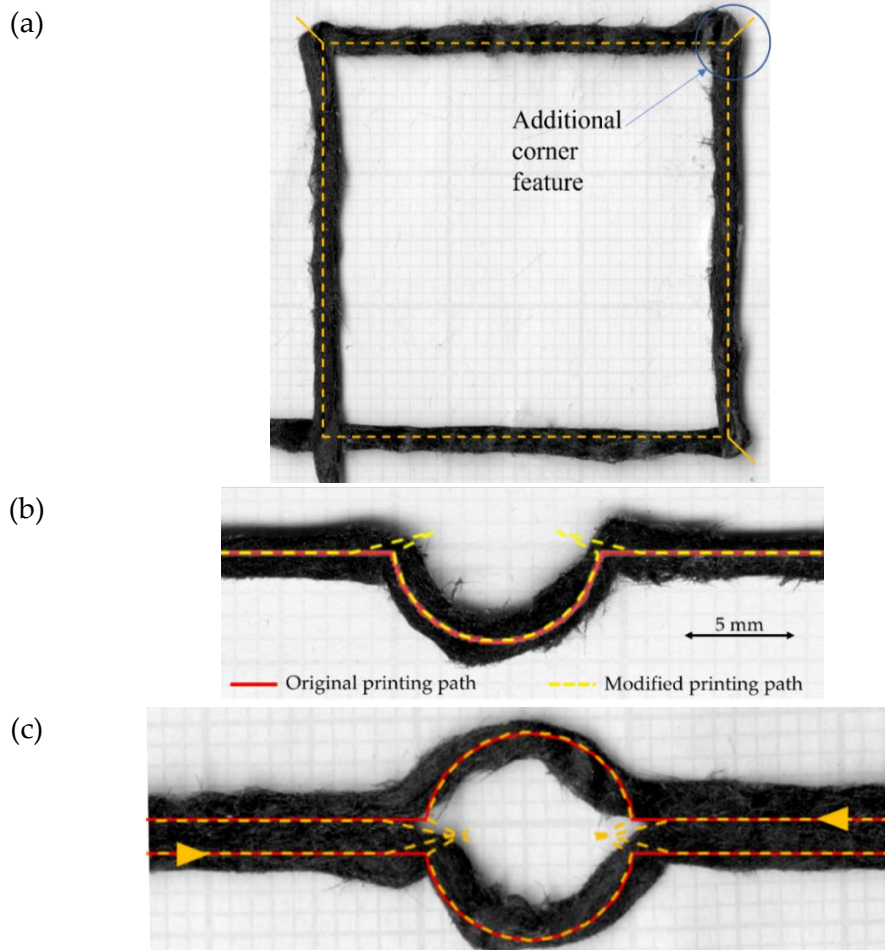


Figure 7.7 Manually adding an overshooting feature at the turning corner to provide a full contact: (a) initial study in a square case; (b) single raster half-circle curvilinear open hole tensile test sample; (c) full-circle curvilinear open hole tensile test sample showing an asymmetric hole shape.

The additional path extended the nozzle movement inwards to the circle more than the defined path before returning to the transition point and entering the curvature. This addition was built again before exiting the curvature as a mirror to the entry. In the single curvilinear case, most of the modified deposited raster followed the desired curvilinear path, but there was a slightly sliding raster from the corner only at the exit of the curvilinear corner. Although this empirical additional path scheme works well with one curvilinear raster, the fabrication of the whole part which has a nozzle moving in the opposite direction to complete the full circular presented an asymmetric hole shape between the entry and exit of the circular section, seen in Figure 7.7(c).

Due to the asymmetric shape hole obtained with the empirical overshooting addition, the additional path was studied in detail to achieve a more accurate deposited raster. This led to, our ultimate printing solution presented in Chapter 6, the study of the nature of the deposition lag after deposition direction changes using a first-order lag equation to predict the mismatch of the deposited raster and the nozzle path. Then, a PI control was added to the equation to create an overshooting feature that could compensate for the nozzle path and bring the deposited raster to the desired path. After fine-tuning the PI controller algorithm for different turning angles, the code was built up and could completely solve the large turning corner problem, as seen in Figure 6.8-6.9. This algorithm works with large-dimension curvilinear paths, *e.g.* 30-mm curve in Figure 7.8(a) showing a low discrepancy between the desired and deposited paths. Yet, it cannot tackle arbitrary turning angles, especially the small recovery distance before the next turning of a small radius of curvature, *e.g.* 10-mm curvilinear (in Figure 7.8(b)). To improve this algorithm and minimize the discrepancy, a camera should be installed in the printer to capture the deposited raster and real-time monitoring sensors should be added to the code to give instant feedback to *in-situ* modify the nozzle path.

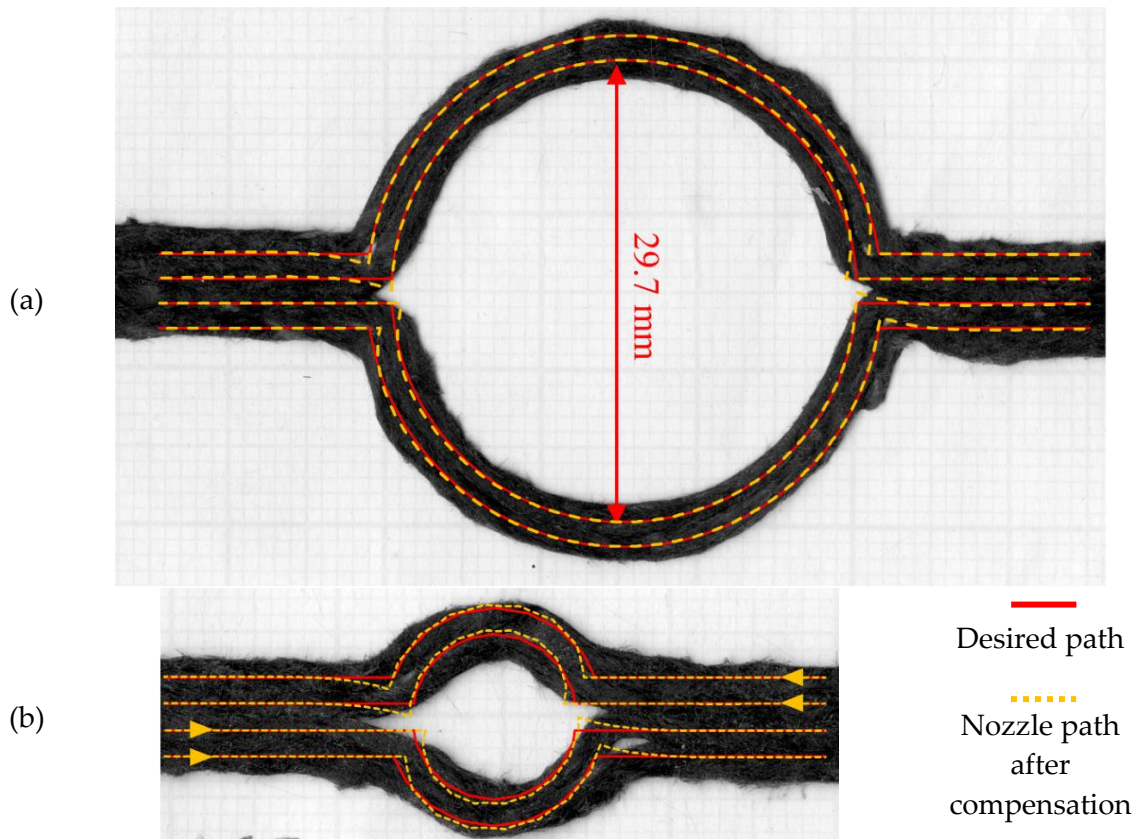


Figure 7.8 Curvilinear open hole printing with the developed algorithm: (a) large hole size 30-mm showing promising deposited hole size and decent deposited raster (recalled from Figure 6.13)); (b) small hole size 10-mm showing large discrepancy.

In this stage of the material development, the current 1-mm diameter filament cannot achieve precise deposition when fabricating the steering radius of below 6 mm, as seen in Figure 7.8. For the first layer, bed adhesion plays an important role in this phenomenon. The 3D printing adhesion tape, blue masking tape, cannot provide sufficient bed adhesion for tight radius steering. Better bed adhesion should be introduced, *e.g.* chemical glue or printing the first layer with neat polymer before printing composite filament. For the subsequent layer, the study of the nozzle height, printing speed and the temperature of the deposition should be considered to provide the proper pressure on the previous layer so that they can build an adhesion between the layers. Another option to increase the steering potential is to reduce the filament diameter. The smaller diameter filament should better fill the curvature gap, but it may create a challenge in the filament forming stage as it can carry lower force during pultrusion.

7.2.3. Inter-raster defects, in-plane and through-thickness, and mitigation

Chapter 5 highlights another printing defect – voids - Figure 5.10(a1). They can be categorized into three groups: (i) improper bonding between the adjacent rasters; “inter-raster microvoids”; (ii) imperfect compaction between layers, “inter-layer microvoids”; and (iii) the joining of the four corners, “inter-raster diamond-shaped voids”. The three mentioned defects are schematically shown in Figure 7.9.

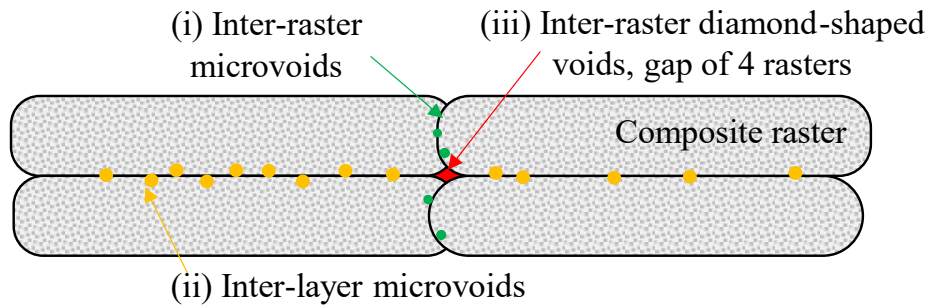


Figure 7.9 Schematic of void formations found on the cross-section of a multilayer DcAFF 3D printing: (i) inter-raster microvoids, (ii) inter-layer microvoids, (iii) large cavity inter-raster diamond-shaped voids.

These through-thickness voids can cause an inter-raster or a layer separation failure under tensile load which reduces the strength of the part. The inter-layer and inter-raster microvoids are the result of the improper polymer fusion between two rasters, as mentioned in Figure 2.3, Chapter 2. The imperfect raster fusion can also be caused by the waviness of the deposition, the inconsistency of the filament diameter along the length of the spool or the fluctuation of fibre content and fibre distribution in the filament. They can be minimized by producing a consistent diameter filament and optimising the printing parameters: *e.g.* printing temperature, layer thickness, raster distance and printing speed, to the range that allows enough time and pressure for the raster fusion and the polymer chain diffusion. However, the inter-raster diamond-shaped voids, caused by the meeting point of the four small raster corners, are the instinct of 3D printing and are generally found in the literature [43, 79]. These diamond-shaped voids present a large cavity in the cross-section. It is more difficult to eliminate the diamond void even when printing with a negative raster gap. The

too-high overlap between two adjacent rasters aiming to completely remove the diamond-shaped void may build up a thicker inter-raster junction, reducing the resolution and creating another weak point in the part.

To eliminate the three mentioned voids in the 3D printed part, an additional manufacturing step was suggested. In this thesis, a post-printing consolidation under heat and pressure was applied to the printed part with inspiration from the compression moulding after printing proposed by 9T labs [18, 194]. In this thesis, the main consolidation was based on an open-moulding technique using a flat metal plate as a tool on the bottom side and vacuum bagging on top to apply vacuum pressure. The open-moulding technique used in the thesis is schematically shown in Figure 7.10 The consolidation reduces voids and strengthens bonding between rasters/layers, but it is at the cost of dimension changing. As presented in Chapter 5, the reduction of the volume accounted for around 20-30% which was a significant change in the part dimension. Although the post-printing consolidation can strengthen the 3D printed part, it changes the character of additive manufacturing: building a near-net shape part within a short time and a single-step process. A broader parametric study of the DcAFF printing, *i.e.* wider range of the studied parameters and other non-studied parameters (*e.g.* bed temperature, raster gap or the stacking pattern), should be considered to minimize the through-thickness defects, increase inter-raster strength and precisely print the part to the desired size and shape. For a clearer understanding of the DcAFF inter-raster bonding behaviour, the mechanical response to compaction load of DcAFF material under high temperature, *e.g.* squeezing flow, spring back, *etc.*, needs to be studied through the modelling/experimental framework. This can help tune the nozzle compaction pressure (related to the nozzle height, printing speed and temperature) to improve the inter-raster strength and this will benefit the in-plane deposition accuracy mentioned above.

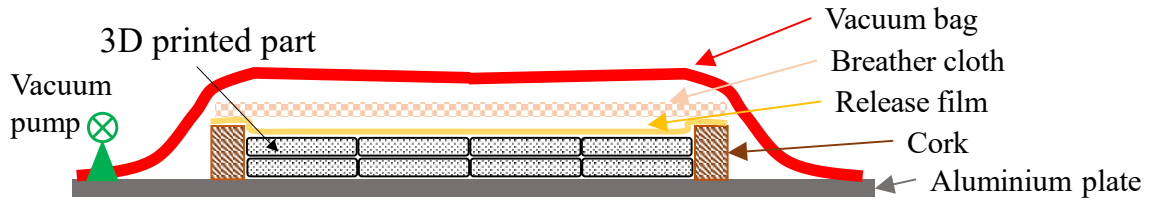


Figure 7.10 Schematic of open moulding for post-printing consolidation of the 3D printed part used in this thesis.

7.3. Performance

To complete the aim of the thesis, both the physical and mechanical performance of the produced filament were investigated and compared to other available 3D printing composite materials.

7.3.1. Fibre alignment

The fibre alignment in each filament forming step: tape, compressed filament (square) and pultruded filament (circular), were evaluated efficiently using μ CT scanner and image-processing, as presented in Chapter 4. The histograms presented in that chapter have been consolidated into the distribution curve presented here in Figure 7.11. The result shows that the designed DcAFF filament-forming machine can improve the fibre alignment from the HiPerDiF-impregnated tape. The DcAFF filament forming machine shows an increase in the amount of fibre aligned within 10° from 63% in the thin tape up to 90% in the square filament. The pultruded filament has no change in the fibre alignment from the square due to the small change in the outer shape. It can be implied that the DcAFF filament forming process can enhance the fibre alignment after the HiPerDiF process and bring the alignment to a higher level than the HiPerDiF alignment process itself achieves. However, these small fibre misalignments can diminish the material properties, so they should be minimized at every stage.

To minimize the fibre misalignment on the surface of the pre-impregnated HiPerDiF tape, a better impregnator is needed to properly infuse the matrix through the preform and cover the fibre which can prevent the movement of the fibres on the

surface. Additionally, it is crucial to minimize any contact between the tape and external surfaces, which can be achieved by designing a new conveyor system that connects the HiPerDiF machine directly to the DcAFF machine without any human interaction. To maximize the fibre alignment in the circular filament, the pultrusion process should be studied in-detail. The optimization between the pultrusion temperature, speed, and the convergent angle of the nozzle should be considered. A flow modelling of the pultrusion should offer a clear understanding of these parameters to achieve a better fibre alignment.

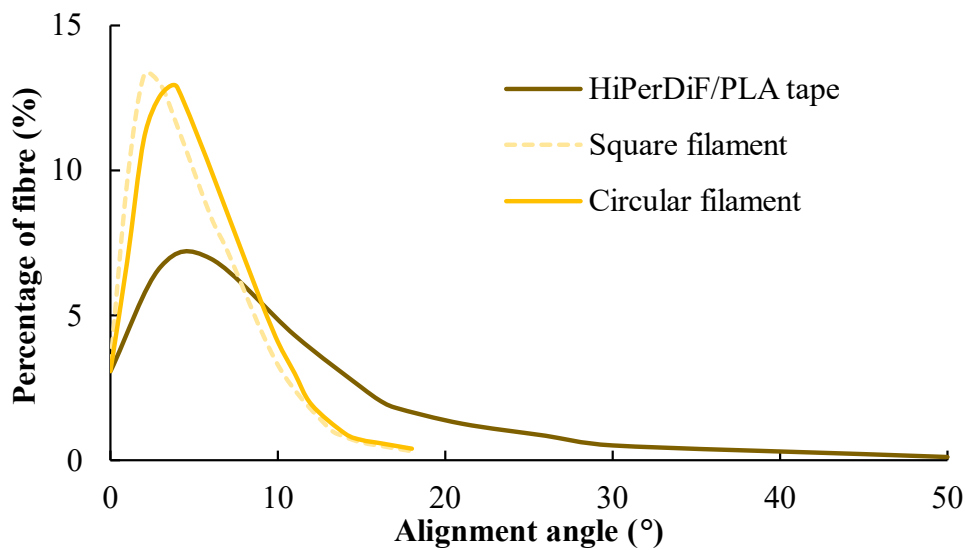


Figure 7.11 Fibre alignment distribution of HiPerDiF-PLA tape (brown), DcAFF square filament (light yellow dash) and DcAFF circular filament (yellow).

Looking forward to the alignment of the printed part, although there is no μ CT scanned result at the moment, it can be implied that the misalignment during printing could be one of the results of the reduction of the tensile properties of the printed part compared to the circular filament (Figure 7.13 below). To ensure the alignment after the deposition, it is imperative to study and optimize printing parameters such as nozzle shape (as mentioned in 2.2.11, Figure 2.16 [159]), printing temperature, speed, and layer thickness. The adjustment of these parameters is crucial in providing adequate pressure to eliminate voids in the filament and minimize back-flow, which can potentially disturb the alignment process.

7.3.2. Fibre volume fraction

The fibre content of the filament at each stage of production was measured using a well-established method, the matrix burn-off technique. The highest achievable fibre content was almost 35 wt% found in the HiPerDiF preform achieved with the lab-scale HiPerDiF machine operated at the highest machine performance; high pump speed and low conveyor belt speed. This fibre content is higher than any available short and discontinuous fibre composite filament available in the literature (~ 5-20 wt%). This is because the aligned fibre in the filament can reduce the nozzle clogging during printing. By contrast, a high amount of randomly aligned short fibre will prevent the molten matrix to flow and cause nozzle clogging, as mentioned in Chapter 2 [27, 45]. Although the high fibre content filament showed poor bed adhesion, it can be used for steering with our printing procedure. The fibre content of DcAFF can be theoretically increased to the level of thermosetting composite for the structural part (~60%) by doubling the amount of fibre in the HiPerDiF system or using a thinner thermoplastic film. Again, the higher fibre content composite may increase the viscosity and it may be difficult to pultrude to a circular shape or deposit through the printing nozzle. It will increase the bending stiffness of the filament while steering to a high curvature path creating adhere issue on the substrate. To tackle that possible problem, other filament production methods and more complicated printing techniques may need to be introduced, *e.g.* adding a compaction roller to the printing head. Hence, in this thesis, the fibre content that was the most used in the thesis is around 25 wt% which is the compromise between mechanical performance and printability.

7.3.3. Mechanical performance

This section will compare the mechanical properties, especially tensile properties, of DcAFF material in each stage of the material development with the normalised fibre content for a fair comparison and discuss the result of each filament manufacturing method and the printing procedure. Then, the tensile properties will be compared to the available composite 3D printing material in the literature including the

commercial continuous fibre filament from Markforged. The tensile stiffness and strength at each stage from manual moulding as the filament (M. Filament), single raster deposition (M. 1-Raster) and single layer printed part (M. 1-Layer) to the semi-automated filament forming machine as a filament (A. Filament), single layer printed part (A. 1-Layer) and finally the multilayer printing (A. Multi-L) were plotted in Figure 7.12 to compare the development of the filament and the different format of the DcAFF material. They were compared to the HiPerDiF-PLA as a thin tape from the previous study by Blok [47]. The post-printing consolidation results are also shown in Figure 7.12. The tensile stiffness and strength of the DcAFF in any form are normalised to 25 wt% fibre content, the most common fibre content level in this thesis. Overall, the properties of the material in different formats are in a similar range especially when they are normalised. The tape from the previous work shows the highest normalised tensile properties because of the good impregnation of the tape, good fibre distribution within the composite, and the failure of the tape that is always perpendicular to the fibre/load direction. The filaments format also failed perpendicular to the load, so their strength is relatively high. Although the filament produced from the DcAFF machine may have slightly higher performance than the manual filament owing to the higher fibre content, after normalisation, the manual and the machined filament show substantially the same properties. It can be implied that the automated method offers a similar performance filament to the 2-piece mould manual technique designed to minimise intra-filament defects. For single-layer printing, there is some failure parallel to the raster, between the raster joint, due to the poor inter-raster bonding. This brought the tensile strength down to the lowest group in the comparison. The multilayer part which has higher structural integration shows better tensile properties than the single-layer part without presenting inter-raster failure. However, layer separation, always observed in the rupture surface, prevents the multilayer strength to increase to a higher level. Removing all the through-thickness defects with the post-printing consolidation can minimise the layer separation and increase the strength of the multilayer part to the

level of the filament, making it fail perpendicularly to the load direction without layer separation. Moreover, the consolidation boosts the stiffness of the multilayer part to the highest one in the comparison.

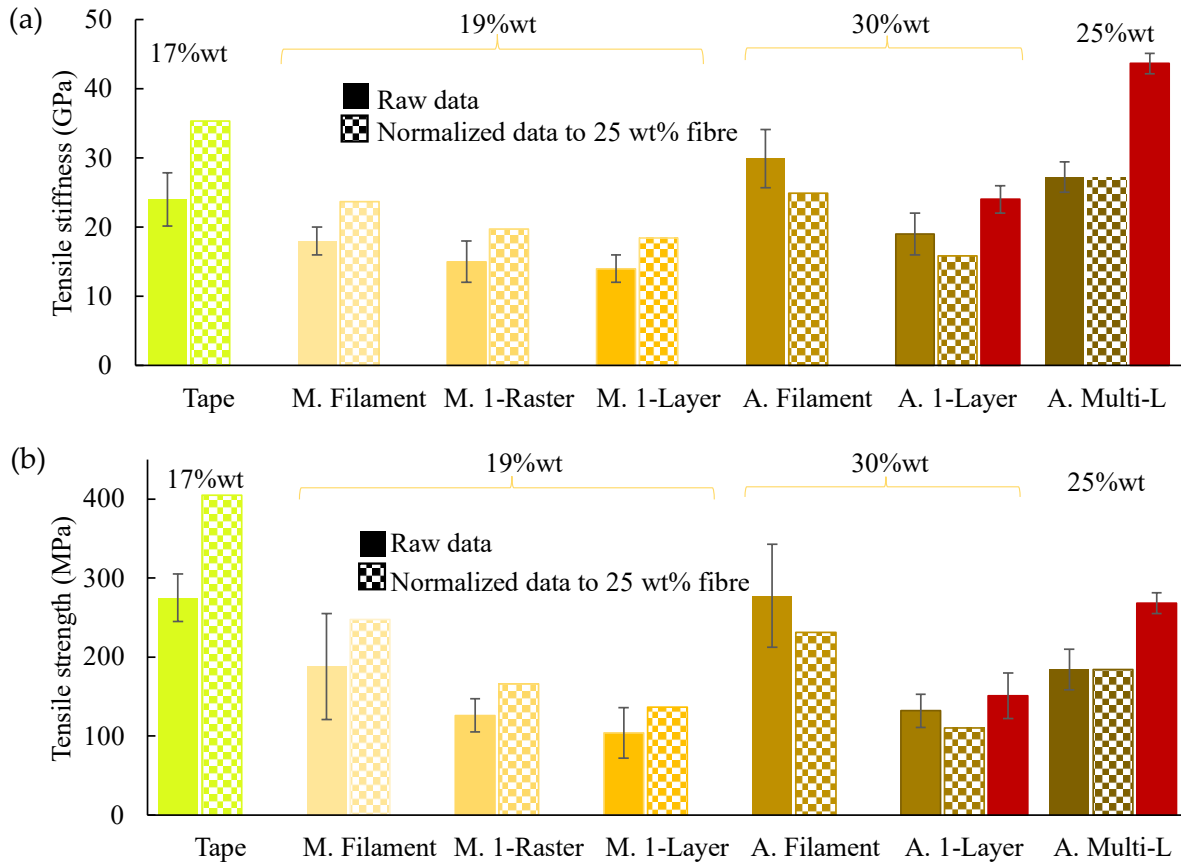


Figure 7.12 Comparison between the different manufacturing techniques and format of DcAFF: manual moulding as the filament (M. Filament), single raster deposition (M. 1-Raster) and single layer printed part (M. 1-Layer) to the semi-automated filament forming process as a filament (A. Filament), single layer printed part (A. 1-Layer) and finally the multilayer printing (A. Multi-L) showing with the properties obtained from the post-printing consolidation technique of the layer printed part (highlighted in red) comparing with the HiPerDiF/PLA tape achieved from the previous study and normalised all the as-printed part result to the fibre content 25 wt%.

The DcAFF material was compared to other composite 3D printing available in the literature presented in Table 2.2-2.4 in Chapter 2. An Asby-style plot of tensile stiffness-strength, Figure 7.13, shows that the DcAFF material shows high tensile properties in both stiffness and strength which offer a possibility to apply the

material in a wide range of applications, *i.e.* both stiffness and strength driven designs.

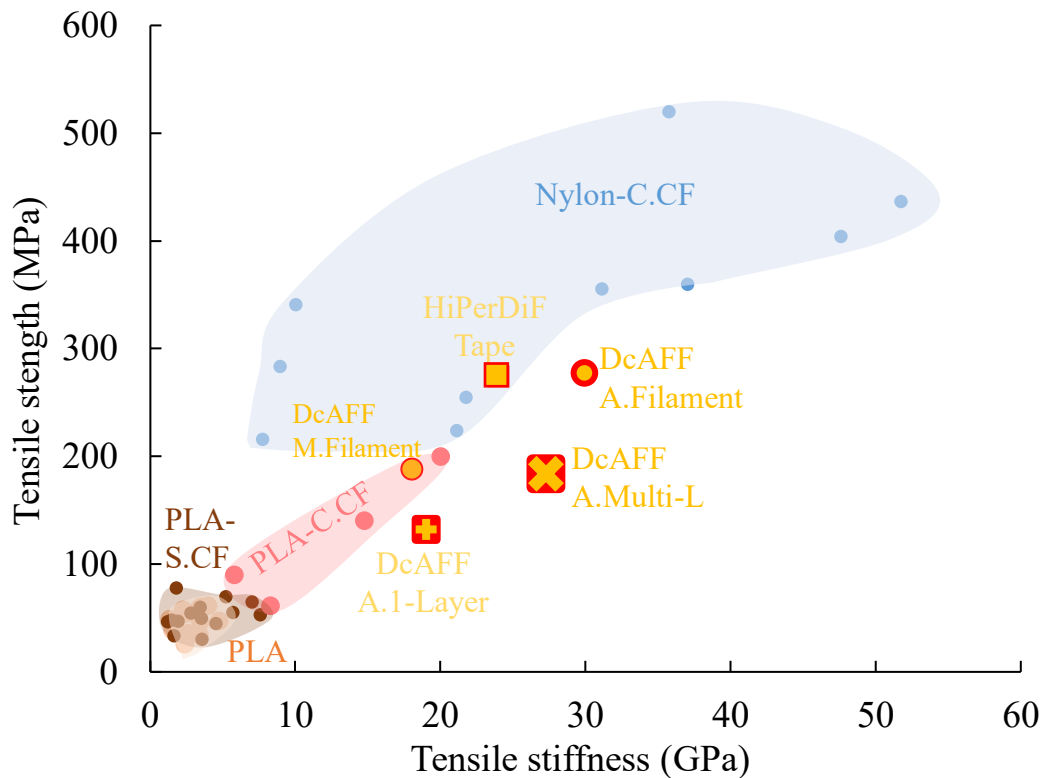


Figure 7.13 Tensile stiffness-strength plot of the available composite 3D printed part from literature: PLA [10, 20, 29, 31, 55, 56, 134, 137, 139-145], PLA-short carbon fibre (PLA-S.CF) [20, 27, 29, 70, 90, 132-137, 159], PLA-continuous carbon fibre (PLA-C.CF) [60, 61, 126, 148-150] and continuous carbon fibre nylon (Nylon-C.CF) [11, 41, 42, 122, 132, 146, 172-174], compared with our DcAFF tensile properties studied in this thesis from the thin tape, single filament forming with the manual and semi-automated technique, DcAFF printed as single-layer and the multilayer printing.

Compared to other 3D printed PLA composites (in Figure 7.13) including the continuous fibre PLA composite in the literature, the DcAFF still shows properties that are relatively higher than those. It can be implied that the use of 3-mm fibre, which is longer than fibre critical length, combined with the fibre alignment from the HiPerDiF process and the filament-forming machine, is sufficient to provide the mechanical properties of a continuous fibre 3D printed composite. Compared with the widely used commercially available 3D printing filament, *i.e.* the nylon/C.CF

manufactured by Markforged, the DcAFF has similar average tensile stiffness, but lower average tensile strength (about 60%) when looking at the multilayer sample. The lower tensile strength of the DcAFF to Markforged continuous fibre filament could be the result of (i) the relatively high fibre content of the pre-impregnated fibre filament, (ii) a better performance matrix system (*i.e.* the high degree of hydrogen bonding present in nylon) and (iii) a special surface treatment technique used by Markforged to improve nylon-carbon fibre bonding. These three fields should be considered in the further development of DcAFF to improve the quality of the produced filament.

The superior trend in the mechanical properties was also found in the SBS testing presented in Chapter 5. The DcAFF also shows a higher SBS strength to other PLA composites 3D printed parts while again being slightly lower than the Markforged nylon carbon fibre.

Apart from the good mechanical performance, the building concept of 3D printing can offer a non-catastrophic failure when fabricating an open hole feature on the structure by steering the small-diameter composite filament around the hole compared to the general material subtraction, *e.g.* cutting or drilling hole. This effect was clearly seen in the single layer, Chapter 4, as the failure turned from breaking through the hole area to the separation of the raster due to the weaker thermoplastic bonding. Since the current printing, *via* a curvilinear path, cannot show a significant increase in the open hole strength, another printing path such as the combination of a concentric ring and curvilinear path in different layers should be considered so that the combination can maintain the hole shape, delay the initial failure and offer a promising strength, as the suggested in the literature [166].

Chapter 8 Thesis conclusion

The present thesis was aimed at producing an FDM filament feedstock based on a PLA thermoplastic matrix reinforced with ADRFCs, obtained through the HiPerDiF technology, with a method that has good potential to be scaled up to an industrial and commercial level. The initial attempt was based on a manual and batch-processing approach. Then, a filament-forming machine was developed with a semi-automated approach and a clear scale-up potential. The DcAFF filament produced with this machine shows a mechanical performance comparable to or even superior to 3D printed composites reported in the literature and a good printing ability, however further work is still needed to improve the product quality and processability. The work done and the key findings are highlighted and listed below in this chapter, along with suggestions for future works.

8.1. Conclusions

The thesis aim, to produce a highly processable and high mechanical performance composite 3D printing filament reinforced with highly aligned discontinuous fibre, was achieved by working on three main study areas: production, printing and performance of the filament. The noteworthy novel outcomes of this thesis can be summarised as follows:

- Among the literature on composite 3D printing, there is no work using the aligned discontinuous fibre (ADFRC) architecture to reinforce a 3D printing material. Moreover, the available filament production and printing methods are not suitable for ADFRCs as they may demolish the aligned fibre architecture and shorten their length below the critical ratio. It is, therefore, necessary to design a new filament-forming process and develop specific printing techniques, particularly for the ADFRC filament.
- The success of the newly developed, 2-piece mould inspired the design of the industrial scalable filament-forming machine with the concept of compressing the thin tape through a tiny gap between two counter-rotating rollers. The fine-

tuned parameters of the rollers: gap, temperature and speed, resulted in a good square cross-section with low internal voids (<5% by volume). Then, the filament was pultruded through a heated nozzle to achieve a smooth surface circular cross-section filament with a diameter of ~0.8-1 mm. The DcAFF machine enhances the fibre alignment throughout the process showing that almost 90% of fibres in the final circular filament are aligned within 10° from the longitudinal axis, as demonstrated by μ CT scanning. This machine has a significantly increased production rate of around half-meter per minute. The produced material can be printed using a general 3D printer with only a nozzle change.

- The filament and the current printing procedure performed well with straight-line printing, *e.g.* a rectangular part for tensile testing, but there is an obvious deviation of the deposited raster from the defined printing path when changing the printing direction, especially the sharp turning corner or small complex geometries. The in-plane printing discrepancy was minimized with the study of first-order lag and the addition of a PI controller to generate an overshooting segment in the nozzle path that can compensate for the sliding of the raster on the printing bed after the deposition. The algorithm works well with large features, but the deviations are highlighted when printing small ones, *e.g.* circular paths with diameters smaller than 10 mm.
- The fibre content of the produced filament ranged between 15-35 wt% which is higher than any available short-fibre composite 3D printing filament available in the literature. Moreover, thanks to the high level of alignment, fibre content does not cause clogging of the nozzle during printing, as reported in the literature for the printing of high-fibre contents.
- In multilayer printing, DcAFF gives better mechanical properties, both in tension and shear, when compared to PLA/S.CF and, more importantly, PLA/C.CF composite 3D printed parts reported in the literature. This demonstrates that the produced filament can perform to the same real-world levels of performance as continuous fibre filaments.

- The curvilinear 3D printing procedure can change the open-hole tensile testing failure from catastrophic, as generally observed for parts produced by material subtraction, to non-catastrophic; the part retains its continuity and still carries a certain amount of load after the initial failure.
- The mechanical performance can be improved with post-printing consolidation which eliminates the inter-raster defects. This can increase the tensile properties by about 50% but it might cause a dimensional change of more than 20%.

8.2. Suggestions for future work

Given the user-friendliness of the filament developed in this thesis and the relatively minor modifications required to generic tabletop 3D printers, *i.e.* the nozzle changing and software update, to allow its usage as feedstock, it is the author's view that the DcAFF could be, in the future, commercialised for domestic use almost in its current state. Considering the extremely promising mechanical performance of the filament, this could be used with more finely tuneable printers to produce more structural components.

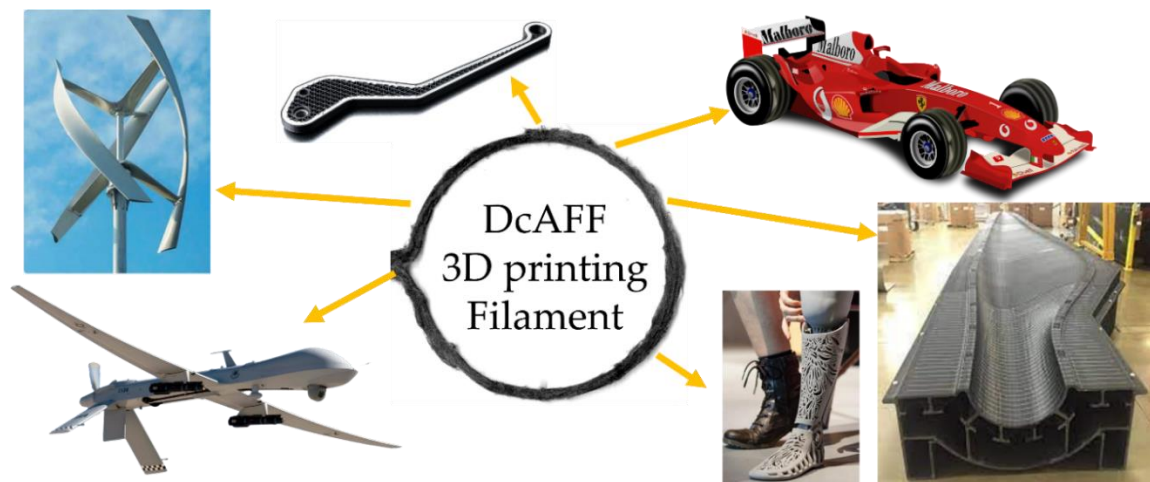


Figure 8.1 Possible application of the high-performance DcAFF filament in the future, *e.g.* automotive replacement parts [195], formula one frame [196], high-strength tooling [197], prosthesis leg [198], UVA parts [199], new design wind turbine [200].

Provided that further developments, suggested below, are successfully completed, it is envisaged that DcAFF could be used to produce one-off or small production

volumes of highly tailored parts, *e.g.* prosthesis or orthoses, mould for composite manufacturing, R&D prototypes for wind tunnels and functional testing, and on-the-go repair or replacement parts, as the examples shown in Figure 8.1. However, a possible commercialisation of DcAFF could only be considered after completing appropriate market research and production costs analysis, after full technology scale-up.

To pave the way for commercialisation, there are some scientific aspects, that have not been addressed in the thesis due to time and resource limitations in the PhD study but need to be addressed to improve performance and add more engineering value to the material. These aspects could also be considered as suggestions for those interested in furthering high-performance fibre-reinforced 3D printing.

The present thesis has demonstrated that the lab-scale 3D printing filament-forming system for ADFRCs can provide a good quality composite filament. The DcAFF machine can be scaled up to an industrial production rate using higher performance components, *e.g.* high precision machined rollers, a high potential heater, more robust motors with a precise controller, and a high wearability pultrusion nozzle. These upgrades should also improve the quality of the produced filament by reducing internal voids and improving fibre distribution.

Despite the fact that the in-plane printing accuracy of the filament was improved with the first-order lag compensation, this still cannot eliminate the discrepancy between the desired and deposited raster when printing a very small complex geometry. A first approach to improve deposition accuracy should be to increase the bed adhesion, for example by printing a first layer of neat thermoplastic or considering a dual nozzle, DcAFF and neat PLA, as seen in Markforged continuous fibre 3D printing. In terms of G-code adaptation, a real-time monitoring system, *i.e.* cameras and sensors, could be added to the 3D printing system to support a closed-loop real-time compensation algorithm and allow *in-situ* path adjustment.

In this thesis, the fibre alignment evolution was studied only during the filament-forming process, from tape to the circular filament, but there is no further study on the deposited raster. The use of μ CT scanning to study fibre alignment should be extended to the deposited raster, also considering the printing of different features should offer further insight to improve both the deposition strategy and the final mechanical performance.

Even though the tensile properties of the DcAFF are significantly better than other PLA-based 3D printing composites, the current DcAFF-PLA material provides lower performance than nylon/C.CF 3D printing. Hence, a higher-performance thermoplastic, *e.g.* nylon, poly(ether ether ketone) (PEEK), or polyetherimide (PEI, ULTEM1000), should be combined with the HiPerDiF fibres to produce a better-performance DcAFF filament. In this thesis, there is no surface treatment of the fibre. Some chemical treatments should be applied to enhance the fibre-matrix interface in order to improve the performance of the composite material. Furthermore, a more extensive characterisation campaign should be undertaken by performing a wide variety of tests, *e.g.* flexural, compressive, in-plane shear, hardness or toughness testing, to produce a data sheet for the DcAFF material.

The performance of the 3D printed part remarkably increases with the post-printing consolidation on an open mould, but it is at the cost of dimension reduction due to the elimination of a large amount of through-thickness voids. A more precise printing, which offers a minimum of the through-thickness voids, plus a closed moulding consolidation should be considered to retain the initial dimension and improve the performance of the printed part.

Appendix A: Microscopic method

The sample for microscopic inspection was cut to a proper size at the interesting position and prepared for potting in Prime 27 epoxy with a slow hardener following a heat treatment to harden the resin in an oven at 70°C for 1 hour. After the potted sample was removed from the mould, it was polished using Bulher EcoMet™ 30 Semi-Automatic Grinder Polisher following a polishing sequence suggested by Buehler® [201]. The polishing step is shown in Table A1. After the final washing, the polished samples were inspected with a Carl Zeiss™ Microscope with different magnifications depending on the type of the samples.

Table A1 Polishing step for microscopy (CW-clockwise, CCW-counter clockwise)

Abrasive	Solution	Load (N)	Base speed	Head speed	Time (min:sec)
Silicon Carbide Sandpaper P400 grit	water-cooled	25	30 CW	330 CW	Until flat
Silicon Carbide Sandpaper P1200 grit	water-cooled	25	30 CW	330 CCW	2
MicroCloth	9µm MetaDi Supreme Diamond	25	30 CW	120 CCW	5
MicroCloth	3µm MetaDi Supreme Diamond	25	30 CW	180 CW	5
MicroCloth	0.05µm MasterPrep Alumina	25	30 CW	120 CCW	1:30

References

- [1] N. Krajangsawasdi, L. G. Blok, I. Hamerton, M. L. Longana, B. K. S. Woods, and D. S. Ivanov, "Fused Deposition Modelling of Fibre Reinforced Polymer Composites: A Parametric Review," *Journal of Composites Science*, vol. 5, no. 1, p. 29, 2021. [Online]. Available: <https://www.mdpi.com/2504-477X/5/1/29>.
- [2] N. Krajangsawasdi, M. L. Longana, I. Hamerton, B. K. Woods, and D. S. Ivanov, "Batch production and fused filament fabrication of highly aligned discontinuous fibre thermoplastic filaments," *Additive Manufacturing*, vol. 48, p. 102359, 2021.
- [3] N. Krajangsawasdi, I. Hamerton, B. K. S. Woods, D. S. Ivanov, and M. L. Longana, "Open Hole Tension of 3D Printed Aligned Discontinuous Composites," *Materials*, vol. 15, no. 23, p. 8698, 2022. [Online]. Available: <https://www.mdpi.com/1996-1944/15/23/8698>.
- [4] N. Krajangsawasdi *et al.*, "DcAFF (Discontinuous Aligned Fibre Filament)–Investigation of mechanical properties of multilayer composites from 3D printing," *Composites Part B: Engineering*, p. 110903, 2023.
- [5] N. Krajangsawasdi, D. H. Nguyen, I. Hamerton, B. K. Woods, D. S. Ivanov, and M. L. Longana, "Steering Potential for Printing Highly Aligned Discontinuous Fibre Composite Filament," *Materials*, vol. 16, no. 8, p. 3279, 2023.
- [6] P. Parandoush and D. Lin, "A review on additive manufacturing of polymer-fiber composites," *Composite Structures*, vol. 182, pp. 36-53, 2017, doi: <https://doi.org/10.1016/j.compstruct.2017.08.088>.
- [7] T. D. Ngo, A. Kashani, G. Imbalzano, K. T. Q. Nguyen, and D. Hui, "Additive manufacturing (3D printing): A review of materials, methods, applications and challenges," *Composites Part B: Engineering*, vol. 143, pp. 172-196, 2018, doi: <https://doi.org/10.1016/j.compositesb.2018.02.012>.
- [8] J. Frketic, T. Dickens, and S. Ramakrishnan, "Automated manufacturing and processing of fiber-reinforced polymer (FRP) composites: An additive review of contemporary and modern techniques for advanced materials manufacturing," *Additive Manufacturing*, vol. 14, pp. 69-86, 2017, doi: <https://doi.org/10.1016/j.addma.2017.01.003>.
- [9] H. J. O'Connor and D. P. Dowling, "Low-pressure additive manufacturing of continuous fiber-reinforced polymer composites," *Polymer Composites*, vol. 40, no. 11, pp. 4329-4339, 2019.
- [10] N. Vinoth Babu *et al.*, "Influence of slicing parameters on surface quality and mechanical properties of 3D-printed CF/PLA composites fabricated by FDM technique," *Materials Technology*, pp. 1-18, 2021.
- [11] J. M. Chacón, M. A. Caminero, P. J. Núñez, E. García-Plaza, I. García-Moreno, and J. M. Reverte, "Additive manufacturing of continuous fibre reinforced thermoplastic composites using fused deposition modelling: Effect of process parameters on mechanical properties," *Composites Science and Technology*, vol. 181, p. 107688, 2019, doi: <https://doi.org/10.1016/j.compscitech.2019.107688>.
- [12] W. Zhang *et al.*, "Interfacial bonding strength of short carbon fiber/acrylonitrile-butadiene-styrene composites fabricated by fused deposition modeling," *Composites Part B: Engineering*, vol. 137, pp. 51-59, 2018, doi: <https://doi.org/10.1016/j.compositesb.2017.11.018>.
- [13] C. Yang, X. Tian, T. Liu, Y. Cao, and D. Li, "3D printing for continuous fiber reinforced thermoplastic composites: mechanism and performance," *Rapid Prototyping Journal*, vol. 23, no. 1, pp. 209-215, 2017, doi: <https://doi.org/10.1108/RPJ-08-2015-0098>.
- [14] G. N. Levy, R. Schindel, and J.-P. Kruth, "Rapid manufacturing and rapid tooling with layer manufacturing (LM) technologies, state of the art and future perspectives," *CIRP annals*, vol. 52, no. 2, pp. 589-609, 2003, doi: [https://doi.org/10.1016/S0007-8506\(07\)60206-6](https://doi.org/10.1016/S0007-8506(07)60206-6).
- [15] X. Wang, M. Jiang, Z. Zhou, J. Gou, and D. Hui, "3D printing of polymer matrix composites: A review and prospective," *Composites Part B: Engineering*, vol. 110, pp. 442-458, 2017, doi: <https://doi.org/10.1016/j.compositesb.2016.11.034>.
- [16] N. Kumar, P. K. Jain, P. Tandon, and P. M. Pandey, "The effect of process parameters on tensile behavior of 3D printed flexible parts of ethylene vinyl acetate (EVA)," *Journal of Manufacturing Processes*, vol. 35, pp. 317-326, 2018, doi: <https://doi.org/10.1016/j.jmapro.2018.08.013>.
- [17] P. Bettini, G. Alitta, G. Sala, and L. Di Landro, "Fused deposition technique for continuous fiber reinforced thermoplastic," *Journal of Materials Engineering and Performance*, vol. 26, no. 2, pp. 843-848, 2017, doi: <https://doi.org/10.1007/s11665-016-2459-8>.
- [18] J. M. Gardner *et al.*, "Additive Manufacturing of Multifunctional Components using High Density Carbon Nanotube Yarn Filaments," NASA Langley Research Center, Hampton, VA, 2016.
- [19] W. Zhong, F. Li, Z. Zhang, L. Song, and Z. Li, "Short fiber reinforced composites for fused deposition modeling," *Materials Science and Engineering: A*, vol. 301, no. 2, pp. 125-130, 2001, doi: [https://doi.org/10.1016/S0921-5093\(00\)01810-4](https://doi.org/10.1016/S0921-5093(00)01810-4).

- [20] M. Ivey, G. W. Melenka, J. P. Carey, and C. Ayranci, "Characterizing short-fiber-reinforced composites produced using additive manufacturing," *Advanced Manufacturing: Polymer & Composites Science*, vol. 3, no. 3, pp. 81-91, 2017, doi: <https://doi.org/10.1080/20550340.2017.1341125>.
- [21] T. Isobe, T. Tanaka, T. Nomura, and R. Yuasa, "Comparison of strength of 3D printing objects using short fiber and continuous long fiber," in *IOP Conference Series: Materials Science and Engineering*, 2018, vol. 406: IOP Publishing, 2018, p. 012042, doi: <https://doi.org/10.1088%2F1757-899x%2F406%2F1%2F012042>.
- [22] A. K. Sood, R. K. Ohdar, and S. S. Mahapatra, "Parametric appraisal of mechanical property of fused deposition modelling processed parts," *Materials and Design*, vol. 31, no. 1, pp. 287-295, 2009, doi: <https://doi.org/10.1016/j.matdes.2009.06.016>.
- [23] G. Sodeifian, S. Ghaseminejad, and A. A. Yousefi, "Preparation of polypropylene/short glass fiber composite as Fused Deposition Modeling (FDM) filament," *Results in Physics*, vol. 12, pp. 205-222, 2019, doi: <https://doi.org/10.1016/j.rinp.2018.11.065>.
- [24] P. Geng *et al.*, "Effects of extrusion speed and printing speed on the 3D printing stability of extruded PEEK filament," *Journal of Manufacturing Processes*, vol. 37, pp. 266-273, 2019, doi: <https://doi.org/10.1016/j.jmapro.2018.11.023>.
- [25] W. Wu, P. Geng, G. Li, D. Zhao, H. Zhang, and J. Zhao, "Influence of layer thickness and raster angle on the mechanical properties of 3D-printed PEEK and a comparative mechanical study between PEEK and ABS," *Materials*, vol. 8, no. 9, pp. 5834-5846, 2015, doi: <https://doi.org/10.3390/ma8095271>.
- [26] J. V. Silva and R. A. Rezende, "Additive Manufacturing and its future impact in logistics," *IFAC Proceedings Volumes*, vol. 46, no. 24, pp. 277-282, 2013, doi: <https://doi.org/10.3182/20130911-3-BR-3021.00126>.
- [27] L. Sang, S. Han, Z. Li, X. Yang, and W. Hou, "Development of short basalt fiber reinforced polylactide composites and their feasible evaluation for 3D printing applications," *Composites Part B: Engineering*, vol. 164, pp. 629-639, 2019, doi: <https://doi.org/10.1016/j.compositesb.2019.01.085>.
- [28] Y. Magdum, D. Pandey, A. Bankar, S. Harshe, V. Parab, and M. Kadam, "Process Parameter Optimization for FDM 3D Printer," *International Research Journal of Engineering and Technology (IRJET)*, vol. 6, pp. 1-6, 2019.
- [29] R. T. L. Ferreira, I. C. Amatte, T. A. Dutra, and D. Burger, "Experimental characterization and micrography of 3D printed PLA and PLA reinforced with short carbon fibers," *Composites Part B: Engineering*, vol. 124, pp. 88-100, 2017, doi: <https://doi.org/10.1016/j.compositesb.2017.05.013>.
- [30] M. Shofner, K. Lozano, F. Rodriguez-Macias, and E. Barrera, "Nanofiber-reinforced polymers prepared by fused deposition modeling," *Journal of Applied Polymer Science*, vol. 89, no. 11, pp. 3081-3090, 2003, doi: <https://doi.org/10.1002/app.12496>.
- [31] A. Lanzotti, E. Pei, M. Grasso, G. Staiano, and M. Martorelli, "The impact of process parameters on mechanical properties of parts fabricated in PLA with an open-source 3-D printer," *Rapid Prototyping Journal*, vol. 21, no. 5, pp. 604-617, 2015, doi: <https://doi.org/10.1108/RPJ-09-2014-0135>.
- [32] J. Cantrell *et al.*, "Experimental characterization of the mechanical properties of 3D-printed ABS and polycarbonate parts," *Rapid Prototyping Journal*, 2017, doi: <https://doi.org/10.1108/RPJ-03-2016-0042>.
- [33] A. R. T. Perez, D. A. Roberson, and R. B. Wicker, "Fracture surface analysis of 3D-printed tensile specimens of novel ABS-based materials," *Journal of Failure Analysis and Prevention*, vol. 14, no. 3, pp. 343-353, 2014, doi: <https://doi.org/10.1007/s11668-014-9803-9>.
- [34] G. C. Onwubolu and F. Rayegani, "Characterization and optimization of mechanical properties of ABS parts manufactured by the fused deposition modelling process," *International Journal of Manufacturing Engineering*, 2014.
- [35] K. J. Christiyan, U. Chandrasekhar, and K. Venkateswarlu, "A study on the influence of process parameters on the Mechanical Properties of 3D printed ABS composite," in *IOP Conference Series: Materials Science and Engineering*, 2016, vol. 114: IOP Publishing, p. 012109.
- [36] R. Walter, K. Friedrich, and M. Gurka, "Characterization of mechanical properties of additively manufactured polymers and composites," in *AIP Conference Proceedings*, 2018, vol. 1981: AIP Publishing LLC, p. 020033, doi: <https://doi.org/10.1063/1.5045895>.
- [37] G. Liao *et al.*, "Properties of oriented carbon fiber/polyamide 12 composite parts fabricated by fused deposition modeling," *Materials & Design*, vol. 139, pp. 283-292, 2018, doi: <https://doi.org/10.1016/j.matdes.2017.11.027>.
- [38] S. S. Banerjee, S. Burbine, N. Kodihalli Shivaprakash, and J. Mead, "3D-printable PP/SEBS thermoplastic elastomeric blends: Preparation and properties," *Polymers*, vol. 11, no. 2, p. 347, 2019.
- [39] A. W. Gebisa and H. G. Lemu, "Influence of 3D Printing FDM Process Parameters on Tensile Property of ULTEM 9085," *Procedia Manufacturing*, vol. 30, pp. 331-338, 2019, doi:

- <https://doi.org/10.1016/j.promfg.2019.02.047>.
- [40] S. Wickramasinghe, T. Do, and P. Tran, "FDM-based 3D printing of polymer and associated composite: A review on mechanical properties, defects and treatments," *Polymers*, vol. 12, no. 7, p. 1529, 2020.
 - [41] M. Mohammadizadeh, A. Imeri, I. Fidan, and M. Elkelany, "3D printed fiber reinforced polymer composites-Structural analysis," *Composites Part B: Engineering*, vol. 175, p. 107112, 2019, doi: <https://doi.org/10.1016/j.compositesb.2019.107112>.
 - [42] F. Van Der Kluft, Y. Koga, A. Todoroki, M. Ueda, Y. Hirano, and R. Matsuzaki, "3D printing of continuous carbon fibre reinforced thermo-plastic (CFRTP) tensile test specimens," *Open Journal of Composite Materials*, vol. 6, no. 1, pp. 18-27, 2016, doi: <http://dx.doi.org/10.4236/ojcm.2016.61003>.
 - [43] L. G. Blok, M. L. Longana, H. Yu, and B. K. Woods, "An investigation into 3D printing of fibre reinforced thermoplastic composites," *Additive Manufacturing*, vol. 22, pp. 176-186, 2018, doi: <https://doi.org/10.1016/j.addma.2018.04.039>.
 - [44] L. J. Love *et al.*, "The importance of carbon fiber to polymer additive manufacturing," *Journal of Materials Research*, vol. 29, no. 17, pp. 1893-1898, 2014, doi: <https://doi.org/10.1557/jmr.2014.212>.
 - [45] H. L. Tekinalp *et al.*, "Highly oriented carbon fiber--polymer composites via additive manufacturing," *Composites Science and Technology*, vol. 105, pp. 144-150, 2014, doi: <https://doi.org/10.1016/j.compscitech.2014.10.009>.
 - [46] M. Such, C. Ward, and K. Potter, "Aligned discontinuous fibre composites: a short history," *Journal of Multifunctional Composites*, vol. 2, no. 3, pp. 155-168, 2014.
 - [47] L. G. Blok, M. L. Longana, and B. K. S. Woods, "Fabrication and characterisation of aligned discontinuous carbon fibre reinforced thermoplastics for automated manufacture," *Materials*, vol. 13, no. 20, p. 4671, 2020, doi: <https://doi.org/10.3390/ma13204671>. Multidisciplinary Digital Publishing Institute.
 - [48] H. Yu, K. D. Potter, and M. R. Wisnom, "A novel manufacturing method for aligned discontinuous fibre composites (High Performance-Discontinuous Fibre method)," *Composites Part A: Applied Science and Manufacturing*, vol. 65, pp. 175-185, 2014, doi: <https://doi.org/10.1016/j.compositesa.2014.06.005>.
 - [49] J. Tang *et al.*, "Hybrid composites of aligned discontinuous carbon fibers and self-reinforced polypropylene under tensile loading," *Composites Part A: Applied Science and Manufacturing*, vol. 123, pp. 97-107, 2019.
 - [50] L. G. Blok, "Development of improved fibre reinforced feedstocks for high performance 3D printing," University of Bristol, 2020.
 - [51] X. Tian, T. Liu, C. Yang, Q. Wang, and D. Li, "Interface and performance of 3D printed continuous carbon fiber reinforced PLA composites," *Composites Part A: Applied Science and Manufacturing*, vol. 88, pp. 198-205, 2016, doi: <https://doi.org/10.1016/j.compositesa.2016.05.032>.
 - [52] F. Ning, W. Cong, Y. Hu, and H. Wang, "Additive manufacturing of carbon fiber-reinforced plastic composites using fused deposition modeling: Effects of process parameters on tensile properties," *Journal of Composite Materials*, vol. 51, no. 4, pp. 451-462, 2017, doi: <https://doi.org/10.1177/0021998316646169>.
 - [53] B. Brenken, E. Barocio, A. Favaloro, V. Kunc, and R. B. Pipes, "Fused filament fabrication of fiber-reinforced polymers: A review," *Additive Manufacturing*, vol. 21, pp. 1-16, 2018, doi: <https://doi.org/10.1016/j.addma.2018.01.002>.
 - [54] F. Ning, W. Cong, J. Qiu, J. Wei, and S. Wang, "Additive manufacturing of carbon fiber reinforced thermoplastic composites using fused deposition modeling," *Composites Part B: Engineering*, vol. 80, pp. 369-378, 2015, doi: <https://doi.org/10.1016/j.compositesb.2015.06.013>.
 - [55] G. Cicala, D. Giordano, C. Tosto, G. Filippone, A. Recca, and I. Blanco, "Polylactide (PLA) filaments a biobased solution for additive manufacturing: Correlating rheology and thermomechanical properties with printing quality," *Materials*, vol. 11, no. 7, p. 1191, 2018, doi: <https://doi.org/10.3390/ma11071191>.
 - [56] Y. Song, Y. Li, W. Song, K. Yee, K.-Y. Lee, and V. L. Tagarielli, "Measurements of the mechanical response of unidirectional 3D-printed PLA," *Materials & Design*, vol. 123, pp. 154-164, 2017, doi: <https://doi.org/10.1016/j.matdes.2017.03.051>.
 - [57] K. J. Christiyen, U. Chandrasekhar, and K. Venkateswarlu, "A study on the influence of process parameters on the Mechanical Properties of 3D printed ABS composite," in *IOP Conference Series: Materials Science and Engineering*, 2016, vol. 114, no. 1: IOP Publishing, 2016, p. 012109, doi: <https://doi.org/10.1088%2F1757-899x%2F114%2F1%2F012109>.
 - [58] M. Caminero, J. M. Chacón, I. García-Moreno, and G. P. Rodríguez, "Impact damage resistance of 3D printed continuous fibre reinforced thermoplastic composites using fused deposition modelling," *Composites Part B: Engineering*, vol. 148, pp. 93-103, 2018, doi: <https://doi.org/10.1016/j.compositesb.2018.04.054>.

- [59] C. E. Duty, T. Drye, and A. Franc, "Material development for tooling applications using big area additive manufacturing (BAAM)," Oak Ridge National Lab.(ORNL), Oak Ridge, TN (United States). Manufacturing Demonstration Facility (MDF), 2015.
- [60] R. Matsuzaki *et al.*, "Three-dimensional printing of continuous-fiber composites by in-nozzle impregnation," *Scientific reports*, vol. 6, p. 23058, 2016, doi: <https://doi.org/10.1038/srep23058>.
- [61] M. Namiki, M. Ueda, A. Todoroki, and Y. Hirano, "3D printing of continuous fiber reinforced plastic," in *SAMPE 2014, International SAMPE Symposium and Exhibition*, Seattle, WA, USA, 2–5 June 2014 2014, Seattle, United States: Society for the Advancement of Material and Process Engineering (SAMPE).
- [62] Z. Hou, X. Tian, J. Zhang, and D. Li, "3D printed continuous fibre reinforced composite corrugated structure," *Composite Structures*, vol. 184, pp. 1005-1010, 2018, doi: <https://doi.org/10.1016/j.compstruct.2017.10.080>.
- [63] D. Yang, H. Zhang, J. Wu, and E. D. McCarthy, "Fibre flow and void formation in 3D printing of short-fibre reinforced thermoplastic composites: An experimental benchmark exercise," *Additive Manufacturing*, vol. 37, p. 101686, 2021.
- [64] B. N. Turner, R. Strong, and S. A. Gold, "A review of melt extrusion additive manufacturing processes: I. Process design and modeling," *Rapid Prototyping Journal*, vol. 20, no. 3, pp. 192-204, 2014, doi: <https://doi.org/10.1108/RPJ-01-2013-0012>.
- [65] Q. Sun, G. Rizvi, C. Bellehumeur, and P. Gu, "Effect of processing conditions on the bonding quality of FDM polymer filaments," *Rapid Prototyping Journal*, vol. 14, no. 2, pp. 72-80, 2008, doi: <https://doi.org/10.1108/13552540810862028>.
- [66] M. A. Nazan, F. R. Ramli, M. R. Alkahari, M. N. Sudin, and M. Abdullah, "Process parameter optimization of 3D printer using response surface method," *ARPJ Journal of Engineering and Applied Sciences*, vol. 12, no. 7, pp. 2291-2296, 2017.
- [67] W. C. Smith and R. W. Dean, "Structural characteristics of fused deposition modeling polycarbonate material," *Polymer testing*, vol. 32, no. 8, pp. 1306-1312, 2013, doi: <https://doi.org/10.1016/j.polymertesting.2013.07.014>.
- [68] I. Durgun and R. Ertan, "Experimental investigation of FDM process for improvement of mechanical properties and production cost," *Rapid Prototyping Journal*, 2014, doi: <https://doi.org/10.1108/RPJ-10-2012-0091>.
- [69] C. E. Duty *et al.*, "Structure and mechanical behavior of Big Area Additive Manufacturing (BAAM) materials," *Rapid Prototyping Journal*, 2017, doi: <https://doi.org/10.1108/RPJ-12-2015-0183>.
- [70] Q. Ding, X. Li, D. Zhang, G. Zhao, and Z. Sun, "Anisotropy of poly (lactic acid)/carbon fiber composites prepared by fused deposition modeling," *Journal of Applied Polymer Science*, vol. 137, no. 23, p. 48786, 2020, doi: <https://doi.org/10.1002/app.48786>.
- [71] K. Wang *et al.*, "Flexure behaviors of ABS-based composites containing carbon and Kevlar fibers by material extrusion 3D printing," *Polymers*, vol. 11, no. 11, p. 1878, 2019, doi: <https://doi.org/10.3390/polym11111878>.
- [72] N. Hill and M. Haghi, "Deposition direction-dependent failure criteria for fused deposition modeling polycarbonate," *Rapid Prototyping Journal*, vol. 20, no. 3, pp. 221-227, 2014, doi: <https://doi.org/10.1108/RPJ-04-2013-0039>.
- [73] O. S. Carneiro, A. Silva, and R. Gomes, "Fused deposition modeling with polypropylene," *Materials & Design*, vol. 83, pp. 768-776, 2015, doi: <https://doi.org/10.1016/j.matdes.2015.06.053>.
- [74] M. Dawoud, I. Taha, and S. J. Ebeid, "Mechanical behaviour of ABS: An experimental study using FDM and injection moulding techniques," *Journal of Manufacturing Processes*, vol. 21, pp. 39-45, 2016, doi: <https://doi.org/10.1016/j.jmapro.2015.11.002>.
- [75] M. S. Hossain, J. Ramos, D. Espalin, M. Perez, and R. Wicker, "Improving tensile mechanical properties of FDM-manufactured specimens via modifying build parameters," in *International Solid Freeform Fabrication Symposium: An Additive Manufacturing Conference.*, Austin, TX, 2013, vol. 2013, pp. 380-392.
- [76] M. E. A. Papon, A. Haque, and R. S. MA, "Effect of nozzle geometry on melt flow simulation and structural property of thermoplastic nanocomposites in fused deposition modeling," in *Proc. American society for composites, Thirty-second technical conference*, 2017.
- [77] R. Comminal, M. Serdeczny, D. Pedersen, and J. Spangenberg, "Numerical modeling of the material deposition and contouring precision in fused deposition modeling," in *Proceedings of the 29th Annual International Solid Freeform Fabrication Symposium*, Austin, TX, USA, 2018, pp. 13-15.
- [78] R. Comminal, M. P. Serdeczny, D. B. Pedersen, and J. Spangenberg, "Motion planning and numerical simulation of material deposition at corners in extrusion additive manufacturing," *Additive Manufacturing*, vol. 29, p. 100753, 2019, doi: <https://doi.org/10.1016/j.addma.2019.06.005>.
- [79] J. F. Rodríguez, J. P. Thomas, and J. E. Renaud, "Mechanical behavior of acrylonitrile butadiene styrene

- (ABS) fused deposition materials. Experimental investigation," *Rapid Prototyping Journal*, 2001.
- [80] M. Too *et al.*, "Investigation of 3D non-random porous structures by fused deposition modelling," *The International Journal of Advanced Manufacturing Technology*, vol. 19, pp. 217-223, 2002.
 - [81] A. Bagsik, V. Schöppner, and E. Klemp, "FDM part quality manufactured with Ultem* 9085," in *14th international scientific conference on polymeric materials*, 2010, vol. 15, pp. 307-315.
 - [82] R. Anitha, S. Arunachalam, and P. Radhakrishnan, "Critical parameters influencing the quality of prototypes in fused deposition modelling," *Journal of Materials Processing Technology*, vol. 118, no. 1-3, pp. 385-388, 2001, doi: [https://doi.org/10.1016/S0924-0136\(01\)00980-3](https://doi.org/10.1016/S0924-0136(01)00980-3).
 - [83] D. Croccolo, M. De Agostinis, and G. Olmi, "Experimental characterization and analytical modelling of the mechanical behaviour of fused deposition processed parts made of ABS-M30," *Computational Materials Science*, vol. 79, pp. 506-518, 2013, doi: <https://doi.org/10.1016/j.commatsci.2013.06.041>.
 - [84] E. Verdejo de Toro, J. Coello Sobrino, A. Martínez Martínez, V. Miguel Eguía, and J. Ayllón Pérez, "Investigation of a Short Carbon Fibre-Reinforced Polyamide and Comparison of Two Manufacturing Processes: Fused Deposition Modelling (FDM) and Polymer Injection Moulding (PIM)," *Materials*, vol. 13, no. 3, p. 672, 2020, doi: <https://doi.org/10.3390/ma13030672>.
 - [85] E. Yasa and K. Ersoy, "Dimensional Accuracy and Mechanical Properties of Chopped Carbon Reinforced Polymers Produced by Material Extrusion Additive Manufacturing," *Materials*, vol. 12, no. 23, p. 3885, 2019, doi: <https://doi.org/10.3390/ma12233885>.
 - [86] E. Yasa, "Anisotropic impact toughness of chopped carbon fiber reinforced nylon fabricated by material-extrusion-based additive manufacturing," *Anadolu University of Sciences & Technology-A: Applied Sciences & Engineering*, vol. 20, no. 2, 2019, doi: <https://doi.org/10.18038/auabtda.498606>.
 - [87] A. K. Aworinde, S. O. Adeosun, F. A. Oyawale, E. T. Akinlabi, and S. A. Akinlabi, "Parametric Effects of Fused Deposition Modelling on the Mechanical Properties of Polylactide Composites: A Review," in *Journal of Physics: Conference Series*, 2019, vol. 1378, no. 2: IOP Publishing, p. 022060.
 - [88] MarkForged. "MarkForged Visual Troubleshooting Guide." MarkForged. <https://support.markforged.com/hc/en-us/articles/205927119-MarkForged-Visual-Troubleshooting-Guide> (accessed 25 March 2020).
 - [89] N. A. Sukindar, M. K. A. Ariffin, B. H. T. Baharudin, C. N. A. Jaafar, and M. I. S. Ismail, "Analyzing the effect of nozzle diameter in fused deposition modeling for extruding polylactic acid using open source 3D printing," *Jurnal Teknologi*, vol. 78, no. 10, 2016, doi: <https://doi.org/10.11113/jt.v78.6265>.
 - [90] E. A. Papon, A. Haque, and S. K. Spear, "Effects of functionalization and annealing in enhancing the interfacial bonding and mechanical properties of 3D printed fiber-reinforced composites," *Materials Today Communications*, vol. 25, p. 101365, 2020.
 - [91] 3D Matter. "What is the best type of plastic for my 3D printing application?" <https://my3dmatter.com/what-is-the-best-type-of-plastic-for-my-3d-printing-application/> (accessed 11 March 2020).
 - [92] 3D Matter. "FDM 3D Printing materials compared." 3D Hubs. <https://www.3dhubs.com/knowledge-base/fdm-3d-printing-materials-compared/> (accessed 20 March 2020).
 - [93] Ultimaker. "Technical data sheet PLA." Ultimaker. <https://ultimaker.com/download/74599/UM180821%20TDS%20PLA%20RB%20V10.pdf> (accessed 15 March 2020).
 - [94] K. Giang. "PLA vs. ABS: What's the difference?" 3dhubs. <https://www.3dhubs.com/knowledge-base/pla-vs-abs-whats-difference/> (accessed 16 March 2020).
 - [95] SD3D Printing. "Technical Data Sheet PLA." SD3D Printing. https://www.sd3d.com/wp-content/uploads/2017/06/MaterialTDS-PLA_01.pdf (accessed 15 March 2020).
 - [96] L. MatWeb. "Overview of materials for Polylactic Acid (PLA) Biopolymer." <http://www.matweb.com/search/DataSheet.aspx?MatGUID=ab96a4c0655c4018a8785ac4031b9278> (accessed 1 May 2020).
 - [97] Simplify3D. "Filament Properties Table." Simplify3D. <https://www.simplify3d.com/support/materials-guide/properties-table/> (accessed 15 March 2020).
 - [98] Ultimaker. "Technical data sheet ABS." Ultimaker. <https://ultimaker.com/download/74640/UM180821%20TDS%20ABS%20RB%20V11.pdf> (accessed 15 March 2020).
 - [99] T. Rogers. "Everything You Need to Know About ABS Plastic." Creative Mechanisms Blog <https://www.creativemechanisms.com/blog/everything-you-need-to-know-about-abs-plastic> (accessed 18 February 2020).
 - [100] B. O'Neal. "Navigating Through the Selection of 3D Printing Materials: Know Your Strengths!" <https://3dprint.com/>. <https://3dprint.com/42417/3d-printing-material-strengths/> (accessed 6 March 2020).
 - [101] L. Chilson. "Comparison of typical 3D printing materials [1]." <http://2015.igem.org/wiki/images/2/24/CamJIC-Specs-Strength.pdf> (accessed 16 February 2020).
 - [102] Ultimaker. "Technical data sheet PP." Ultimaker. <https://ultimaker.com/download/74977/UM180821%20TDS%20PP%20RB%20V11.pdf> (accessed 15 March 2020).

- [103] Engineering ToolBox. "Young's Modulus - Tensile and Yield Strength for common Materials." https://www.engineeringtoolbox.com/young-modulus-d_417.html (accessed 1 May 2020).
- [104] Designerdata. "PP." [https://designerdata.nl/materials/plastics/thermo-plastics/polypropylene-\(cop.\)](https://designerdata.nl/materials/plastics/thermo-plastics/polypropylene-(cop.)) (accessed 1 May 2020).
- [105] Vexma Technologies. "Polycarbonate (PC)." Vexma Technologies Pvt Ltd <https://vexmatech.com/PC-polycarbonate-FDM-technology-3dprinting-material.html> (accessed 8 March 2020).
- [106] Ultimaker. "Technical data sheet PC." Ultimaker. <https://ultimaker.com/download/74975/UM180821%20TDS%20PC%20RB%20V11.pdf> (accessed 20 March 2020).
- [107] Javelin. "PC (Polycarbonate)." <https://www.javelin-tech.com/3d/stratasys-materials/pc/> (accessed 1 May 2020).
- [108] Stratasys. "FORTUS PC (Polycarbonate)." http://producto3d.com/wp-content/uploads/2018/01/FDM_PCPPropertiesReport.pdf (accessed 1 May 2020).
- [109] BCN3D. "Unlock a wide range of applications with the revamped industrial-grade BCN3D Filaments portfolio." <https://www.bcn3d.com/revamped-industrial-grade-bcn3d-basf-mitsubishi-filaments-portfolio/> (accessed 16 March 2020).
- [110] Ultimaker. "Technical Data Sheet Nylon." Ultimaker. <https://ultimaker.com/download/74598/UM180821%20TDS%20Nylon%20RB%20V10.pdf> (accessed 1 May 2020).
- [111] Fillamentum. "Technical Data Sheet Nylon FX256." https://www.materialpro3d.cz/user/related_files/fillamentum_nylon_fx256_-_technical_data_sheet.pdf (accessed 1 May 2020).
- [112] Fast Radius. "Know your materials: PA 12." Fast Radius. <https://www.fastradius.com/resources/polyamide-12/> (accessed 18 March 2020).
- [113] Markforged Inc. "Material Datasheet Composite." <https://www-objects.markforged.com/craft/materials/CompositesV5.2.pdf> (accessed 18 January 2023).
- [114] 3D4Maker.com. "PEI Filament Ultem 1010." https://www.multi-3dprint.nl/images/3d4makers/TDS_PEI_ULTEM_1010.pdf (accessed 10 February 2020).
- [115] Stratasys. "ULTEM™ 1010 resin." <https://www.stratasys.com/materials/search/ultem1010> (accessed 28 March 2020).
- [116] Sabic. "ULTEM™ RESIN." <https://www.sabic.com/en/products/specialties/ultem-resins/ultem-resin> (accessed 1 May 2020).
- [117] 3dgence. "PEEK Filament " http://support.3dgence.com/twoje-pliki/downloader/1352/TDS_PEEK_Filament_1.pdf (accessed 20 November 2020).
- [118] Theplasticshop. "Ketron@1000 PEEK." https://www.theplasticshop.co.uk/plastic_technical_data_sheets/peek_1000_technical_data_sheet.pdf (accessed 23 March 2020).
- [119] CURBELL plastics. "PEEK Strong, stiff plastic with outstanding chemical resistance; performs over a wide range of temps." <https://www.curbellplastics.com/Research-Solutions/Technical-Resources/Technical-Resources/PEEK-Data-Sheet> (accessed 28 March 2020).
- [120] A. Wilson, "1 - The formation of dry, wet, spunlaid and other types of nonwovens," *Applications of Nonwovens in Technical Textiles*, pp. 3-17, 2010, doi: <https://doi.org/10.1533/9781845699741.1.3>.
- [121] P. Zhuo, S. Li, I. Ashcroft, A. Jones, and J. Pu, "3D printing of continuous fibre reinforced thermoplastic composites," in *the 21st International Conference on Composite Materials, ICCM21, ID, 2017*, vol. 4265.
- [122] H. Al Abadi, H.-T. Thai, V. Paton-Cole, and V. I. Patel, "Elastic properties of 3D printed fibre-reinforced structures," *Composite Structures*, vol. 193, pp. 8-18, 2018, doi: <https://doi.org/10.1016/j.compstruct.2018.03.051>.
- [123] A. D. Pertuz-Comas, J. G. Díaz, O. J. Meneses-Duran, N. Y. Niño-Álvarez, and J. León-Becerra, "Flexural Fatigue in a Polymer Matrix Composite Material Reinforced with Continuous Kevlar Fibers Fabricated by Additive Manufacturing," *Polymers*, vol. 14, no. 17, p. 3586, 2022. [Online]. Available: <https://www.mdpi.com/2073-4360/14/17/3586>.
- [124] K. Saeed *et al.*, "Characterization of continuous carbon fibre reinforced 3D printed polymer composites with varying fibre volume fractions," *Composite Structures*, vol. 282, p. 115033, 2022.
- [125] D. Yavas, Z. Zhang, Q. Liu, and D. Wu, "Interlaminar shear behavior of continuous and short carbon fiber reinforced polymer composites fabricated by additive manufacturing," *Composites Part B: Engineering*, vol. 204, p. 108460, 2021.
- [126] N. Li, Y. Li, and S. Liu, "Rapid prototyping of continuous carbon fiber reinforced polylactic acid composites by 3D printing," *Journal of Materials Processing Technology*, vol. 238, pp. 218-225, 2016, doi: <https://doi.org/10.1016/j.jmatprotec.2016.07.025>.
- [127] G. Chabaud, M. Castro, C. Denoual, and A. Le Duigou, "Hygromechanical properties of 3D printed continuous carbon and glass fibre reinforced polyamide composite for outdoor structural applications,"

- Additive Manufacturing*, vol. 26, pp. 94-105, 2019.
- [128] B. P. Heller, D. E. Smith, and D. A. Jack, "Effects of extrudate swell and nozzle geometry on fiber orientation in Fused Filament Fabrication nozzle flow," *Additive Manufacturing*, vol. 12, pp. 252-264, 2016, doi: <https://doi.org/10.1016/j.addma.2016.06.005>.
 - [129] T. Mulholland, S. Goris, J. Boxleitner, T. Osswald, and N. Rudolph, "Fiber Orientation Effects in Fused Filament Fabrication of Air-Cooled Heat Exchangers," *JOM*, vol. 70, no. 3, pp. 298-302, 2018, doi: <https://doi.org/10.1007/s11837-017-2733-8>.
 - [130] T. Hofstätter *et al.*, "Distribution and orientation of carbon fibers in polylactic acid parts produced by fused deposition modeling," in *ASPE Summer Topical Meeting 2016*, 2016.
 - [131] M. Rinaldi, M. Bragaglia, and F. Nanni, "Mechanical performance of 3D printed polyether-ether-ketone nanocomposites: An experimental and analytic approach," *Composite Structures*, vol. 305, p. 116459, 2023.
 - [132] T. Isobe, T. Tanaka, T. Nomura, and R. Yuasa, "Comparison of strength of 3D printing objects using short fiber and continuous long fiber," in *13th International Conference on Textile Composites (TEXCOMP-13)*, Milan, Italy, 17–19 September 2018 2018: IOP Publishing, p. 012042, doi: <https://doi.org/10.1088%2F1757-899x%2F406%2F1%2F012042>.
 - [133] R. Omer, H. S. Mali, and S. K. Singh, "Tensile performance of additively manufactured short carbon fibre-PLA composites: neural networking and GA for prediction and optimisation," *Plastics, Rubber and Composites*, vol. 49, pp. 271-280, 2020.
 - [134] M. Vinyas, S. Athul, and D. Harursampath, "Mechanical characterization of the Poly lactic acid (PLA) composites prepared through the Fused Deposition Modelling process," *Materials Research Express*, vol. 6, no. 10, p. 105359, 2019.
 - [135] G. Zhao *et al.*, "Tensile properties of 3D-printed CNT-SGF reinforced PLA composites," *Composites Science and Technology*, p. 109333, 2022.
 - [136] N. Giani, L. Mazzocchetti, T. Benelli, F. Picchioni, and L. Giorgini, "Towards sustainability in 3D printing of thermoplastic composites: evaluation of recycled carbon fibers as reinforcing agent for FDM filament production and 3D printing," *Composites Part A: Applied Science and Manufacturing*, p. 107002, 2022.
 - [137] A. El Magri, K. El Mabrouk, S. Vaudreuil, and M. Ebn Touhami, "Mechanical properties of CF-reinforced PLA parts manufactured by fused deposition modeling," *Journal of Thermoplastic Composite Materials*, vol. 34, pp. 581-595, 2021.
 - [138] F. Folgar and C. L. Tucker III, "Orientation behavior of fibers in concentrated suspensions," *Journal of reinforced plastics and composites*, vol. 3, no. 2, pp. 98-119, 1984, doi: <https://doi.org/10.1177/073168448400300201>.
 - [139] T. Yao, J. Ye, Z. Deng, K. Zhang, Y. Ma, and H. Ouyang, "Tensile failure strength and separation angle of FDM 3D printing PLA material: Experimental and theoretical analyses," *Composites Part B: Engineering*, vol. 188, p. 107894, 2020.
 - [140] S. Wang, Y. Ma, Z. Deng, S. Zhang, and J. Cai, "Effects of fused deposition modeling process parameters on tensile, dynamic mechanical properties of 3D printed polylactic acid materials," *Polymer testing*, vol. 86, p. 106483, 2020.
 - [141] S. R. Rajpurohit and H. K. Dave, "Analysis of tensile strength of a fused filament fabricated PLA part using an open-source 3D printer," *The International Journal of Advanced Manufacturing Technology*, vol. 101, no. 5-8, pp. 1525-1536, 2019.
 - [142] A. Rodríguez-Panes, J. Claver, and A. M. Camacho, "The influence of manufacturing parameters on the mechanical behaviour of PLA and ABS pieces manufactured by FDM: A comparative analysis," *Materials*, vol. 11, no. 8, p. 1333, 2018.
 - [143] B. Tymrak, M. Kreiger, and J. M. Pearce, "Mechanical properties of components fabricated with open-source 3-D printers under realistic environmental conditions," *Materials & Design*, vol. 58, pp. 242-246, 2014.
 - [144] T. Yao, Z. Deng, K. Zhang, and S. Li, "A method to predict the ultimate tensile strength of 3D printing polylactic acid (PLA) materials with different printing orientations," *Composites Part B: Engineering*, vol. 163, pp. 393-402, 2019.
 - [145] M. F. Afrose, S. Masood, P. Iovenitti, M. Nikzad, and I. Sbarski, "Effects of part build orientations on fatigue behaviour of FDM-processed PLA material," *Progress in Additive Manufacturing*, vol. 1, no. 1-2, pp. 21-28, 2016.
 - [146] A. N. Dickson, J. N. Barry, K. A. McDonnell, and D. P. Dowling, "Fabrication of continuous carbon, glass and Kevlar fibre reinforced polymer composites using additive manufacturing," *Additive Manufacturing*, vol. 16, pp. 146-152, 2017, doi: <https://doi.org/10.1016/j.addma.2017.06.004>.

- [147] Z. Zhang, Y. Long, Z. Yang, K. Fu, and Y. Li, "An investigation into printing pressure of 3D printed continuous carbon fiber reinforced composites," *Composites Part A: Applied Science and Manufacturing*, vol. 162, p. 107162, 2022.
- [148] A. A. Zia *et al.*, "Mechanical and energy absorption behaviors of 3D printed continuous carbon/Kevlar hybrid thread reinforced PLA composites," *Composite Structures*, vol. 303, p. 116386, 2023.
- [149] F. N. Chaudhry, S. I. Butt, A. Mubashar, A. B. Naveed, S. H. Imran, and Z. Faping, "Effect of carbon fibre on reinforcement of thermoplastics using FDM and RSM," *Journal of Thermoplastic Composite Materials*, vol. 35, pp. 352-374, 2022.
- [150] M. Heidari-Rarani, M. Rafiee-Afarani, and A. Zahedi, "Mechanical characterization of FDM 3D printing of continuous carbon fiber reinforced PLA composites," *Composites Part B: Engineering*, vol. 175, p. 107147, 2019.
- [151] J. Tey, W. Ding, W. Yeo, Y. King, and L. Saw, "3D printing of continuous kevlar reinforced polymer composite through coextrusion method," *IOP Conference Series: Earth and Environmental Science*, vol. 463, no. 1, p. 012091, 2020.
- [152] 3D4Makers B.V. "PLA Filament." https://cdn.shopify.com/s/files/1/0762/2839/files/TDS_PLA_Filament.pdf?1776946288798946561 (accessed 16 January 2021).
- [153] Y. Wan, Y. Wang, X. Xu, and Q. Li, "In vitro degradation behavior of carbon fiber-reinforced PLA composites and influence of interfacial adhesion strength," *Journal of applied polymer science*, vol. 82, no. 1, pp. 150-158, 2001.
- [154] 3D4Makers B.V. "PLA Filament." https://cdn.shopify.com/s/files/1/0762/2839/files/TDS_PLA_Filament.pdf?1776946288798946561 (accessed 16 January 2021).
- [155] Teijin Carbon. "Tenax@Short Fiber Product Data Sheet Chopped Fiber with Thermoplastic Sizing." <https://www.teijincarbon.com/products/tenaxr-carbon-fiber/tenaxr-short-fibers> (accessed 12 October 2020).
- [156] R. Yee and T. Stephens, "A TGA technique for determining graphite fiber content in epoxy composites," *Thermochimica Acta*, vol. 272, pp. 191-199, 1996.
- [157] Stephanie. "Modified Thompson Tau Test." <https://www.statisticshowto.com/modified-thompson-tau-test/> (accessed 15 December 2020).
- [158] A. Le Duigou, A. Barbé, E. Guillou, and M. Castro, "3D printing of continuous flax fibre reinforced biocomposites for structural applications," *Materials & Design*, vol. 180, p. 107884, 2019.
- [159] M. E. A. Papon, A. Haque, and R. S. MA, "Effect of nozzle geometry on melt flow simulation and structural property of thermoplastic nanocomposites in fused deposition modeling," in *the American Society for Composites, Thirty-Second Technical Conference*, West Lafayette, IN, USA, , 23–25 October 2017 2017.
- [160] Y. Ibrahim, A. Elkholy, J. S. Schofield, G. W. Melenka, and R. Kempers, "Effective thermal conductivity of 3D-printed continuous fiber polymer composites," *Advanced Manufacturing: Polymer & Composites Science*, vol. 6, no. 1, pp. 17-28, 2020.
- [161] I. Straumit, S. V. Lomov, and M. Wevers, "Quantification of the internal structure and automatic generation of voxel models of textile composites from X-ray computed tomography data," *Composites Part A: Applied Science and Manufacturing*, vol. 69, pp. 150-158, 2015.
- [162] M. Hartwich, N. Höhn, H. Mayr, K. Sandau, and R. Stengler, *FASEP ultra-automated analysis of fibre length distribution in glass-fibre-reinforced products* (SPIE Europe Optical Metrology). SPIE, 2009.
- [163] N. Krajangsawasdi, B. K. S. Woods, I. Hamerton, D. S. Ivanov, and M. L. Longana, "Highly Aligned Discontinuous Fibre Composite Filaments for Fused Deposition Modelling: Open-Hole Case Study," in *Composites Meet Sustainability – Proceedings of the 20th European Conference on Composite Materials, ECCM20*, Lausanne, Switzerland, 26–30 June 2022 2022.
- [164] S. Grieder *et al.*, "Consolidation of Additive Manufactured Continuous Carbon Fiber Reinforced Polyamide 12 Composites and the Development of Process-Related Numerical Simulation Methods," *Polymers*, vol. 14, no. 16, p. 3429, 2022.
- [165] S. H. Sanei, A. Arndt, and R. Doles, "Open hole tensile testing of 3D printed continuous carbon fiber reinforced composites," *Journal of Composite Materials*, vol. 54, no. 20, pp. 2687-2695, 2020.
- [166] H. Zhang, A. Li, J. Wu, B. Sun, C. Wang, and D. Yang, "Effectiveness of fibre placement in 3D printed open-hole composites under uniaxial tension," *Composites Science and Technology*, vol. 220, p. 109269, 2022.
- [167] S. B. Khan, S. Irfan, S. S. Lam, X. Sun, and S. Chen, "3D printed nanofiltration membrane technology for waste water distillation," *Journal of Water Process Engineering*, vol. 49, p. 102958, 2022.
- [168] S. Khan, K. Fayazbakhsh, Z. Fawaz, and M. A. Nik, "Curvilinear variable stiffness 3D printing technology for improved open-hole tensile strength," *Additive Manufacturing*, vol. 24, pp. 378-385, 2018.

- [169] N. Li *et al.*, "Path-designed 3D printing for topological optimized continuous carbon fibre reinforced composite structures," *Composites Part B: Engineering*, vol. 182, p. 107612, 2020.
- [170] B. C. Kim, K. Potter, and P. M. Weaver, "Continuous tow shearing for manufacturing variable angle tow composites," *Composites Part A: Applied Science and Manufacturing*, vol. 43, no. 8, pp. 1347-1356, 2012.
- [171] L. Goodfellow Cambridge. "Poly L lactic acid - Biopolymer - Film." <https://www.goodfellow.com/uk/en-gb/displayitemdetails/p/me33-fm-000150/poly-l-lactic-acid-biopolymer-film> (accessed 11 November 2022, 2022).
- [172] K. Agarwal, S. K. Kuchipudi, B. Girard, and M. Houser, "Mechanical properties of fiber reinforced polymer composites: A comparative study of conventional and additive manufacturing methods," *Journal of Composite Materials*, vol. 52, no. 23, pp. 3173-3181, 2018.
- [173] C. Oztan *et al.*, "Microstructure and mechanical properties of three dimensional-printed continuous fiber composites," *Journal of Composite Materials*, vol. 53, no. 2, pp. 271-280, 2019.
- [174] S. H. R. Sanei, Z. Lash, J. Servey, F. Gardone, and C. P. Nikhare, "Mechanical properties of 3D printed fiber reinforced thermoplastic," in *ASME International Mechanical Engineering Congress and Exposition*, 2019, vol. 59490: American Society of Mechanical Engineers, p. V012T10A016.
- [175] H. Mei, Z. Ali, I. Ali, and L. Cheng, "Tailoring strength and modulus by 3D printing different continuous fibers and filled structures into composites," *Advanced Composites and Hybrid Materials*, vol. 2, no. 2, pp. 312-319, 2019.
- [176] A. international, "ASTM D2344/D2344M-22 Standard Test Method for Short-Beam Strength of Polymer Matrix Composite Materials and Their Laminates," 16 August 2022 2022, vol. 15.03.
- [177] C. Pascual-González *et al.*, "Post-processing effects on microstructure, interlaminar and thermal properties of 3D printed continuous carbon fibre composites," *Composites Part B: Engineering*, vol. 210, p. 108652, 2021.
- [178] Z. Xin, Y. Ma, Y. Chen, B. Wang, H. Xiao, and Y. Duan, "Fusion-bonding performance of short and continuous carbon fiber synergistic reinforced composites using fused filament fabrication," *Composites Part B: Engineering*, vol. 248, p. 110370, 2023.
- [179] X. Wang, X. Zhao, Z. Wu, Z. Zhu, and Z. Wang, "Interlaminar shear behavior of basalt FRP and hybrid FRP laminates," *Journal of Composite Materials*, vol. 50, no. 8, pp. 1073-1084, 2016.
- [180] M. Caminero, J. Chacón, I. García-Moreno, and J. Reverte, "Interlaminar bonding performance of 3D printed continuous fibre reinforced thermoplastic composites using fused deposition modelling," *Polymer Testing*, vol. 68, pp. 415-423, 2018.
- [181] R. Matsuzaki *et al.*, "Effects of set curvature and fiber bundle size on the printed radius of curvature by a continuous carbon fiber composite 3D printer," *Additive Manufacturing*, vol. 24, pp. 93-102, 2018.
- [182] T. Fruleux, M. Castro, D. Correa, K. Wang, R. Matsuzaki, and A. Le Duigou, "Geometric limitations of 3D printed continuous flax-fiber reinforced biocomposites cellular lattice structures," *Composites Part C: Open Access*, vol. 9, p. 100313, 2022.
- [183] J.-R. Ai, F. Peng, P. Joo, and B. D. Vogt, "Enhanced Dimensional Accuracy of Material Extrusion 3D-Printed Plastics through Filament Architecture," *ACS Applied Polymer Materials*, vol. 3, no. 5, pp. 2518-2528, 2021.
- [184] H. Shiratori, A. Todoroki, M. Ueda, R. Matsuzaki, and Y. Hirano, "Mechanism of folding a fiber bundle in the curved section of 3D printed carbon fiber reinforced plastics," *Advanced Composite Materials*, vol. 29, no. 3, pp. 247-257, 2020.
- [185] M. Yamawaki and Y. Kouno, "Fabrication and mechanical characterization of continuous carbon fiber-reinforced thermoplastic using a preform by three-dimensional printing and via hot-press molding," *Advanced Composite Materials*, vol. 27, no. 2, pp. 209-219, 2018.
- [186] U. Delli and S. Chang, "Automated process monitoring in 3D printing using supervised machine learning," *Procedia Manufacturing*, vol. 26, pp. 865-870, 2018.
- [187] Z. Jin, Z. Zhang, and G. X. Gu, "Autonomous in-situ correction of fused deposition modeling printers using computer vision and deep learning," *Manufacturing Letters*, vol. 22, pp. 11-15, 2019.
- [188] L. Lu, J. Hou, S. Yuan, X. Yao, Y. Li, and J. Zhu, "Deep learning-assisted real-time defect detection and closed-loop adjustment for additive manufacturing of continuous fiber-reinforced polymer composites," *Robotics and Computer-Integrated Manufacturing*, vol. 79, p. 102431, 2023.
- [189] K. J. Åström and T. Hägglund, "The future of PID control," *Control engineering practice*, vol. 9, no. 11, pp. 1163-1175, 2001.
- [190] K. Sugiyama, R. Matsuzaki, M. Ueda, A. Todoroki, and Y. Hirano, "3D printing of composite sandwich structures using continuous carbon fiber and fiber tension," *Composites Part A: Applied Science and Manufacturing*, vol. 113, pp. 114-121, 2018.
- [191] S. Reich, S. Berndt, C. Kühne, and H. Herstell, "Accuracy of 3D-Printed Occlusal Devices of Different

- Volumes Using a Digital Light Processing Printer," *Applied Sciences*, vol. 12, no. 3, p. 1576, 2022. [Online]. Available: <https://www.mdpi.com/2076-3417/12/3/1576>.
- [192] S. M. F. Kabir, K. Mathur, and A.-F. M. Seyam, "The Road to Improved Fiber-Reinforced 3D Printing Technology," *Technologies*, vol. 8, no. 4, p. 51, 2020. [Online]. Available: <https://www.mdpi.com/2227-7080/8/4/51>.
- [193] J. Zhang, Z. Zhou, F. Zhang, Y. Tan, Y. Tu, and B. Yang, "Performance of 3D-Printed Continuous-Carbon-Fiber-Reinforced Plastics with Pressure," *Materials*, vol. 13, no. 2, p. 471, 2020. [Online]. Available: <https://www.mdpi.com/1996-1944/13/2/471>.
- [194] 9T lab. "RED SERIES®ADDITIVE FUSION SOLUTION." www.9tlabs.com/solutions/additive-fusion-solution (accessed 9 January 2023).
- [195] Composites world. "Markforged raises \$82 million to expand product line." <https://www.compositesworld.com/news/markforged-raises-82-million-to-expand-product-line> (accessed 19 January 2023).
- [196] "Formula 1." <https://www.pinterest.co.uk/pin/559713059945253739/> (accessed 19 January 2023).
- [197] B. K. Post *et al.*, "Big area additive manufacturing application in wind turbine molds," in *2017 International Solid Freeform Fabrication Symposium*, University of Texas at Austin, 2017.
- [198] N. H. Simpson. "Prosthetic Leg (3D printed)." <https://www.behance.net/gallery/17815481/Natasha-Hope-Simpson-Prosthetic-Leg-%283D-printed%29> (accessed 19 January 2023).
- [199] "Aircraft Military Drone." <https://www.pngall.com/military-drone-png> (accessed 19 January 2023).
- [200] J. Sloan. "Off-grid turbine: Helix in the wind." <https://www.compositesworld.com/articles/off-grid-turbine-helix-in-the-wind> (accessed 19 January 2023).
- [201] Buehler SumMet, *The Sum of Our Experience: A Guide to Materials Preparation and Analysis*. 2018.